Exploring Himawari-8 Geostationary Observations for the Advanced Coastal Monitoring of the Great Barrier Reef

Larissa Patricio Valerio

June 2021

For the Degree of Doctor of Philosophy

College of Science and Engineering

James Cook University

Statement of Contribution of Others

This thesis was conducted under the shared supervision of:

- Dr. Scott Smithers, Associate Professor, College of Science and Engineering, James Cook University (JCU), Townsville, Australia
- Dr. Michelle Devlin, Senior Research Scientist, Centre of Environment, Fisheries and Aquaculture Science (CEFAS), Lowestoft, United Kingdom.
- Dr. Thomas Schroeder, Senior Research Scientist, Commonwealth Scientific Industrial Research Organization (CSIRO), Oceans and Atmosphere, Brisbane, Australia.

Dr. Thomas Schroeder proposed the topic of this thesis. The supervisory team contributed to the conceptual development, design, data analysis, interpretation, and editorial assistance for all chapters of this thesis, as well as for conference presentations. Dr. Thomas Schroeder provided access to the Artificial Neural Network inversion codes and tools for plotting and parameterization of the MOMO radiative transfer code. Prof. Juergen Fischer (Institute of Space Sciences, Department of Earth Sciences, *Freie Universitaet Berlin*) kindly provided access to the MOMO radiative transfer code. Dr. Britta Schaffellke, Michelle Skuza and Dr. Renee Gruber (AIMS) provided access to valuable *in situ* data.

Dr. Yi Qin (CSIRO O&A) provided the tools for acquiring and processing Himawari-8 data and the cloud masks. Dr. David Blondeau-Patissier (CSIRO O&A) helped with processing the ancillary datasets and provided valuable assistance with IDL programming. Erin Kenna (CSIRO O&A) facilitated general data processing and mapping in Python. Dr. Liz Tynan (JCU), Dr. Ellie Bergstrom, Dr. John Gittings and Dr. Tim Malthus (CSIRO O&A) helped with reviews, discussions, and useful suggestions.

Acknowledgements

I am deeply indebted to my supervisors, Michelle, Scott, and Thomas for their continuous support, hard work, patience, kindness and understanding. I would like to extend my deepest gratitude to Thomas Schroeder for offering me the opportunity of doing my PhD research at CSIRO. Thomas has made a colossal contribution to the technical development of this thesis, and I feel privileged to have learned so much from him. I hope this dissertation modestly reflects his unparalleled efforts in teaching, guiding, and providing essential feedback to the successful completion of my PhD. I wholeheartedly thank Scott Smithers, for allowing my candidature to run as smoothly as possible and for offering a solid, safe, and friendly ground for my personal and professional development. Scott's instrumental participation on the evolution of my writing and presentation skills is also greatly appreciated. I am extremely grateful to Michelle Devlin, for her inspiring optimism, encouragement, and profound belief in my work. Michelle's extensive expertise has provided invaluable insights on the practical implications of this thesis for the monitoring and management of the Great Barrier Reef.

My gratitude also goes to the CSIRO staff and colleagues, for their assistance and comradery. Thanks to JCU staff for their administrative assistance, to the Wellbeing support team for invaluable counselling sessions. This work would have not been possible without the financial support provided by the Brazilian government (*CNPq*, process n° 2016339/2014-3) to cover stipend and tuition fees from July 2015 to July 2019. JCU provided critical pandemic relief funding from May to October 2020 through the Extraordinary Student Support, a Competitive Research Training Grant for attendance to the XXIV Ocean Optics conference (Croatia, 2018) and to the Australian Marine Sciences Association (AMSA) conference (Fremantle, 2019). CSIRO is acknowledged for providing office space and access to computer infrastructure at the Ecosciences Precinct in Brisbane (2016-2021). The Japan Meteorological Agency is acknowledged for the operation of Himawari-8 and data distribution through the Australian Bureau of Meteorology. The *in-situ* data was sourced from Australia's Integrated Marine Observing System (IMOS) – IMOS is enabled by the National Collaborative Research Infrastructure Strategy (NCRIS).

I would like to thank my parents for having invested so heavily in my education and for unconditionally supporting my academic achievements. I am grateful to all the IOCCG 2016 Summer Lecture Series colleagues and lecturers for sharing their knowledge and passion. My genuine gratitude to Gina, Cecilia, John, Julian, Leonie, Erin, Ellie, Jaramar, Tessa, Catherine & Erick for their everlasting care and encouragement and to all my friends here and there and elsewhere, for keeping me afloat while I navigated these uncharted waters.

To 'Vó Maria', whose hugs I miss the most.

What the tide scribbles in the mud

I know these waters well, I fancy
but I remember what is still to come,
one day I will be fine ash, suspended
in a column of light, dispersed
like the silt at the tide's beck and call
impeding the passage of ships
and supporting the strutting of stilts

poaka, kuaka, tōrea, kawau,

and overhead a frenzy of terns
wheeling and diving
the mud-backed mirrors flashing their messages
a hundred urgent ways to say one thing,

at the end, the sure and certain hope,
first the scattering and then the gathering
into the sea's warm and kindly arms

William Butler Smith (Anne French)

Abstract

Remote sensing of ocean colour has been fundamental to the synoptic-scale monitoring of marine water quality of the Great Barrier Reef (GBR). However, polar orbiting satellites such as MODIS-Aqua and Sentinel-3 have insufficient revisit capability for observing diurnal variability in highly dynamic coastal environments such as the GBR. To overcome this limitation, this work presents a physics-based coastal ocean colour algorithm for the Advanced Himawari Imager (AHI) on-board Himawari-8 geostationary satellite. Despite being designed for meteorological applications, AHI offers the opportunity to estimate ocean colour features every 10 minutes, in four broad visible and near-infrared spectral bands and at 1 km^2 spatial resolution. Chapter 1 situated the research in the context of relevant literature, identified research gaps and defined thesis objectives. In Chapter 2, coupled ocean-atmosphere radiative transfer simulations of the AHI bands were carried out for a realistic range of in-water and atmospheric optical properties of the GBR and for a wide range of solar and observation geometries. The simulations were used to develop an inverse model based on Artificial Neural Network techniques to estimate Total Suspended Solids (TSS), Chlorophyll-a concentration (CHL) and Yellow substances (YEL) directly from the top-of atmosphere spectral reflectances. In Chapter 3, the algorithm was validated with concurrent *in situ* data across the coastal GBR and the detection limits were assessed in Chapter 4. CHL retrievals presented relative errors up to 70% with absolute errors around 4 mg m^{-3} and large negative bias of 0.47 mg m^{-3}. Conversely, YEL was retrieved with relative errors around 57% and absolute errors of 3.4 m^{-1} and bias around -0.36 m^{-1}. On the other hand, TSS retrievals presented relative errors up to 75% and absolute errors of 2 mg L^{-1}, low positive bias of 0.014 within the validation range of 0.14 to 24 mg L^{-1}. The detection limit for TSS retrievals from Himawari-8 is 0.25 mg L^{-1}, comparable to those of the gravimetric method for TSS determination, of 0.4 mg L^{-1}. Finally in Chapter 5, the TSS algorithm was applied to resolve for the first time, diurnal-scale water quality fluctuations in the coastal GBR from 10-minutes Himawari-8 observations. The applications demonstrate the potential of more frequent observations for the improvement of monitoring and management of the water quality in the GBR.

Table of Contents

List of Figures

List of Tables

List of Symbols

Symbol	Description	Units
a	Absorption coefficient	m^{-1}
a_{phy}	Absorption coefficient of phytoplankton	m^{-1}
a_{nap}	Absorption coefficient of non-algal particles	m^{-1}
a_{yel}	Absorption coefficient of yellow substances	m^{-1}
a_w	Absorption coefficient of pure water	m^{-1}
a_{O_3}	Absorption coefficient of ozone	m^{-1}
A	Area	m^2
b	Scattering coefficient	m^{-1}
b_p	Scattering coefficient of particles	m^{-1}
b_w	Scattering coefficient of pure water	m^{-1}
b_b	Backscattering coefficient	m^{-1}
b_p^*	Mass specific scattering coefficient of particles	$m^2 g^{-1}$
$\tilde{b}_b$	Backscattering probability ratio	dimensionless
β	Volume scattering function	$m^{-1} sr^{-1}$
$\tilde{\beta}$	Scattering phase function	sr^{-1}
$\tilde{\beta}_R$	Rayleigh scattering phase function	sr^{-1}
c	Attenuation coefficient	m^{-1}
CHL	Chlorophyll-a concentration	$mg\ m^{-3}$
CH_4	Methane	dimensionless
CO	Carbon Oxide	dimensionless
CO_2	Carbon Dioxide	dimensionless
E	Spectral Irradiance	$W\ m^{-2}\ nm^{-1}$
E_d	Spectral Downwelling Irradiance	$W\ m^{-2}\ nm^{-1}$
E_u	Spectral Upwelling Irradiance	$W\ m^{-2}\ nm^{-1}$
$\overline{F}_{ø}$	Mean Extra-Terrestrial Solar Irradiance	$W m^2 sr^{-1} \mu m^{-1}$
$F_{ø}$	Sun-Earth Distance Corrected $\overline{F}_{ø}$	$W m^2 sr^{-1} \mu m^{-1}$
H_2SO_4	Sulfuric acid	dimensionless
H_2O	Water	dimensionless
L	Spectral Radiance	$W\ m^{-2} sr^{-1} nm^{-1}$
L_{TOA}	Spectral Radiance at the Top of the Atmosphere	$W\ m^{-2} sr^{-1} nm^{-1}$
M	Total air mass	dimensionless
$\widetilde{M}$	Median value of a pixel-box	dimensionless
μ	Mean value	dimensionless
$\bar{X}$	Temporal aggregated observation by the mean value	dimensionless
m	*In situ* measurement	dimensionless
N_2O	Nitrous Oxide	dimensionless

N	Number of elements or samples	dimensionless
$\boldsymbol{n}$	Number of neurons	dimensionless
O_2	Oxygen	dimensionless
$[O_3]$	Ozone concentration	Dobson Units (DU)
p	Satellite product	dimensionless
P	Atmospheric pressure	hPa
P_0	Standard atmospheric pressure (1013.25)	hPa
Q	Flux of radiant energy	Joules
R	Radiance ratio (diffuse reflectance)	dimensionless
R_{rs}^{TOA}	Remote sensing reflectance at the top of the atmosphere	sr^{-1}
σ	Standard deviation	dimensionless
S	Sigmoid function	dimensionless
S_{NAP}	Spectral slope of non-algal particle absorption	nm^{-1}
S_{YEL}	Spectral slope of yellow substances absorption	nm^{-1}
t	Time	hours, minutes, or seconds
Δt	Time difference	
τ	Optical thickness	dimensionless
τ_a	Aerosol Optical thickness	dimensionless
τ_{O_3}	Ozone Optical thickness	dimensionless
τ_R	Rayleigh Optical thickness	dimensionless
T_{O_3}	Transmission due to ozone molecules	dimensionless
TSS	Total suspended solids concentration	$mg\ L^{-1}$
v	Volume in litres, megalitres or cubic metres	$\mathrm{L}, \mathrm{ML}, m^3$
δ	Depolarization factor	dimensionless
$\Delta\phi$	Relative azimuth angle	degrees
θ_s	Solar zenith angle	degrees
θ_v	Viewing zenith angle	degrees
θ	Scattering angle	degrees
Ω	Spatial aperture or solid angle	sr
λ	Wavelength	$\mu m, nm$
ω_0	Single scattering albedo	dimensionless
w	Wind speed	ms^{-1}
$\boldsymbol{W}$	Weight matrix	dimensionless
$\vec{x}$	Input vector	dimensionless
(x, y, z)	Three-dimensional Cartesian coordinates	dimensionless
z	Vertical coordinate, depth, thickness of a medium	m
$\vec{y}_o$	Computed output vector	dimensionless
$\vec{y}_t$	Target output vector	dimensionless
YEL	Yellow substances absorption (443 nm)	m^{-1}

List of Abbreviations

ABI	Advanced Baseline Imager
ACTFR	Australian Centre for Tropical Freshwater Research
AERONET	Aerosol Robotic Network
AEST	Australian Eastern Standard Time
AGGOBS	Aggregated Observations
AGGTSS	Aggregated Total Suspended Solids
AGRI	Advanced Geostationary Radiation Imager
AHI	Advanced Himawari Imager
AIMS	Australian Institute for Marine Sciences
AM	Aerosol Assemblage
AMI	Advanced Meteorological Imager
ANN	Artificial Neural Networks
AODN	Australian Observation Data Network
AOP	Apparent Optical Properties
AU	Astronomical Units
L-BFGS	Limited Broyden Fletcher Goldfarb Shanno
BODB	Bio-Optical Data Base
BOM	Bureau of Meteorology
CALIOP	Cloud-Aerosol Lidar with Orthogonal Polarization
CMA	China Meteorological Administration
COASTLOOC	Coastal Surveillance Through Observations of Ocean Colour
COMS	Communication Ocean and Meteorological Satellite
CSIRO	Commonwealth Scientific and Industrial Research Organization
CZCS	Coastal Zone Colour Scanner
DN	Digital Numbers
DOY	Day of the Year
DU	Dobson Units
ECO-BB9	Environmental Characterization Optics - Backscattering Instrument
EMS	Environmental Modelling Suite
ESA	European Space Agency
ETM	Enhanced Thematic Mapper
FCI	Flexible Combined Imager
FNU	Formazin Nephelometric Unit
FY	FengYun
GBRMPA	Great Barrier Reef Marine Park Authority
GBR	Great Barrier Reef
GCOM	Global Change Observation Mission
GEO	Geostationary Earth Orbit

GF/F	Glass Fibre Filter
GIS	Geographic Information System
GLMIR	Geosynchronous Littoral Imaging and Monitoring Radiometer
GOCI	Geostationary Ocean Colour Imager
GOES	Geostationary Operational Environmental Satellite
HID	Hidden Layer Neurons
HITRAN	High-Resolution Transmission Molecular Absorption
HPLC	High Performance Liquid Chromatography
HSD	Himawari-8 Standard Data
IMOS	Integrated Marine Observation System
IOCCG	International Ocean Colour Coordinating Group
IOP	Inherent Optical Properties
JAXA	Japan Aerospace Exploration Agency
JCU	James Cook University
JMA	Japan Meteorological Agency
KARI	Korea Aerospace Research Institute
KIOST	Korean Institute of Ocean Science and Technology
KOMPSAT	Korean Multi-Purpose Satellite
LEO	Low Earth Orbit
LJCO	Lucinda Jetty Coastal Observatory
LMI	Linear Matrix Inversion
MAPE	Mean Absolute Percentage Error
MERIS	Medium Resolution Imaging Spectrometer
MET	Meteorological
METEOSAT	Meteorological Satellites
ML	Mega Litres
MLP	Multilayer Perceptron
MM	Masking Method
MMP	Marine Monitoring Program
MODIS	Moderate Resolution Imaging Spectrometer
MOMO	Matrix Operator Model
MSE	Mean Squared Error
MSI	Multi Spectral Instrument
MSQ	Maritime Safety Queensland
MTG	Meteosat Third Generation
MTSAT	Multi-functional Transport Satellite
NAP	Non-Algal Particles
NASA	National Aeronautics and Space Administration
NCAR	National Centre for Atmospheric Research
NCEP	National Centre for Environmental Prediction
NCI	National Computing Infrastructure

NIR	Near Infrared Radiation
NOAA	National Oceanic Atmospheric Administration
NPP	National Polar-orbiting Partnership
NRM	Natural Resource Management
O&A	Oceans & Atmosphere
OC	Ocean Colour
OLI	Operational Land Imager
PCA	Principal Component Analysis
PPS	Principal Point of Sun glint
PSU	Practical Salinity Units
QGIS	Quantum-GIS
QGOV	Queensland Government
QLD	Queensland
RGB	Red, Green, Blue
RMSE	Root Mean Squared Errors
RT	Radiative Transfer
RTE	Radiative Transfer Equation
RV	Research Vessel
SBUV	Solar Backscatter Ultraviolet Radiometer,
SCIATRAN	Radiative Transfer Model and Retrieval Algorithm
SEVIRI	Spinning Enhanced Visible and Infrared Imager
SGLI	Second Generation GLobal Imager
SINGOBS	Single Observation
SINGTSS	Single Total Suspended Solids
SNR	Signal to Noise Ratios
SNPP	Suomi National Polar-orbiting Partnership
SWIR	Short Wave Infrared Radiation
TOA	Top of the Atmosphere
TOAST	Total Ozone Analysis using SBUV/2 and TOVS
TOVS	TIROS Operational Vertical Sounder
TRN	Training Dataset
TST	Testing Dataset
UNESCO	United Nations Educational, Scientific and Cultural Organization
UTC	Coordinated Universal Time
UV	Ultra-Violet Radiation
VIIRS	Visible Infrared Imaging Radiometer Suite
VIS	Visible Radiation
VNIR	Visible and Near Infrared Radiation
VSF	Volume Scattering Function
WCP	World Climate Research Programme
WQP	Water Quality Parameters

Chapter 1: Introduction

The Great Barrier Reef (GBR) of Australia is an iconic, biodiverse, and complex ecosystem. With nearly 3,000 coral reefs distributed along the Queensland coastline (~2,300 km), the GBR is large enough to be visible from space (Figure 1.1). Due to its intrinsic ecological value, the GBR Marine Park was listed as a World Heritage Site to be managed and protected for future generations (Great Barrier Reef Marine Park Authority, 1975, 1981). However, despite this protection, the GBR has been negatively affected by the direct and indirect impacts of natural and anthropogenic pressures such as climate change (Hughes et al., 2018a; 2018b) and declining water quality (Waterhouse et al., 2017a; Wolff et al., 2018; Brodie et al., 2019).

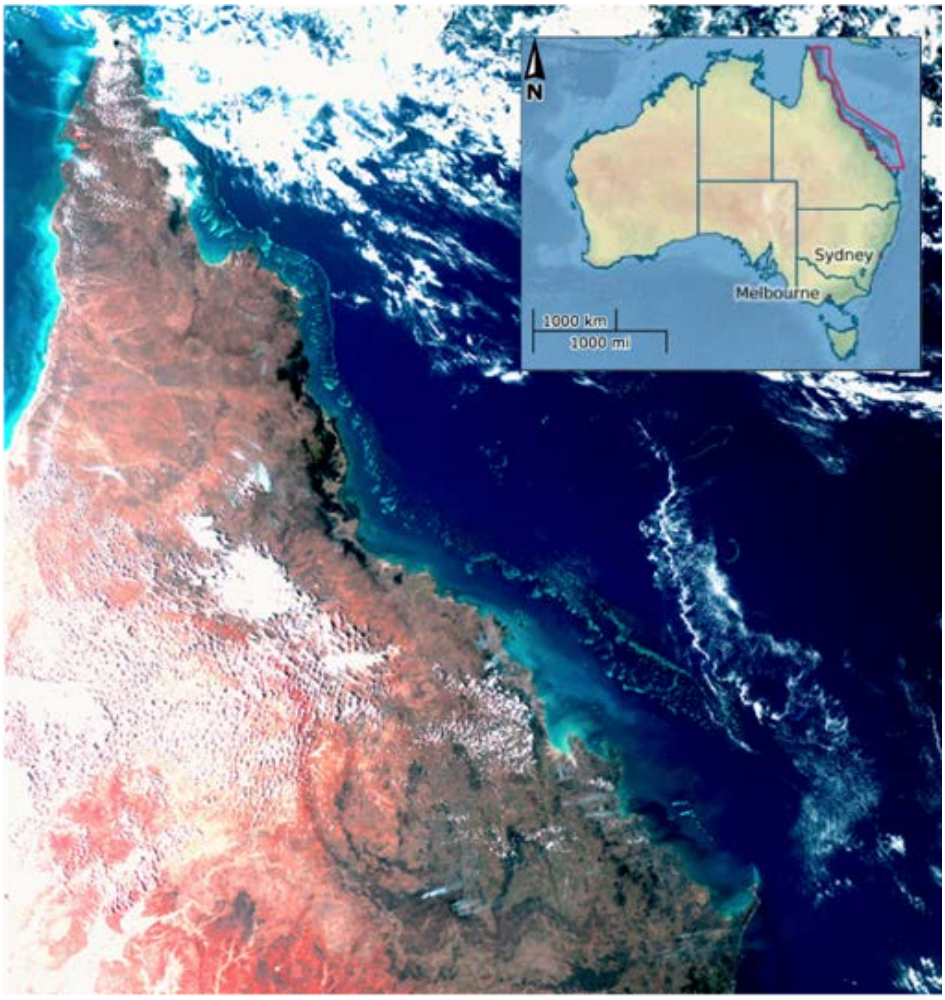

Figure 1.1: Himawari-8 near-true colour composite of the Queensland coast and adjacent coastal waters including the Great Barrier Reef. A map of Australia is enclosed for reference, with the GBR Marine Park delineated in red. Image scanned on 27th of October 2017 at 05:00 UTC (15:00 AEST).

Water quality decline is commonly associated with modifications to catchment land-use and seasonal freshwater runoff to the GBR (Fabricius et al., 2014; Kroon et al., 2016; Bainbridge et al., 2018;

Waterhouse et al., 2018). Thirty-five major rivers drain into the GBR lagoon[1], comprising the largest external source of 'new' nutrients to the GBR (Bartley et al., 2017). However, the terrestrial sediment and nutrient concentrations annually entering the GBR have increased more than 5-fold since European settlement (Furnas, 2003; McCulloch et al., 2003; McKergow et al., 2005; Kroon et al., 2012).

Acute and chronic exposure of coral reefs to excess nutrients and fine suspended sediments is linked to increased coral mortality rates, as well as compromised resilience and recovery following disturbance events (Fabricius, 2005; De'ath et al., 2012; Ricardo et al., 2015; Lam et al., 2018; Ortiz et al., 2018; MacNeil et al., 2019; Mellin et al., 2019; Thompson et al., 2021). Likewise, declining water quality negatively impact seagrass abundance (Petus et al., 2016; Wooldridge, 2017; McKenzie et al., 2021) and may drive outbreaks of coral-eating crown-of-thorns starfish (Brodie et al., 2017; Pratchett et al., 2017; Matthews et al., 2020). Hence, adequate monitoring of water quality fluctuations in the GBR lagoon is crucial for ensuring appropriate management and protection of its ecosystems. Ocean colour remote sensing observations, biogeochemical modelling and *in situ* water quality sampling have been used to monitor the GBR from daily to inter-annual temporal scales (Devlin et al., 2015b; Gruber et al., 2020; State of Queensland and Commonwealth of Australia, 2021). However, the GBR is subject to high-frequency coastal processes, such as tides, winds, episodic floods, and algal blooms (Blondeau-Patissier et al., 2018; Petus et al., 2019). Therefore, hourly to diurnal observations at relevant spatial resolutions are required to resolve the complex water quality dynamics and for the successful monitoring and management of the entire GBR. The scope of this literature review is to:

a. Summarise the current knowledge on the dynamics of water quality in the GBR.
b. Describe how remote sensing of ocean colour has been incorporated into the marine monitoring program of the GBR and to identify the needs for improved monitoring.
c. Explore the use of geostationary remote sensing observations as an alternative for the advanced monitoring of the GBR at diurnal scales.

[1] The GBR lagoon is defined here as the water body between the Queensland coastline and the outer reefs.

1.1 Coastal Water Quality in the GBR

Declining water quality in the GBR has been largely associated with the seasonal delivery of freshwater runoff from adjacent catchments to the coastal waters. Catchment runoff carries a complex mixture of sediments, nutrients and contaminants, discharged in discrete flood events and forming turbidity plumes in the GBR (Furnas, 2003; Devlin et al., 2015b). The volumes of freshwater runoff are controlled by a range of factors that regulate the rainfall such as monsoonal variations, tropical cyclones and global climate variability (Lough, 2007; Waters et al., 2014). The freshwater inputs are more significant during the wet season (November to April inclusive), because two-thirds of the total annual rainfall occurs in this period (Devlin, 2005).

The loads of sediments and other contaminants may be increased up to 100 times above ambient concentrations in the inshore GBR (i.e., depths lower than ~30 m) during floods (Devlin et al., 2012a). For instance, the Burdekin River catchment is a major source of freshwater, sediment, and nutrient inputs to the GBR lagoon (Kroon et al., 2012). It covers around 130,000 km^2, which represents approximately one third of the area draining into the GBR, most of which (93%) has been modified for uses such as beef grazing and sugar cane (Lewis et al., 2006). During average floods, the Burdekin discharges about 3 to 5 million ML/event, or around ~100,000 ML/day compared to base flow conditions (~1000 ML/day) (Lewis et al., 2006). As a result, it has been estimated that ~5 millions of tonnes of sediments are exported during an average flood event, a 10 times increase compared to estimated 'natural' loads (~500,000 tonnes per year) (Brodie et al., 2009). Conversely, in years of very large to extreme flood events, such as those followed by landfall of tropical cyclones, the Burdekin River may discharge more than 30 million ML of freshwater annually (Lewis et al., 2006).

On entering the coastal waters[2] of the GBR, the freshwater turbidity plumes are subject to short temporal scale (hourly to weekly) oceanographic processes, such as tides and winds (Wolanski, 1994; Xiao et al., 2019), driving diurnal to seasonal changes in the water quality parameters (Oubelkheir et al., 2006; Blondeau-Patissier et al., 2009). The plume may rapidly change its dispersal direction (North to South) within a day in response to changing winds (Devlin et al., 2001; Lewis et al., 2006). During calm wind conditions, the plume can move offshore and south, whereas during strong south-easterly winds the plumes are generally restricted near-shore and move northward (Devlin et al., 2001; Devlin and Brodie, 2005). Turbidity plumes may travel further than 100 km from the stream mouth, but derived material, such as particulate and dissolved substances may be detected nearly 200 km away from the terrigenous source (Devlin, 2005; Devlin and Brodie, 2005; Schroeder et al., 2012). For

[2]Coastal waters are defined by the Australian Marine Jurisdiction as the maritime area within 3 nautical miles (~5km) from the mainland. However, in this work, coastal waters include those within the GBR lagoon subject to the above-mentioned coastal processes, particularly to tides and freshwater runoff.

example, the Moderate Resolution Imaging Spectrometer (MODIS/Aqua) near-true colour composite (Figure 1.2) shows the Burdekin River plume (light brown) nearly reaching the reef matrix, about ~50 km from its mouth.

Figure 1.2: MODIS/Aqua satellite near-true colour image of the Burdekin River flood plume on 22nd of February 2008. In this near-true colour image, it is possible to distinguish coastal turbid waters from oceanic deep blue waters. A few scattered clouds (white) and sun glint effects are visible in the top-left side of the image, close to Hinchinbrook Island (Image courtesy: Dieter Tracy).

In addition, tidal fluxes may drive hourly to diurnal fluctuations in Total Suspended Solids (TSS) concentrations over a short spatial scale (few kilometres) (Bainbridge et al., 2012; Fabricius et al., 2014). In the wet season, parameters such as Chlorophyll-a concentration (CHL, indicative of nutrient input) may vary by a factor of 6 within 12 hours (Oubelkheir et al., 2014). In the dry season, semidiurnal tides may promote a smaller but substantial CHL variation (1.6 times), whereas TSS may increase by a factor of 20 at the same site in the coastal GBR (Oubelkheir et al., 2006). However, during flood events, the regular tidal variability and local currents may be overlaid with the high loads of freshwater discharge, characterising intricate hydrodynamic processes in the coastal GBR (Oubelkheir et al., 2014; Xiao et al., 2019).

The resuspension of particles due to tidal variability, and potentially by winds, is illustrated in Figure 1.3, between 15th and 20th of June 2011, during a typical dry season month in the GBR. Two

subsequent near-true colour observations were acquired from the Medium Resolution Imaging Spectrometer (MERIS) satellite sensor in the Whitsundays Islands region. On the left image (15th June 2011), turbid waters, indicated by the mix of blue/green, are observed between the coastline and the outer reefs during changes of the tidal phase. Meanwhile, the right panel image (20th June 2011) illustrates a strong colour separation between deep blue waters and the shallower coastal waters (turquoise), where resuspended material is trapped inshore.

Figure 1.3: Great Barrier Reef near Whitsundays Islands, observed with MERIS during different tidal cycles. Resuspension is affecting the optical properties as visible in the image of the 15th of June 2011. Five days later (20th of June 2011), MERIS observed the same region during high tide conditions (Image courtesy of Thomas Schroeder).

The images of Figure 1.3 illustrated a marked variation in turbidity when observations are taken at different tidal stages, suggesting that trends in water quality may be biased by ignoring the strong effects of short-term coastal processes (Eleveld et al., 2014). Conversely, continuous *in situ* measurements (Oubelkheir et al., 2006; Brodie et al., 2010; Blondeau-Patissier et al., 2011; Soja-Woźniak et al., 2019), as well as results from biogeochemical modelling (Xiao et al., 2019; Skerratt et al., 2019) revealed the short-temporal (hourly to daily) variability of water quality parameters, such as

CHL and TSS in the coastal GBR. In this context, diurnal observations at relevant spatial scales are critical for the accurate monitoring of water quality in the GBR.

1.2 Water Quality Monitoring: Current Status and Limitations

The Australian and Queensland governments are committed to ensure the GBR water quality reaches a sustainable level by 2050, currently investing more than $600 million in the *Reef 2050 Water Quality Improvement Plan* (Reef Plan, hereafter) through to 2022. The Reef Plan is a major component of the *Reef 2050 Long-Term Sustainability Plan* (State of Queensland and Commonwealth of Australia, 2018b, a). The Reef Plan was underpinned by a *Scientific Consensus Statement* (Waterhouse et al., 2017b) and has been supported by a comprehensive monitoring and evaluation program – *The Paddock to Reef Integrated Monitoring, Modelling and Reporting* (Paddock to Reef, hereafter), since 2009.

The Marine Monitoring Program (MMP) is the long-term water quality and ecosystem monitoring program for the inshore GBR (Haynes et al., 2005). The inshore GBR is located generally within 20 km from the coastline and comprises about 8% of the Marine Park. However, the ecosystems within this relatively small area (mangroves, coral reefs, seagrass beds) are at greatest risk from declining water quality (Fabricius et al., 2005; Schaffelke et al., 2005; McKenzie et al., 2021; Thompson et al., 2021). The Great Barrier Reef Marine Park Authority (GBRMPA) leads the management of the MMP program in partnership with a variety of organisations, such as the Australian Institute of Marine Sciences (AIMS), James Cook University (JCU) and the Commonwealth Scientific and Industrial Research Organization (CSIRO).

As an integral part of the Paddock to Reef program, the MMP inshore water quality monitoring component aims to "*assess the long-term effectiveness of the Reef Plan in reversing the decline in water quality of runoff originating from the GBR catchments"* (Haynes et al., 2005). The MMP has been conducted since 2005 and was designed to measure the annual condition and long-term trends in inshore water quality, based on *in situ* sampling and remote sensing observations. Therefore, the MMP had assessed the properties, composition, and spatial dynamics of river plumes to understand the sources, transport and effects of terrestrial pollution entering the GBR (Devlin et al., 2015a; Brando et al., 2015; Waterhouse et al., 2018; Gruber et al., 2019; Gruber et al., 2020). Key Water-Quality Parameters (WQP) such as TSS, CHL and absorption of yellow substances (YEL) are monitored *in situ* at variable temporal scales, contributing towards understanding water quality and coastal processes (Schaffelke et al., 2005; Schaffelke et al., 2012).

The MMP water quality program is sustained by a coastal network of permanent and event-based monitoring stations operating since 2005 (Figure 1.4), measuring parameters such as of dissolved

and particulate nutrients, TSS, CHL, YEL, temperature, salinity, and Secchi depth (Gruber et al., 2020). In summary, 58 ambient sites are routinely monitored 5-10 times per year (wet and dry season) depending on the focus region, with more frequent sampling during the wet season (event-based sites). Meanwhile, 27 event-based water sampling sites (same measurements as routine) are monitored only during large flood events, spatially concentrated close to some of the main river mouths (Tully, Herbert, and Burdekin), but absent near others. Additionally, 15 of the routinely sampled sites are equipped with autonomous instruments to collect continuous records of turbidity and CHL (2007-present).

Under the MMP, environmentally-based water quality guideline trigger values (or thresholds) were developed to support the ongoing strategies aimed at halting and reversing the decline of water quality entering the GBR (Great Barrier Reef Marine Park Authority, 2010). Figure 1.5 illustrates the annual and seasonal guideline thresholds for CHL and TSS within cross-shelf zones (inshore, midshelf and offshore) determined for the six Natural Resource Management (NRM) regions of the GBR. The guideline thresholds describe the maximum concentrations of water quality parameters that should not be exceeded for the protection and maintenance of marine species and ecosystem health (Great Barrier Reef Marine Park Authority, 2010). The guideline thresholds were based on annual and seasonal averages of historical *in situ* data (including CHL and TSS) collected in the GBR (De'ath and Fabricius, 2008).

Whilst *in situ* observations are crucial, the current MMP monitoring stations are coarsely distributed (distant 10-200 km) and mainly confined to the inshore GBR (within 20 km from the shoreline). Additionally, they are scarcely sampled to match the temporal and spatial scale of coastal processes, making it difficult to derive more accurate correlations between ecological shifts and biophysical drivers (Devlin et al., 2015b). Although more frequent surveys are taken annually during the wet season (Devlin et al., 2015a), samplings are spatially and temporally limited by the ship transit time, difficulties to access the sites and concerns for the safety and welfare of monitoring staff (Devlin et al., 2010). Besides, routine *in situ* monitoring of the southern coastal waters of the GBR (Fitzroy and Burnett-Mary NRM) or in remote areas (Cape York) is largely limited or lacking.

Monitoring water quality at an appropriate spatial scale and frequency is critical to obtain reliable estimates of material exported in flood plumes to coastal waters (Devlin et al., 2001). To follow the synoptic variability of coastal processes that regulate water quality in the GBR, it is crucial to observe the diurnal variability (at least hourly) at a fine spatial resolution (300 m to 1 km) with broad area coverage (tens to hundreds of kilometres). However, the current *in situ* sampling strategies are site-specific and insufficient in numbers to completely characterize the water quality parameters and its variability over the whole area of the GBR. Thus, a fast, flexible, and integral approach is still required

to track the rapidly changing conditions in the GBR coastal waters, and satellite observations offer a suitable alternative.

Annual assessments of inshore water quality currently rely on the interpretation of remote sensing observations and of biogeochemical modelling results to identify values exceeding the guideline thresholds within the GBR (Australian and Queensland Governments, 2020; Baird et al., 2020). The status and progress of marine water quality indicators towards achieving the goals set in the Reef Plan are annually evaluated and disclosed in the Reef Report Card (State of Queensland and Commonwealth of Australia, 2021). Although slow improvements have been observed on a regional scale, poor water quality continues to affect many inshore areas, with emphasis on the terrestrial export of fine sediments (Waterhouse et al., 2017a; Great Barrier Reef Marine Park Authority, 2019a). Hence, the ongoing effort in monitoring water quality is a priority for the GBRMPA to support the health and resilience of the coastal and inshore ecosystems of the GBR.

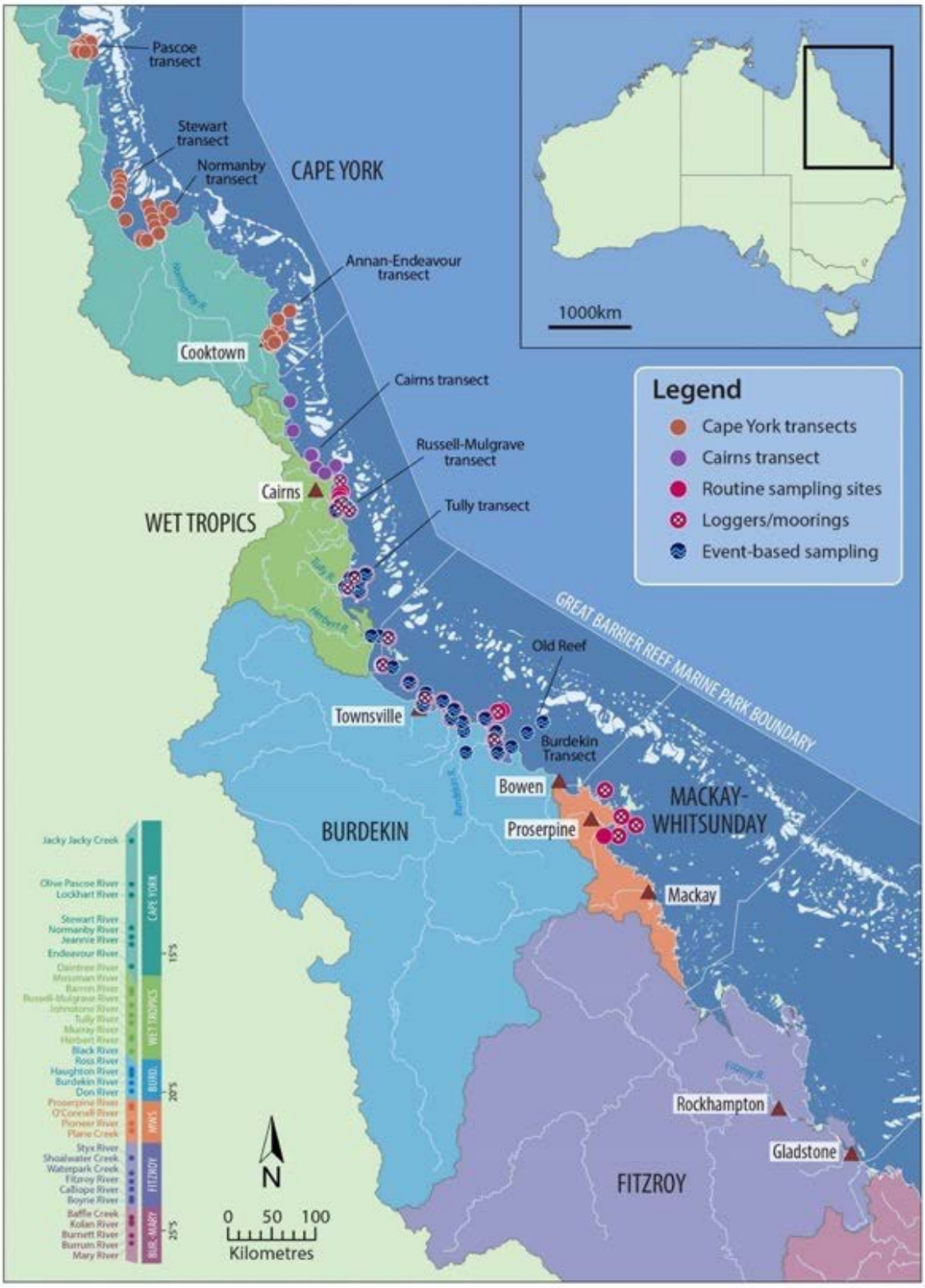

Figure 1.4: MMP water quality monitoring sampling sites in the GBR Marine Park, from 2015 onwards, with Cape York transects added in 2017. The NRM region boundaries are represented by coloured catchment areas with grey lines extending these boundaries into the Marine Park. Image credit: Gruber et al. (2020).

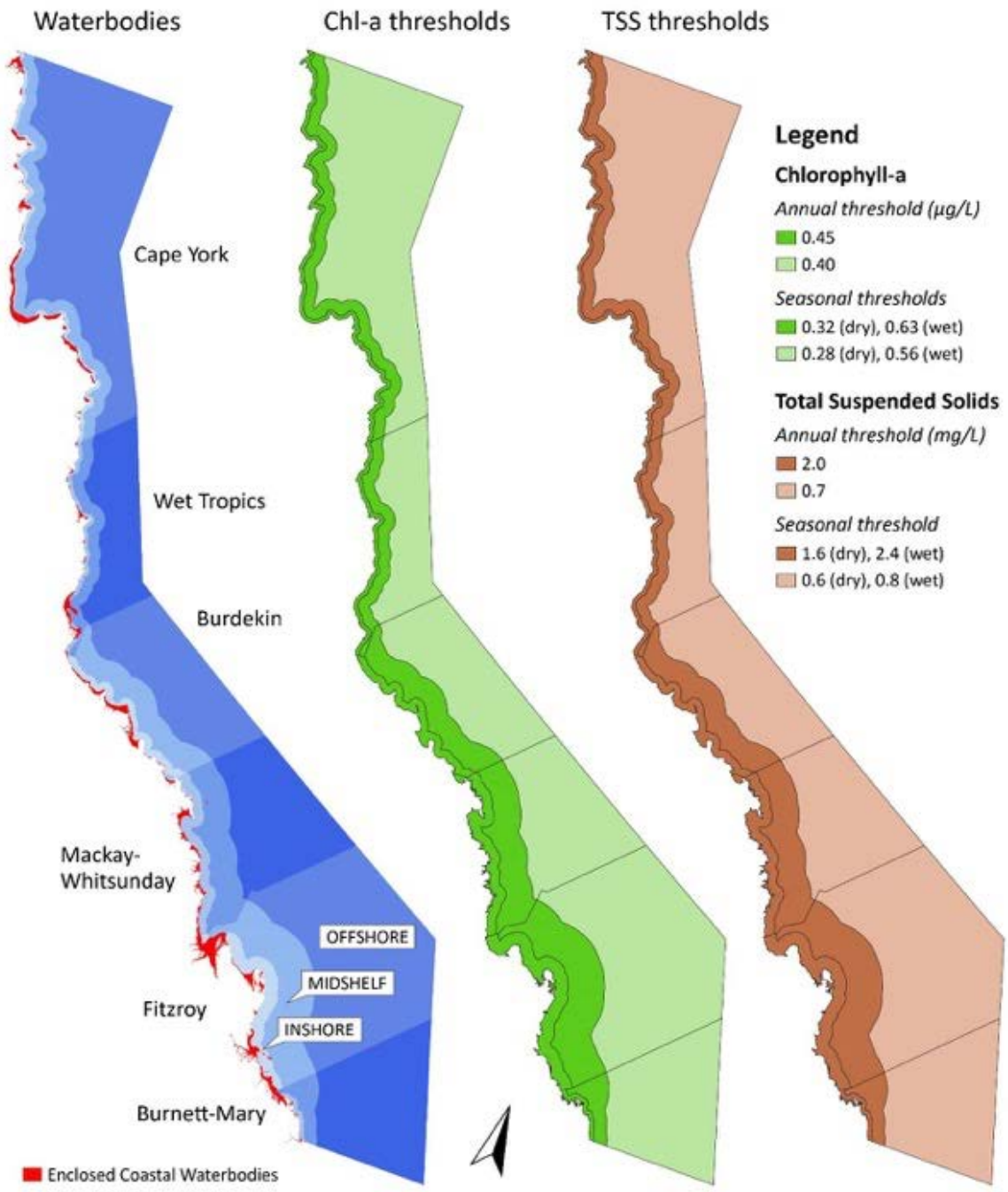

Figure 1.5: Waterbody boundaries (inshore, midshelf and offshore), annual and seasonal water quality guideline thresholds for CHL and TSS concentrations in the GBR Marine Park area. Image credit: Tracey et al. (2016).

1.3 Ocean Colour Remote Sensing for Synoptic Water Quality Assessments

Remote sensing observations have been employed to monitor the GBR for almost 40 years, offering daily observations of the entire Marine Park (344,400 km²) at fine spatial resolutions (from meters to a few kilometres). The first studies focused on mapping coral reefs and coastal habitats with meter-scale resolution sensors designed for land observations, such as with the Landsat missions (Claasen et al., 1984; Jupp et al., 1985; Kuchler et al., 1986). The proof-of-concept mission Coastal Zone Colour Scanner (CZCS) was launched in 1978, and endorsed the first synoptic investigations of water quality in the GBR (Gabric et al., 1990). Since then, ocean colour sensors such as MODIS/Aqua (2002-present) and OLCI/Sentinel-3 (2016-present), have become a valuable and cost-effective source of data to examine daily to inter-annual dynamics of water quality (Schroeder et al., 2012; Weeks et al., 2012; Devlin et al., 2015b; Cherukuru et al., 2017; Petus et al., 2019; Gruber et al., 2020).

From 2007, the use of remotely sensed imagery became part of the MMP water quality framework for tracking and mapping flood plumes extent, and to quantify parameters such as CHL and TSS (Brando et al., 2008; Devlin et al., 2008). The annual MMP reports describe the seasonal and inter-annual spatial variability of the wet-season flood plumes, water types classification and quantification of the loads of particulate suspended material delivered to the GBR (Devlin et al., 2015a; Brando et al., 2015; Petus et al., 2016; Petus et al., 2019; Gruber et al., 2020). Ocean colour sensors onboard Low Earth Orbit (LEO) satellites, such as the MODIS/Aqua, have provided a long-term record (2002-present) of daily observations utilised to monitor and map flood plumes extent, discriminate water types and to determine water quality conditions in the GBR (Brodie et al., 2010; McKinna et al., 2011; Schroeder et al., 2012; Alvarez-Romero et al., 2013; Devlin et al., 2013; Petus et al., 2014b; Devlin et al., 2015a; Petus et al., 2016; Fabricius et al., 2016). LEO observations from the Medium Resolution Imaging Spectrometer (MERIS/Envisat) have been employed for the detection and monitoring of seasonal algal blooms linked with riverine runoff and resuspension in the coastal GBR (Blondeau-Patissier et al., 2014b; Blondeau-Patissier et al., 2018).

Additional investigations have demonstrated the potential of daily ocean colour data to model the ecological responses to water quality changes (King et al., 2002; Devlin et al., 2012a; King et al., 2014; Petus et al., 2014a; Thompson et al., 2014; Petus et al., 2016; Baird et al., 2016; Baird et al., 2020; Skerratt et al., 2020). More recently, the new generation of European ocean colour sensors, Sentinel-3 OLCI, have been employed for seasonal and annual monitoring of GBR water quality (Petus et al., 2019). The qualitative technique developed by Petus et al. (2019) is an integral part of the MMP for mapping the frequency and exposure of the GBR ecosystems to different water types (Gruber et al., 2020).

Nevertheless, the advantage of monitoring turbid plumes and water quality from space is still limited by the regular and complete acquisition of cloud-free imagery over the location of the plume,

which mainly depends on the satellite revisit frequency (temporal resolution), swath width and orbital schedule. While the Earth rotates, the LEO satellites orbit the globe from North to South poles at ~700 km altitude. Hence, the LEO satellites complete an orbit within 90 minutes, scanning a new area approximately at the same local time every day. However, depending on the swath width of the scene, large inter-orbital gaps can yield an incomplete coverage of specific areas, especially near the equator. For instance, the MODIS/Aqua satellite, with a swath width of 2330 km, scans eastern Australia every day between 13:00 to 14:30h local time, often acquiring a rather incomplete coverage of the GBR (see Figure 1.6).

Figure 1.6: Global near-true colour composite of MODIS/Aqua satellite sensor overpass over Australia and East Asia on 13th October 2012. Note the inter-orbital data gaps, particularly over Australia and in the GBR region, as well as the intense cloud cover and bright patches of sun-glint along the scan track. Image credit: National Oceanic and Atmospheric Administration (2021).

Because of its characteristic orbital scheduling and swath, the LEO ocean colour sensors scan the same geographic area within one or two days at best. In addition, the time-lag between two consecutive and identical orbits (i.e., revisit periodicity) commonly varies between one or two weeks. This implies that coastal areas are observed during different tidal cycles by the LEO satellites (Figure 1.7), which is too coarse to effectively monitor dynamic coastal processes with diurnal or sub-diurnal variability (Ruddick et al., 2012; Ruddick et al., 2014).

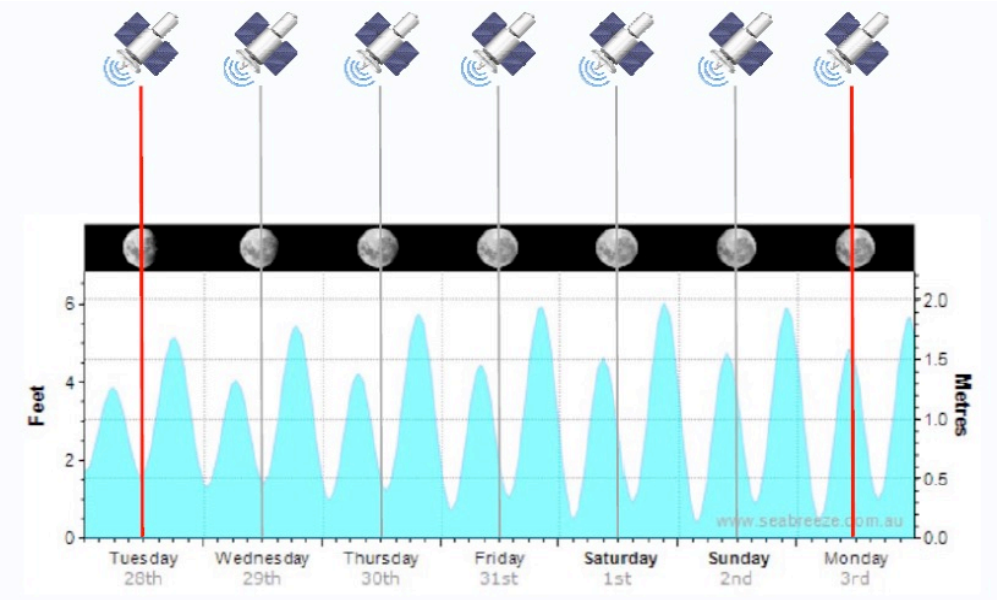

Figure 1.7: Tidal chart for Sydney, illustrating the daily LEO satellite observation during different tidal stages. The red lines denote observations at low and high tide conditions (image courtesy of Thomas Schroeder).

For instance, Eleveld et al. (2014) demonstrated that TSS concentrations derived from the MERIS sensor are biased by tidal aliasing . The acquisition of images during the spring tides matched only low tidal ranges, while the acquisition during the neap tides matched only high tidal ranges, which frequently over or underestimated TSS at distinct sections of the estuary (Eleveld et al., 2014). Therefore, many short scale processes such as tidal changes in turbidity and wind-induced resuspension are misrepresented by the LEO daily observations (Eleveld, 2012; Eleveld et al., 2014). Consequently, the temporal capability of LEO satellites is insufficient to develop a comprehensive observational system for monitoring coastal waters (IOCCG, 2012b).

Additionally, the ocean colour imagery may be largely affected by the presence of clouds and sun specular reflection (sun-glint), further extending the period between useful observations (Sirjacobs et al., 2011). This occasionally requires a weekly to monthly set of daily images from the same area to composite a cloudless view of the ocean, which would be greatly improved with more frequent observations, such as with hourly images. Nevertheless, an accurate description of hourly to diurnal scale variability of water quality for the entire GBR remains impossible to achieve with LEO observations only. Despite these limitations, researchers and environmental managers still rely on LEO ocean colour satellites for acquiring cost-effective spatial information of the global oceans. Therefore, high-frequency fluctuations in water quality, such as with phytoplankton diel cycles, migration of flood plumes, tidal and wind driven resuspension have been insufficiently sampled and investigated in the GBR.

Enhanced spatial-temporal observations would provide a better understanding on how the fluctuations of coastal processes drive water quality changes in the inshore GBR. Additionally, high-frequency water quality observations over regular spatial scales (each 1 km^2 to the whole GBR) may provide valuable inputs to biogeochemical, hydrological, and ecological models (Steven et al., 2019; Baird et al., 2020; Skerratt et al., 2020; IOCCG, 2020). Assimilation of daily remote sensing observations, such as from MODIS/Aqua, into the eReefs model has provided reasonable and realistic evidence of water quality dynamics in the GBR (Jones et al., 2016; Baird et al., 2016; Xiao et al., 2019; Skerratt et al., 2019; Steven et al., 2019; Skerratt et al., 2020; Baird et al., 2020; Soja-Woźniak et al., 2020). A more frequent (minutes to hourly) and accurate dataset of near-real time spatial observations would offer a quantitative, prompt tool to devise guidelines for better quality water entering in the GBR. The next section presents an overview of the possible uses of the geostationary-orbit satellites as a new source of remote sensing data to provide more frequent imagery and water quality products over the GBR.

1.3.1 The Geostationary Point-of-View

Satellites on a Geostationary Earth Orbit (GEO) are positioned at an altitude of about 35,800 km, hovering over the equator and synchronised with the Earth's rotation on a fixed longitude and viewing geometry. This allows near continuous observation of a large area of the globe, (full disk scans about 40% of the Earth's surface), at higher frequency (minutes to hours) compared to the daily revisit of LEO platforms, particularly over the tropics (IOCCG, 2012b). This exceptional observation frequency increases the likelihood of obtaining clear images over the same location, as isolated clouds pass rapidly, and the sun-glint disk moves through time at a location (Zhao and Feng, 2020). This offers a significant advantage over LEO satellite observations, where atmospheric and geometric features as well as revisit periodicity can result in prolonged data gaps (Feng and Hu, 2016; Hu et al., 2019). Observing ocean colour from daily to less than hourly basis is a vast improvement, suggesting the potential to capture water quality fluctuations not previously possible (IOCCG, 2012b).

The temporal dynamics of rapidly changing coastal processes, such as of turbidity plumes and harmful algal blooms have been effectively monitored since 2010, with hourly images from the world's first Geostationary Ocean Colour Imager, GOCI-I (Ruddick et al., 2012; Minghelli et al., 2019; Wang et al., 2020; Jiang et al., 2020; Feng et al., 2020). Although GOCI-I coverage is limited to northeast Asia (Korea, China, and Japan), its success provided a useful case for the future development of global GEO ocean colour missions (Ruddick et al., 2012; Ruddick et al., 2014; Lou and Hu, 2014). GOCI-I was followed by the launch of GOCI-II in February 2020, with an expanded suite of spectral channels and offering only one full disk observation per day covering Australia and East Asia (Yang et al., 2018). At the time of writing this thesis, GOCI-II full disk observations were not publicly accessible. In addition, the only ocean colour mission onboard a GEO satellite expected to be launched in the next few years

is the NASA Geosynchronous Littoral Imaging and Monitoring Radiometer (GLMIR). However, GLMIR will observe the Americas only.

GEO satellites are, however, globally employed for meteorological observations, and recent technological advances have leveraged their capabilities for collecting data over the oceans, allowing more dynamic processes to be observed from space (IOCCG, 2012b; Ruddick et al., 2014; Kwiatkowska et al., 2015). The next-generation (i.e., improved spatial and spectral resolution) of GEO meteorological sensors, such as the Himawari-8, typically provide a full disk image within 10-30 minutes at 1 km^2 spatial resolution at the sub-satellite point, for the visible and near infrared bands (Table 1.1). In addition, they are equipped with an increased number of bands in the visible spectrum (2 or 3 instead of only one band) combined with improved radiometric sensitivity (signal-to-noise ratios) and onboard calibration capabilities. These advances allowed, for the first time, a near-true coloured visualization of the Earth from a geostationary point of view in near-real time (Miller et al., 2016).

The next-generation of meteorological sensors onboard a GEO platform (GEO sensors, hereafter) offer the opportunity to explore the ocean colour with a reduced number of spectral bands, compared to minimum requirements (IOCCG, 1998). For instance, the spectral and radiometric characteristics of the Spinning Enhanced Visible and Infrared Imager (SEVIRI) instrument, with one visible band at 635 nm, have proved sufficient for monitoring the diurnal variability of coastal turbidity plumes (Neukermans et al., 2009; Neukermans et al., 2012b; Ruddick et al., 2012; Vanhellemont et al., 2014; Kwiatkowska et al., 2015). This is not surprising, since turbidity plumes present a strong signal compared to adjacent clear waters and are easily identified from aerial photographs or from true colour images (Devlin et al., 2012b; Devlin et al., 2015b). Conversely, it has been proved difficult to accurately estimate pigment concentrations with the visible and near infrared bands of GEO sensors due to their limited spectral capabilities and the stringent sensitivity required to derive CHL (Murakami, 2016b; Lavigne and Ruddick, 2018). However, reaching a high signal-to-noise from a GEO orbit satellite may be improved as the integration time can be increased by temporal aggregation (more photons captured) to reduce noise (IOCCG, 2012b; Ruddick et al., 2014; Murakami, 2016b; Lavigne and Ruddick, 2018).

In addition, deriving ocean colour products from GEO sensors is mainly limited by the lack of sufficient spectral bands that satisfy the current ocean colour algorithms (IOCCG, 2012a, b). Studies suggest that to estimate two or three independent ocean colour variables, at least five visible bands and one infrared band are necessary (Sathyendranath et al., 1989; Sathyendranath et al., 1994; IOCCG, 1998; Lee et al., 2007). An additional challenge is imposed by the complexity of coastal waters optical properties, since traditional inverse methods for ocean colour parameters retrieval may not be suitable to isolate the optical components that impact the ocean colour (Ioannou et al., 2013). Moreover, accurate atmospheric correction is fundamental for the reliable retrieval of ocean colour products,

especially because the water-leaving signal from the ocean is weak compared with the strong signal from clouds and atmosphere. Accurate atmospheric correction becomes particularly difficult for GEO observations at high viewing angles (> 70˚ or at the edge of the full disk) due to the increased path length through the atmosphere (Ruddick et al., 2012).

A non-exhaustive description of current sensors onboard LEO and GEO orbits with capabilities for ocean colour monitoring in the GBR is provided in Table 1.1. There are currently 6 ocean colour and 2 land focused (LEO) sensors available for observations over the GBR, with bands matching those of the next-generation GEO meteorological satellite sensors. Nevertheless, the significant number of observations offered by a single GEO sensor (up to 48 images a day from Himawari-8, between 8 a.m. – 4 p.m.) exceeds the likely effort of combining and utilising ocean colour data from multiple platforms for diurnal assessments (Bracaglia et al., 2019; Bracaglia et al., 2020). In addition, due to the distinctive orbital characteristics of these multiple ocean colour sensors, same day overlapping of observations from multiple platforms is difficult in the GBR.

Himawari-8 has been providing ultra-high frequent (every 2.5 minutes for target area to 10 minutes full disk) meteorological observations over Australia and East Asia, since July 2015. Recent studies have demonstrated the feasibility of Himawari-8 observations for detection of TSS in coastal waters (Dorji and Fearns, 2018; Ding et al., 2020; Hafeez et al., 2021) and for CHL in the open ocean (Murakami, 2016b). The results from Himawari-8 suggest an exciting opportunity for monitoring of dynamic coastal processes in the GBR. However, an advanced physics-based method with extensive validation is needed for reliably extracting ocean colour products from a meteorological sensor in coastal waters (Neukermans et al., 2009; Ruddick et al., 2014; Lavigne and Ruddick, 2018). The following section describes the characteristics of Himawari-8 and its suitability for deriving ocean colour products in the coastal GBR.

Table 1.1: Comparative table of currently operational LEO and GEO satellite missions that offer observations over the GBR, with launch dates in ascending chronological order. Details of sensor specifications, such as the visible (VIS), near-infrared (NIR) and short-wave infrared (SWIR) bands comparable to the Himawari-8 set, mission objectives, spatial and temporal resolutions are included. Data sourced from the Observing Systems Capability Analysis and Review Tool (2021).

	Satellite/Sensor	*Agency*	*Mission*[3]	*Launch*	*Bands*	*VIS 0.4*	*VIS 0.5*	*VIS 0.6*	*NIR 0.8*	*SWIR 1.6*	*SWIR 2.3*	*Spatial Resolution*	*Temporal Resolution*
LEO	AQUA/MODIS	NASA	OC	2002	36	0.48	0.53	0.66	0.87	1.6	2.1	0.25 – 1 km	1 - 2 days
	SNPP/VIIIRS	NASA	OC	2011	22	0.48	0.55	0.67	0.86	1.6	2.2	0.3 – 0.75 km	1 - 2 days
	Sentinel-2A/MSI	ESA	LAND	2015	13	0.49	0.56	0.67	0.86	1.6	2.2	0.01 – 0.02 km	5 days
	Sentinel-3A/OLCI	ESA	OC	2016	21	0.49	0.51	0.67	0.86	-	-	0.3 – 1.2 km	2 days
	Sentinel-2B/MSI	ESA	LAND	2017	13	0.49	0.56	0.67	0.86	1.6	2.2	0.01 – 0.02 km	5 days
	GCOM-C/SGLI	JAXA	OC	2017	19	0.49	0.53	0.67	0.86	1.6	2.2	0.25 – 1 km	3 days
	NOAA-20/VIIRS	NOAA/NASA	OC	2017	22	0.48	0.55	0.67	0.86	1.6	2.2	0.3 – 0.7 km	1 - 2 days
	Sentinel-3B/OLCI	ESA	OC	2018	21	0.49	0.51	0.67	0.86	-	-	0.3 – 1.2 km	2 days
GEO[4]	Himawari-8/AHI	JAXA	MET	2014	16	0.47	0.51	0.64	0.86	1.6	2.3	0.5 - 1 km	10 min
	Himawari-9/AHI*	JAXA	MET	2016	16	0.47	0.51	0.64	0.86	1.6	2.3	0.5 - 1 km	10 min
	KOMPSAT-2A/AMI	KARI/KIOST	MET	2018	16	0.45	0.51	0.64	0.86	1.6	-	0.5 – 2 km	60 min
	KOMPSAT-2B/GOCI-II	KARI/KIOST	OC	2020	13	0.49	0.51	0.66	0.86	-	-	0.25 – 1 km	1 day

[3] OC refers to Ocean Colour, LAND to Land and MET to Meteorological missions.

[4] List of GEO meteorological sensors currently offering Full Disk observations scanning the GBR

*Himawari-9 is on stand-by as of 2021.

1.3.2 The Himawari-8 Advanced Himawari Imager

Since the launch of Himawari-8 (in October 2014) and Himawari-9 (in 2016 and on standby) by the Japanese Space Agency (JAXA), more frequent observations are now available over Australia and East Asia. The Himawari-8/9 Advanced Himawari Imager (AHI) is the 3rd generation meteorological instrument onboard this GEO platform, succeeding the Multi-functional Transport Satellite (MTSAT-1R and 2) missions. Himawari-8 has been operational since July 2015 with an expected lifetime until 2022. Himawari-9 is planned to succeed Himawari-8 and operate until 2029. The Himawari-8/9 generation payloads were developed to provide high-frequency, high-resolution, multi-band data to enable better numerical weather prediction and environmental monitoring capabilities (Bessho et al., 2016). The Himawari-8 data is provided by the Japanese Meteorological Agency (JMA) to the Australian Bureau of Meteorology (BOM) and distributed to the research community through the National Computing Infrastructure (NCI).

Himawari-8 is positioned at 140.7˚E longitude and offers the opportunity to observe Australia every 10 minutes, capturing at least 48 daily observations over the same location between 8 a.m. to 4 p.m. AEST. The AHI instrument comprises 16 spectral bands, three of which are in the visible spectrum centred at 470 nm, 510 nm and at 640 nm and one near-infrared band centred at 865 nm[5] (Da, 2015). The VNIR bands have 1 km of spatial resolution, except for the 640 nm, with 0.5 km. The remaining 12 bands in the infrared spectrum, including the short-wave infrared (SWIR at 1.6 and 2.3µm) channels have 2 km spatial resolution. Figure 1.8 illustrates AHI's spectral response functions of the VNIR bands, overlaid with the transmission of atmospheric gases and of ozone. In comparison, the MTSAT-2 Imager onboard Himawari-7 mission, operational between 2010 and 2016, had one visible band centred at 670 nm with 1.25 km spatial resolution. Additionally, Himawari-8/9 is the first GEO meteorological imager equipped with a solar diffuser to perform on-board calibration and to track the radiometric stability of the visible and near-infrared sensors (Yu and Wu, 2016).

Whilst the AHI instrument was designed to be a meteorological sensor, an extensive range of applications for monitoring and management of land and oceanic areas have the potential to be derived, including for ocean colour (Murakami, 2016b; Chen et al., 2019; Hsu et al., 2020; Hafeez et al., 2021). The high temporal resolution of Himawari-8 allows the monitoring of ocean properties from sub-hourly to annual time scales. Additionally, Himawari-8's single wide swath (i.e., full disk) enables the synoptic visualization of the entire GBR lagoon and the adjacent oceanic basin without inter-orbital

[5]For convention, the Himawari-8 visible (or VIS) bands centred at 470, 510 and 640 nm are called blue, green and red bands, respectively while the 856 nm is called the near-infrared (NIR) band. The names and central wavelengths of the VIS and NIR (VNIR) bands will be used interchangeably through the text.

data gaps (Figure 1.9). The VNIR bands of Himawari-8 AHI instrument (Table 1.2) enable the estimation of strong marine optical signals, such as those from highly turbid waters (Doxaran et al., 2005; Doxaran et al., 2014; Kwiatkowska et al., 2015). Although the AHI SWIR bands are of interest for atmospheric correction in optically complex waters (Wang and Shi, 2007; Vanhellemont and Ruddick, 2015; Ibrahim et al., 2019), their 2 km spatial resolution was considered too coarse for the coastal GBR.

While the Himawari-8 VNIR bands (Table 1.2) provide inferior sensitivity compared to contemporary ocean colour sensors (Hu et al., 2012b; Japan Meteorological Agency, 2015), the high observation frequency is likely to increase accuracy of derived ocean colour products for assessments of long-term dynamics (Lee et al., 2012). Uncertainty assessment of Himawari-8 observations and derived products is, however, only possible by comparison with concurrent, continuous, and more frequent *in situ* observations, such as the IMOS/LJCO data set in the GBR (in section 1.4).

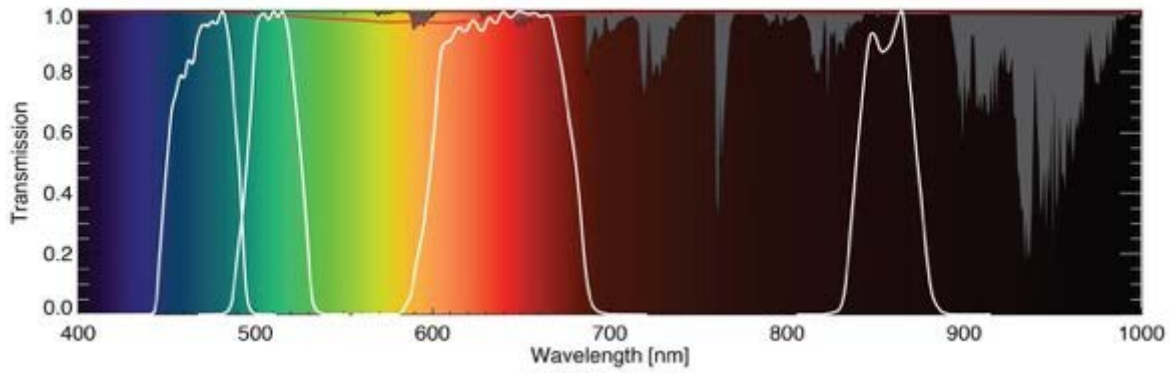

Figure 1.8: Himawari-8 spectral response functions of the visible and infrared bands (solid white lines) with the transmission of the atmospheric gases (grey filled line) and the ozone transmission line (red solid line) between 400 and 1000 nm.

Table 1.2: Himawari-8 Advanced Himawari Imager bands configuration utilised in this work.

Band # (name)	*Central wavelengths (bandwidth)*	*Spatial Resolution at Subsatellite point*	*SNR @100% albedo*
#1 (blue)	470.64 nm (45.37 nm)	1 km	585 (641.5)
#2 (green)	510.00 nm (37.41 nm)	1 km	645 (601.9)
#3 (red)	639.15 nm (90.02 nm)	0.5 km	459 (519.3)
#4 (NIR)	856.69 nm (42.40 nm)	1 km	420 (309.3)

Figure 1.9: Near-true colour of Himawari-8 full disk observation on 25th of February 2021. Image source: National Institute of Information and Communications Technology (2021).

1.3.3 Ocean Colour Algorithms for Optically Complex Waters

Utilising spectral measurements from an aircraft, Clarke et al. (1970) demonstrated that the ocean colour was quantitatively associated to the phytoplankton derived CHL measured in the water. However, the spectral characteristics of aquatic environments may be influenced by components other than CHL, such as with particulate and dissolved substances from inorganic and organic origin (Morel and Prieur, 1977). Thus, the accurate retrieval of biogeochemical parameters from ocean colour satellite observations is a complex task, requiring algorithms to be developed and validated for the region of interest, with appropriate removal of the atmospheric signal.

The optical complexity of diverse aquatic environments, particularly of coastal waters, lead to the classification of water types based on the covariance between optically active or bio-optical parameters (Morel and Prieur, 1977; Gordon and Morel, 1983; Morel, 1988; Werdell and Bailey, 2005). The aquatic environments dominated by the presence and variability of phytoplankton CHL and its detrital products have been classified as Case 1 waters (Morel and Prieur, 1977; Gordon et al., 1980).

Deep blue waters, such as in the great ocean gyres generally fall in this type (Morel and Maritorena, 2001). However, Case 1 waters may also be present in coastal areas and on the continental shelves that have no runoff from rivers and estuaries, especially in arid climates (Gordon and Morel, 1983). Meanwhile, waters belonging to the Case 2 type are dominated by inorganic particles and organic substances of terrestrial origin that are not linearly correlated with the phytoplankton biomass (Morel and Prieur, 1977; Morel, 1980). Case 2 waters include a complex mixture of active optical constituents that shift the watercolour from the clear deep blue to green and brown. These waters can be found in coastal, estuarine and shallow regions under the influence of river runoff, bottom re-suspension, coastal erosion or zones highly impacted by anthropogenic activities (D'Alimonte et al., 2004). The water type classification has been useful to derive appropriate ocean colour inversion algorithms and to evaluate their performance and limitations. The development of methods for the inversion of remote sensing data to bio-optical parameters in optically complex Case 2 waters is a research field of high priority for the ocean colour community (Chapron et al., 2008; Saulquin et al., 2016).

The ocean colour algorithms can be classified in two major groups: the empirical regression techniques and the model-based approaches (IOCCG, 2000). The empirical algorithms are routinely developed based on large optical datasets where simple or multiple regressions are applied between the biogeochemical parameters and the ratios of radiance reflectance (O'Reilly et al., 1998; Lee et al., 2002). The band-ratio technique is easy to derive, implement and test due to its mathematical simplicity and stable results for Case 1 waters, being widely spread for the development of global scale operational ocean colour products, such as CHL (Lee et al., 2015). However, these algorithms are sensitive to regional or seasonal changes in the bio-optical composition and to the presence of uncorrelated particles and substances (Joint and Groom, 2000; Dierssen, 2010; Bowers et al., 2012). For instance, globally-tuned empirical algorithms show errors of up to 375% when applied to retrieve water quality parameters in the coastal GBR (Qin et al., 2007; Schroeder et al., 2018). Therefore, the application of empirical algorithms should be limited to waters with similar characteristics to those for which they were developed (Lee et al., 2002).

More robust inversion techniques, such as the model-based approaches, were developed to simultaneously obtain the concentration of particles and substances beyond CHL, from ocean colour. These models make use of bio-optical assumptions and of radiative transfer simulations to compute the light propagation from the water to the sensor, i.e., the forward model, prior to inversion. The inversion algorithm is then stipulated based on mathematical principles to map, as accurately as possible, the inverse relationship between the radiance or reflectance spectra to the desired in-water constituents (IOCCG, 2000). Multiple model-based approaches have been developed in the past, such as the algebraic or semi-analytical methods, the non-linear optimization algorithms (Roesler and Perry,

1995; Lee et al., 1999; Maritorena et al., 2002; Brando et al., 2012), and the Artificial Neural Networks (Schiller and Doerffer, 1999). Detailed description of these methods are provided in IOCCG (2000).

Empirical and semi-analytical algorithms have been recently developed for the retrieval of ocean colour parameters with the Himawari-8 meteorological observations (Murakami, 2016b; Dorji and Fearns, 2018; Ding et al., 2020). Murakami (2016b) developed an algorithm to estimate CHL, whereas Dorji and Fearns (2018), Ding et al. (2020) and Hafeez et al. (2021) to estimate TSS. However, none of these algorithms were parameterised and validated for the coastal waters of the GBR, and thus, they may yield large deviations making them unsuitable for applications to this region. In addition, these algorithms require extensive computation of the atmospheric parameters for correction prior to ocean colour retrievals.

Alternatively, the direct inversion of satellite observations into water quality parameters have been explored using Multi-Layer Perceptron (MLP) Artificial Neural Networks (ANN) (Schroeder et al., 2007b). MLP ANN is one of possible mathematical tools used to approximately solve non-linear complex problems and inspired by the architecture, self-organization, flexibility, adaptability and processing capabilities of the human brain (Jain et al., 1996; Hinton et al., 2012). The term MLP refers to a class of ANN composed of multiple layers of individual, idealised and interconnected neurons (Minsky and Papert, 1969). The use of MLP ANN (hereafter ANN for brevity) has surged in the past few decades due to an exponential increase in computing power, improved learning algorithms and availability of large datasets. Conversely, the development of remote sensing geophysical products with ANN has increased because of its efficiency and robustness in solving inverse problems. The main advantages of ANN over previous ocean colour inversion methods are:

- Universal approximation capabilities – it can represent or approximate any functional relationship (Hornik, 1991);
- Fault tolerance – it may provide robustness and tolerance against imprecision and uncertainty from noisy inputs (Torres-Huitzil and Girau, 2017);
- Although the training may be time-consuming, the ANN algorithm is fast and can be applied routinely for satellite data mass production (Schiller and Doerffer, 2005).

Therefore, ANN has been successfully applied for mapping pollutants (Leifer et al., 2012; Laurentiis et al., 2020), forecasting and modelling dynamic natural events such as precipitation and fire spread (Reichstein et al., 2019), and for ocean colour retrievals (Schroeder et al., 2007b). In the past 20 years, studies have explored the feasibility of ANN algorithms for ocean colour water quality retrievals in several coastal settings (Table 1.3). These studies employed ocean colour sensors, such as MERIS (Juhls et al., 2019), the Sentinels 2 and 3 (Brockmann et al., 2016; Hieronymi, 2019), VIIRS (El-Habashi

et al., 2019), the Hyperspectral Imager for the Coastal Ocean (Pahlevan et al., 2020), and GOCI-I (Feng et al., 2020).

A summary of relevant peer-reviewed publications describing MLP ANN approaches to retrieve ocean colour parameters from several dedicated sensors is presented in (Table 1.3). However, it is out of the scope of this section to compare results from these studies, only a summary of the work relevant for this thesis is presented. Overall, most studies concentrated their efforts in retrieving ocean colour parameters in the coastal waters of the Mediterranean, North Atlantic and in the North Sea. Ocean colour ANN algorithms have performed well in both Cases 1 and 2 waters, achieving higher retrieval accuracies compared to more traditional techniques, such as band-ratio algorithms (Schiller and Doerffer, 1999; Keiner, 1999).

Table 1.3: Summary of peer reviewed papers on development and implementation of ANN inversion algorithms for the retrieval of ocean colour products for oceanic and coastal waters around the globe.

Literature (Case 1 and Case 2 waters)	*Sensor*	*Regions Applied*
Gross et al. (1999) and Keiner (1999); Gross et al. (2000); Dzwonkowski and Yan (2005); Jamet et al. (2005); Brajard et al. (2006a, 2006b); Jamet et al. (2012)	SeaWiFS	Delaware Bay, California Coast, Mediterranean Sea, English Channel
Schiller and Doerffer (1999); Buckton et al. (1999); Dransfeld et al. (2004); Schiller and Doerffer (2005); Doerffer and Schiller (2007); Schroeder et al. (2007b); González Vilas et al. (2011); D'Alimonte et al. (2012); Juhls et al. (2019)	MERIS	North Sea, Mediterranean Sea, Baltic Sea, Arctic Ocean
Keiner and Yan (1998)	Landsat-TM	Delaware Bay
Tanaka et al. (2004)	OCTS	Northwest Pacific (Japan)
Ioannou et al. (2011, 2013); Chen et al. (2015); Yu et al. (2020)	MODIS	North Atlantic, Global oceanic and coastal waters.
El-Habashi et al. (2017); Ahmed et al. (2017); El-Habashi et al. (2019)	VIIRS	West Florida Shelf
Tian et al. (2016); Yanyan et al. (2018); Qiu et al. (2018); Feng et al. (2020)	GOCI	Bohai Sea Hangzhou Bay Yellow Sea
Brockmann et al. (2016), Hieronymi et al. (2017); Hieronymi (2019); Toming et al. (2017); Marzano et al. (2020)	Sentinel-3 (OLCI); Sentinel-2 (MSI)	Baltic Sea Mediterranean Sea
Krasnopolsky et al. (2018)	Multiple sensors	Global Oceans;
Pahlevan et al. (2020);	Hyperspectral	Chesapeake Bay

The ANN algorithm presented by Schroeder (2005); (2007b) successfully retrieved ocean colour products in turbid coastal waters with the MERIS sensor bands. The one-step inversion was suitable to derive Case 2 TSS and YEL with comparable performance of a two-step inversion with explicit atmospheric correction (Schroeder, 2005). Likewise, reasonable accuracy was achieved for retrievals in the transition zone between coastal and open ocean waters (between Case 1 and Case 2). This is of great advantage for ocean colour retrievals in the GBR, which presents a wide range of concentrations of water quality parameters, such as particulate and dissolved materials (Furnas, 2003). Thus, a physics-based inversion method employing ANN is well suited for the retrieval of ocean colour products in the optically complex coastal waters of the GBR and may be ideal for the inversion of large and more frequent observations such as those from Himawari-8.

1.4 *In situ* Datasets to Support Algorithm Parameterization and Validation

Coastal waters can have complex optical variability (Morel and Prieur, 1977; Lee et al., 2002), requiring model-based techniques for the accurate retrieval of water quality parameters from remote sensing. Besides, extensive algorithm validation and parameterization are required to reliably derive ocean colour parameters in coastal and optically complex waters, such as in the GBR (Brando et al., 2015). In this context, the MMP *in situ* water quality monitoring network has facilitated the validation and improvement of ocean colour products derived from remote sensing observations in the coastal waters of the GBR (Gruber et al., 2020). The historical record of *in situ* data of CHL, TSS and YEL collected by AIMS as part of the MMP is freely available through the Australian Observation Data Network (AODN) portal and has been valuable for ocean colour validation activities in the coastal GBR. However, *in situ* data collected for the MMP is not specifically tailored for ocean colour validation activities, and studies still report a lack of sufficient *in situ* validation data in several GBR coastal systems under the influence of freshwater runoff (Brando et al., 2015).

A comprehensive database of coastal and open ocean *in situ* observations, including physical, chemical, and biological variables is available Australia wide through the Integrated Marine Observing System (IMOS). Within IMOS, the Ocean Colour Sub-facility supports the archiving of raw satellite data, as well as the collection of *in situ* observation for algorithm development and validation activities. In this framework, the Lucinda Jetty Coastal Observatory (LJCO, 18.52˚S, 146.39˚E) is a semi-autonomous facility operated by CSIRO and located in the Wet Tropics region within the coastal waters of the GBR World Heritage Area (Brando et al., 2010). The facility (Figure 1.10) is situated at the end of the longest jetty in the southern hemisphere (5.8 km), close to the Herbert River Estuary and to the Hinchinbrook Channel, where tides range up to 4 m (Bureau of Meteorology of Australia, 2016).

LJCO is the only observatory in the southern hemisphere that provides a simultaneous and continuous time series of above water radiometry (integrated with NASA's AERONET-OC), and in-water optical properties, atmospheric, meteorological, and sea-state measurements. Also, sea surface discrete water samples are taken on fortnightly basis to derive the concentration of water quality parameters such as CHL, TSS and YEL. A more detailed description of the measurements can be found in the LJCO dedicated webpage[6]. The IMOS/LJCO has been operational since 2014, which coincides with the launch and operation of Himawari-8. More frequent and concurrent *in situ* data is fundamental to explore the full capacity of Himawari-8 through validation exercises.

Figure 1.10: The Integrated Marine Observing System (IMOS) Lucinda Jetty Coastal Observatory (LJCO) installations in the coastal waters of the Great Barrier Reef World Heritage Area (29/01/2016). Image courtesy of Dr. Thomas Schroeder.

[6] http://coast-rs-1.it.csiro.au/

1.5 Thesis Objectives

The limited capability to detect diurnal ocean colour from space has hindered the development of a broader understanding of coastal processes affecting water quality dynamics in the GBR. As described above, GEO satellites offer ultra-high temporal revisit frequencies compared to LEO satellites, presenting an opportunity to explore diurnal variations in ocean colour from space. Recent technological advances have also allowed multiple visible bands to be included in the payload of the next-generation geostationary meteorological sensors, with promising results for ocean colour monitoring at diurnal scales yielded from these developments. With modern computational capabilities, vast amounts of data can be explored, and advanced machine learning techniques applied to retrieve near-real time ocean colour products from space. Moreover, the ability to assess the accuracy of ocean colour remote sensing products has been significantly improved with the increased availability of ground truth data for validation, such as those from IMOS/LJCO.

The aim of this thesis is to critically examine the possibility of using Himawari-8 observations to derive diurnal water quality products for the advanced monitoring and management of the coastal waters of the GBR. The thesis is organised in four data chapters, each one addressing a research objective relevant to this aim. The research objectives are:

a) Development of a physics-based ocean colour algorithm for Himawari-8

b) Validation of the algorithm against *in situ* data collected in the GBR

c) Assessment of the detection limits of the method; and

d) Application of diurnal observations from Himawari-8 to the advanced monitoring of water quality in the GBR.

Figure 1.11 illustrates the conceptual framework of this thesis. Chapter 2 reports on the design and parameterization of a physics-based ocean colour algorithm for the coastal GBR, utilising radiative transfer simulations and inversion with Artificial Neural Networks. Chapter 3 assesses the ability of the algorithm to accurately retrieve ocean colour products from Himawari-8, compared to concurrent ground truth data collected in the GBR. Chapter 4 evaluates the quantitative and qualitative limitations of the present method associated with Himawari-8 radiometric quality and resolution. Finally, Chapter 5 demonstrates the ability of Himawari-8 products for the monitoring of diurnal variations in water quality in the GBR.

Thesis Framework:

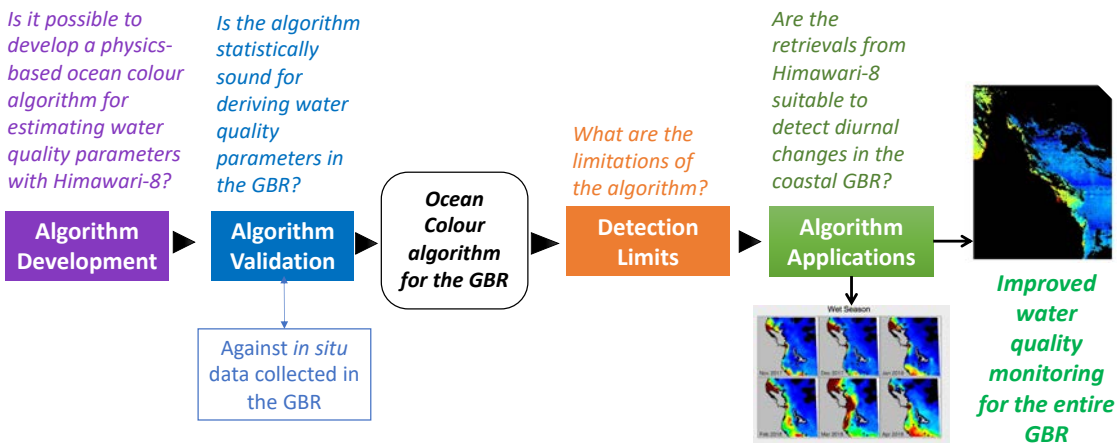

Figure 1.11: Framework of thesis structure, with research questions associated with each data chapter.

Chapter 2: A Physics-based Ocean Colour Algorithm for Himawari-8

Although several ocean colour algorithms may be available for satellite retrieval of coastal water quality parameters, they are either not suited for the optical complexity of the GBR or not suited for the Himawari-8 observations. Given the optical complexity of the GBR waters and the singularity of Himawari-8 as a non-ocean colour sensor, a physics-based algorithm with ANN inversion was tested. The one-step inversion algorithm was developed to estimate the concentration of CHL, TSS and YEL directly from Himawari-8 top-of-the atmosphere (TOA) observations. The specific objectives of the Algorithm Development chapter are to:

- Investigate the sensitivity of the Himawari-8 bands to detect changes in CHL, TSS and YEL.
- Generate a large dataset of simulated radiances for the training and testing of ANN inversions.
- Train and test several ANN ocean colour inversion experiments to estimate CHL, TSS and YEL in the coastal GBR.

A conceptual framework of this chapter is shown in Figure 2.1. In summary, the angular distribution of the TOA radiances was simulated at the visible and near-infrared (VNIR) Himawari-8 bands with an existing coupled ocean-atmosphere radiative transfer (RT) model (Fischer and Grassl, 1984; Fell and Fischer, 2001), i.e., the forward model. The RT simulations included realistic variations in water quality parameters, atmospheric and illumination conditions. Then, several ANN experiments were designed, trained, tested to retrieve CHL, TSS and YEL at the Himawari-8 bands based on the simulated TOA radiances, i.e., the inversion model. Finally, the ANN outputs were statistically assessed against the RT synthetic water quality inputs. The section 2.1 of this chapter describes the theoretical background for parameterization of the coupled ocean-atmosphere radiative transfer simulations. The section 2.2 presents the radiative transfer model and sensitivity analysis results, as well as the dataset generated for training and testing the ANN experiments. The section 2.3 presents the development of the inversion algorithm with ANN for Himawari-8.

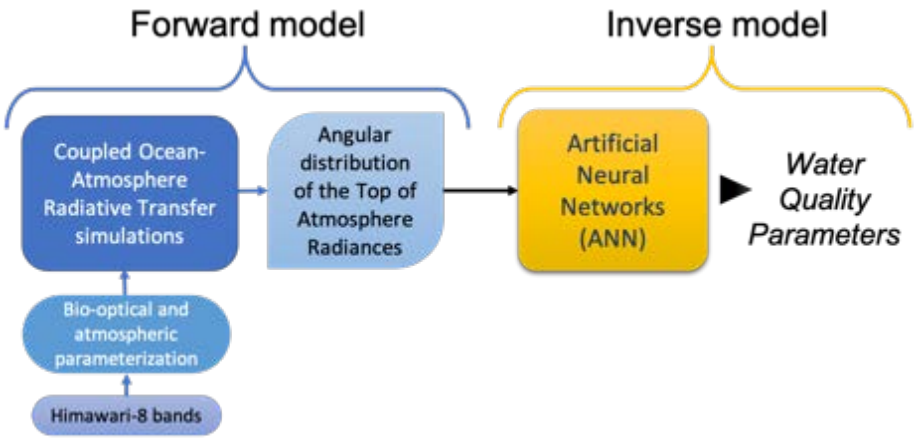

Figure 2.1: Conceptual model of the physics-based ocean colour algorithm developed for Himawari-8.

2.1 Theoretical Background

The scope of this section is to present fundamental background physics required to understand the radiation budget between the ocean and the atmosphere and thus, to accurately retrieve water quality information from satellite remote sensing. Nomenclature and symbols of radiometric parameters follow the classic work of Mobley (1994), which adopts the recommendations of the Committee on Radiant Energy in the Sea of the International Association of Physical Science of the Ocean (Morel and Smith, 1982). For clarity, only the quantities applied in the present work are introduced. Detailed reviews of ocean radiative transfer can be found in Mobley (1994), Kirk (1994, 2010), Bukata et al. (1995), and in Zaneveld et al. (2005). In addition, the reports of the International Ocean Colour Coordinating Group (IOCCG, 2000), as well as the National Aeronautical and Space Administration (NASA) protocols for radiometric measurements in (Mueller, 2003), provide a wealth of information on ocean colour remote sensing.

2.1.1 Optical Properties of Aquatic Mediums

Aquatic environments contain dissolved substances and particles of organic and inorganic origin, such as minerals (fine suspended sediments), living organisms (phytoplankton) and products from the breakdown of organic matter (yellow substances and cell fragments). Depending on the concentration and type, these substances and particles may alter the colour of the water, and thus they are called optically active constituents. The optically active constituents change water colour by modulating the magnitude and spectral characteristics of the incident electromagnetic radiation. The resultant water leaving radiances, containing information about the water colour and its constituents, can be detected by sensors on board LEO or GEO satellites.

Critical analysis of the inherent and apparent optical properties (IOPs and AOPs) related to the optically active constituents are fundamental to quantitatively define and model the aquatic environment. The Inherent Optical Properties (IOPs), such as absorption and scattering, characterise the intrinsic behaviour of each optically active constituent, regardless of the environmental and illumination conditions. The IOPs can be translated into the ocean colour or water quality relevant parameters through bio-optical models (Morel, 1988; Morel, 2001). Meanwhile, the Apparent Optical Properties (AOPs) describe the spectral changes in electromagnetic radiation due to changes in colour (i.e., IOPs), considering the environmental and illumination conditions. Therefore, from knowing the IOPs, the spectral characteristics of the AOPs can be derived for several illumination and environmental conditions, which is the task of the radiative transfer simulations employed in this work. The AOPs simulated at the VNIR bands of Himawari-8 were the basis for training and testing an ocean colour inversion algorithm with ANN.

2.1.1.1 Inherent Optical Properties

The IOPs are mainly determined by the concentration and types of constituents present in the aquatic medium, independent of the ambient light field structure. The magnitude and spectral shape of IOPs can be measured with instruments *in situ* and in laboratory through filtration and subsequent analysis of discrete water samples. The relevant IOPs in the context of this work are the absorption and scattering (and volume scattering function) coefficients of pure water, phytoplankton, yellow substances and of non-algal particles or inorganic suspended matter.

The absorption (a) is the property that describes the photon removal from the incident beam of light while the scattering (b), is the property that describes the changes in the direction of photons propagation. The total attenuation of the light (c) in the water is the sum of the radiation loss by absorption and scattering properties of all optically active constituents, including of the pure water itself. The attenuation, scattering and absorption coefficients, with units per metre $[m^{-1}]$ are wavelength dependent (λ), which is omitted for brevity:

$$c = a + b \qquad \text{Eq. 2.1}$$

The spectral absorption coefficient $a\,(\lambda)$ is the fraction of radiant flux of photons $(\Phi\ in\ Watts)$ that is absorbed within a specific layer of thickness z (Eq. 2.2):

$$a \equiv \frac{d\Phi_a}{\Phi_i\, dz} \qquad \text{Eq. 2.2}$$

According to the *Beer-Lambert* law of extinction (Beer, 1852), the total absorption (or total scattering) is linearly proportional to the sum of all absorbing (or scattering) constituents within a medium. The total absorption coefficient a can be expanded to the individual contributions of phytoplankton (a_{phy}), non-algal or inorganic particles (a_{nap}), yellow substances (a_{yel}), and the contribution of pure water itself (a_w) (Gordon, 1989) (wavelength dependent):

$$a = a_{phy} + a_{nap} + a_{yel} + a_w \qquad \text{Eq. 2.3}$$

Meanwhile, the total scattering coefficient (b) describes the change in the incident radiation flux (Φ_i) due to scattering within a layer of thickness z, regardless of angular distribution:

$$b = \frac{d\Phi_b}{\Phi_i\, dz} \qquad \text{Eq. 2.4}$$

In water bodies, the total scattering is mainly a function of the contribution of pure sea water molecules and particles:

$$b = b_p + b_w \quad \text{Eq. 2.5}$$

The Volume Scattering Function (VSF), or the angular distribution of the scattered radiation $\beta(\psi, \lambda)$, quantitatively describes how much of the incident radiation flux $\Phi\,(\theta, \lambda)$ is deflected in a spatial aperture angle $(0 < \Omega < 180^{\circ})$, relative to the direction of incidence of the radiation flux (θ).

$$\beta\,(\psi, \lambda) = \frac{d\Phi\,(\theta, \lambda)}{\Phi\,(\lambda)} \frac{1}{d\Omega\; dz}\; [m^{-1} sr^{-1}] \quad \text{Eq. 2.6}$$

Integrating $\beta(\psi, \lambda)$ over all scattering directions gives the spectral scattering coefficient $b(\lambda)$:

$$b(\lambda) = 2\pi \int_0^{\pi} \beta(\theta, \lambda)\, sin\, \theta\; d\theta\; [m^{-1}] \quad \text{Eq. 2.7}$$

The VSF can be partitioned into the forward $(0 < \theta < \pi/2\,)$ and back $(\pi/2 < \theta < \pi)$ scattering coefficients $b_f(\lambda)$ and $b_b(\lambda)$ respectively:

$$b_b(\lambda) = 2\pi \int_{\pi/2}^{\pi} \beta(\theta, \lambda)\, sin\, \theta\; d\theta\; [m^{-1}] \quad \text{Eq. 2.8}$$

$$b_f(\lambda) = 2\pi \int_0^{\pi/2} \beta(\theta, \lambda)\, sin\, \theta\; d\theta\; [m^{-1}] \quad \text{Eq. 2.9}$$

The backscattering (b_b) coefficient may be due to pure water itself, turbulence, bubbles, colloids, and particles (Stramski et al., 2004). However, it is mainly described by the backscattering of pure water (b_{bw}) and particulate material (b_{bp}) of organic and inorganic origin (phytoplankton and non-algal particles):

$$b_b(\lambda) = b_{bp}(\lambda) + b_{bw}(\lambda) \quad \text{Eq. 2.10}$$

Finally, the scattering phase function or $\tilde{\beta}\,(\theta, \lambda)$ has been widely utilised to simulate the scattering behaviour of several particles. The scattering phase function is a measure of the angular distribution of scattering regardless of its magnitude (Stramski et al., 2004) and is often approximated by an analytical formula, such as from Fournier and Forand (1994) for oceanic waters. The scattering phase function, or the ratio of the VSF to the scattering coefficient can be calculated for a specific wavelength (λ) and for a scattering angle (θ):

$$\tilde{\beta}(\theta,\lambda) = \frac{\beta(\theta,\lambda)}{b} \qquad \text{Eq. 2.11}$$

The parameterization of the specific IOPs relevant to this work are described in the next subsections.

a. Absorption by Pure Water and Scattering by Pure Seawater

Pure water is defined as distilled water without any particles, substances or salts dissolved in it. Pure water molecules strongly absorb ultraviolet (100 - 400 nm) and infrared (800 nm – 1 mm) light, while strongly scattering blue light (~ 450 - 500 nm) (Morel, 1974). Small quantities of water are transparent but with the increasing optical thickness (deep waters), pure water shows a predominant blue colour. Pure seawater consists of pure water molecules and dissolved salts (mainly chloride and sodium), with average salinity of 35 PSU for the open ocean. Salinity does not affect visible light absorption, however, it is shown to be relevant for scattering (Zhang et al., 2009). The absorption coefficient of pure water (a_w) utilised in this work was defined by Pope and Fry (1997) for the visible bands (412-727.5 nm - Figure 2.5) and by Hale and Querry (1973) for wavelengths between 750-1000 nm. Meanwhile, the pure seawater scattering coefficient was expressed as a wavelength dependent power law based in Morel (1974), defined for a global salinity average of 35 PSU:

$$b_w(\lambda) = 0.00288\left(\frac{\lambda}{500}\right)^{-4.32} \qquad \text{Eq. 2.12}$$

b. Absorption by Phytoplankton and Detritus (organic particles)

Phytoplankton or microalgae organisms like diatoms, dinoflagellates and cyanobacteria are crucial for the primary productivity of the oceans (Behrenfeld and Falkowski, 1997). They are microscopic autotrophic cellular organisms with variable sizes (0.2 µm to 200 µm), shapes, builds and physiologies. Their most abundant photosynthetic pigment, chlorophyll-a, strongly absorbs visible light, especially in the blue and red part of the spectrum (peaks at 440 nm and 675 nm). Light absorption spectra may vary in magnitude and shape depending on the species and taxa (Sathyendranath et al., 1987; Ciotti et al., 2002). Detritus is the product of the degradation of all dead particulate organic material, including phytoplankton cells (Bricaud et al., 1998). The spectral absorption of phytoplankton and detritus (sum of all organic particles), a_{phy}, was parameterized as:

$$a_{phy}(\lambda) = A_{phy}(\lambda)\,[CHL]^{B_{phy}} \qquad \text{Eq. 2.13}$$

In Eq. 2.13, A_{phy} and B_{phy} are tabulated coefficients (Bricaud et al., 1998), and CHL is the concentration of total chlorophyll-a pigment.

c. Absorption by Non-Algal Particles

Non-Algal Particles (NAP) are mainly found suspended near coastal waters and consist predominantly of minerals such as feldspars, clay, calcite, sand, quartz, and metal oxides (Mobley, 1994). NAP may originate from atmospheric deposition, be resuspended from bottom sediments, or delivered by erosion and fluvial discharge. The spectral absorption of all NAP retained in a filter (a_{NAP}), disregarding the pigment absorption due to phytoplankton particles (through pigment bleaching), for a given wavelength λ is calculated as in Eq. 2.14 and in Eq. 2.15:

$$a_{NAP}(\lambda) = a_{NAP}(443)e^{-S_{NAP}(\lambda-443)} \quad \text{Eq. 2.14}$$

$$a_{NAP}(443) = A_{NAP}\, TSS^{B_{NAP}} \quad \text{Eq. 2.15}$$

In this work, the $A_{NAP} = 0.0216$ and $B_{NAP} = 1.0247$ coefficients were taken from Babin (2000), and the mean slope $S_{NAP} = 0.012$ was adapted based on *in situ* average values for the GBR between 2002 and 2013 (Figure 2.2).

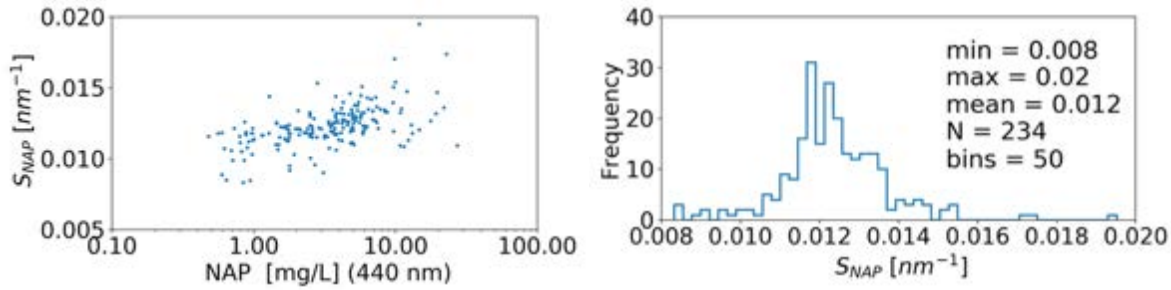

Figure 2.2: The top panel presents the relationship between the NAP concentrations (mg L^{-1}) and S_{NAP}. The bottom panel presents the frequency distribution and descriptive statistics of S_{NAP} from in situ samples collected in the GBR from 2002 to 2013.

d. Scattering by Inorganic and Organic Particles

TSS or suspended matter is a measure of the total dried weight of all the material retained in a filter after filtration of a volume of water. The retained material is a composition of all living and nonliving buoyant particles of organic and inorganic origin, including phytoplankton cells, bacteria, colloids and minerals (Babin et al., 2003a; Stramski et al., 2004). Here, the contribution of organic and inorganic particles was combined to derive the particulate scattering b_p following the parameterization in Babin (2000), where b_p^* is the mass specific scattering coefficient of TSS particles:

$$b_p(\lambda) = b_p^*(\lambda)[TSS] \quad \text{Eq. 2.16}$$

The average ratio between the b_p coefficient at 550 nm and the concurrent TSS concentrations from 92 in situ GBR samples was calculated via Eq. 2.16. The resultant average b_p^* (Figure 2.3) calculated for the GBR waters (0.31 m^2g^{-1}) is comparable to the value acquired by Babin (2000) in coastal waters of Europe (0.5 m^2g^{-1}).

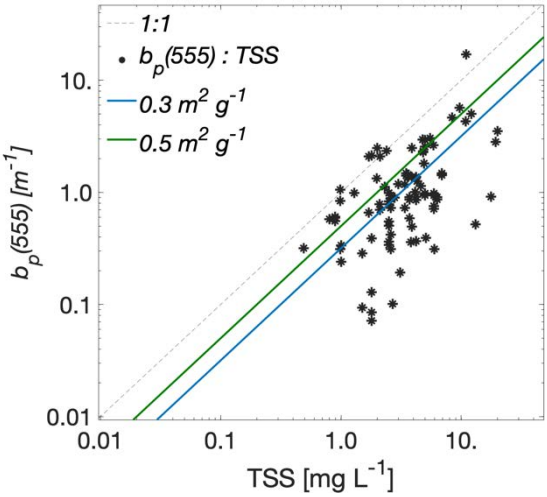

Figure 2.3: Scatter plot between the b_p coefficient at 555 nm and TSS for 92 samples taken between 2002 and 2015 in the GBR waters. The straight solid lines indicate the mass-specific scattering coefficient of particles b_p^* calculated for the GBR (blue) and for European waters (green).

The backscattering probability, which is derived from the VSF, may be highly variable depending on the wavelength and the ratio between YEL and TSS, particularly in Case 2 waters (Zhang, 2003). To account for the likely variations in particulate matter occurring in the GBR, the backscattering probability model provided by in Zhang et al. (2002) and Zhang (2003) for Case 2 waters was calculated. The Zhang (2003) model is a wavelength dependent function of the ratio between the organic to inorganic particulate matter. The fraction of organic particulate matter was represented by the YEL absorption at 443 nm:

$$\tilde{b}_b(\lambda) = f\left(\frac{YEL}{TSS}\right)(\lambda) \quad \text{Eq. 2.17}$$

The backscattering probability was calculated and employed for selection of the scattering phase function, $\tilde{\beta}(\theta, \lambda)$.

e. Absorption by Yellow Substances

The yellow substances (YEL), also known as coloured dissolved organic matter, *gelbstoff* and gilvin, are composed of fulvic and humic acids resulting from the decay and bacterial degradation of plant material (Nelson and Coble, 2009). The YEL pool in coastal waters can originate from terrestrial runoff (Schroeder et al., 2012) or be associated with *in situ* biological activity, such as the degradation of phytoplankton cells (Kinsey et al., 2018). YEL strongly absorbs ultraviolet and blue visible light with exponential decrease towards longer wavelengths. Depending on its concentration, it modulates the watercolour from yellow to brown and largely influences light dynamics in surface waters (Kirk, 1994, 2010). The spectral absorption $a_{YEL}(\lambda)$ is determined in the laboratory by the spectrophotometric reading of a filtered water sample, where the polycarbonate membrane filter has pore size of 0.2µm (Clementson et al., 2004). The spectral absorption coefficient $a_{YEL}(\lambda)$ was modelled according to Bricaud et al. (1981), as in Eq. 2.18 and the coefficient S_{YEL} was derived from *in situ* data from the GBR (Figure 2.4).

$$a_{YEL}(\lambda) = a_{YEL}(443)e^{-S_{YEL}(\lambda-443)} \qquad \text{Eq. 2.18}$$

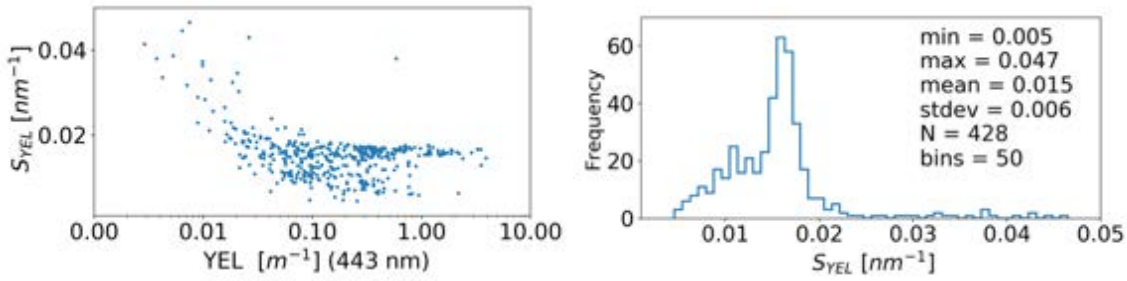

Figure 2.4: The top panel presents the relationship between absorption of YEL at 443 nm and S_{YEL} calculated for 429 *in situ* GBR samples. The bottom panel shows the frequency distribution of the S_{YEL} parameter and descriptive statistics.

The modelled spectral absorption of a_w, a_{phy}, a_{YEL} and a_{NAP} are demonstrated in Figure 2.5 for CHL, YEL and TSS concentrations (10 mg m^{-3}, 0.1 m^{-1} and 10 mg L^{-1} respectively) derived from arbitrary *in situ* data from the coastal GBR. Additionally, the spectral response function for the Himawari-8 VNIR bands is overlayed in Figure 2.5, where the central bands in the blue (470 nm), green (510 nm), red (640 nm) and near-infrared (856 nm) regions. The bio-optical models presented in section 2.1.1.1 were employed to generate a large bio-optical database for the radiative transfer calculations with the MOMO code and IOPs were calculated for the central wavelengths of Himawari-8 bands. The water quality parameters input to the bio-optical models are described in section 2.2.2.

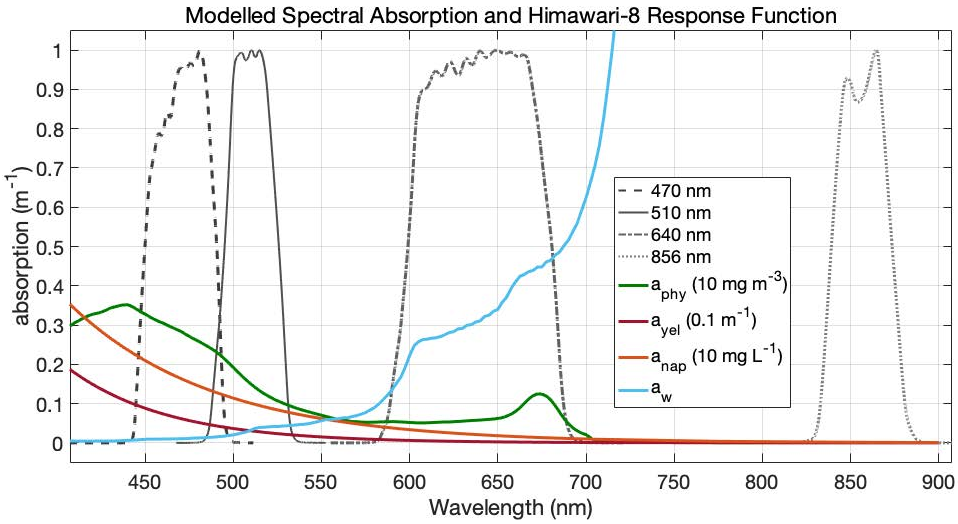

Figure 2.5: Modelled spectral absorption of a_w (blue solid line), a_{phy} (green curve) a_{YEL} and a_{NAP} (orange and red solid lines, respectively) and overlaid Himawari-8 spectral response function for the visible and near-infrared bands (black lines).

2.1.1.2 Apparent Optical Properties

The Apparent Optical Properties (AOPs) are the properties utilised to describe the magnitude and geometrical distribution of the light field (Mobley, 1994). The spectral magnitude and shape of AOPs change with variations on type and concentration of substances in the aquatic and atmospheric mediums (i.e., IOPs) and on the directional structure of the ambient light field (solar and observer zenith and azimuth angles). The AOPs can be derived from radiometric measurements taken *in situ* or from ocean colour satellite observations. This section briefly describes the AOPs relevant to this work, however, an in-depth description is found in Mobley (1994).

Radiometry is the science that measures and characterizes the electromagnetic energy in terms of power or radiant flux. The radiance and irradiance quantities are convenient measures to derive the distribution of the radiant flux at defined spectral ranges. Radiance, or the spectral radiance $L\ (\theta, \phi, \lambda)$ is the flux of radiant energy (Q) in Joules, per unit of time (t), per unit of solid angle (Ω), coming from a given direction (zenith and azimuth angles, θ and ϕ respectively) per unit area (A) normal to the incident beam at a given wavelength (λ), units of $W\ m^{-2} sr^{-1} nm^{-1}$. All other radiometric quantities can be derived from $L\ (\theta, \phi, \lambda)$.

$$L\ (\theta, \phi, \lambda) = \frac{\Delta Q}{\Delta t\ \Delta A\ \Delta \Omega\ \Delta \lambda} \qquad \text{Eq. 2.19}$$

When the light is emitted isotropically from a source (such as from the Sun) and converge/incident onto a surface area, this radiant flux is called irradiance (E), or the flux of radiant intensity per unit area, expressed in $W\ m^{-2}$. The spectral irradiance $E(\lambda)$ is the irradiance of a surface

per unit frequency or wavelength (λ) with units of $W\ m^{-2}\ nm^{-1}$. Considering a plane surface perpendicular to the beam direction, the plane irradiance is the cosine-weighted integration of the radiance flux over the hemisphere. The irradiance integrated from the whole upper hemisphere is called downwelling spectral irradiance $E_d\ (\lambda)$, while the upwelling spectral irradiance $E_u\ (\lambda)$ is the one integrated from the whole lower hemisphere (Eq. 2.20 and Eq. 2.21). In the ocean-atmosphere system, the incoming sunlight (i.e., the downwelling irradiance, E_d) is attenuated in its path by scattering and absorption processes due to the presence of air molecules and particles in the atmosphere. The remaining light is transmitted to the ocean layer and gets attenuated by absorption and scattering of water molecules, dissolved substances, and particles. The upwelling irradiance (E_u) is the total upwelling light jointly affected by the ocean and atmosphere.

$$E_d(\lambda) = \int_0^{2\pi} d\phi \int_0^{\frac{\pi}{2}} L\ (\theta, \phi, \lambda)\ cos\ \theta\ sin\ \theta d\theta \qquad \text{Eq. 2.20}$$

$$E_u(\lambda) = -\int_0^{2\pi} d\phi \int_{\frac{\pi}{2}}^{\pi} L\ (\theta, \phi, \lambda)\ cos\ \theta\ sin\ \theta d\theta \qquad \text{Eq. 2.21}$$

Satellite sensors measure ocean and atmosphere radiances from altitudes of at least 700 km (~35,000 km for geostationary satellites). The sensors are placed at an altitude above the top of the atmosphere (TOA), which is the given altitude where the atmospheric pressure or mass becomes negligible. The TOA is also the upper limit of molecular physicochemical interactions in the atmosphere and its altitude depends on the parameter being analysed. For the radiative transfer simulations employed in this study, the TOA is located at 50 km of altitude. The sun-earth distance corrected extra-terrestrial solar irradiance $(F_ø)$ arriving at TOA is defined as:

$$F_ø = \epsilon(\mathrm{DOY}) \cdot \overline{F_ø} \qquad \text{Eq. 2.22,}$$

where ϵ is the multiplicative distance correction factor for a given day of the year (DOY) and $\overline{F_ø}$ is the mean extraterrestrial solar constant. The satellite sensors detect the TOA radiances (L_{TOA}) for a given solar and viewing zenith and relative azimuth directions $(\theta_s, \theta_v, \Delta\phi)$. Normalising L_{TOA} by $F_ø$, gives the TOA Remote Sensing Reflectance (R_{rs}^{TOA}) in units of steradian (sr^{-1}):

$$R_{rs}^{TOA}\ (\theta_v, \theta_s, \Delta\phi, \lambda) = \left[\frac{L_{TOA}(\theta_v, \theta_s, \Delta\phi, \lambda)}{F_ø(\lambda)}\right] \qquad \text{Eq. 2.23}$$

Finally, the single scattering albedo (ω_0) describes the relative contribution of total scattering $b(\lambda)$ to total attenuation $c(\lambda)$:

$$\omega_0(\lambda) \equiv \frac{b(\lambda)}{a(\lambda) + b(\lambda)} \equiv \frac{b(\lambda)}{c(\lambda)} \qquad \text{Eq. 2.24}$$

In mediums where the total attenuation $c(\lambda)$ is largely due to scattering, ω_0 is near one; otherwise, in mediums where $c(\lambda)$ is mainly due to absorption, ω_0 is near zero. The inputs for the MOMO code are the total scattering (b) and attenuation (c) coefficients, the single scattering albedo (ω_o) and the scattering phase functions $(\tilde{\beta})$. The present radiative transfer simulations output L_{TOA} normalised by an extraterrestrial solar irradiance of $F_{ø} = 1$ in each band.

2.1.2 Optical Properties of the Atmosphere

Dedicated multispectral satellites measure the solar radiance reflected by the land-ocean-atmosphere system at the TOA. According to the Earth's global energy budget (Trenberth et al., 2009; Stephens et al., 2012) about one third of the total incoming solar radiation is reflected back as shortwave radiation (i.e., visible and infrared light). More than two-thirds of the shortwave reflectance arising to the satellite sensors derive from the atmosphere (Gordon, 1978), making the ocean reflectances modest in comparison. Consequently, ocean colour remote sensing requires the accurate determination of the atmospheric effects to retrieve the true ocean reflectance values. In this section, the optical properties of the atmosphere considered in the coupled ocean-atmosphere radiative transfer simulations were described. The atmospheric parameterization of the present radiative transfer simulations follows the one in Schroeder (2005) and in Schroeder et al. (2007a); (2007b). All basic definitions of inherent and apparent optical properties, such as scattering and absorption coefficients and phase functions, already introduced in section 2.1.1, continue to apply to the description of the atmospheric scatterers and absorbers.

The optical thickness (τ) expresses the magnitude of light attenuation (c) within a medium with of thickness (z), due to the absorbing and scattering of particles and molecules:

$$\tau(\lambda) \stackrel{\text{def}}{=} \int_0^l c(\lambda) dz \qquad \text{Eq. 2.25}$$

The total optical thickness of the atmosphere (τ) can be decomposed into its partial contributions due to scattering and absorption of aerosol particles (τ_a), the Rayleigh scattering by molecules (τ_R), the absorption by ozone molecules (τ_{O_3}) and by other gases (τ_g), all of which are wavelength dependent:

$$\tau = \tau_g + \tau_{O_3} + \tau_a + \tau_R \quad \text{Eq. 2.26}$$

The parameterization of each of these components to the total optical thickness of the atmosphere will be briefly described in the following subsections.

2.1.2.1 Gas absorption

The electromagnetic radiation travelling through the atmosphere is selectively absorbed by gases such as oxygen (O_2), water vapor (H_2O), carbon dioxide (CO_2), carbon monoxide (CO), ozone (O_3), methane (CH_4) and nitrous oxide (N_2O). The atmospheric gases transmission (except for O_3) were derived from the High-Resolution Transmission Molecular Absorption (HITRAN) database (Gordon et al., 2017) and implemented in the radiative transfer simulations via the modified k-distribution model of Bennartz and Fischer (2000). Ozone gas (O_3) molecules are most abundant in the stratosphere and contribute to the absorption of electromagnetic radiation in the ultraviolet, infrared and in the visible spectrum, the latter which is mostly absorbing between 530 and 650 nm. Thus, the absorption of stratospheric ozone influences the radiance and irradiance transmissions through the atmosphere at the Himawari-8 visible bands, particularly at the 640 nm band. In this study, radiative transfer simulations were employed assuming a default ozone loading of 344 Dobson Units (DU) (Committee on Extension to the Standard Atmosphere, 1976). The ozone transmission at 344 DU is calculated as:

$$T_{O_3}(\lambda, \theta_s, \theta_v) = e^{-(\tau_{O_3} M)} \quad \text{Eq. 2.27}$$

$$\tau_{O_3}(\lambda) = a_{O_3}[O_3] \quad \text{Eq. 2.28}$$

In Eq. 2.27, M is the total air mass ($M = (1/cos\,\theta_s) + (1/cos\,\theta_v)$), θ_v is the satellite viewing angle, θ_s is the solar zenith angle and τ_{O_3} is the ozone optical thickness per band. At each Himawari-8 band, τ_{O_3} is calculated as the ozone concentration $[O_3]$ multiplied by its absorption coefficient a_{O_3}, following Eq. 2.28.

2.1.2.2 Rayleigh scattering

The Rayleigh optical thickness is predominantly due to scattering of particles or molecules that have radius much smaller than the wavelength amplitude (in units of nm or µm) or photon frequency (in Hertz – Hz) of the incident radiation. The most common application of Rayleigh scattering theory is to the gaseous molecular scattering in the atmosphere (Hansen and Travis, 1974). The Rayleigh optical thickness has inverse power dependence with wavelength:

$$\tau_R \cong \lambda^{-4.09} \qquad \text{Eq. 2.29}$$

Because of the strong wavelength dependence, the Rayleigh scattering is more significant in shorter wavelengths of the visible spectrum, which explains why a cloud-free and clear sky is predominantly blue. The Rayleigh scattering largely depends on the number of molecules in the atmosphere, which in turn depends on the atmospheric pressure. The vertical profile of attenuation due to molecules or gases in the atmosphere can be computed from the approximate formula given by Hansen and Travis (1974):

$$\tau_R = {}^{P}/_{P_0} . [0.008569\lambda^{-4}(1 + 0.0113\lambda^{-2} + 0.00013\lambda^{-4})] \qquad \text{Eq. 2.30}$$

In equation Eq. 2.30, the wavelength amplitude (λ) have units of micrometres (µm), P is the given sea level atmospheric pressure and $P_0 = 1013.25\ hPa$ is the standard sea level atmospheric pressure (Committee on Extension to the Standard Atmosphere, 1976). Considering molecular anisotropy, the Rayleigh scattering phase function is computed as in Eq. 2.31, where $\delta = 0.0279$ is the depolarization factor (Young, 1980), and θ is the scattering angle:

$$\tilde{\beta}_R(\theta) = \frac{3}{16\pi(1 + 2\gamma)}[(1 + 3\gamma) + (1 - \gamma)cos^2(\theta)] \qquad \text{Eq. 2.31}$$

$$\gamma = \frac{\delta}{2 - \delta} \qquad \text{Eq. 2.32}$$

Figure 2.6 demonstrates the exponential decay of the Rayleigh optical thickness with wavelength, for small and large atmospheric sea level pressures (980 and 1040 hPa, respectively).

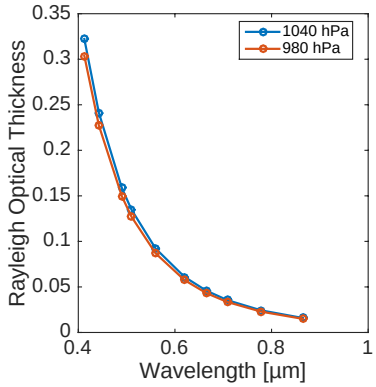

Figure 2.6: Rayleigh Optical Thickness calculated for 980 and 1040 hPa atmospheric pressures.

2.1.2.3 Aerosol scattering

Aerosols are particles or droplets suspended in the air, with size ranging from 10^{-3} to 10 µm, including haze, smoke, fumes, dust, mist, sea salt, etc., from natural or anthropogenic sources (Hidy, 2003). Compared to atmospheric gases, the distribution of aerosol particles is spatially and temporally heterogeneous on global scale (Graßl, 2011). The scattering by atmospheric particles with radius larger than the wavelength amplitude is treated numerically with the Mie theory (Mie, 1908), considering the size distribution and the complex refractive index of each particle. The Mie computations are utilised in the present work to derive the extinction coefficient (c), the phase function $(\tilde{\beta})$ and the single scattering albedo ω_0 of each aerosol component.

Based on extensive measurements of aerosol concentrations, size distribution and optical properties, several aerosol models have been developed to represent variable atmospheric conditions, including the dependency of aerosols to relative humidity (Shettle and Fenn, 1979). An aerosol model is defined as a homogeneous mixture of aerosol components at defined proportions. A few basic aerosol components were utilised to build aerosol models for the Mie calculations, following the works of Shettle and Fenn (1979) and the World Climate Research Programme (1986) report. A summary of the vertical distribution of the aerosol models utilised in this work, as well as the volumes and numbers of particles for each aerosol component are presented in Table 2.1.

Table 2.1: Vertical distribution of the aerosol models utilised in this work, as well as the volume and number of particles for each aerosol component. Due to rounding, the sum of the total number of particles in the continental model slightly deviates from 100%.

Aerosol Model	*Components*	*Volume [%]*	*Particles [%]*	*Vertical distribution*
Maritime[1]	Rural	10	99	Boundary layer: 0-2 km
	Oceanic	90	1	
Continental[1]	Water Soluble	29	93.87	Troposphere: 2-12 km
	Dust-like	70	0.0002	
	Soot	1	6.1230	
Stratospheric[2]	H_2SO_4	100	100	Stratosphere: 12-50 km

[1] Shettle and Fenn (1979), [2] World Climate Research Programme (1986)

The Maritime model includes the oceanic aerosols represented by a sea salt solution in water, plus a small contribution of the rural aerosol component, which includes a mixture of water-soluble particles (70%) and dust (30%). The Continental model is a mixture of water soluble, dust-like and soot particles. The Stratospheric model is an aqueous solution of 75% of sulphuric acid (H_2SO_4) and 25% of water in the stratosphere (World Climate Research Programme, 1986). The particle size distribution of the Maritime and Continental aerosol models is represented by the sum of two-lognormal distributions, as in the Equation 1 of the work of Shettle and Fenn (1979). The particle size distribution of the

Stratospheric model is represented by a Modified Gamma Size distribution (Deirmendjian, 1962). A description of the atmospheric model is provided in the following section.

2.1.3 Environmental Effects that were not Included in the Radiative Transfer Simulations

Environmental effects, such as sun glint, bottom reflectivity, inelastic scattering, and whitecaps also influence the remote sensing reflectance at the satellite sensor. This section briefly outlines the effects potentially affecting L_{TOA}, but not considered in the present radiative transfer simulations.

2.1.3.1 Bottom reflectance

The solar radiation can penetrate as deep as 200 m in very clear waters, particularly in the spectral transparency window of 450-600 nm (Cannizzaro and Carder, 2006). Optically shallow waters may be defined as those where the bottom (seagrass meadows, coral reefs and/or sand) is optically visible from an above water observer or a satellite sensor. In such cases, the bottom contributes to the reflectance signal, potentially affecting the retrieval of water quality parameters (Cannizzaro and Carder, 2006; Barnes et al., 2013; Reichstetter et al., 2015; McKinna et al., 2015; McKinna and Werdell, 2018). However, with increasing water depth (~>20m) and in optically deep or turbid waters, such as estuarine influenced areas, the bottom reflectance can be neglected (Reichstetter et al., 2015). To reduce the ambiguity of retrieving L_{TOA} and ocean colour parameters in coastal waters, the present simulations were set up for a geometric ocean depth of 500 m, assuming no influence of the bottom. However, it should be noted that water pixels immediately adjacent to the coastline (within 1 km) and over shallow reefs may be influenced by the bottom reflectance. These areas are then identified and masked out in the Himawari-8 derived products. Conversely, in shallow (<20 m) but optically deep or turbid waters, the interpretation of Himawari-8 products was linked to water depth measurements, particularly for the validation analysis.

2.1.3.2 Sun glint

Sun glint is the direct solar radiation specularly reflected by the ocean surface. It affects remote sensing observations when the sensor is viewing a target that is directly opposite to the Sun (low relative azimuth angle – forward scattering), and when the solar and sensor zenith angles are equivalent. The glint radiance is stronger than the water-leaving radiance, covering the ocean colour image with a very bright patch. Therefore, glinted areas must be either glint corrected for determining the ocean colour parameters (Hedley et al., 2005; Steinmetz et al., 2011; Brockmann et al., 2016; Vanhellemont, 2019), or masked to avoid erroneous outputs. By default, the MOMO simulations include the effect of the specular reflectance on the water leaving radiance according to the Cox and Munk (1954) method. In this study, the simulated L_{TOA}were corrected for glint effects prior to ANN

training (see Section 2.3.2) because a sun glint correction procedure is not available for Himawari-8 observations. A mask was developed (section 2.4.2.3) to remove the glinted area in the Himawari-8 derived ocean colour products.

2.1.3.3 Whitecaps

Whitecaps or sea foam generally result from waves breaking at the sea surface, which is largely dependent on the wind speed. The fractional reflectivity of whitecaps contributes to the L_{TOA} predominantly between 410 nm to 670 nm (Moore et al., 2000; IOCCG, 2019; Dierssen, 2019). However, its effects on augmentation of reflectance are reduced for wind speeds lower than ~4 ms^{-1} (Moore et al., 2000). Additionally, the relative size of wave-generated whitecaps is small (up to tens of meters) compared to the spatial resolution of the pixels from most ocean colour satellite sensors (1 km^2 for Himawari-8). As a result, the identification and masking of whitecaps is impractical, such as with sub-pixel sized clouds. A simple parameterization of whitecaps contribution dependent on wind speed is suggested for correction of the radiometric signal.

2.1.3.4 Inelastic scattering

The inelastic scattering occurs when a molecule, after receiving electromagnetic energy, emits energy in a wavelength longer than the incident one, by modifying its vibrational or rotational state (Kirk, 2010). This effect is observed in water molecules (i.e., rotational Raman scattering), and it largely contributes to the upwelling of shortwave visible radiation in clear oceanic Case 1 waters (Bartlett et al., 1998; Gordon, 1999; Gordon, 2014), particularly at 635 nm or longer. In Case 2 waters, however, the Raman effects are largely reduced due to the strong interaction of light with particles and substances. Conversely, about 1% of the incident radiation absorbed by phytoplankton is re-emitted (Kirk, 2010). The CHL fluorescence re-emission peaks at around 685 nm and linearly increases with CHL (Morel and Prieur, 1977; Gordon, 1979; Lin et al., 1984; Gower and Borstad, 1990). In fact, satellite detection of CHL fluorescence has been widely applied to improve understanding of phytoplankton physiology and estimates of primary productivity (Babin et al., 1996; Behrenfeld et al., 2009; Browning et al., 2014; Lin et al., 2016). However, the Himawari-8 broad visible bands, particularly in the red part of the spectrum (640 nm with 90 nm bandwidth), are not centred at the peak of CHL fluorescence. Likewise, fluorescence becomes significant from 430 nm to 580 nm, with a peak at 450 nm in waters with high content of YEL (Kirk, 2010). However, CHL and YEL fluorescence are less detectable in Case 2 waters because the likely mixture with suspended minerals or TSS (from 1 mg L^{-1}) can reduce the fluorescence leaving the water (Bukata et al., 2004). Therefore, it is assumed that the effects of Raman scattering, CHL and YEL fluorescence can be negligible at the Himawari-8 bands and for the coastal GBR and are not accounted for in the present algorithm.

2.1.3.5 Polarization

Electromagnetic radiation from the Sun, which is naturally unpolarized, may become partially polarized when interacting with atmospheric particles and molecules. Ignoring the effects of polarization may yield between 5 and 10% errors in the simulated L_{TOA} (Kotchenova et al., 2006). However, the present radiative transfer simulations with MOMO do not consider the effects of polarization.

2.1.3.6 Bidirectional reflectance (BRDF)

The ocean surface is not isotropic, i.e., the water leaving reflectance has angular dependency to the illumination conditions and to the optical properties of the waters itself (Morel and Gentili, 1996). Bidirectionally-induced errors are as low as 1% for solar angles within 60˚ (Gordon and Franz, 2008) and thus, the effects of bidirectional reflectance distribution function (BRDF) were not included in the present radiative transfer simulations.

2.1.3.7 Other effects

Although a few radiative transfer models consider the curvature of the earth in the ocean-atmosphere system (Rozanov et al., 2014; Ramon et al., 2019), the present model assumes a plane-parallel geometry. The plane parallel geometry is a reasonable assumption for retrievals where $\theta_s < 70^{\circ}$ (Ding and Gordon, 1994), which is compatible to the θ_s ranges of the present simulations.

The optical characteristics of water and ice clouds are not included in the atmospheric parameterization and clouds were identified and masked with an algorithm developed for Himawari-8 (Qin et al., 2019). Although large patches (> 1 km^2) of surface bio-slicks (Whitney et al., 2021) and oil spills (Brekke and Solberg, 2005; Blondeau-Patissier et al., 2020) may be detected by the Himawari-8 bands, these features were not considered in the present algorithm.

2.2 Forward Model: Radiative Transfer Simulations

In this chapter, a coupled ocean-atmosphere radiative transfer model was utilised to simulate the VNIR bands of Himawari-8 for a realistic range of in-water and atmospheric optical properties. Several numerical solutions are available for simulating the spectral fluxes and radiances distribution from the ocean based on the Radiative Transfer Equation. For instance, HydroLight (Mobley, 1989) is one of the most widely used models to compute the in-water light field based on radiative transfer theory. However, it does not account for atmospheric absorption and scattering properties, which is fundamental for retrieving accurate TOA radiances for inverse modelling of the satellite signal. For the purpose of coupled ocean-atmosphere radiative transfer simulations, there are multiple validated models, including: the Matrix-Operator MOdel (MOMO) (Fischer and Grassl (1984); Fell and Fischer (2001)); the R-System for Transfer of Atmospheric Radiation (RSTAR5b) (Nakajima et al., 2003); the Second Simulation of a Satellite Signal in the Solar Spectrum (S6V1) -(Kotchenova et al., 2006); the Coupled Atmosphere–Ocean-Discrete-Ordinate Radiative Transfer (CAO-DISORT) (Spurr et al., 2007); the SCIATRAN software package (Rozanov et al., 2002; Blum et al., 2012); and more recently the Texas A&M University Vector Radiative Transfer Model (TAMU-VRTM) (Ding et al., 2019) and the Speed-Up Monte-Carlo Advanced Radiative Transfer code with GPU (SMART-G) (Ramon et al., 2019). The differences between these models are mainly due to the availability of source code, numerical treatment, and configuration to a specific sensor.

In this work, a scalar version of the MOMO code was used for simulations of the VNIR Himawari-8 bands (at L_{TOA}) in a coupled ocean-atmosphere system for varying in-water concentrations of CHL, TSS and YEL. MOMO has been validated against analytical solutions (Fell and Fischer, 2001) with deviations below 0.1% for solar and observation zenith angles smaller than 60˚. Additionally, MOMO shows good agreement when compared with other frequently employed coupled ocean-atmosphere radiative transfer models (Blum et al., 2012). Hence, it has been used for the algorithm development activities of the MERIS sensor (Schroeder et al., 2007a; 2007b; Hollstein and Fischer, 2012) and in applications to ocean colour remote sensing (Zhang, 2003; He et al., 2014). The main advantage of MOMO is due to its high computational efficiency, which allows simulating the light propagation in an optically thick medium, (Plass et al., 1973), such as in the aquatic environments. Thus, MOMO is convenient for the development of remote sensing algorithms for ocean colour retrievals.

MOMO solves the Radiative Transfer Equation (RTE) to quantify the direction and intensity change of a monochromatic beam of light within a medium. In other words, MOMO calculates the unpolarised L_{TOA} distributions for selected discrete relative azimuth, solar and observation zenith angles in the ocean-atmosphere system. In the RTE, the intensity that leaves the system and the intensity that enters it must be equal to the algebraic sum of the power losses and gains due to absorption and scattering.

To obtain an accurate solution, the RTE must be solved numerically. MOMO uses the *Doubling-Adding* method (van de Hulst, 1963) to perform multiple scattering calculations within the atmospheric optical layers. In summary, to calculate the radiation in the upward and downward directions, each layer is subdivided in very thin optical layers, where the radiative transfer is resolved on the assumption of single scattering. The elementary layers with the same optical properties are summed (*Doubling*) for the inclusion of multiple scattering. Then, the layers with different optical properties are added, which allows to calculate the reflection and transmission properties of combined layers to compute the final output. MOMO's numerical treatment is described in detail by Fell and Fischer (2001), and references therein.

In the present study, the ocean-atmosphere system is stratified in several horizontally homogeneous plane-parallel layers where the optical properties depend on the vertical coordinate only (1-dimension). In each layer, the types and concentrations of aquatic and atmospheric optical constituents defined are considered. The inputs to the MOMO code are the total scattering (b) and attenuation (c) coefficients, the single scattering albedo (ω_o) and the scattering phase functions $(\tilde{\beta})$. In a similar approach, the scattering and attenuation coefficients due to air molecules are adapted to each layer, considering the vertical profile of the atmospheric pressure.

A first round of MOMO-RT simulations was conducted to evaluate the Himawari-8 sensors' ability to detect a wide range of water quality parameters for the coastal GBR (sensitivity analysis). A second round of radiative transfer simulations was employed to generate a large number of outputs (>90 million) for the training and testing of several ANN inversion experiments, without an explicit atmospheric correction procedure (one-step inversion). The MOMO simulations were set up for the Himawari-8 VNIR bands, at specific atmospheric and aquatic conditions, which are described in the next subsections.

2.2.1 The Atmospheric Parameterization

The simulated atmosphere is 50 km thick and divided into 11 layers where the vertical profiles of pressure, temperature and humidity are given by the Committee on Extension to the Standard Atmosphere (1976). The attenuation by Rayleigh scattering follows the vertical profile of the Committee on Extension to the Standard Atmosphere (1976) and is parameterized with atmospheric pressures of 980 hPa and 1040 hPa. The atmosphere is split into the Boundary layer (0-2 km), the free Troposphere (2-12 km) and the Stratosphere (12-50 km), (Figure 2.7). In each layer, the simulations were performed for eight distinct aerosol assemblages (AM). Each AM is composed of the three main aerosol models, Maritime, Continental and Stratospheric (Table 2.1), and four values of relative humidity (70%, 80%, 90% and 99%). The Boundary layer and the Troposphere contain five values of

aerosol optical thickness (τ_a) at 550 nm, proportionally distributed through the eight AM (Figure 2.7), while the Stratosphere has a fixed value of τ_a.

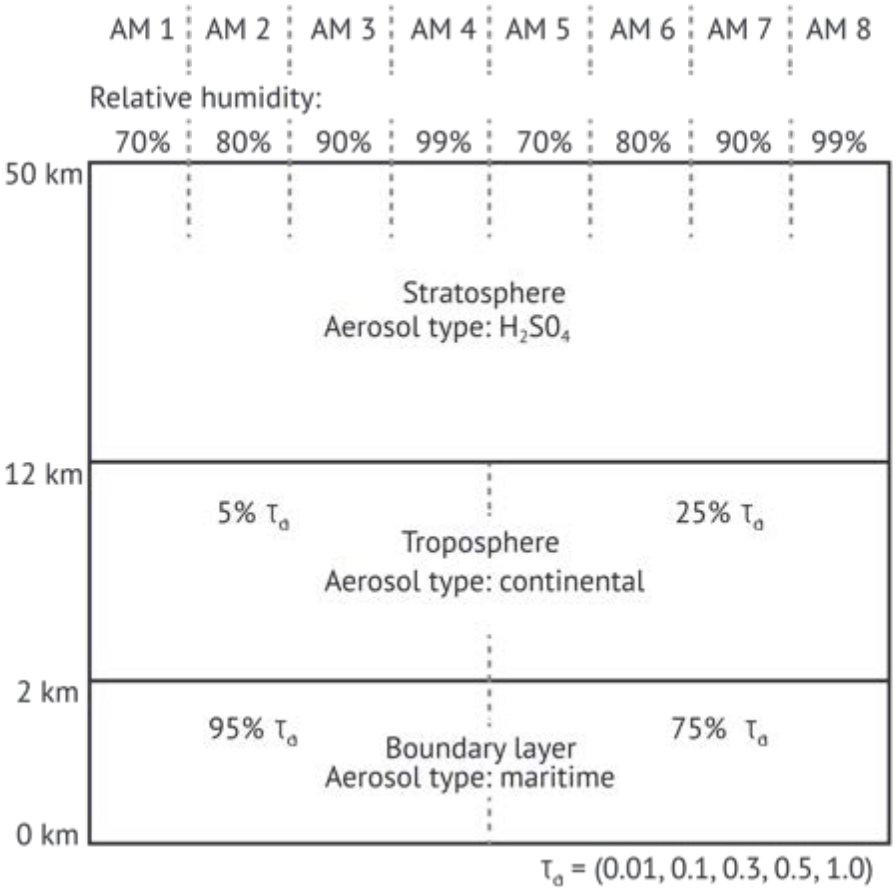

Figure 2.7: Illustrative diagram of the atmospheric model setup for the radiative transfer simulations in this study, based on Schroeder et al. (2007b), and adapted from Ebert (2009).

The τ_a ranges were set up based on *in situ* measurements from the sun-photometer of the Aerosol Robotic Network - AERONET (Holben et al., 1998; AERONET, 2020) installed at LJCO. The τ_a was evaluated with Level 2 (calibrated and quality assured) data between 2009-2010 and 2013-2015. The τ_a inputs at 550 nm ranges approximately from 0.01 to 0.7 (Figure 2.8), comprising a very broad variability of τ_a (two orders of magnitude). The general configuration of the coupled ocean-atmospheric model is summarized in Table 2.2 along with the geometric parameters and the Himawari-8 bands utilised in this study. The top of atmosphere radiances (L_{TOA}) were simulated for 17 solar and observation angles and 25 equally spaced relative azimuth angles.

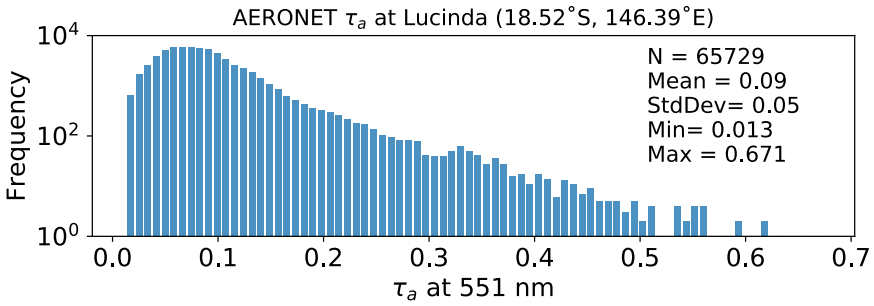

Figure 2.8: Histogram of AERONET τ_a (551 nm) sampled at LJCO between 2009-2010 and 2013-2015. Descriptive statistics of τ_a is provided, with the number of samples per bin in logarithmic scale.

Table 2.2: Summary of the atmospheric and geometric components for parameterization of the radiative transfer simulations.

Atmospheric Parameters	
Altitude of the plane-parallel layers	0, 1, 1.5, 2, 2.5, 3, 3.5, 4, 8, 12, 50 km
Relative humidity	70, 80, 90, 95, 99%
τ_a *for Continental and Maritime models*	0.01, 0.1, 0.3, 0.5, 1.0 (550 nm)
τ_a *for the Stratospheric model*	0.005 (550 nm)
Atmospheric Surface Pressure	980, 1040 hPa
Wind Speed at 10 m	1.5 m/s
Total Column Ozone	344 DU
Gases absorption	HITRAN database (O_2, O_3, H_2O, N_2O, CH_4, CO, CO2)
Vertical profiles	Relative humidity, Atmospheric Pressure and Temperature (Committee on Extension to the Standard Atmosphere, 1976)
Geometric Parameters	
θ_s	17 angles between 0˚and 87.14˚
$\Delta\phi$	25 angles between 0˚and 180.0˚
θ_v	17 angles between 0˚ and 87.14˚

2.2.2 The Aquatic Parameterization

The simulations were set up for realistic water quality fluctuations, represented by multiple and unique instances of synthetic CHL, TSS and YEL combinations. Each unique combination of synthetic CHL, TSS and YEL is referred to hereafter as a triplet. The triplets served as inputs to the bio-optical models parameterized for the GBR waters (as in section 2.1.1.1), generating a pool of IOPs for the radiative transfer simulations. The triplets' values followed the ranges and concentrations of *in situ* CHL,

TSS and YEL acquired in the GBR (Table 2.3) and compiled from the IMOS bio-optical database[7]. The *in-situ* dataset was acquired by CSIRO and AIMS between 2002 and 2015 during several research voyages and at fixed location facilities, including at LJCO.

Table 2.3: Descriptive statistics of *in situ* CHL, TSS and YEL acquired in the GBR between 2002 and 2015.

Water Quality Parameter	*Minimum*	*Maximum*	*Mean*	*Std. Dev.*	*N*
CHL (mg m^{-3})	0.05	15	0.7	1.3	1467
TSS (mg L^{-1})	0.02	85	3.4	6.5	1425
YEL (m^{-1})	0.004	2.4	0.3	0.4	417

The derived IOPs were distributed homogeneously through the simulated ocean layer. The sea surface roughness was modelled for a wind speed of 1.5 m s^{-1}, based on the wave facet model of Cox and Munk (1954). Although varying wind speed is suitable to better resolve sun and sky glint effects, a single wind speed was chosen to restrict the number of solutions. The following subsections describe the concentrations and ranges of synthetic CHL, TSS and YEL defined for the sensitivity analysis and for the simulated training and testing datasets.

2.2.2.1 Concentrations and Ranges for the Sensitivity Analysis

The Himawari-8 sensitivity to detect changes in CHL, TSS and YEL was tested in 6 experimental simulations utilising a selected number of triplets. The first three sensitivity experiments (SE_{CHL}, SE_{TSS} and SE_{YEL}) tested the variability of L_{TOA} when changing one water quality parameter at a time, whilst the other two water quality parameters remained constant. For instance, the SE_{CHL} experiment simulated 5 L_{TOA} spectra from 5 triplets with varying CHL (0.01, 0.1, 1.0,10.0 and 15.0 mg m^{-3}) combined to constant TSS and YEL values (5.0 mg L^{-1} and 0.5 m^{-1}).

The second round of experiments (SE_{CHL_TSS}, SE_{YEL_CHL} and SE_{YEL_TSS}) tested the variability of L_{TOA} when simultaneously changing two water quality parameters, whilst the third one was fixed. The experiments encompassed a broad range (3 to 4 orders magnitude) of CHL, TSS and YEL values (Table 2.4), roughly following the ranges of *in situ* data values from the coastal GBR (Table 2.3). The ranges of CHL, YEL and TSS were slightly adjusted in each subsequent experiment for a comprehensive analysis. All sensitivity experiments were simulated with an τ_a of 0.015 (at 550 nm) and a sea level atmospheric pressure of 1040 hPa. The spectral variations of simulated L_{TOA} were presented for θ_s = 41.4˚, θ_v = 0.08˚, $\Delta\phi$ = 180.0˚, emulating the Himawari-8 sub-satellite field-of-view while looking away from the sun and not affected by specular reflectance, or sun glint.

[7] The IMOS Bio-optical Database is available online through the Australian Ocean Data Network, A. (2020). Australia's Integrated Marine Observing System (IMOS). Retrieved from https://portal.aodn.org.au/ (accessed on 20/02/2017).

Table 2.4: Concentrations and ranges of CHL, TSS and YEL assigned to the sensitivity experiments.

Experiment	*CHL [mg m^{-3}]*	*TSS [mg L^{-1}]*	*YEL [m^{-1}]*
SE_{CHL}	0.01 to 15.0	5.0	0.5
SE_{YEL}	1.0	5.0	0.001 to 3.0
SE_{TSS}	1.0	0.05 to 100.0	0.5
SE_{CHL_TSS}	0.01 to 30.0	1.0 to 100.0	0.5
SE_{YEL_CHL}	0.01 to 30.0	0.5	0.005 to 3.0
SE_{YEL_TSS}	0.5	0.5 to 100.0	0.005 to 3.0

2.2.2.2 Concentrations and Ranges for ANN Training and Testing

In this section, a large data pool of synthetic CHL, TSS and YEL was randomly generated for the radiative transfer simulations. For an effective ANN inversion performance, the simulated training dataset needs to cover the ranges of variability observed in the GBR waters. Therefore, the ranges of synthetic CHL, TSS and YEL were defined based on the dispersion of *in situ* correlated concentrations of CHL, TSS and YEL (Figure 2.9), following the approach by Zhang (2003). The upper and lower limits, indicated by the solid black lines in Figure 2.9, were calculated by adjusting the coefficients of Eq. 2.33, Eq. 2.34, and Eq. 2.35, utilising the maximum and minimum values of *in situ* CHL, TSS and YEL from (Table 2.3). In general, the position of the upper and lower limits suggests that the coastal waters of the GBR include a wide range of bio-optical variability compared to European coastal waters. Additionally, the dispersion of correlated concentrations indicates a degree of dependency between each water quality parameter. The calculated upper and lower limits constrained the *in-situ* dataset to the combinations more likely to occur in the GBR, and the ranges were employed to determine the synthetic water quality parameters (Table 2.5). With this approach, the number of radiative transfer calculations is greatly reduced whilst realistically representing the bio-optical properties in the GBR.

Table 2.5: Ranges of CHL, TSS and YEL determined for radiative transfer simulations.

WQP	*Minimum*	*Maximum*
CHL (mg m^{-3})	0.01	15
TSS (mg L^{-1})	0.01	100.0
YEL (m^{-1})	0.002	2.5

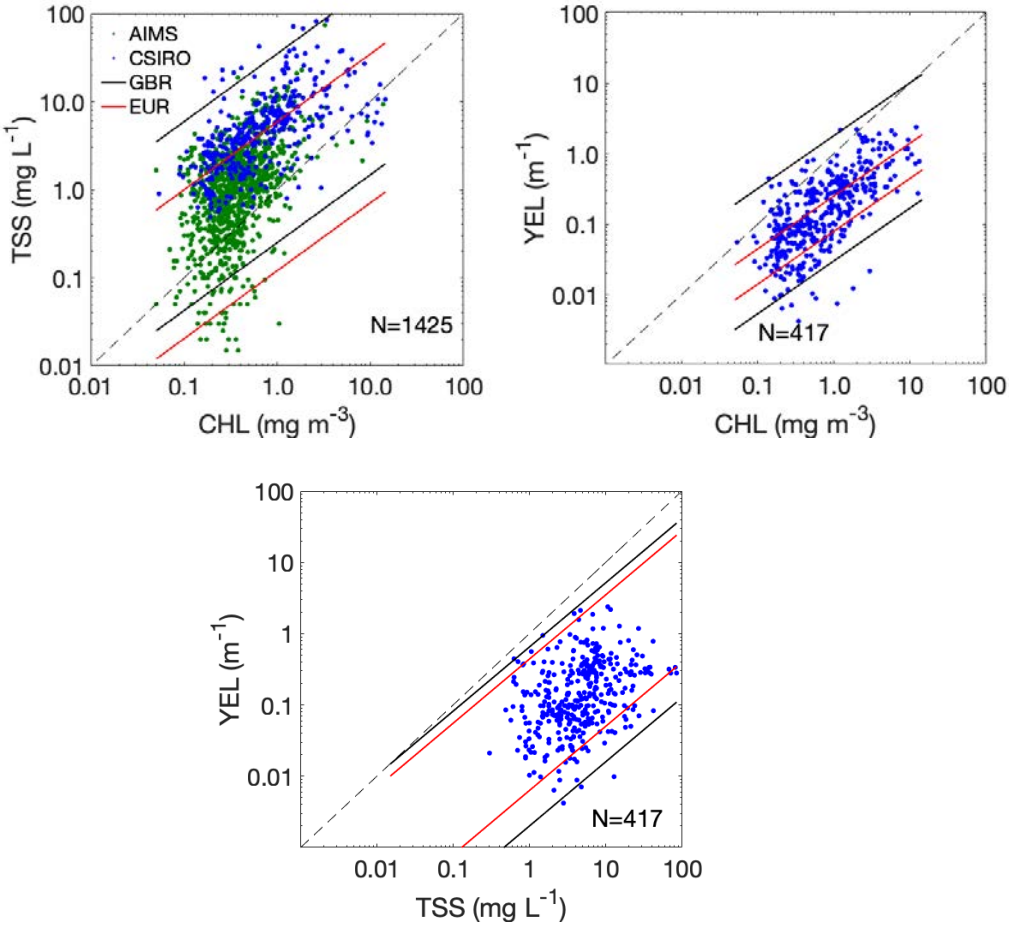

Figure 2.9: Scatter plots between concurrent in situ samples of CHL, TSS and YEL (logarithmic scale), where the solid lines indicate the upper and lower limits of variability defined for the coastal GBR (black solid lines) and for coastal and oceanic European waters (red solid lines). The scatterplot comprises data from AIMS (green dots) and from CSIRO (blue dots).

The synthetic CHL, TSS and YEL values were derived by specifying concentration dependencies, as in Eq. 2.33, Eq. 2.34, and Eq. 2.35, and evenly distributed in a logarithmic space, so each order of magnitude was similarly represented. First, a random CHL is selected between 0.01 and 15 mg m^{-3}. For the selected CHL, a value of TSS is randomly selected between 0.01 and 100 mg L^{-1}, according to Eq. 2.33, and so on for YEL, according to Eq. 2.34 and Eq. 2.35. This approach was repeated until enough unique correlated combinations of CHL, TSS and YEL were generated within the upper and lower limits established, whilst avoiding duplicated simulations (Figure 2.10). The ANN inversion method can interpolate and derive values within the upper and lower limits, including within the gaps observed in Figure 2.10. Each set of triples (totalling 40) were translated into IOPs (following section 2.1.1.1) and associated to the 4 VNIR Himawari-8 bands, to 5 τ_a, 2 atmospheric pressures and 8 atmospheric assemblages described in section 2.2.1. As a result, a total of 12,800 inputs $(40 \times 4 \times 5 \times 2 \times 8)$, were generated for the radiative transfer simulations. Each input was associated to 16 sun zenith angles, 25 relative azimuth angles and 16 observation zenith angles, yielding approximately ~ 90 million values of

L_{TOA} were computed as outputs of the radiative transfer simulations. A training and a testing subset, comprising 100 000 L_{TOA} values each, were randomly extracted from this extensive simulated dataset to speed up the ANN inversions. The size of the training and testing subsets followed previous attempts on estimating ocean colour parameters with the ANN method (Zhang et al., 2003; Ebert, 2009). Figure 2.11 illustrates the frequency distribution of synthetic CHL, TSS and YEL values for the generated training dataset.

$$TSS_{min}(CHL) = 0.25[CHL]^{0.77}, \qquad TSS_{max}(CHL) = 35.0[CHL]^{0.77} \qquad \text{Eq. 2.33}$$

$$YEL_{min}(CHL) = 0.03[CHL]^{0.75}, \qquad YEL_{max}(CHL) = 1.8[CHL]^{0.75} \qquad \text{Eq. 2.34}$$

$$YEL_{min}(\mathrm{TSS}) = 0.002[TSS]^{0.9}, \qquad YEL_{max}(TSS) = 0.65[TSS]^{0.9} \qquad \text{Eq. 2.35}$$

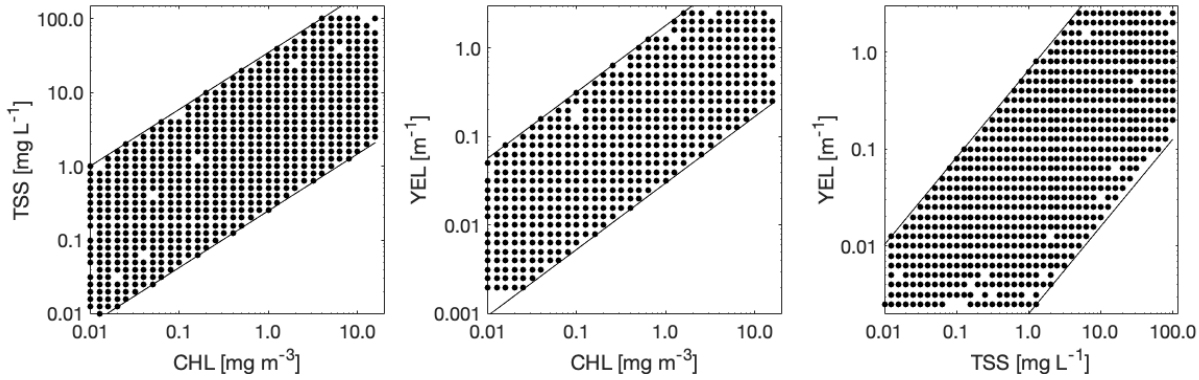

Figure 2.10: Scatter plot between stochastically generated and evenly distributed CHL, TSS and YEL, in logarithmic space. The parallel solid lines are the calculated upper and lower limits between each correlated water quality parameter.

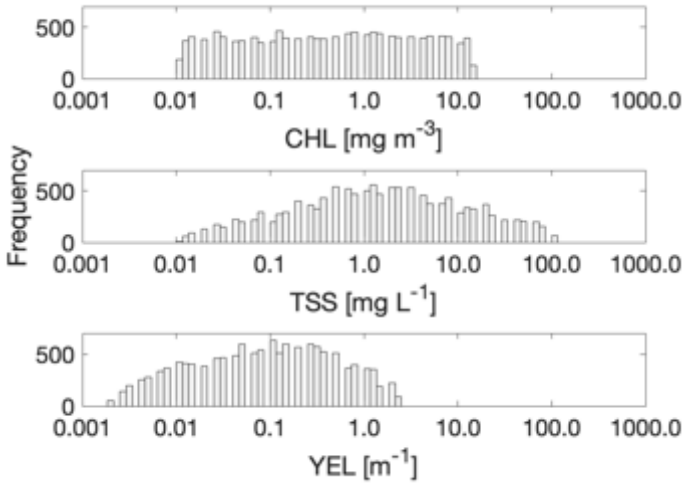

Figure 2.11: Frequency distribution of logarithmic values of CHL, TSS and YEL, containing 12,800 randomly generated synthetic triples of water quality parameters.

2.2.3 Sensitivity analysis results

The objective of this analysis was to verify if the VNIR bands of Himawari-8 can detect changes at L_{TOA} due to realistic fluctuations of CHL, TSS and YEL. The Figure 2.12 show the variability of simulated L_{TOA} for up to 4 order magnitude increases in CHL (SE_{CHL}), TSS (SE_{YSS}) and YEL (SE_{YEL}). The individual increases of simulated L_{TOA} accounted for the joint contribution of the oceanic and atmospheric signals. Nevertheless, the spectral signatures due to varying CHL, TSS and YEL indicate the potential of Himawari-8 bands for ocean colour retrievals directly from L_{TOA}.

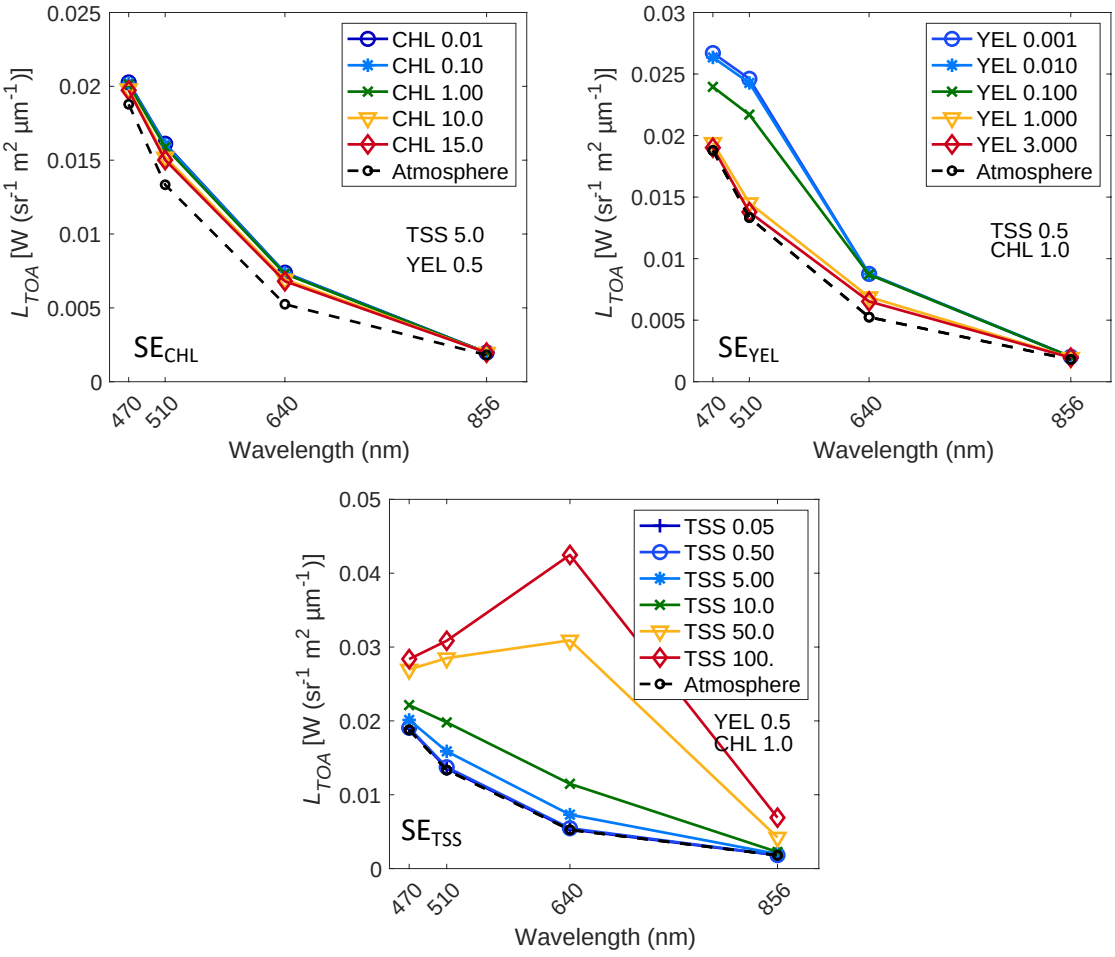

Figure 2.12: Top of atmosphere radiances (L_{TOA}) at the Himawari-8 VNIR bands as a function of varying CHL, TSS and YEL triplets. The black dashed line represents the atmospheric signal for a totally absorbing ocean. Note the different vertical scale between plots.

The 3 to 4 order magnitude fluctuations of CHL and YEL were less detectable than those of TSS. For increasing CHL and YEL values, the reflectance signal was reduced to such extent that the L_{TOA} is mostly due to the atmospheric signal. Conversely, TSS fluctuations lower than 0.5 mg L^{-1} may be more difficult to determine from L_{TOA} because of the relative strength of the atmospheric signal. Yet, the fluctuations in TSS were pronounced, particularly for the 640 nm band and for TSS larger than 10 mg L^{-1}, a value which is often observed in the coastal GBR (Table 2.3) particularly during floods.

The experiment SE_{CHL_TSS} (Figure 2.13) simulated L_{TOA} for simultaneous changes of CHL and TSS and for a constant YEL absorption of 0.5 m^{-1}. The visible bands were largely affected by TSS higher than 10 mg L^{-1}, particularly at the 640 nm, as previously demonstrated (Figure 2.12, SE_{TSS}). In this case, while TSS values increased from 10 to 100 mg L^{-1}, the 640 nm L_{TOA} increased 3 to 4-fold (0.01 to 0.04 W sr^{-1} m^{-2} μm^{-1}). The visible bands were only slightly affected by CHL larger than 1 mg m^{-3}, while the 856 nm band had no sensitivity to 3 order magnitude changes in CHL or TSS.

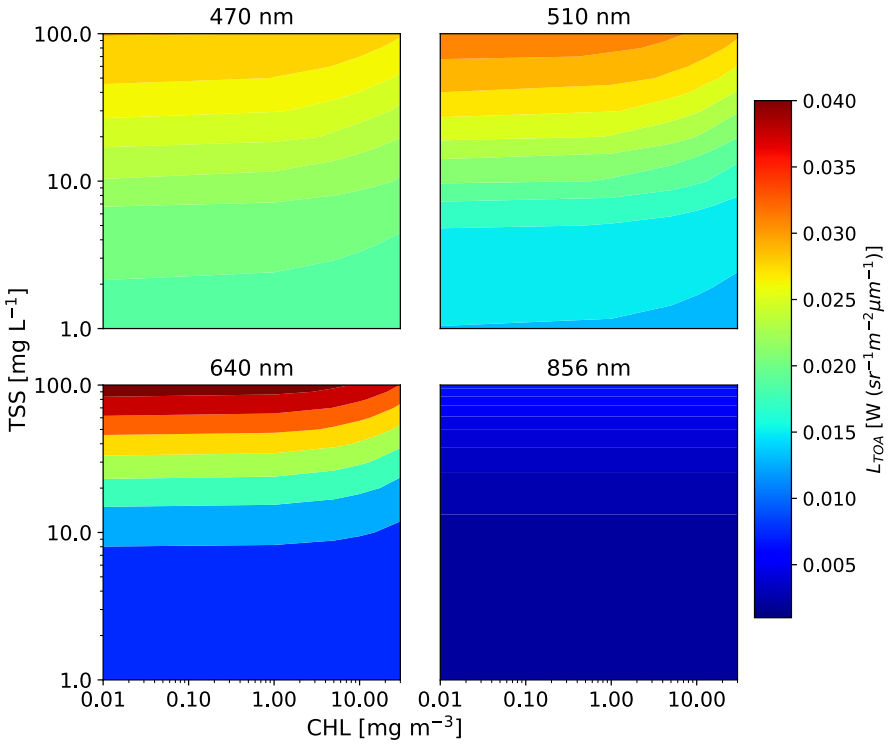

Figure 2.13: L_{TOA} variability at the VNIR Himawari-8 bands for simultaneously varying TSS and CHL (SE_{CHL_TSS}).

The experiment SE_{YEL_CHL} (Figure 2.14) had a simultaneous variability of CHL and YEL and a constant TSS of 0.5 mg L^{-1}. As expected, simultaneous increases in CHL and YEL largely decreased L_{TOA} at the 470 nm and 510 nm bands, associated with their overlapping absorption features in the visible spectrum. The 470 nm band was mostly insensitive to any increases in CHL, for YEL > 0.1 m^{-1}. As a result, the determination of CHL from Himawari-8 may be difficult in high YEL waters (> 0.1 m^{-1}), such as during floods in the coastal GBR. The 640 and 856 nm bands were otherwise insensitive to any changes in CHL and YEL.

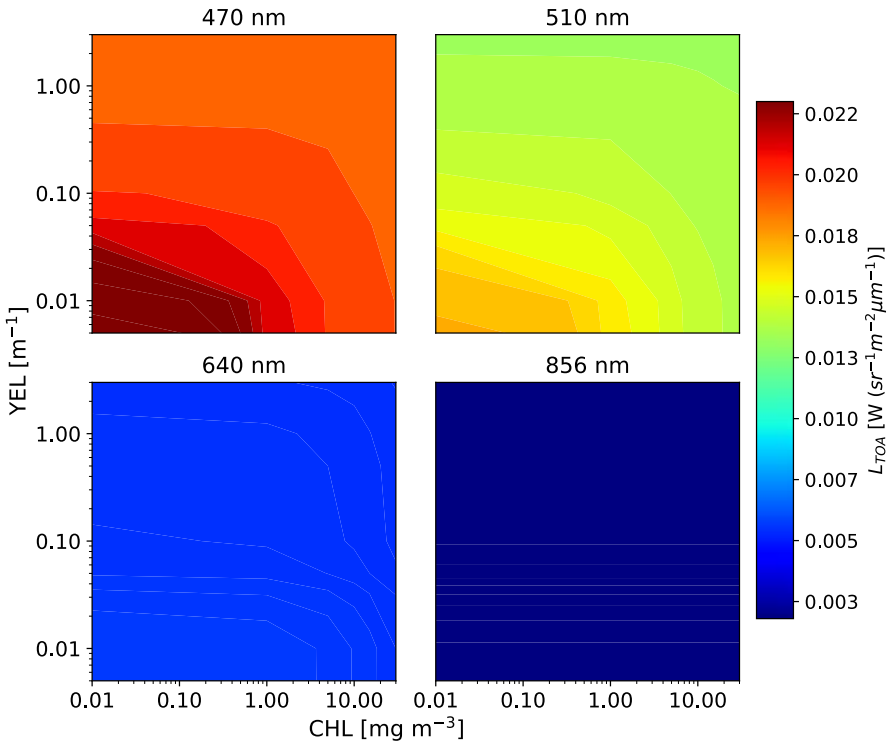

Figure 2.14: L_{TOA} variability at the VNIR Himawari-8 bands for simultaneous fluctuations of CHL and YEL for a constant TSS of 0.5 mg L^{-1} (SE_{YEL_CHL}).

The experiment SE_{TSS_YEL} (Figure 2.15) presented simultaneous variable concentrations of TSS and YEL and a constant CHL value of 0.5 mg m^{-3}. In general, TSS is the main driver of changes at L_{TOA}, particularly at the 640 nm band. However, increases in YEL (> 1 m^{-1}) largely impacted the visible bands of Himawari-8. The TSS contribution can be neglected at 856 nm, indicating that the NIR band may be useful for atmospheric corrections in turbid coastal waters.

All Himawari-8 bands investigated here were highly impacted by optical changes in the atmosphere and by the variability of the solar angles. The variations in L_{TOA} for increasing values of τ_a and for distinct θ_s (41˚, 70˚ and 80˚) are presented in Figure 2.16. The Himawari-8 VNIR bands were sensitive to 3-order magnitude increments in τ_a (from 0.01 to 1.5). The highest τ_a recorded at LJCO between 2015-2019 was 0.67, which is within the ranges of the present radiative transfer simulations. The L_{TOA} magnitudes consistently decreased as θ_s increased from 41˚ to 81˚. The spectral shape of L_{TOA} remained unaffected by the 3-order magnitude increments in τ_a, a characteristic that helps the separation of the atmospheric and ocean signals with ANN inversion. However, the discrimination of several levels of τ_a is compromised for $\theta_s \geq 70^{\circ}$ because of the increasing atmospheric path lengths. The spectral inversion of the simulated L_{TOA} for the Himawari-8 bands with an ANN technique is described in the next section.

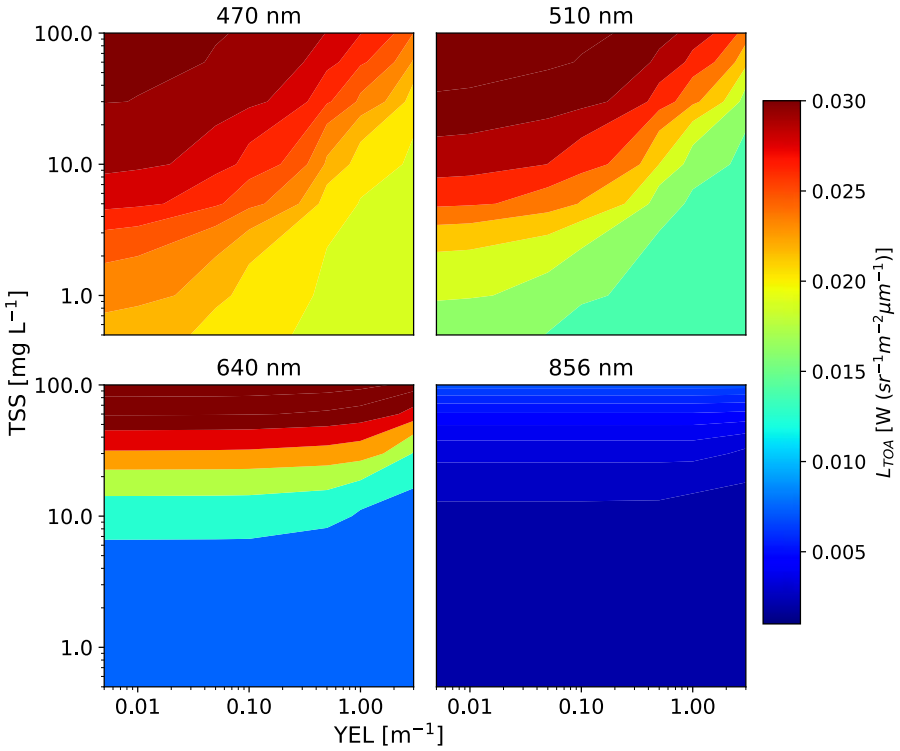

Figure 2.15: L_{TOA} variability at the VNIR Himawari-8 bands for simultaneous fluctuations of TSS and YEL for a constant CHL of 0.5 mg m^{-3} (SE_{TSS_YEL}).

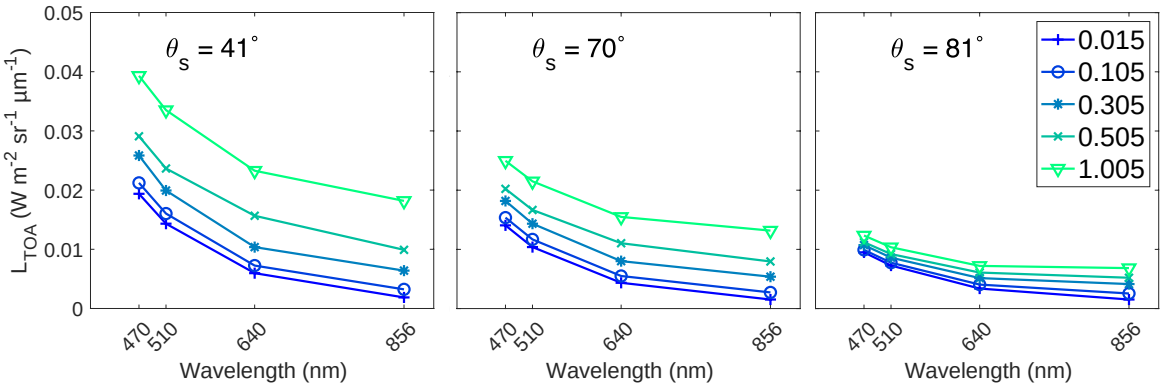

Figure 2.16: L_{TOA} distribution for three orders magnitude increases in τ_a at the Himawari-8 bands. The radiative transfer simulations were employed for θ_v = 0.08˚, ϕ =180˚ and CHL of 0.5 mg m^{-3}, TSS of 2.0 mg L^{-1} and YEL of 0.5 m^{-1}. The left, middle and right panels illustrate the L_{TOA} variability for θ_s of 41˚, 70˚ and 81˚, respectively.

2.3 Inverse Model: Artificial Neural Networks

In this study, an inversion model with ANN is employed to approximate the functional relationship between the Himawari-8 L_{TOA} and the ocean colour products. There are many different types of ANN and machine learning algorithms, however, the focus of this study is on the Feed-Forward Multilayer Perceptron (MLP) (Minsky and Papert, 1969). The MLP includes layers of individual, idealised and interconnected computing elements called neurons. In this work, the MLP comprises an input layer, a hidden layer, and an output layer. The input layer has a neuron attributed for each of the input parameters. In the hidden layer, the artificial neurons sum up the weighted input signals, distort that value non-linearly and subsequently forward their output to the output layer. Each neuron is connected to the next layer of neurons by a weight, which are estimated during a supervised learning procedure. The supervised learning or training phase is where the network 'learns' the association between the simulated input patterns and the associated target outputs. This association is mathematically a highly non-linear regression.

Meanwhile, the testing phase checks the generalization power of the algorithm for independent (unskilled) data. The feed-forward MLP does not contain feedback loops, it can approximate a set of input signals to the output data associating the neurons subsequently in one direction only and is therefore called a feed-forward network. The training procedure can be visualised in Figure 2.17 and is described as follows:

- The input neurons (n_i) receive the input vector $(\vec{x})$, containing simulated radiances and ancillary data, and propagates it to the hidden layer neurons (n_h).
- Then, each hidden neuron sums up the weighted incoming signals and applies a non-linear transfer function to compute an output that is passed to the output neuron (n_o).
- The cost function (i.e., mean squared errors, MSE – Eq. 2.36) between the target outputs $(\vec{y}_t)$ and the computed outputs $(\vec{y}_o)$ is calculated, and the internal weights $(\boldsymbol{W})$ of the network are adjusted.
- The training of the ANN is repeated until the cost function (MSE) between output and target value is minimised.

$$MSE = \frac{\sum(\vec{y}_c - \vec{y}_t)^2}{N} \qquad \text{Eq. 2.36}$$

The cost function is minimised by adapting the weight matrices $(\boldsymbol{W_1}, \boldsymbol{W_2})$ iteratively using a Limited Memory Broyden-Fletcher-Goldfarb-Shanno (L-BFGS) optimization algorithm (Liu and Nocedal, 1989). For a three-layer ANN architecture, the complete analytic function is given by Eq. 2.37, where

S_1 and S_2 are the transfer functions, $\boldsymbol{W_1}$ and $\boldsymbol{W_2}$ are the weight matrices, $\vec{x}$ is the input vector and $\vec{y}_c$ is the computed output vector.

$$\vec{y}_c = S_2 \times \{\boldsymbol{W_2} \times S_1(\boldsymbol{W_1} \times \vec{x})\} \quad \text{Eq. 2.37}$$

In this work, the transfer or activation function is linear for the output layer (S_1), whereas a sigmoid activation function (Eq. 2.38) was employed in the hidden layer (S_2):

$$S(x) = (1 + e^{-x})^{-1} \quad \text{Eq. 2.39}$$

The number of neurons in the input and output layers are determined by the number of input and output parameters of the problem. However, there is no analytical method to derive the number of neurons in the hidden layer, requiring several experimental attempts to determine its optimal quantity. However, the ANN loses its power of generalization for unskilled (testing) data if too many neurons are chosen for the hidden layer. In other words, the ANN learns too well the training dataset (overfitting) and is not able to generalize the solution for an independent testing dataset. Furthermore, too many neurons are computationally expensive and take more time to train. On the other hand, the error minimization is largely limited if too few neurons are selected. Hence, for a realistic approximation, it is necessary to design and train multiple ANN experiments with different configurations and test their performance against an independent dataset.

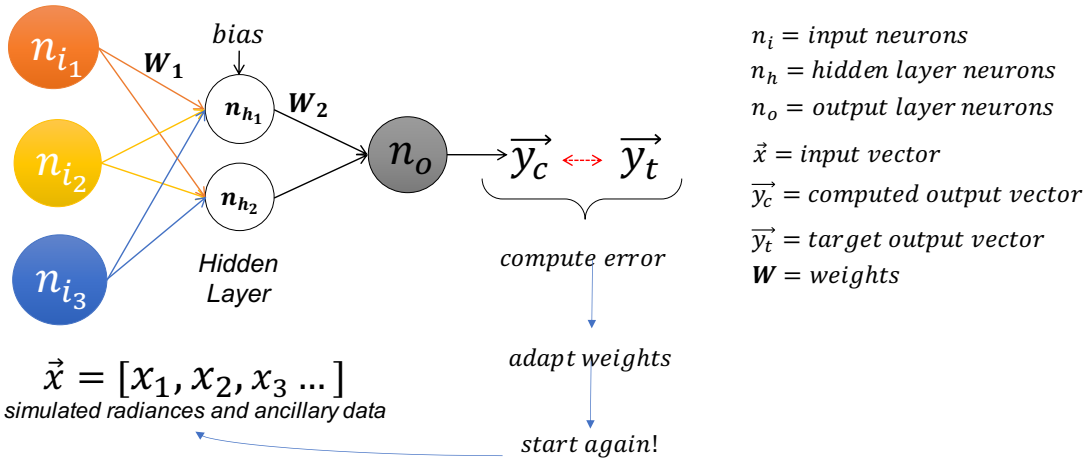

Figure 2.17: Artificial Neural Network Multilayer Perceptron diagram. Each neuron is connected to the next by a specific weight, which is adapted in the supervised learning procedure, until the cost function between the output and the target value are minimized.

The success and generalization capability of the ANN approach strongly depends on the quality, representativeness, and size of the training data set. A simulated training dataset (from Section 2.2.2.1)

was utilised for training the ANN and an independent simulated testing dataset was used to test the generalization power for unskilled data. Only the training datasets were used to develop the method. Details of experimental setup and input data preparation are provided in the next section.

2.3.1 Experimental Setup

In this work, 160 ANN experiments were devised for estimating CHL, TSS and YEL from radiative transfer simulated data. Four separate sets of experiments were prepared, one set designed for the simultaneous retrieval of CHL, TSS and YEL, and 3 other sets specifically designed for the retrieval of individual constituents in separate. Each set contained 40 ANN experiments equally distributed into 4 main groups with distinctive configurations. An overview of the groups and sets of experiments are shown in Table 2.6. Two groups (A and B) were setup with Principal Component Analysis (PCA) as a pre-processing step to decorrelate the L_{TOA} inputs. In addition, two groups (B and D) were setup with 0.8% of Gaussian distributed noise added to the L_{TOA} inputs in each band to test the ANN robustness to noisy inputs. The chosen percentage noise added to the synthetic L_{TOA} assumes a relatively lower radiometric sensitivity of the VNIR bands of Himawari-8 for oceanic targets, compared to those estimated at 100% albedo (~0.1 and 0.2%) (Japan Meteorological Agency, 2015). Additionally, a control group (C) was designed without PCA and noise. Finally, each set/group of experiments were designed by varying the number of hidden layer neurons from 10 to 100, with increments of 10 (i.e., 10, 20, 30, … 100). For instance, the experiment P000 had 10 hidden layer neurons and P009 had 100. All experiments were trained for 1000 iterations over the entire training and testing dataset. The cost function (Eq. 2.36) computed over the entire training dataset was evaluated for each experiment.

Table 2.6: Summary of designed experiments by sets and groups and associated configurations. Four main groups of experiments were designed for inclusion (or not) of PCA decorrelation and added radiometric noise. Three sets of experiments were designed for individual retrieval of CHL, TSS and YEL, plus one set for simultaneous retrieval of CHL, TSS and YEL.

Sets (outputs)	*Group A: with PCA*	*Group B: Noise and PCA*	*Group C: Control*	*Group D: Noise*
Set 1 (CHL, TSS, YEL)	P000-P009	P010-P019	P020-P029	P030-P039
Set 2 (CHL)	P040-P049	P050-P059	P060-P069	P070-P079
Set 3 (TSS)	P080-P089	P090-P099	P100-P109	P110-P119
Set 4 (YEL)	P120-P129	P130-P139	P140-P149	P150-P159

2.3.2 Data Preparation

Each ANN experiment was trained and tested with a randomly extracted subset of the radiative transfer simulated dataset. The training and testing dataset had each 100 000 input vectors $(\vec{x})$ containing the following parameters:

- Simulated L_{TOA} at 470, 510, 640 and 856 nm
- Sea level atmospheric pressure (between 980 and 1040 hPa)
- Solar zenith angles – θ_s, delimited between 0˚ and 70˚
- Geometric parameters in cartesian coordinates (x, y, z)

The training and testing datasets were delimited for input vectors where $\theta_s \leq 70^{\circ}$, following results of sensitivity analysis (section 2.2.3). Each input vector was associated to the respective logarithmic concentration of the synthetic CHL, TSS and YEL (Figure 2.10), which are the target outputs to be approximated by the supervised learning procedure. The relative azimuth $(\Delta\phi)$ is the absolute difference between the solar and satellite azimuth angles, mapped between 0˚ and 180˚. However, at the centre of the satellite image, the relative azimuth is discontinuous affecting the inversions. Thus, the relative azimuth and satellite observation (θ_v) angles were transformed into cartesian coordinates (x, y, z), with continuous values ranging from -1 to 1:

$$x = sin\,\theta_v\,cos\,\Delta\phi$$

$$y = sin\,\theta_v\,sin\,\Delta\phi \qquad \text{Eq. 2.40}$$

$$z = cos\,\theta_v$$

Additionally, the radiative transfer simulated datasets implicitly contain the contribution of sun glint effects, depending on the angular geometry between satellite and sensor. In this work, Himawari-8 observations affected by sun glint were masked due to the difficulty of extracting spectral information of the ocean colour from glinted pixels. The simulated training and testing datasets were corrected for sun glint to facilitate functional approximation of the ANN inversion. First, the radiance contributions due to sun glint for a gas and aerosol-free atmosphere over a totally absorbing ocean were determined. Then, the simulated sun glint radiances were multiplied to the transmission of the ocean-atmosphere system and subtracted from the simulated L_{TOA} to be corrected.

2.3.3 Training and Testing Results

The MSE is presented in Figure 2.18 for all sets of experiments (Set 1 to Set 4 – colour coded). The MSE was particularly high for Set 1 experiments (red lines), to simultaneously retrieve CHL, TSS and YEL. The experiments to retrieve TSS (Set 3, green lines) generally presented the lowest MSE compared

to the other sets of experiments. The MSE at the 1000th iteration is shown in Figure 2.19, for each group and set versus the number of hidden layer neurons. As expected, the MSE generally decreased with increasing hidden layer neurons, particularly when adding up to 50 neurons to the network. However, the effects of increasing the number of neurons from 50 to 100 were negligible, indicating that networks with > 50 neurons may lose their generalization power when dealing with unskilled testing datasets.

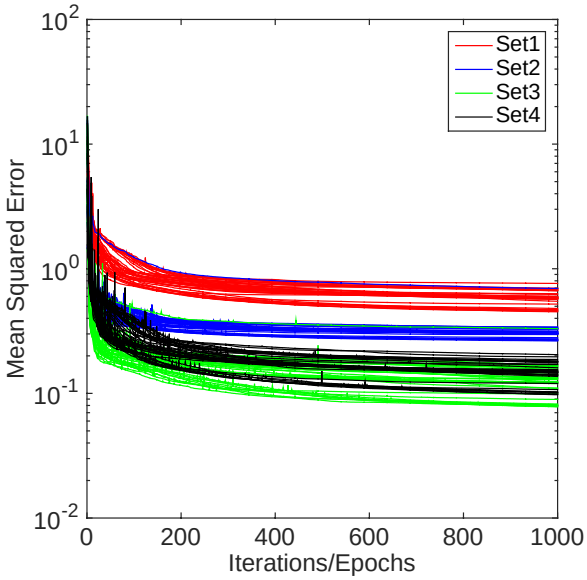

Figure 2.18: Log-linear plot of the overall MSE for 1000 iterations of 160 ANN experiments colour coded by experimental set. The Set 1 experiments were designed for the simultaneous output of CHL, TSS and YEL, while the Set 2 for CHL, Set 3 for TSS and Set 4 for the output of YEL.

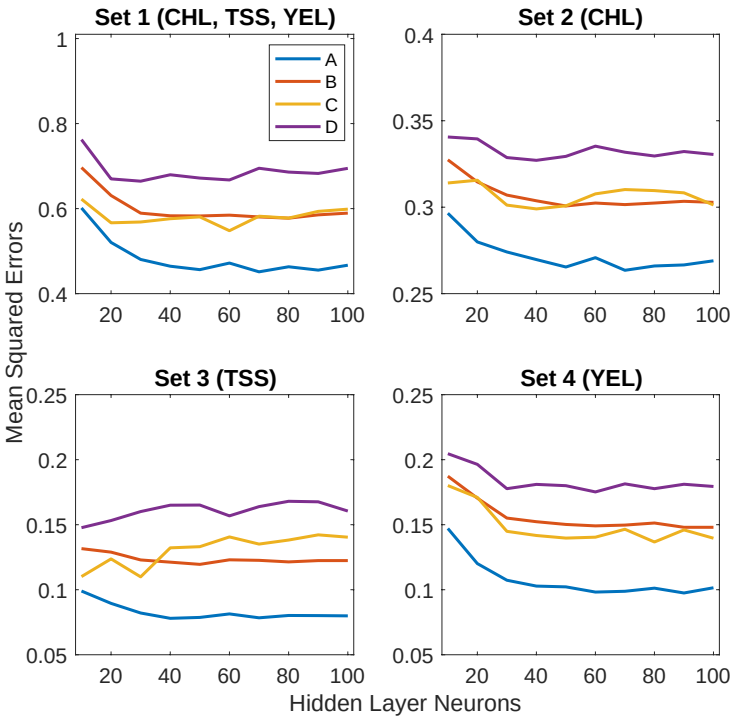

Figure 2.19: Variability of MSE at the 1000th iteration versus the number of hidden layer neurons for all sets and groups (A, B, C and D, colour coded) of ANN experiments designed. Note the different scale of each plot.

The separate retrieval of CHL, TSS and YEL (Sets 2, 3 and 4) resulted in lower overall MSE, compared to Set 1 experiments. Therefore, the following results are described for Set 2, 3 and 4 experiments. The experiments within group A (with PCA) presented lower MSE (< 0.1) when compared to groups B, C and D. This stresses the importance of decorrelating the radiance input data prior to inversions. As expected, adding noise (groups B and D) consistently increased the MSE, particularly when PCA was not included (group D). However, the B and D experiments demonstrated the ANN's ability of dealing with noisy inputs, which is useful for the inversion of low signal-to-noise observations, such as of the Himawari-8. The experiments of Set 3 (TSS) C and D groups (control and added noise, respectively) presented anomalous increases of MSE with increasing hidden layer neurons. These experiments did not include PCA decorrelation of input radiances, and their results suggested that the ambiguity of input information needs to be reduced for TSS retrievals. Therefore, the experiments within group B (noise and PCA) and with 50 hidden layer neurons were selected for checking the network's performance with respect to the training and testing datasets. The Figure 2.20 presents the density scatterplots of CHL, TSS and YEL output from ANN training and testing (TRN and TST, respectively), versus the associated synthetic CHL, TSS and YEL modelled in the radiative transfer (RT) simulations (target outputs).

The synthetic CHL, TSS and YEL values (horizontal axis) are equally distributed in the logarithmic scale, such as in the graphics of Figure 2.10. The corresponding ANN outputs are distributed in the vertical axis. As expected, the training and testing outputs yielded similar RMSE and distribution of outputs. This result indicates that the ANN experiments show good functional approximation and are not overfitting to the training dataset. The majority of the CHL, TSS and YEL matched values are concentrated around the 1:1 line, however, the spread of values away from this trend (blue dots) indicate where the ANN yields larger errors. The errors in the one-step inversion may be associated to the increased number of solutions found by the ANN for the multiple sun and observation geometries and atmospheric conditions overlaid to the water leaving radiances (Schroeder, 2005). The graphics of Figure 2.20 indicate that CHL and YEL may be retrieved with large errors across the entire range of values estimated. Meanwhile, TSS concentrations above 1 mg L^{-1} are more accurately estimated due to the strong backscattering of suspended matter, potentially superimposing the signal of the atmosphere. However, accurate retrievals of TSS below 1 mg L^{-1} might be problematic, likely associated with the strength of the atmospheric signal compared to the radiances of moderate to clear waters. Note, however, that the ANN experiments illustrated in Figure 2.20 were not necessarily the best performance algorithms for water quality retrievals. Validation against *in situ* data collected in the GBR is necessary to verify the ANN's ability for inversion of real Himawari-8 observations into water quality parameters. The validation of ANN experiments within group B is presented in Chapter 3 (Algorithm Validation).

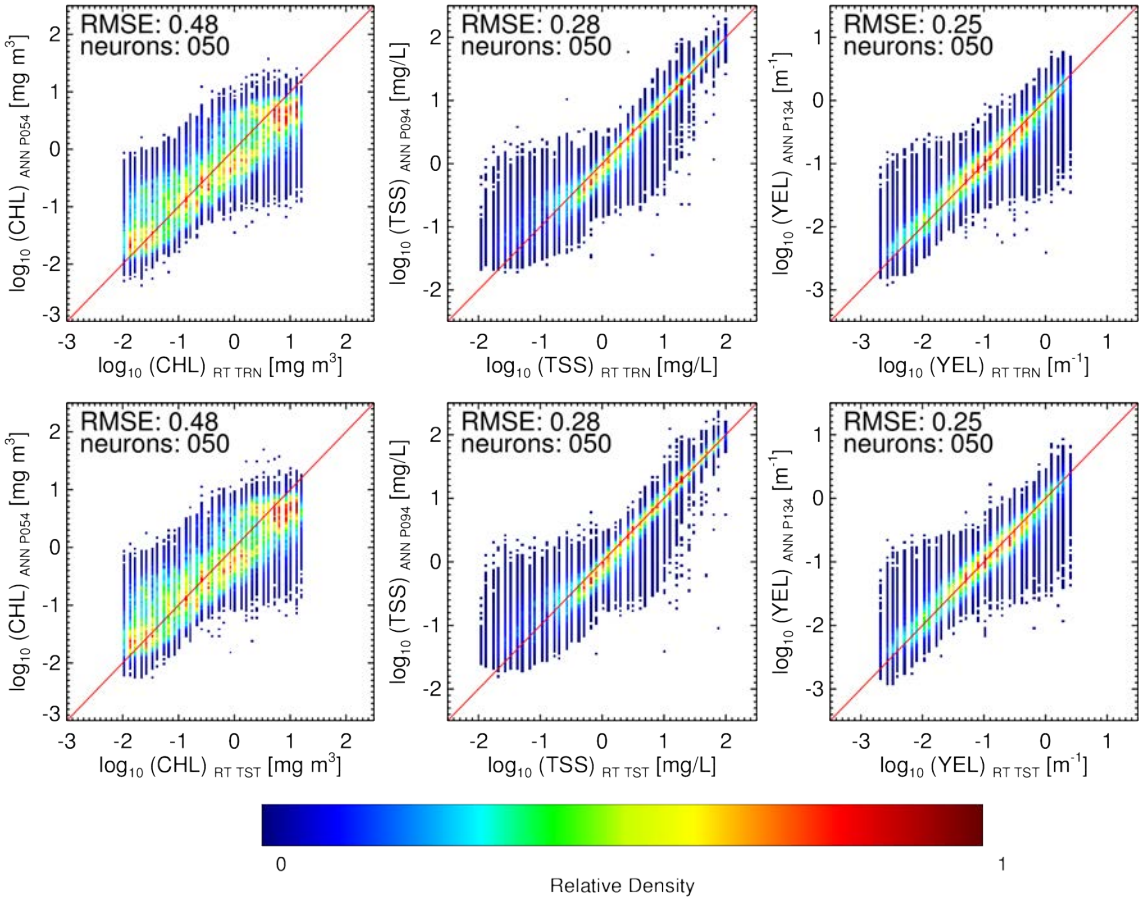

Figure 2.20: Training (TRN – top panel) and testing (TST – bottom panel) density scatter plots between synthetic CHL_{RT}, TSS_{RT} and YEL_{RT} and ANN retrievals (CHL_{ANN}, TSS_{ANN} and YEL_{ANN}) values in logarithmic scale. The colour scale describes the relative density of the matched values mapped between 0 to 1 (from blue to red).

2.4 The Himawari-8 Water Quality Processor

This section summarises all basic processing steps from acquisition of Himawari-8 to inversion and masking of products. The procedures described in this section were utilised in Chapters 3 to 5.

2.4.1 Acquiring and processing Himawari-8 observations

Full disk Himawari-8 observations at Level 1 (L1) were accessed through the National Computer Infrastructure (NCI) mass storage data system. L1 observations include Himawari-8 Standard Data (HSD) uncalibrated digital numbers (DN) on a fixed grid relative to an ideal geostationary satellite viewpoint (Japan Meteorological Agency, 2017). With a pre-existent processing tool (Figure 2.21), the fixed grid was geolocated (i.e., associated to latitudes and longitudes) on a geostationary projection and navigation coefficients were applied to L1. Navigation errors are mostly less than 1 km at subsatellite point (Tabata et al., 2016). The uncalibrated geolocated array was transformed into Level 2 (L2) TOA radiances L_{TOA} $(Wm^{-2}sr^{-1}\mu m^{-1})$ through the application of post-launch measured calibration coefficients. The calibration coefficients are updated in July every year and are added to the header of the HSD file (Japan Meteorological Agency, 2020).

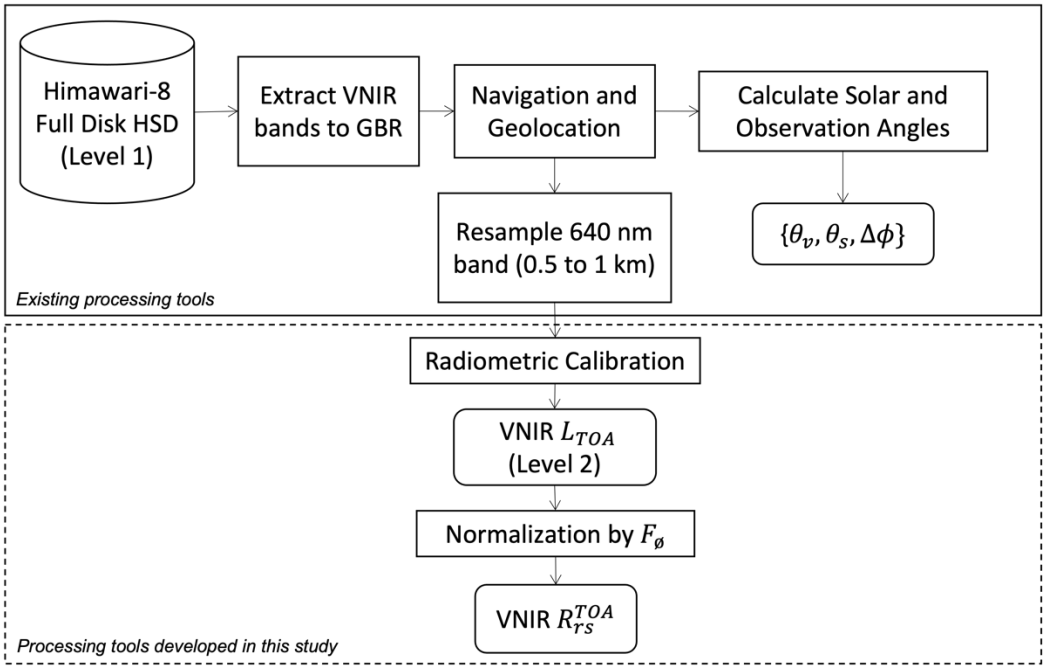

Figure 2.21: Flow diagram of existing processing flow for Himawari-8 L1 to L2. HSD refers to Himawari-8 Standard Data, GBR refers to Great Barrier Reef, VNIR refers to the Himawari-8 visible and near-infrared bands (470, 510, 640, and 856 nm).

The 640 nm band grid was resampled from 0.5 km to 1 km to match the resolution of the associated VNIR bands utilised in this study. The L2 calibrated L_{TOA} radiances were normalised by the extra-terrestrial solar irradiance $(F_ø)$ for each band. $F_ø$ was calculated as a function of the day of the

year, as in Eq. 2.22, and using the mean extra-terrestrial solar irradiance $\overline{F_{ø}}$ values based on Kurucz (1995) adapted for the Himawari-8 bands (Table 2.7). The resultant R_{rs}^{TOA} at the VNIR Himawari-8 bands were the inputs to the inversion method.

Table 2.7: Mean extraterrestrial solar irradiance $\overline{F_{ø}}$ $(Wm^2sr^{-1}\mu m^{-1})$ adapted for the visible and near-infrared bands of Himawari-8.

Himawari -8 Bands	$\overline{F_{ø}}$
470 nm	2015.3606
510 nm	1891.1653
640 nm	1631.5726
865 nm	971.8778

In addition, the solar and sensor zenith angles (θ_s, θ_v, respectively) and the relative azimuth angle, $\Delta\phi$ were calculated for each pixel of the satellite image as a function of location (latitude and longitude) and local time, following existing procedures provided by Japan Meteorological Agency (2017). The relative azimuth $\Delta\phi$ was computed as the difference between the solar and sensor azimuth angles and re-mapped as a positive angle between 0˚ and 180˚ to match the configuration of the radiative transfer simulations. The $\Delta\phi$ of 0˚ refers to the forward scattering angle, as looking to the pixel facing the Sun, whereas a $\Delta\phi$ of 180˚ refers to the backscattering, as looking to the pixel with the sun behind the viewer's position. The θ_v and θ_s are calculated as 90˚ minus the respective solar or satellite elevation angle relative to the horizon. Figure 2.22 illustrates the position of the Sun and satellite sensor relative to a cartesian coordinate system (x, y, z), the respective zenith (θ_s, θ_v) and relative azimuth $(\Delta\phi)$ angles. Figure 2.23 illustrates the spatial distribution of Himawari-8 θ_s, θ_v and $\Delta\phi$ angles for a given day.

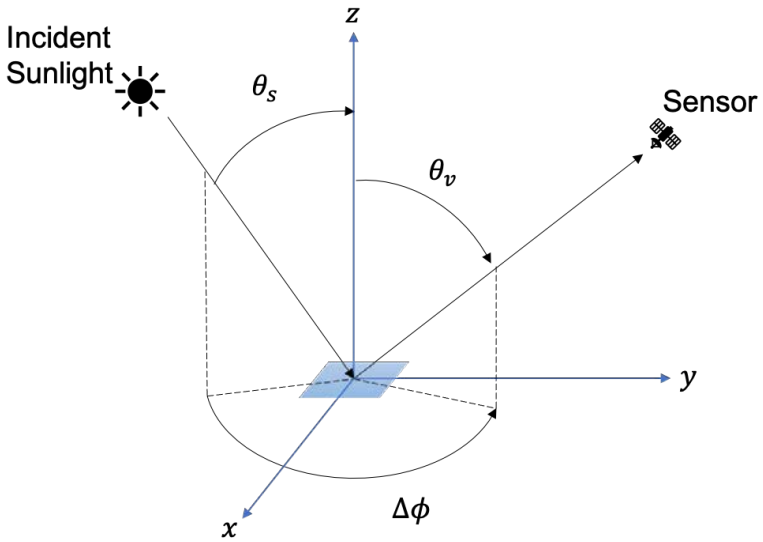

Figure 2.22: Coordinate system (x, y, z) and definition of the relevant geometric parameters: θ_s and θ_v are the solar and viewing zenith angles, respectively and $\Delta\phi$ is the relative azimuth angle.

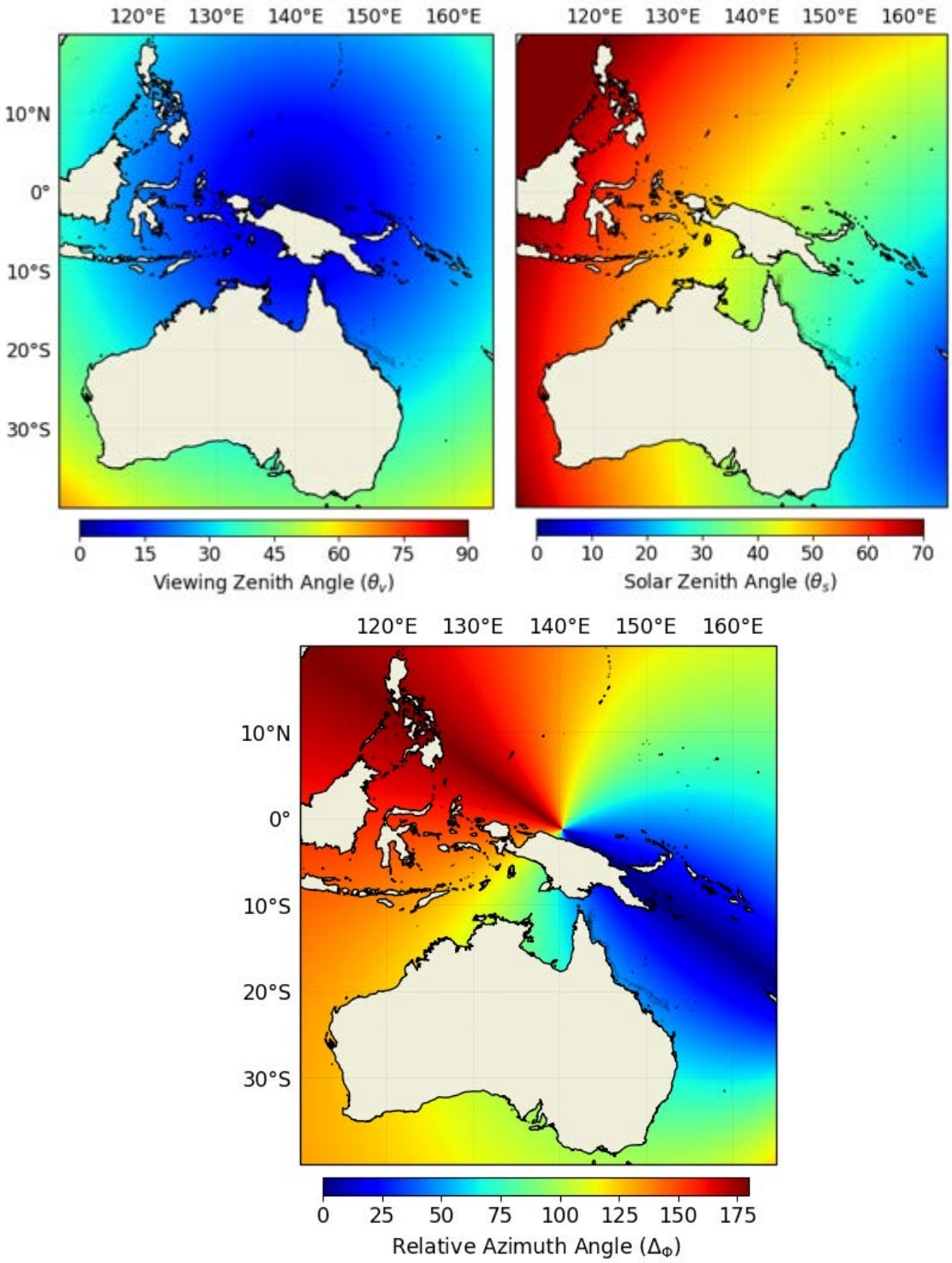

Figure 2.23: Himawari-8 sensor Viewing Zenith Angle (θ_v), on top-left panel, Solar Zenith Angle (θ_s), on top-right panel and Relative Azimuth Angle, $\Delta\phi$, (on bottom panel) over Southeast Asia and Oceania, at 0000 UTC on 21 December 2018.

2.4.2 Masking Himawari-8 observations

All pixels containing features, such as emerging surfaces (i.e., land, coral reefs), clouds, sun glint, dust and smoke plumes should be avoided/masked prior to validation and application of ocean colour products. These features encompass spectral characteristics in the VNIR, that unless excluded, may confound characterisation of the ocean colour spectrum. For instance, when analysing a near-true colour imagery, some semi-transparent clouds (i.e., cirrus) may be visually confounded to coastal turbid water pixels. If the pixels containing non-ocean colour features are not properly identified and masked out, they are likely to result in inaccurate or incorrect derived products, biasing the analysis. This section summarises the main features identified in the Himawari-8 observations and the masking approaches utilised.

2.4.2.1 Cloud masking

Cloud masking of Himawari-8 observations was developed by Qin et al. (2019) for the Australian continent and surrounding waters. The masks were developed utilising the VNIR and thermal infrared bands of Himawari-8 at 2 km spatial resolution and validated against data from the Cloud-Aerosol Lidar with Orthogonal Polarization (CALIOP). The algorithm was tailored to the masking of cirrus, cumulus, and stratus clouds, in addition to fog, saturated pixels, aerosols from dust and smoke plumes. The algorithm achieved a maximum accuracy of 98% when Himawari-8 pixels were completely clear or cloudy. However, larger errors occurred when mapping partially cloudy pixels (clouds smaller than 2 km), which is potentially due to the discrepancy between CALIOP's circular laser beam (70 m diameter at every 330 m) and Himawari-8 pixels (at 2 km). It is likely that not all sub-pixel sized clouds are properly masked, and a careful visual inspection of the images is required prior to validation match up.

The 2 km resolution cloud mask was resampled to the 1 km GBR grid and the two-way confidence threshold of a pixel being clear or cloudy was applied to the mask. According to Qin et al. (2019), the minimum threshold recommended is 3 out of 15, which is sufficient to mask most cloud types and smoke plumes, such as those in Figure 2.24. The higher the confidence threshold applied, the better the masking of all potential cloudy pixels; however, due to the two-way confidence approach, the masking of clear pixels is proportionally increased. The confidence thresholds were tested for different cloud types (semi-transparent and sub-pixel size or fractional clouds), over clear and turbid waters and an intermediate-high conservative level (8 out of 15) was chosen. Red-Green-Blue (RGB) or near true colour composites of Himawari-8 visible bands (640, 510 and 470 nm) are demonstrated over turbid areas and for different cloud types (Figure 2.24) and with respective masking.

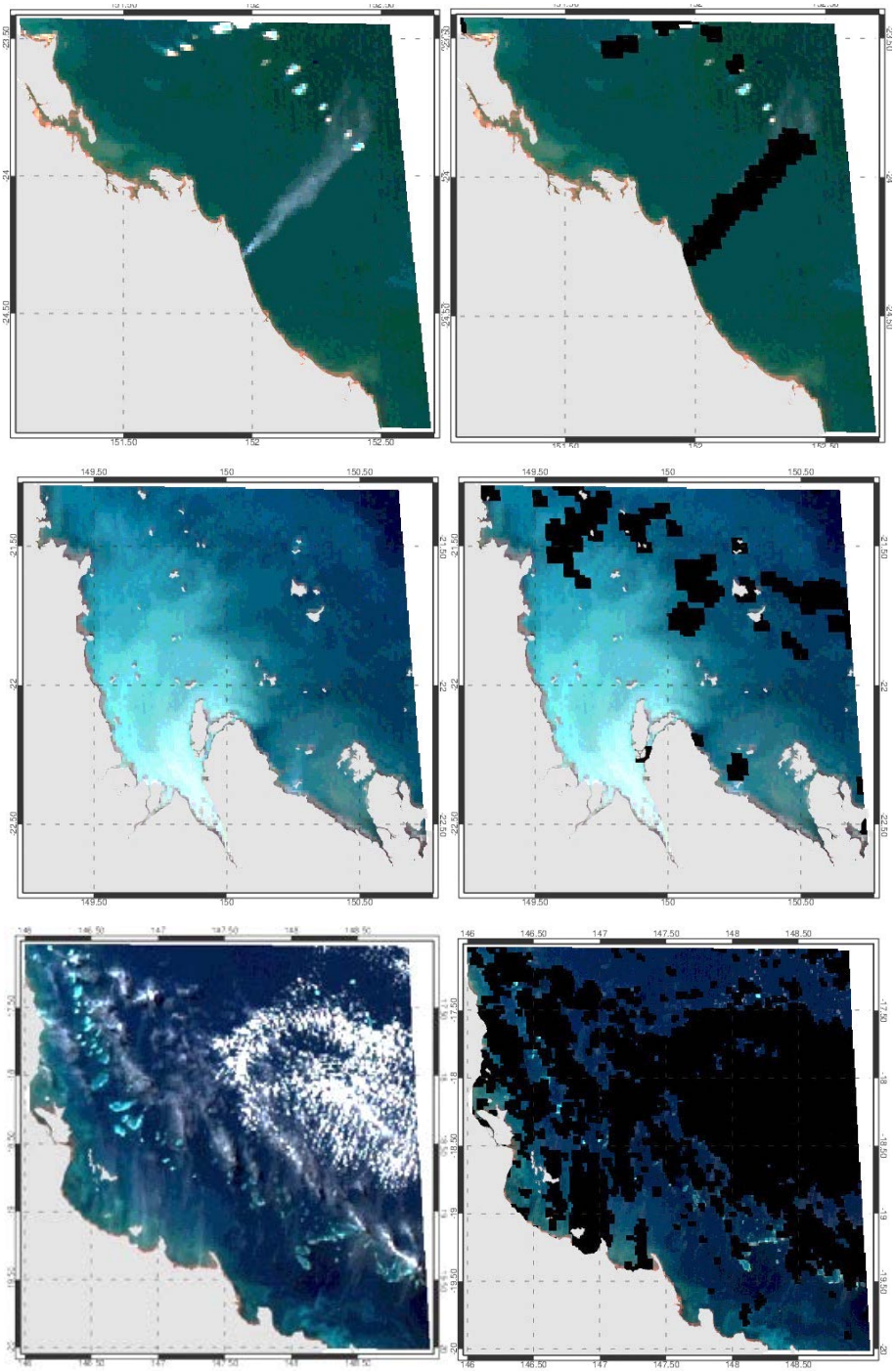

Figure 2.24: Himawari-8 near-true colour composite (of bands 640, 510 and 470 nm) in the coastal GBR featuring unmasked (left panel) and masked areas (right panel in black). Top panels present masking of biomass burning smoke plume, middle panels present cloud masking over a turbid water setting and bottom panels present the masking of semi-transparent and fractional clouds. Coral reefs (white/cyan features) were not masked in this scene. Land and islands are masked in grey.

2.4.2.2 Land and coral reefs masking

Pixels identified as emerged surfaces such as continental areas, islands and shoals were masked with a combined coarse and finer resolution mask. The coarse land mask with 1 km spatial resolution covered the main continental areas. The fine resolution (at 250 m spatial resolution) mask covered

features such as the coral reefs within the GBR Marine Park, islands and shoals (Great Barrier Reef Marine Park Authority, 2014). The fine and coarse resolution masks were combined into a single land-reef mask and interpolated to a 1 km grid to match the Himawari-8 observations, as illustrated in Figure 2.25.

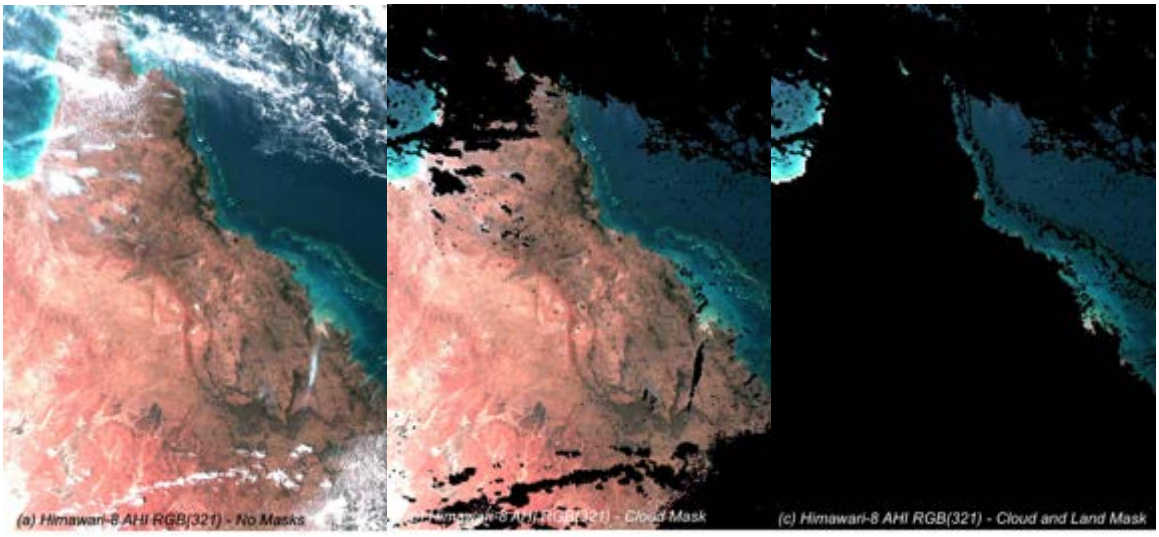

Figure 2.25: Himawari-8 near-true colour composite (640, 510, 470 nm) in left panel; same composite masked for clouds (central panel); and masked for clouds, land, reefs, and shoals (right panel).

2.4.2.3 Sun glint masking

The specular reflection of the solar radiation over the ocean (i.e., sun glint) increases the magnitude and flattens the spectral shape of L_{TOA} in all bands. Atmospheric, ocean colour and benthic habitat retrievals from sun glinted areas are very challenging (Wang and Bailey, 2001; Hedley et al., 2005; Hu, 2011) and glint removal techniques are an emerging field in ocean colour remote sensing (Bernardo et al., 2018; Zorrilla et al., 2019; Chami et al., 2020). Alternatively, sun glint contaminated pixels are identified and masked, nevertheless resulting in major data loss. Geostationary observations are impacted by sun glint all year long, covering the ocean at diurnal scales with a circular-elliptical glinted area (i.e., sun disk), particularly over equatorial regions between 10˚N and 10˚S latitude (Emecen et al., 2006; Gardashov and Eminov, 2015). Because this study includes Himawari-8 observations scanned between 10˚S and 22˚S, the area affected by sun glint was identified and masked out from each 10-minute data utilised. The sun glint mask was created by calculating the coordinates of the principal point of sun glint (PPS in Figure 2.26) as a function of the day of the year (solar inclination), local hour, latitude and longitude (Emecen et al., 2006), at 1 km spatial resolution.

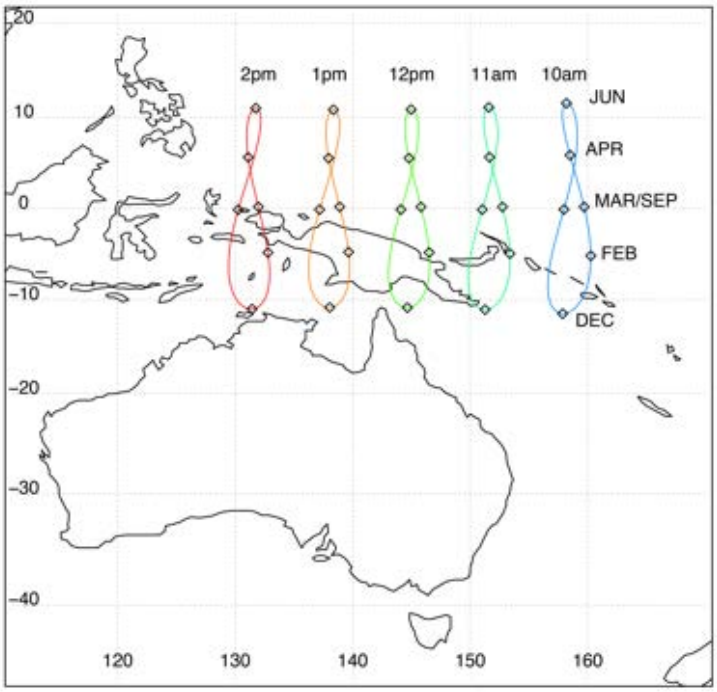

Figure 2.26: Yearly trajectory of the Principal Point of Sun-glint (PPS) from 10 a.m. to 2 p.m. local time (AEST) over Australia and Southeast Asia. The markers indicate solstice and equinox periods (March, June, September, and December) as well as April and February for reference.

The contour of the sun disk was buffered for a circular radius of 1300 km from the coordinates of the PPS. The radius size was chosen after a series of tests employed to ensure minimum coverage of the main sun disk area (Figure 2.27). Residual glint might be present surrounding the circular buffer due to increased wind speed, sea surface waves, all of which are known to increase the area influenced by sun glint (Cox and Munk, 1954). Furthermore, the sun disk image may present an elliptical shape depending on the relationship between the observation and sun zenith angles and the day of the year (Emecen et al., 2006). However, the present sun glint masking approach was sufficient to appropriately cover the coastal GBR area for validation and application of Himawari-8 observations to ocean colour retrievals.

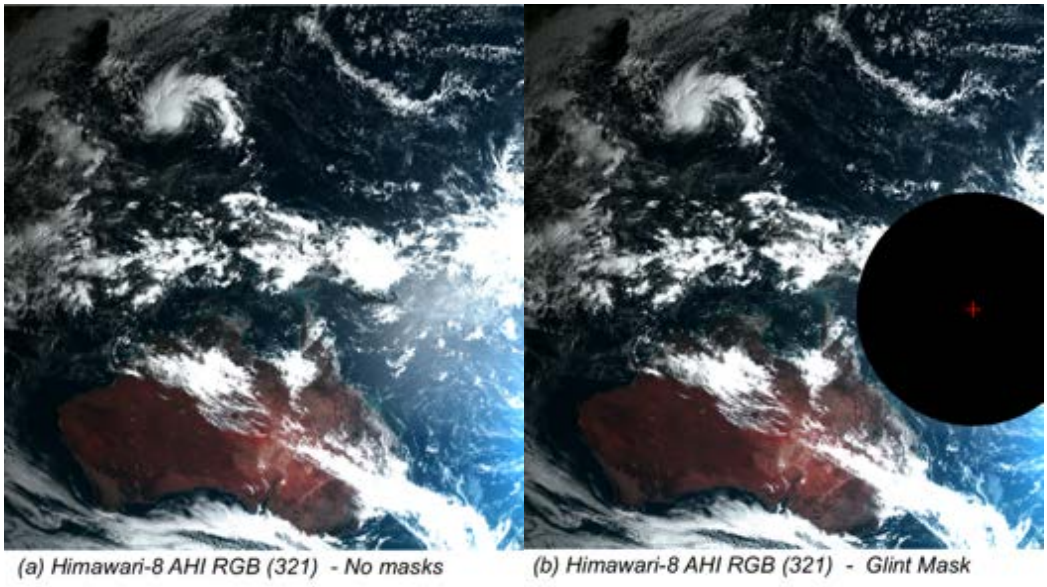

Figure 2.27: Unmasked Himawari-8 near-true colour composite (of bands 640, 510, 470 nm) over Australia and Southeast Asia (left panel, a), and associated sun glint mask (black disk) overlayed to the near-true colour composite (right panel, b). The location of the Principal Point of Sun glint (PPS) is marked with a red cross centred at the sun disk.

2.4.3 Ancillary data

Molecular absorption and scattering in the atmosphere were simulated for constant values of ozone concentration and mean sea level pressure. Thus, prior to inversions, the Himawari-8 observations were normalised pixel-by-pixel with near-concurrent satellite observations of Total Column Ozone. The mean sea level pressure was utilised as an ancillary input to the inversion procedure. Uncertainties associated with the ancillary products may arise from differences in spatial resolution, geometries, and time of acquisition, which were not accounted for in this study. The ancillary data of ozone and mean sea level pressure is described in detail in the following sections.

2.4.3.1 Total Column Ozone correction factor

Ozone gas (O_3) molecules are mostly abundant in the stratosphere and contribute to the absorption of solar incoming and outgoing radiances in the visible spectrum, mostly between 530 and 650 nm (i.e., *Chappuis* absorption band), as well as in the ultraviolet and infrared spectral regions. Thus, the absorption of ozone influences the radiance and irradiance transmissions through the atmosphere at the Himawari-8 visible bands. In this study, radiative transfer simulations were employed assuming a default ozone loading of 344 Dobson Units (DU) (Committee on Extension to the Standard Atmosphere, 1976). However, stratospheric ozone has temporal and spatial variability and thus a normalization of the Himawari-8 radiances for the transmission due to observational ozone absorption was performed for each band prior to the ANN inversions.

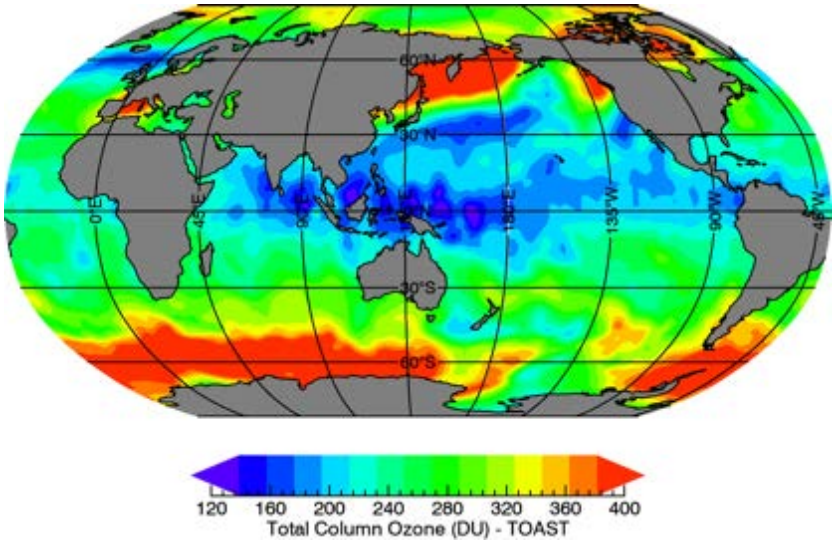

Figure 2.28: Global distribution of Total Column Ozone (Dobson Units - DU) from Total Ozone Analysis using SBUV/2 and TOVS (TOAST), for a given day. Data source: National Oceanic and Atmospheric Administration (2020b).

First, the ozone transmission (T_{O_3}) and ozone optical thickness (τ_{O_3}) were calculated for the Himawari-8 observations with absorption coefficient of ozone (a_{O_3}) provided in Linke (1953) and a default ozone concentration $[O_3]$ of 344 DU, as utilised in the radiative transfer simulations (Eq. 2.41 and Eq. 2.42). Then, T_{O_3} and τ_{O_3} were calculated for observational $[O_3]$ derived from the Total Ozone Analysis from Stratospheric and Tropospheric Satellite Sources (TOAST) dataset (National Oceanic and Atmospheric Administration, 2020b). The correction factor (CF - Eq. 2.43) calculated for each Himawari-8 bands was applied to the R_{rs}^{TOA} prior to inversion.

$$\tau_{O_3}(\lambda) = a_{O_3}[O_3] \quad \text{Eq. 2.41}$$

$$T_{O_3}(\lambda, \theta_s, \Delta\phi) = e^{-(\tau_{O_3}\{(1/cos\,\theta_s)+(1/cos\,\Delta\phi)\})} \quad \text{Eq. 2.42}$$

$$CF(\lambda) = \frac{T_{O_3}^{TOAST}}{T_{O_3}^{344DU}} \quad \text{Eq. 2.43}$$

The TOAST product with spatial resolution of 1.25 by 1 degrees and daily temporal resolution (illustrated in Figure 2.28) was resampled to 1 km for compliance with the grids of the Himawari-8 VNIR observations. Finally, the Himawari-8 observations were normalised at each band by the ratio between the transmission of TOAST-derived ozone to the transmission computed for 344 DU (Eq. 2.43). Since Total Column Ozone concentration varies with space and time, there is an unaccounted uncertainty related to time differences between the ozone measurement and the time of the Himawari-8 scan.

2.4.3.2 *Sea Level Atmospheric Pressure*

As in described in section 2.1.2.2, the Rayleigh optical thickness (τ_R) is derived as a function of the sea level atmospheric pressure. The Himawari-8 bands were simulated for two sea level pressures of 980 and 1040 hPa. Therefore, for a realistic approximation, mean sea level atmospheric pressure data from NCEP/NCAR Reanalysis 2 (Kalnay et al., 1996; Kistler et al., 2001; Kanamitsu et al., 2002), were utilised as inputs for the inversion of Himawari-8 observations. The data is available from the National Oceanic and Atmospheric Administration (2020a) averaged every 6 hours (0, 6, 12, 18 UTC) and sampled on a regular global grid of 2.5 degrees spatial resolution. The closest concurrent sea level atmospheric pressure data to the Himawari-8 observation was acquired and interpolated to the 1km Himawari-8 GBR grid. A global map of the mean sea level atmospheric pressure is presented in Figure 2.29 for illustration purposes.

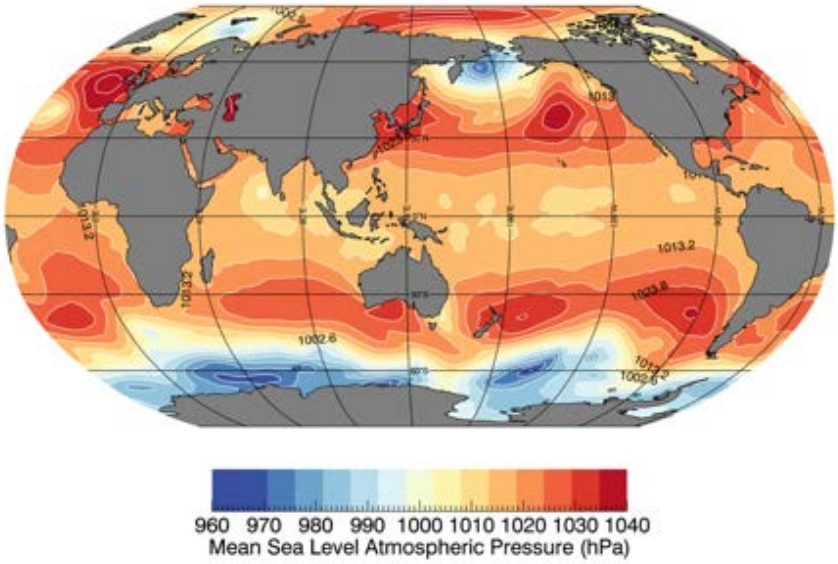

Figure 2.29: Global NCEP/NCAR Mean Sea Level Atmospheric Pressure (hPa) distribution for a given day. Data source: National Oceanic and Atmospheric Administration (2020a).

2.4.4 Water Quality Retrievals

The inputs to the ANN were: the Himawari-8 R_{rs}^{TOA} observations in the VNIR bands (470, 510, 640 and 856 nm) corrected for ozone transmission factor, associated solar and viewing zenith and azimuth angles, $\theta_v, \theta_s, \Delta\phi$, transformed into cartesian coordinates (section 2.3.2), and the mean sea level atmospheric pressure. The retrieved WQP, associated masks and metadata were saved in a NetCDF file, including pixelwise associated flags for out-of-range inputs (R_{rs}^{TOA}) and outputs (CHL, TSS and YEL). The ranges of valid L_{TOA} inputs and CHL, TSS and YEL outputs were defined based on the radiative transfer simulated dataset, following Schaale and Schroeder (2013). For instance, if a certain

pixel's input and/or output exceeded the simulated ranges, the pixel received a corresponding bitwise flag (1 for RT input flag, 2 for CHL, 4 for YEL and 8 for TSS, when deriving all WQP simultaneously). The input and output flags were summed for each pixel of the Himawari-8 grid. The resultant array of flags for out-of-range values were named 'ANN flags' for brevity and the associated byte flags were applied to the water quality products prior to analysis (Figure 2.30).

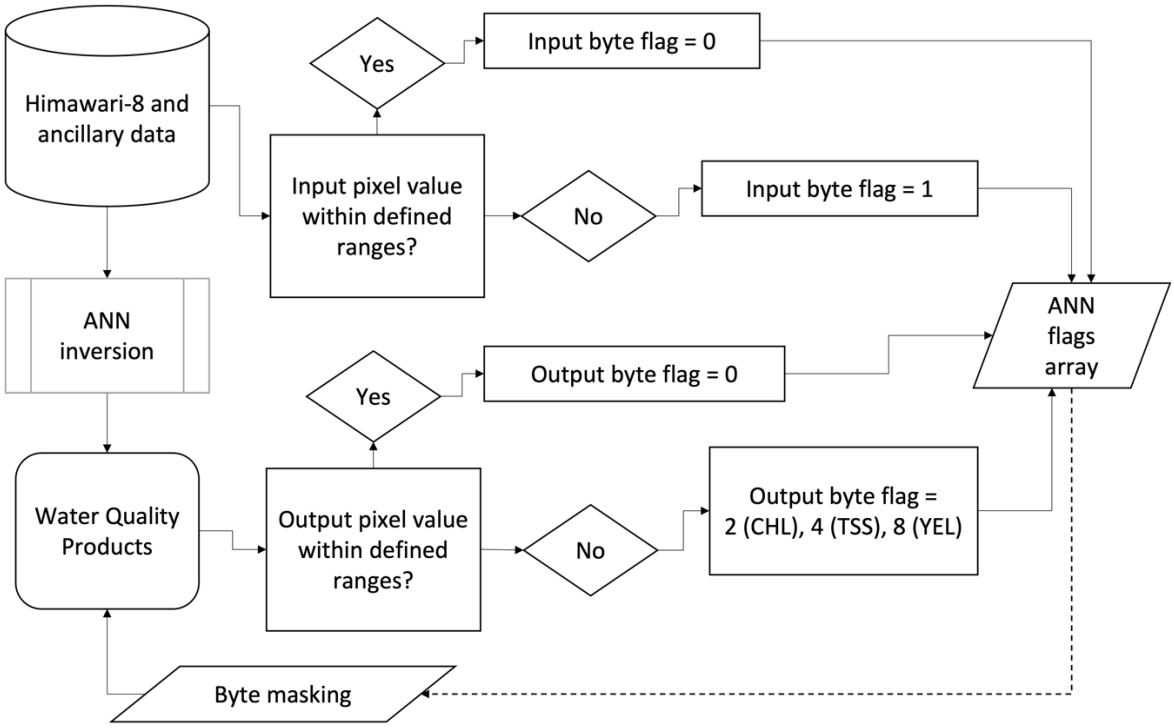

Figure 2.30: Schematic diagram of the Water Quality Retrieval with inversion of Himawari-8 and ancillary datasets. The procedure for identifying and masking out-of-range input and output values is described. The 'ANN flags' byte mask array is utilised for masking the Water Quality Products array.

2.5 Discussion of Algorithm Development Chapter

Chapter 2 focused on developing a physics-based algorithm for estimating ocean colour parameters with Himawari-8 in the GBR. Coupled ocean-atmosphere radiative transfer simulations of the Himawari-8 bands were performed for realistic combinations of CHL, TSS and YEL, parameterized for the optical variability of the GBR. The simulations output the angular distribution of the normalised L_{TOA} at the Himawari-8 visible and near-infrared bands. A sensitivity analysis of the outputs revealed that Himawari-8 VNIR bands are suited for the detection of optical changes in the coastal GBR. However, the determination of CHL and YEL in the coastal GBR may be a difficult task, given their overlapping absorption features and the spectral resolution and positioning of the Himawari-8 blue and green bands, at 470 nm and 510 nm. Nevertheless, the Himawari-8 bands, particularly the 640 nm, are well suited to detect optical changes due to variable TSS from ~ 0.5 to 100.0 mg L^{-1}, as previously suggested (Dorji and Fearns, 2018; Ding et al., 2020).

The simulations were also valuable to investigate the influence of the atmospheric path signal at variable θ_s and for 3 orders magnitude increases in aerosol loading (τ_a). Simulating the angular distribution of L_{TOA} is particularly important because Himawari-8 takes continuous observations at every 10 minutes, comprising a large range of solar and observation zenith and azimuth changes within a single day. However, for Himawari-8 observations at high θ_s (>70˚), it might be difficult to retrieve CHL, TSS and YEL from L_{TOA} with accuracy. This is because the atmospheric path length linearly increases with θ_s, modifying the magnitude and spectral characteristics of L_{TOA} and masking the ocean colour signal. In addition, the simulations demonstrated that the Himawari-8 bands are sensitive to changes in τ_a. Aerosol particles in the atmosphere effectively absorb and scatter light in the blue-green visible wavelengths, masking the spectral shape and magnitude of the ocean colour and leading to major retrieval errors. In some extreme cases, the aerosol loading from biomass burning and dust storms can be confounded with the spectral characteristics of turbid coastal waters, and such pixels should be identified and avoided. Hence, the accurate separation of the atmospheric and marine signal is detrimental for the correct retrieval of ocean colour parameters.

The radiative transfer simulations were employed to generate large and independent training and testing datasets for the development of an ANN inversion algorithm. The ANN training was employed to learn the functional relationship between the Himawari-8 R_{rs}^{TOA} and the optical water quality parameters CHL, TSS and YEL. The testing dataset was used for verifying generalization ability of the ANN experiments for independent or unskilled data. The several ANN experiments were designed with a variable number of hidden layer neurons, added Gaussian noise and PCA decorrelation of inputs. The experiments designed with PCA decorrelation of radiance inputs presented improved performance compared to those without decorrelation, particularly for the retrievals of TSS.

In summary, the physics-based method developed in this chapter may be utilized for estimating the ocean colour water quality parameters at the Himawari-8 bands for variable optical, geometrical, and environmental conditions. However, a validation utilising real observations from Himawari-8 and *in situ* data of CHL, TSS and YEL collected in the coastal GBR is necessary to fully evaluate the algorithm's performance and to choose the best experiment for water quality retrievals.

Chapter 3: Algorithm Validation

Ocean colour algorithms are computational and mathematical tools employed to quantify water quality parameters from satellite observations. However, ocean colour algorithms are imperfect representations of a complex phenomenon and validation is a fundamental step for the assessment of algorithms' performance and potential uncertainties (Bailey and Werdell, 2006). Generally, the satellite derived products are statistically verified against concurrent *in situ* measurements[8]. The algorithms within accepted levels of accuracy are typically applied to derive ocean colour products relevant for water quality monitoring (Schroeder et al., 2012; Brando et al., 2012; Brando et al., 2015). Ideally, the most suitable ocean colour algorithms can retrieve water quality parameters from remote sensing observations in a quantitatively accurate and reliable way (Brewin et al., 2015). However, the accuracy requirements of ocean colour products depend on the satellite mission objectives, the end-user applications, and on the optical complexity of the waters investigated (Donlon, 2011; IOCCG, 2018). Algorithm validation is especially challenging in optically complex waters due to the high spatiotemporal variability of optical properties and the scale mismatch between *in situ* measurements and satellite observations (Doerffer, 2002).

Himawari-8 10-minute observations offer an opportunity to monitor water quality at diurnal scales in the GBR, given that derived products are accurately retrieved. In Chapter 2, multiple physics-based ocean colour algorithms with ANN inversion were developed for deriving CHL, TSS and YEL from Himawari-8 in the coastal GBR. In this chapter, the algorithms' performances were evaluated and the most appropriate was selected to estimate water quality products from Himawari-8.

Validation protocols have been developed to set standard practices and to assist in reducing the uncertainties associated with the potential spatiotemporal mismatch between satellite observations and *in situ* measurements (IOCCG, 2019). The validation protocol utilised in this study follows the experience of previous validation exercises for ocean colour remote sensing in Australia, including in the coastal GBR (Schroeder et al., 2016, 2017, 2018). The above-mentioned studies described processing steps for extraction of satellite observations (concurrent to *in situ* measurements), as well as useful statistical performance metrics, which were implemented in this validation exercise. The accuracy of present retrievals was compared to the results previously obtained in the GBR, and to the recommended accuracy requirements for retrievals in optically complex waters (Donlon, 2011). In the next sections, further details of methods and results are presented.

[8] Satellite data are defined as 'observations' and *in situ* data as measurements throughout this thesis.

3.1 Methods

3.1.1 Great Barrier Reef *in situ* dataset

Measurements of TSS, CHL and YEL sampled in the GBR lagoon were selected for validation of the multiple ANN algorithms developed in this study. This *in situ* validation dataset is completely independent and was not utilised in the algorithm development phase. Sea surface (< 1 m) water samples were collected between 2015 and 2018 during several research expeditions and at fixed-location monitoring facilities, managed by the Australian Institute of Marine Sciences (AIMS) and by the Commonwealth Scientific and Industrial Research Organization (CSIRO).

The data provided by AIMS include CHL, TSS and YEL collected for the Long-Term Marine Monitoring Program and at the National Reference Station *Yongala*. The CSIRO database includes CHL, TSS and YEL measured fortnightly at the Lucinda Jetty Coastal Observatory (LJCO). Additionally, bio-optical data collected during CSIRO campaigns (i.e., on the Fitzroy River estuary after Cyclone Debbie, from 9 to 11 April 2017) and during voyages of the RV Investigator within the GBR were also used in this validation exercise. The AIMS and CSIRO water quality datasets are part of the Integrated Marine Observing System (IMOS) Bio-Optical Database (BODB). The dataset was accessed through the Australian Ocean Data Network (AODN) portal (Australian Ocean Data Network, 2020), except for Fitzroy data from CSIRO and recent AIMS data (2018 to present). Figure 3.1 and Figure 3.2 present the histogram and spatial distributions (colour coded with respective concentrations) of the quality controlled *in situ* data sampled in the GBR.

The AIMS and CSIRO laboratories use different methods to determine CHL, TSS and YEL. However, in this validation exercise, the datasets from AIMS and CSIRO have been combined. AIMS determined CHL based on the fluorometric method of Strickland and Parsons (1972), using a Turner Designs 10AU fluorometer with wavelengths and calibration equations specified in Jeffrey and Humphrey (1975). The fluorometric method measures the natural fluorescence of CHL from a filtered sea water sample. Detection limits are calculated and reported in each batch of data, but the optimal working range is from 0.05 to 5 mg m^{-3} for a 100 ml sample. Details of the method employed by AIMS can be found in Great Barrier Reef Marine Park Authority (2019b).

The CSIRO Oceans & Atmosphere (O&A) laboratory in Hobart determine CHL using High Performance Liquid Chromatography (HPLC) following a slightly modified method from Van Heukelem and Thomas (2001), which is described in detail in Hooker et al. (2012). In summary, sea water samples are collected in 25 mm GF/F filters and stored in liquid nitrogen until laboratory analysis. The HPLC method is focused on resolving Chlorophyll-*a* pigments (divinyl and monovinyl), phaeopigments and accessory pigments (such as Chlorophyll-*b* and *c*) through chromatography (Mueller, 2003). The CHL

utilised in this study refers to the total chlorophyll-a, which is the sum of the divinyl and monovinyl counterparts. The HPLC is usually more precise and is widely preferred over the fluorometric method (Trees et al., 1985; Mueller, 2003; Marrari et al., 2006).

Both CSIRO and AIMS use the gravimetric method to measure the total concentration of suspended solids (TSS) in seawater, which are summarised below. The method consists of measuring the dry weight of suspended solids from a known volume of seawater sample after it has been vacuum filtered on a pre-weighted membrane filter. AIMS filters the seawater samples on a polycarbonate membrane filter (0.4 µm pore size by 47 mm diameter), and the filters are dried overnight at 60˚C. The dry weight of a wet filter blank is utilised for baseline correction. After baseline correction, the result is divided by the volume of filtered seawater. The AIMS method was tested after a series of wet filter blank trials and the lowest TSS that can be accurately measured is 0.36 mg L^{-1}. Further details on the methodology employed by AIMS is described in Great Barrier Reef Marine Park Authority (2019b).

Meanwhile, CSIRO analyses three equal sets (triplicates) of surface water samples filtered under low vacuum onto a GF/F 0.7 µm pore size and 47 mm diameter filter for TSS determination. Prior to sampling and analysis, the filters are pre-washed with MilliQ water, pre-ashed at 450˚C and pre-weighted. Post seawater filtration, 50 ml of distilled water is rinsed over the filters to remove salts and each filter is stored flat in a Petri dish at 4˚C until analysis. The filters are dried at 60˚C to determine the total weight of suspended solids. The final TSS is derived by taking the median and standard deviation from the TSS triplicate set. Details of the TSS method utilised by CSIRO are further described in Soja-Woźniak et al. (2019).

Yellow substances (YEL) or coloured dissolved organic compounds derived from the degradation of plant matter strongly absorb ultraviolet and short-wave visible light. AIMS and CSIRO laboratories estimate YEL absorption by the spectrophotometric method. Both laboratories present slight differences in methodology, which are briefly described. AIMS utilises a Shimadzu UV-1800 spectrophotometer (240 to 700 nm). Water samples from a Niskin bottle are filtered in a clean syringe through the 0.2 µm poly-sulfone (Pall-Acropack supor membrane) filter. CSIRO, on the other hand, uses a GBC-916 ultraviolet/visible (UV/VIS) spectrophotometer (200 to 900 nm) for determination of YEL. First, the seawater sample is passed through a glass fibre filter (GF/F) prior to filtration on polycarbonate Millipore 0.22 µm filter. Then, the filtrate sample is placed in a 10 cm path length cuvette for reading in the spectrophotometer. The YEL absorbance reading is subtracted from a reading of a MiliQ (Millipore) water for baseline correction. The absorption coefficient at a specific wavelength (443 nm in this study) is calculated considering the volume of water analysed (usually for a 10 ml cuvette), converting the absorbance reading from decadic to natural logarithm and normalizing the absorbance to zero at around 600-700 nm. An exponential fit is applied to the calculated YEL spectra and the YEL

absorption at 443 nm is then derived. Detection limits for YEL analysis are mainly determined by the photometric accuracy of the spectrophotometer, which can range from 0.004 to 0.013 m^{-1} (Nelson and Coble, 2009). More details of the methods used by AIMS and CSIRO are reported in Great Barrier Reef Marine Park Authority (2019b) and in Clementson et al. (2001); Clementson et al. (2004) for the methods employed by CSIRO.

In situ data points within 1 km from coastline or reefs were excluded from the analysis to reduce uncertainties due to potentially strong reflectance effects from land and reefs (Bulgarelli and Zibordi, 2018). Samples were taken at variable isobaths (1.5 m to 40 m) with the shallowest datasets having TSS > 10 mg L^{-1}, characterising optically deep waters. CHL and TSS measurements totalled 347 each, while YEL samples totalled 149 entries, of which 17 were sampled without simultaneous measurements of CHL and TSS. Figure 3.1 presents histogram plots with descriptive statistics of CHL (a), TSS (b) and YEL (c). *In situ* CHL presented a two-order magnitude range from 0.02 to 4.76 mg m^{-3}, and a mean of 0.59 mg m^{-3}. Meanwhile, TSS ranged from 0.01 to 85 mg L^{-1} with a mean of 3.5 mg L^{-1} and YEL from 0.003 to 1.77 m^{-1} with a mean of 0.21 m^{-1}, both varying three orders of magnitude during the period analysed (2015-2018). All three WQP presented log-normal distributions, indicating that the most frequently occurring values are lower than the mean value of the entire dataset.

Most data points were located within the GBR lagoon (Figure 3.2) whilst two were located seaward of the outer barrier reef. The data points were distributed between the central and southern GBR (-15˚S to -21˚S), with a few data points sampled further south in Keppel Bay, at the mouth of the Fitzroy River (YEL only). The *in-situ* data presented in Figure 3.2 were collected in different seasons between 2015 and 2018, and thus the spatial patterns (colour coded by concentration) may also be influenced by temporal variations.

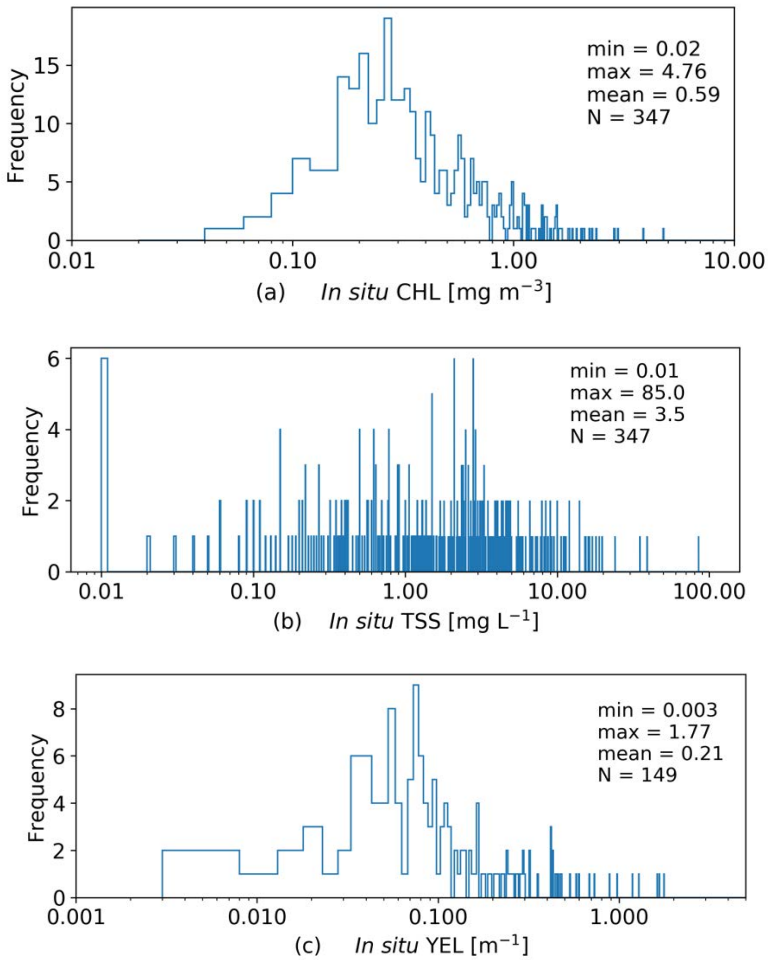

Figure 3.1: Frequency distribution log-linear plots for *in situ* CHL (a), TSS (b) and YEL (c) and summary statistics.

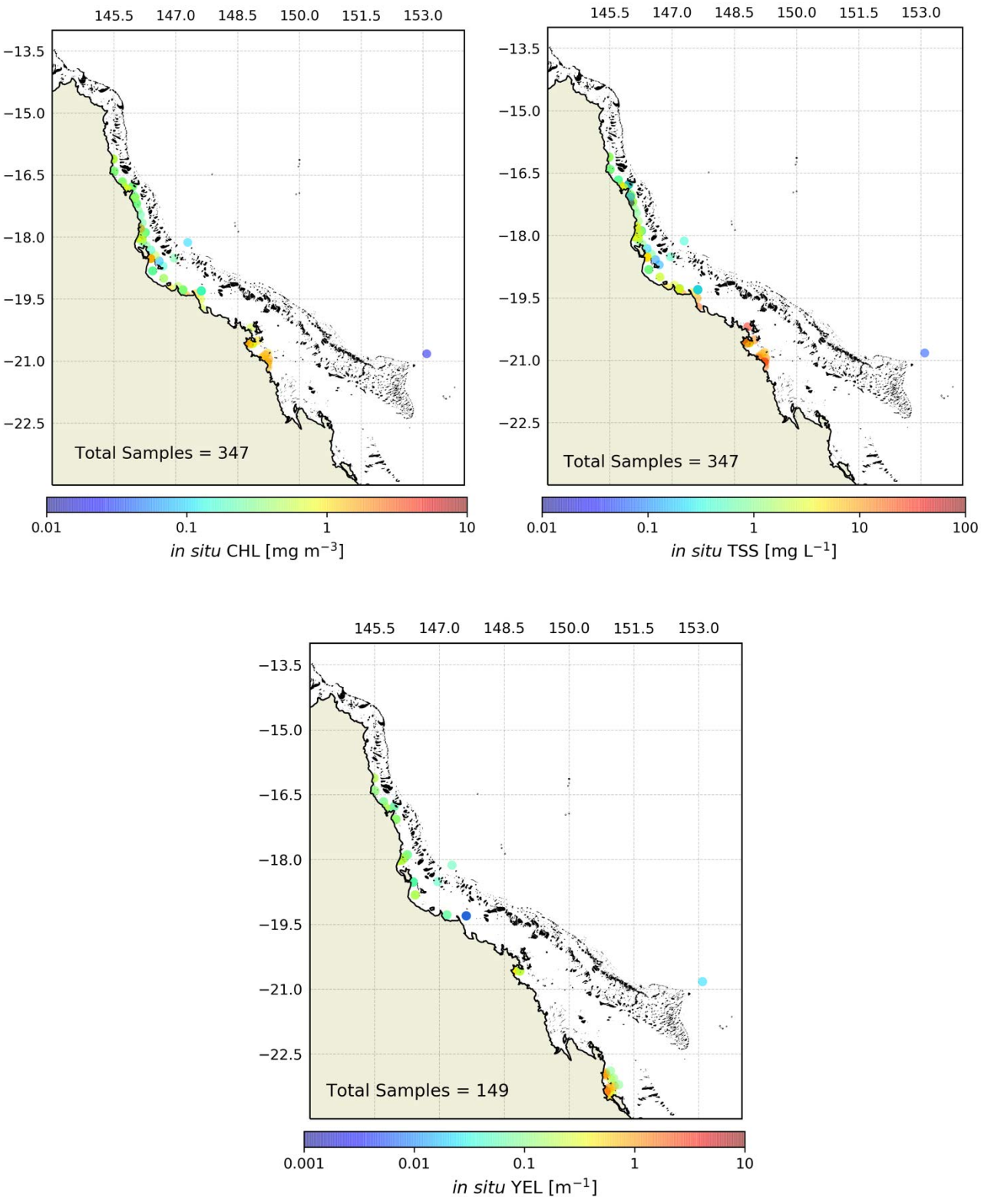

Figure 3.2 Spatial distributions of *in situ* CHL, TSS and YEL sampled between 2015 and 2018 in the GBR Marine Park. The present dataset includes samples collected by AIMS and CSIRO (including at LJCO and onboard the RV Investigator).

3.1.2 Selection of Himawari-8 observations

Himawari-8 scans at least 48 images a day (8 a.m. to 4 p.m.), an unprecedented number of observations for ocean colour validation and applications. The chances of concurrently matching an *in-situ* measurement against a product derived from Himawari-8 increases 24 times, compared to the constellation of sensors providing 1 to 2 observations per day (i.e., MODIS/Aqua, Sentinel-3, VIIRS, etc.). This is particularly relevant because cloud cover is one of the main limitations to ocean colour data availability (Sirjacobs et al., 2011; Ruddick et al., 2014).

It is recommended that the time difference Δt between an *in situ* measurement and the matching satellite observation is minimised as much as possible to avoid discrepancies due to the rapid optical changes in coastal waters. Doerffer (2002) recommends matchups with a Δt of ±30 minutes or less in coastal waters while IOCCG (2019) recommends Δt ±1 hour or less, depending on the optical complexity. The high-frequent scanning schedule of Himawari-8 allows a Δt of 10 minutes or less, between each measurement and observation. Additionally, multiple Himawari-8 observations can be combined within a timeframe (i.e., hourly) for reducing environmental noise, to eliminate potential outliers and to increase the sensor's signal to noise ratios, improving estimates and validation performances (IOCCG, 2012b; Ruddick et al., 2014; Lavigne and Ruddick, 2018). This study took advantage of the intensive temporal coverage of Himawari-8 to test validating each *in situ* measurement against:

a) the closest 10-minute Himawari-8 WQP product (temporal approach I – TA-I).
b) an hourly composite of Himawari-8 WQP products (temporal approach II – TA-II).

Therefore, all available Himawari-8 observations scanned within ±30 minutes from the recorded *in situ* timestamp, were acquired for validation. Some observations were not available because of Himawari-8 quarterly scheduled maintenance (usually at every 2:40 UTC ~ 12:40 p.m. AEST). The selected Himawari-8 full disk VNIR observations were acquired and extracted to the GBR area (10˚S to 29˚S and 140˚E to 155˚E), according to section 2.4.1.

3.1.3 Water Quality Retrievals for Validation

This section described the general procedure employed in this validation exercise, for both temporal approaches. The algorithms designed to retrieve CHL, TSS and YEL, with PCA de-correlation of radiance inputs and added noise (Group B, Set 2 to 4, see section 2.3.1) were chosen for evaluation. Selected and processed 10-minute Himawari-8 observations at the VNIR bands, with associated geometry $(\theta_v, \theta_s, \Delta\phi)$, were subset to 3-by-3-pixel box, centred at the coordinates of each concurrent *in situ* datapoint (via nearest neighbour distance). Likewise, 3-by-3-pixel subsets of concurrent masks (i.e., clouds, land, and sun glint) and ancillary data (i.e., ozone and pressure) were taken. Additionally,

concurrent *in situ* measurements (CHL, TSS and YEL) and metadata (date, time, latitude, longitude, collector, station, water depth, distance from the coast and from reefs) were included in the validation dataset. The θ_s of Himawari-8 observations utilised in this validation exercise ranged from 12 to 55 degrees. True colour RGB composites of selected Himawari-8 observations were visually inspected to eliminate matchups in waters with sharp gradients in optical properties (i.e., turbidity fronts). The Himawari-8 subsets were processed with the chosen ANN inversion algorithms for WQP retrievals.

The retrieved WQP 3-by-3-pixel subsets were masked for clouds, land, and sun glint. Only those subsets with 2 or less pixels masked per pixel-box were considered valid for matchup. In addition, the WQP subsets were filtered for any occurrence of ANN flags (section 2.4.4). For a systematic approach, if any pixel within a subset was out-of-range, the entire matchup was discarded. This criterion was designed to guarantee that only entirely valid estimates were allowed for performance assessment. Moreover, the validation dataset was filtered to eliminate matchups where *in situ* TSS values were lower than 0.1 mg L^{-1}. The trained and tested ANN experiments consistently demonstrated high errors for TSS values below this threshold (see Figure 2.20 in section 2.3.3), which might be associated with the relatively strong influence of the atmospheric path radiance compared to the water leaving radiances over optically clear waters (Dorji and Fearns, 2018). Finally, the median (spatial aggregate of pixels within subset) and the standard deviation of each valid subset were computed, excluding masked pixels. The median value of retrieved CHL, TSS and YEL were statistically compared against their concurrent *in situ* counterparts. An overview of the validation procedure is illustrated in Figure 3.3, and details about the temporal approaches are described in the next subsection.

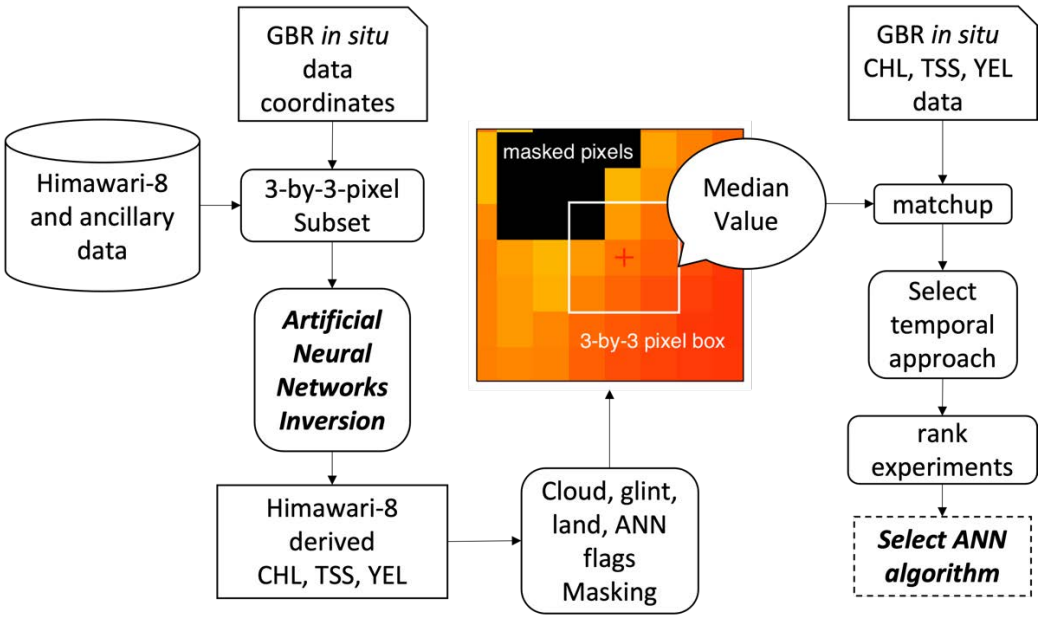

Figure 3.3: A simplified overview of the algorithm validation procedure.

3.1.4 Testing Temporal Approaches

In this thesis, two temporal approaches were tested for validation, TA-I and TA-II. For TA-I, the closest Himawari-8 derived WQP subset product scanned within 5 minutes (Δt = ±5 min) from the *in situ* time stamp was utilised in TA-I. For TA-II, an hourly composite (i.e., the average) of 4 to 6 valid subset products were computed (Figure 3.4). If less than 4 single valid products were available within an hour, the matchup was discarded. The temporal aggregation procedure $(\bar{X})$ disregarded any pixels masked in each valid subset. On both temporal approaches, the median value $(\widetilde{M})$ of all valid pixels within a subset product was used for matchup against concurrent *in situ* measurement. The approaches were statistically compared utilising the matchups available for both TA-I and TA-II. The approach with the best overall performance was chosen for further ranking and selection of ANN experiments.

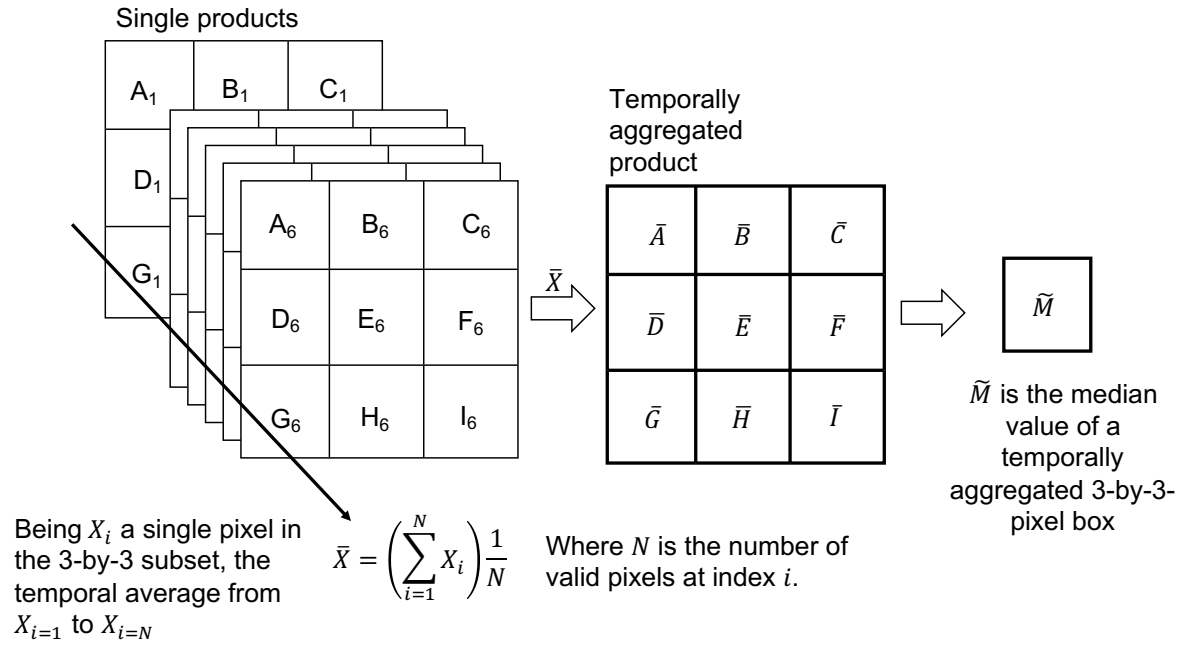

Figure 3.4: Schematic diagram of temporal aggregation employed in Temporal Approach-II. In this example, all 6 subsets acquired within an hour were valid for aggregation.

3.1.5 Statistical Descriptors and Performance Evaluation

The ANN experiments were evaluated with regards to their Root Mean Squared Error (RMSE – or absolute error), mean Bias, Mean Absolute Percentage Error (MAPE – or relative error), and the coefficient of determination (R^2), following Schroeder et al. (2018). Considering that *in situ* CHL, TSS and YEL present a log-normal distribution (Figure 3.1), the ANN outputs were computed in logarithmic scale ($\log_{10}$). The *in-situ* dataset was transformed accordingly for comparison and statistical analysis. Bias, R^2 and RMSE were calculated in $\log_{10}$ space and MAPE was calculated in linear space. In Eq. 3.1 to

Eq. 3.4, m refers to *in situ* measurements, p refers to satellite derived products, and N is the number of samples or valid matchups.

$$RMSE = \sqrt{\frac{1}{N}\sum(m-p)^2} \quad \text{Eq. 3.1}$$

$$MAPE = \frac{100}{N}\sum\frac{|p-m|}{m} \quad \text{Eq. 3.2}$$

$$R^2 = \left[\frac{N(\sum mp) - (\sum m)(\sum p)}{\sqrt{[N\sum m^2 - (\sum p)^2][N\sum p^2 - (\sum p)^2]}}\right]^2 \quad \text{Eq. 3.3}$$

$$Bias = \frac{1}{N}\sum(m-p) \quad \text{Eq. 3.4}$$

3.1.6 Rank Experiments and Select ANN algorithm

The final validation analysis consists in statistically evaluating the WQP retrievals from Himawari-8 against *in situ* measurements for the selected temporal approach. First, for each individual WQP, the top 3 ANN experiments with lowest RMSE were selected and their statistical metrics were tabulated for comparison. The RMSE is the metric of choice for ranking the experiments because the objective of the ANN is to minimise the cost function, i.e., the Mean Squared Error. Scatterplots of matching *in situ* and Himawari-8 products were utilised to visually interpret the top-3 experiments. Preference was given for those experiments with the lowest RMSE and MAPE errors, as well as a Bias close to zero and highest R^2. Additionally, the stability to retrieve WQP for a range of simulated scenarios was assessed by recalling the independent simulated test dataset with the selected ANN experiments. The RMSE was evaluated for bins of equally spaced logarithmic concentrations of WQP. Ideally, the computed RMSE values for a given concentration bin is expected to be lower than the respective concentration. Moreover, the experiment's sensitivity to retrieve WQP for a range of solar zenith angles were investigated. Finally, the best performing ANN experiment with the lowest number of neurons in the hidden layer was chosen, to reduce the computational efforts for the inversion of Himawari-8 observations over the entire GBR.

3.2 Validation Results

Figure 3.5 presents the statistical comparison between TA-I and TA-II performance for all ANN experiments within group B to separately retrieve CHL, TSS and YEL. The performance of TSS retrievals significantly improved when employing aggregated observations, with lower MAPE, RMSE and higher R^2. Conversely, TA-II retrieved CHL with lower MAPE while YEL was retrieved with larger MAPE values. However, CHL and YEL were consistently retrieved with large RMSE and negative bias for both temporal approaches tested.

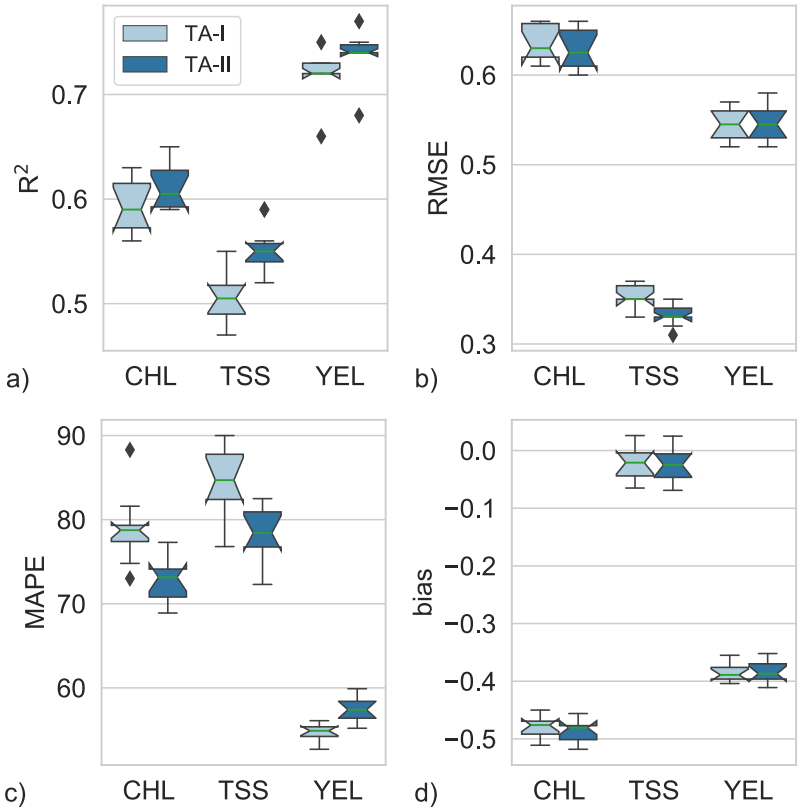

Figure 3.5 Boxplot of statistical metrics comparing temporal approaches TA-I (light blue boxes) and TA-II (dark blue boxes) for concurrently available data points.

The performance of ANN experiments was then evaluated with TA-II given that this temporal approach demonstrated lower MAPE, RMSE higher R^2 compared to TA-I. The statistical performance and the sensitivity of estimating CHL, TSS and YEL in the GBR was calculated for the top-3 ANN experiments.

3.2.1 Chlorophyll-*a* Concentration (CHL)

Matchup statistics for *in situ* CHL concentrations ranging from 0.07 to 2.8 mg m^{-3} are summarized in Table 3.1 for the top 3 ANN experiments within group B. The three selected experiments presented similar statistical performances, with RMSE of 4 mg m^{-3}, MAPE at 70% and mean negative

bias around 0.47 mg m^{-3}. Although the experiments yielded a positive correlation between observations and measurements, a consistent underestimate was observed for retrieval of *in situ* CHL below 1 mg m^{-3} (Figure 3.6). A few retrieved CHL values presented large standard deviations (error bars in Figure 3.6), indicating 2 orders of magnitude variations within a 3-by-3-pixel box.

Table 3.1: Matchup statistics of the top 3 ANN experiments for CHL retrievals in ascending order of RMSE. The experiment's identifiers are compiled in the first column, followed by the number of hidden layer neurons (HID) column. N is the number of valid matchups. Except for MAPE, all statistics were calculated in logarithmic base 10 scale. Units for 10^{RMSE} are in mg m^{-3}.

AHI Hourly aggregated CHL (mg m^{-3}), N = 48

ANN	HID	R^2	MAPE	RMSE	10^{RMSE}	Bias
P053	**40**	**0.59**	**70**	**0.60**	**3.9**	**-0.47**
P056	70	0.59	71	0.61	4.0	-0.47
P051	20	0.62	71	0.62	4.1	-0.48

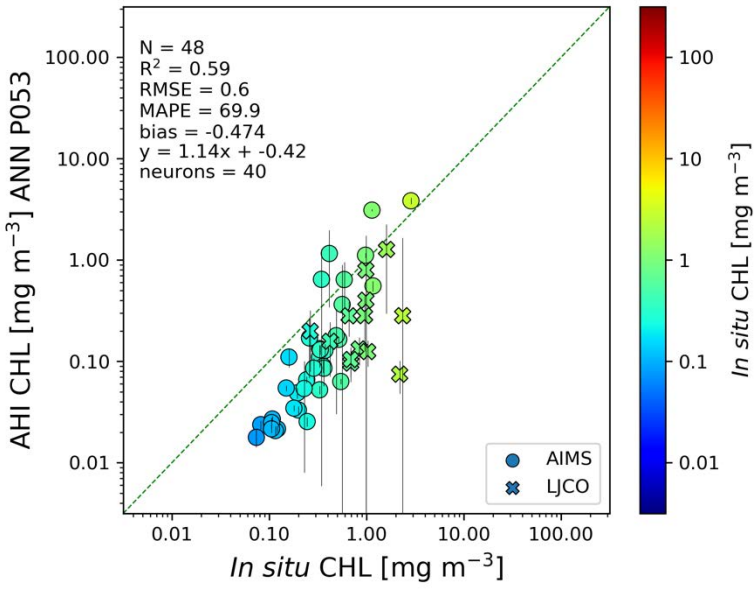

Figure 3.6: Log-Log scatterplot between *in situ* and hourly derived AHI CHL for P053 ANN experiment. *In situ* CHL are colour coded in logarithmic scale. Error bars were computed as the standard deviation of AHI derived CHL within a 3-by-3-pixel box. The circular and cross symbol markers indicate *in situ* data collected by AIMS and at LJCO, respectively.

Conversely, the recall of a simulated testing dataset (Figure 3.7) for the top 3 ANN experiments revealed that CHL between 0.01 and 1 mg m^{-3} may be retrieved with RMSE errors well above 100%, corroborating patterns of Figure 3.6. In addition, according to the recall of a simulated test dataset, the CHL retrievals at 0.4 mg m^{-3} were largely impacted by θ_s between 0˚ and 70˚ (Figure 3.8). The P053 and P056 experiments demonstrated reasonable retrieval stability for CHL at 5.0 mg m^{-3}, for θ_s < 60˚.

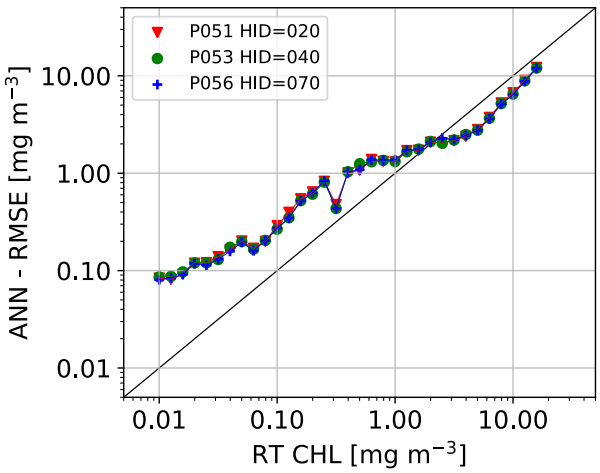

Figure 3.7: Simulated CHL and associated retrieval RMSE errors from ANN recalls of the independent testing dataset (*N*=100 000). The retrieval errors are demonstrated for the top 3 ANN experiments (P051, P053, P056) ranked in this validation exercise.

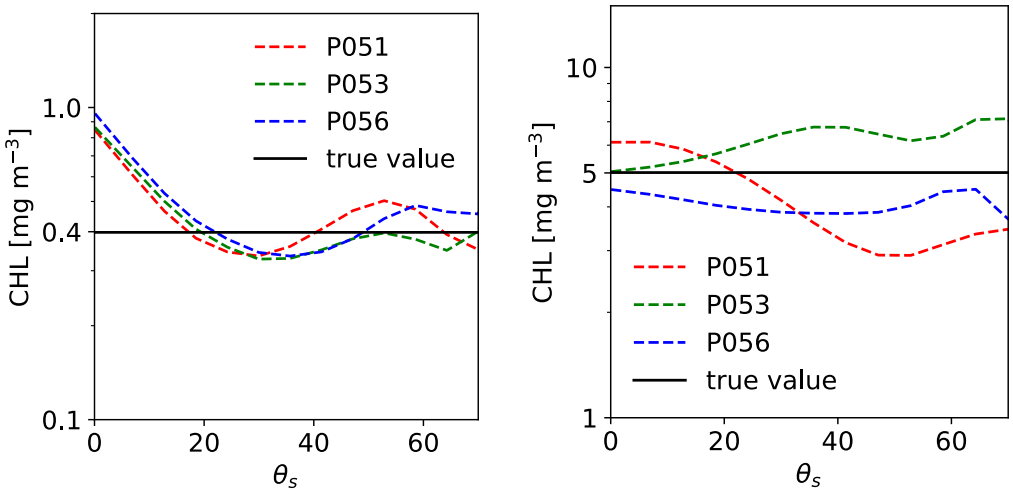

Figure 3.8: Variability of retrieved CHL for θ_s between 0 and 70 degrees, $\Delta\phi$ of 180 degrees and θ_v of 24 degrees with the top-3 performing ANN experiments. The solid horizontal lines correspond to the synthetic CHL values (0.4 and 5.0 mg m^{-3}) input to the bio-optical models for the RT simulations. The dashed lines represent the retrievals for each ANN experiment selected. Note different ranges of CHL in logarithmic scale.

3.2.2 Total Suspended Solids (TSS)

The performance of estimating TSS ranging from 0.14 to 24 mg L^{-1} is summarized in Table 3.2 for the top 3 experiments within group B. The TSS experiments presented a positive R^2 with variable MAPE between 75 and 80% and RMSE between 2.08 to 2.18 mg L^{-1}. Mean bias fluctuated between positive and negative values as low as 0.005 mg L^{-1}, with TSS values below 1 mg L^{-1} being generally overestimated (Figure 3.9). As for CHL retrievals of Figure 3.6, two retrieved TSS data points presented

large standard deviations (error bars in Figure 3.9), indicating 2 to 3 orders of magnitude variations within a 3-by-3-pixel box.

Table 3.2 Matchup statistics of the top 3 ANN experiments for TSS retrievals in ascending order of RMSE. The experiment's identifiers were compiled in the first column, followed by the number of hidden layer neurons (HID) and N is the number of valid matchups. Except for MAPE, all statistics were calculated in logarithmic base 10 scale. Units for 10^{RMSE} are in mg L^{-1}.

AHI Hourly Aggregated TSS (mg L^{-1}), N=46

ANN	HID	R^2	MAPE	RMSE	10^{RMSE}	Bias
P094	**50**	**0.57**	**75**	**0.32**	**2.08**	**0.014**
P098	90	0.57	78	0.32	2.08	0.005
P092	30	0.54	80	0.33	2.13	-0.011

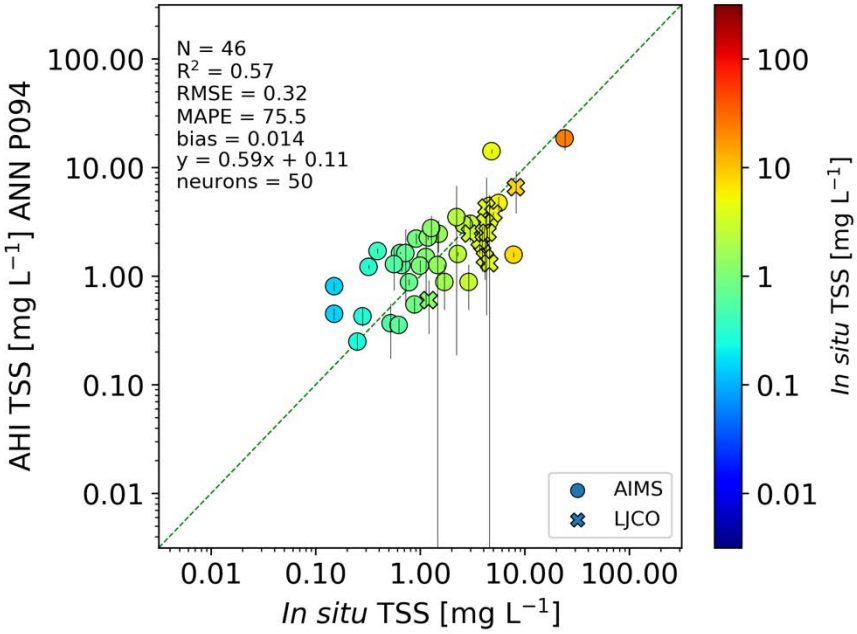

Figure 3.9: between *in situ* and hourly derived AHI TSS for P094 ANN experiment. *In situ* TSS are colour coded in logarithmic scale. Error bars were computed as the standard deviation of AHI derived TSS within a 3-by-3-pixel box. The circular and cross symbol markers indicate *in situ* data collected by AIMS and at LJCO, respectively.

Conversely, the recall of a simulated testing dataset for the top 3 ANN experiments (Figure 3.10) revealed that TSS below 1 mg L^{-1} may be retrieved with up to one order magnitude errors, indicating poor retrievals in optically clear waters. Nevertheless, the simulated retrievals demonstrated that TSS larger than 1 mg L^{-1} may be estimated with good accuracy from Himawari-8. In addition, the algorithm's performance was marginally impacted by θ_s < 70˚ (Figure 3.11Figure 3.8), providing reasonable stability for TSS retrievals between 0.2 and 2 mg L^{-1}.

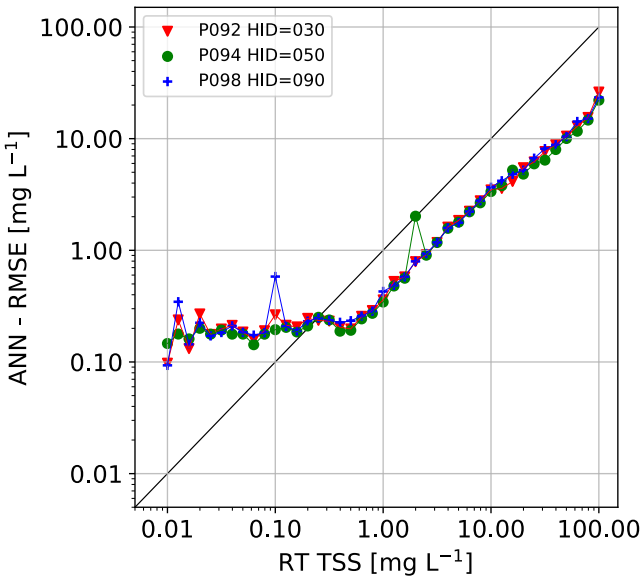

Figure 3.10: Simulated TSS and associated retrieval RMSE errors from ANN recalls of an independent testing dataset. The retrieval errors are demonstrated for the top 3 ANN experiments (P092, P094, P098) ranked in this validation exercise.

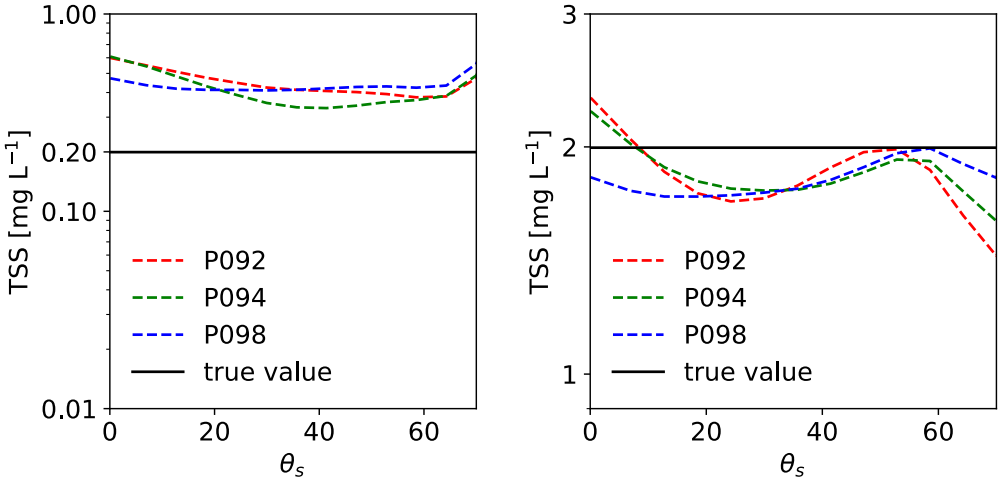

Figure 3.11: Variability of retrieved TSS for θ_s between 0 and 70 degrees, $\Delta\phi$ of 180 degrees and θ_v of 24 degrees with the top-3 performing ANN experiments. The solid horizontal lines correspond to the synthetic TSS values (0.2 and 2.0 mg L^{-1}) input to the bio-optical models for the RT simulations. The dashed lines represent the retrievals for each ANN experiment selected. Note different ranges of TSS in logarithmic scale.

3.2.3 Yellow Substances (YEL)

The performance of estimating YEL absorption (at 443 nm) between 0.017 to 1.77 m^{-1} is summarized for the 3 best ANN experiments in Table 3.3. Although YEL experiments yielded a high and positive correlation (R^2 ~0.7), the retrievals were largely underestimated (bias ~ -0.4 m^{-1}), presented with large RMSE (~3.5 m^{-1}) and moderate MAPE (~57%). As for CHL and TSS retrievals, two YEL data points

presented large standard deviations (error bars), indicating 2 to 3 orders of magnitude variations within a 3-by-3-pixel box.

Table 3.3: Matchup statistics of top 3 ANN experiments for YEL retrievals in ascending order of RMSE. The experiment's identifiers are compiled in the first column, followed by the number of hidden layer neurons (HID) column. N is the number of valid matchups. Except for MAPE, all statistics were calculated in logarithmic base 10 scale. Units for 10^{RMSE} are in m^{-1}.

AHI Hourly Aggregated YEL, N=33

ANN	HID	R^2	MAPE	RMSE	10^{RMSE}	Bias
P139	**100**	**0.71**	**57.7**	**0.53**	**3.38**	**-0.368**
P135	60	0.71	56.8	0.54	3.46	-0.394
P136	70	0.70	56.3	0.54	3.46	-0.367

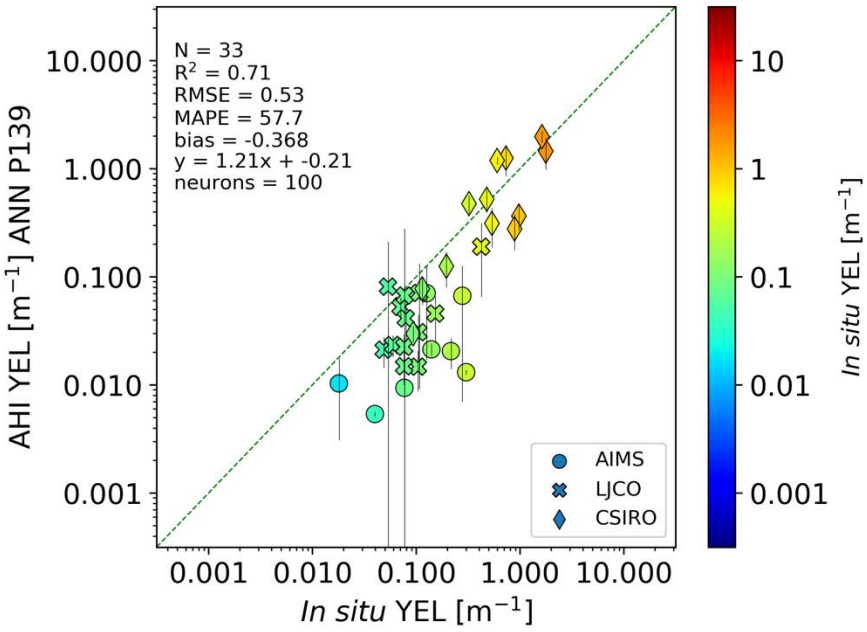

Figure 3.12: Log-Log scatterplots of AHI derived hourly YEL matchups for P0139 ANN experiment. *In situ* YEL are colour coded in logarithmic scale. Error bars were computed as the standard deviation of AHI derived YEL within a 3-by-3-pixel box. The circular, cross and diamond symbol markers indicate *in situ* data collected by AIMS, at LJCO, and by CSIRO at Fitzroy River mouth, respectively.

The top 3 ANN experiments consistently underestimated YEL below ~0.1 m^{-1} (Figure 3.12), corroborating simulated patterns (Figure 3.13). Nevertheless, YEL larger than 1 m^{-1} were retrieved with reasonable accuracy, indicating satisfactory performance in coastal waters, particularly for *in situ* YEL collected by CSIRO in the surrounding waters of the Fitzroy River plume (diamond markers in Figure 3.12). In addition, the YEL algorithm's performance was slightly impacted by θ_s < 70˚ (Figure 3.14), indicating reasonable stability for YEL retrievals between 0.1 and 0.25 m^{-1}, at variable atmospheric path lengths.

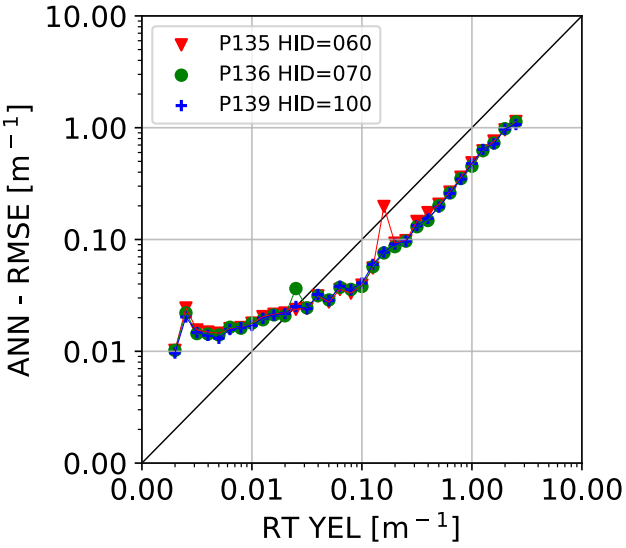

Figure 3.13: Simulated YEL and associated retrieval RMSE errors from ANN recalls of an independent testing dataset. The retrieval errors are demonstrated for the top 3 ANN experiments (P135, P136, P139) ranked in this validation exercise.

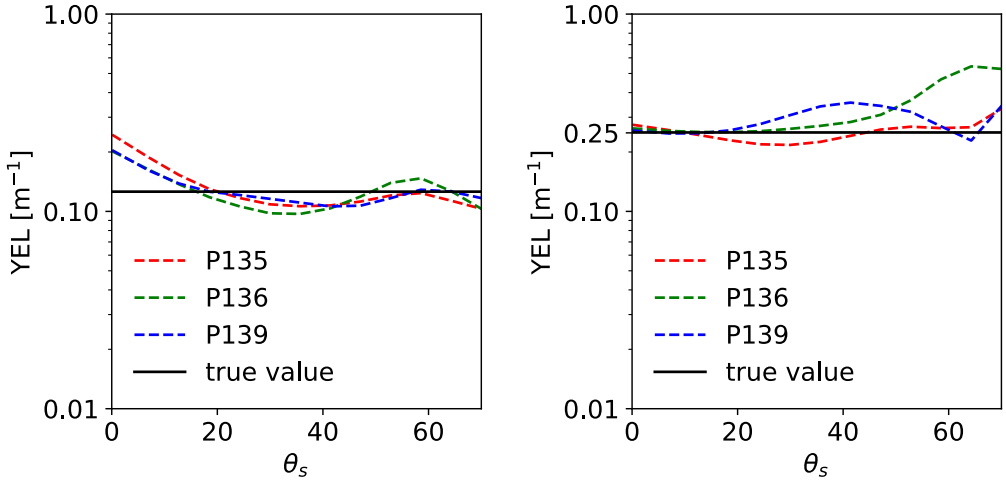

Figure 3.14: Variability of RMSE to retrieve YEL for a range of θ_s with the selected ANN experiments. The solid horizontal lines correspond to the synthetic CHL values (0.12 and 0.25 m^{-1}) input to the bio-optical models for the RT simulations. The dashed lines represent the RMSE errors for YEL retrievals at θ_s between 0 and 60 degrees, $\Delta\phi$ at 180 degrees and VZA of 24 degrees.

3.3 Discussion of Algorithm Validation Chapter

Chapter 3 focused on the statistical assessment of the physics-based inversion algorithms developed for retrieving CHL, TSS and YEL in the GBR, from Himawari-8 observations. The selected and quality controlled Himawari-8 observations, concurrent to *in situ* measurement data, were processed with 30 PCA-designed ANN inversion experiments. Given the exceptional number of Himawari-8 observations available for validation, we tested the efficacy of degrading the temporal resolution for improved retrieval performances, as suggested by Lavigne and Ruddick (2018). This chapter discusses the assessment of tested temporal approaches and the individual performance of CHL, TSS and YEL retrievals for the ocean colour algorithms developed.

3.3.1 Evaluation of temporal approaches

Products derived every 10 minutes and from hourly aggregates of Himawari-8 observations were evaluated and compared as two distinct temporal approaches for validation (TA-I and TA-II respectively). TA-I minimises the temporal mismatch between observations and *in situ* measurements, which is desirable for validation of coastal ocean colour products (Doerffer, 2002). Meanwhile, TA-II utilised hourly aggregates of 10-minute derived products to reduce signal-dependent noise (Lavigne and Ruddick, 2018). In general, the retrieval performances of CHL and TSS were significantly improved when using TA-II compared to products derived with TA-I. However, the retrieval of YEL substances yielded slightly higher errors when with TA-II. Nevertheless, the temporal averaging of products generally improved the accuracy of ocean colour retrievals from Himawari-8, as it has been previously suggested (Ruddick et al., 2014; Murakami, 2016b; Lavigne and Ruddick, 2018). Moreover, the algorithm's performance has potentially benefited from the visual inspection of RGB composites to detect unmasked clouds and subsets with heterogeneous optical properties. However, due to the large number of matchups available, visual inspection of RGB is time consuming and subjective. Further automation of visual quality control is suggested for fast and objectively identification of undetected clouds and heterogeneous pixel-box subsets. Neural network algorithms have been increasingly employed to detect cloud and cloud shadow features, and suggest a potential improvement of current techniques based on spectral information of the infrared and thermal bands (Segal-Rozenhaimer et al., 2020).

3.3.2 Chlorophyll-a Retrievals from Himawari-8

The top-performance ANN algorithm for CHL was the P053 with 40 hidden-layer neurons. Although CHL between 0.07 to 2.87 mg m^{-3} were estimated with RMSE errors as high as 4 mg m^{-3}, retrievals were achieved with MAPE of 70%, within the mission targets defined for Level 2 Sentinel-3

CHL products in Case 2 waters (Donlon, 2011). The poor performance of discriminating CHL with Himawari-8 in the coastal GBR may be largely due to the spectral and radiometric characteristics of the Himawari-8 sensor. Himawari-8-AHI offers 3 visible bands (centred at 470, 510 and 640 nm) with 30 to 80 nm bandwidth, depending on the band. Additionally, Himawari-8 AHI's 11-bit radiometric resolution is moderate compared to 14 and 12 bits from contemporary ocean colour sensors such as Sentinel-3 OLCI and MODIS/Aqua respectively. For instance, SeaWiFS observations (at 10 bits and 20-40 nm bandwidth in the VNIR bands) were utilised to assess the impact of radiometric resolution on ocean colour estimates (Hu et al., 2001). Hu et al. (2001) reported up to ±60% errors for Case 1 waters CHL estimates, when the expected accuracy was of ±35%, with a two to three-fold variation of values in adjacent pixels. These errors are usually seen as a speckle or graininess across the image and decreased with increasing concentrations of CHL (Hu et al., 2012b). However, Lavigne and Ruddick (2018) reported relatively low (10%) radiometric errors when simulating Case 1 CHL from meteorological observations of the Flexible Combined Imager (FCI) on board the geostationary Meteosat Third Generation satellite. The authors reported that a spatial-temporal aggregation of observations was key to reduce FCI's radiometric noise and improve atmospheric correction of the visible bands.

Meanwhile, Murakami (2016b) Himawari-8 mixed band ratio algorithm (at 470/510 and 510/640 nm) presented MAPE within 51% for CHL lower than 0.3 mg m^{-3}. However, estimates of CHL between 0.3 and 3 mg m^{-3} are still a challenge because the Himawari-8 green band is centred at 510 nm. In contrast, the green bands on ocean colour sensors are usually centred at around 545-565 nm to measure CHL's peak reflectance (IOCCG, 2012b). Furthermore, band ratio algorithms are inappropriate to derive CHL in optically complex waters because of the strong influence of YEL in the green and blue parts of the spectrum. However, Murakami (2016b) showed that Himawari-8 red band centred at 640 nm can be useful for estimating CHL larger than 5 mg m^{-3} due to backscattering of larger phytoplankton particles (i.e., harmful algal blooms and *Trichodesmium* sp.). In fact, the 10-minute Himawari-8 observations at 1 km spatial resolution have successfully been utilised for detecting floating algae in inland waters and provided more observations than the hourly GOCI ones (Chen et al., 2019). Thus, Himawari-8 observations have the potential for ultra-high frequency algal bloom detection in the coastal GBR, compared to contemporary approaches (McKinna et al., 2011; 2014a; Blondeau-Patissier et al., 2018).

Top of atmosphere radiances are largely affected by scattering of aerosols in the blue bands, which affects the retrieval of CHL at low concentrations (i.e., below 1 mg m^{-3}). Accordingly, the present model might benefit from utilising an explicit atmospheric correction, as demonstrated by the ANN approach developed by Schroeder (2007a; 2007b). The atmospheric correction of Schroeder et al. (2007a) has successfully been applied in GBR waters for retrieval of water leaving radiances from

MODIS/Aqua and these have been widely utilised for estimating CHL in the GBR (Brando et al., 2015). Furthermore, an atmospheric correction including NIR and Short-Wave Infrared (SWIR) observations are suggested to improve CHL retrievals in clear waters, considering aerosols are spatially homogeneous (Lavigne and Ruddick, 2018).

The bio-optical model used to parametrize the relationship between CHL and phytoplankton absorption was based on an extensive dataset sampled at diverse regions and trophic conditions in the global oceans (Bricaud et al., 1995). However, this parameterization might not encompass the entire spectrum of bio-optical variations found in the GBR lagoonal waters, adding further uncertainties to the retrievals. Regionalised bio-optical parameterizations between CHL and phytoplankton absorption based on data sampled in the GBR coastal waters have been suggested as alternatives to more generalized assumptions (Oubelkheir et al., 2006; Blondeau-Patissier et al., 2009; Brando et al., 2012). Additionally, the present validation dataset combines CHL measured by fluorimetry and by HPLC methods, both having distinct detection limits and accuracies, and potential impacts on retrievals need to be further evaluated. In summary, the algorithm developed here is not the most suitable for the accurate retrieval of CHL lower than 1 mg m^{-3} in the coastal waters of the GBR. Further validation and regionalised parameterizations should be included for more robust assessment of algorithm performance and potential applications in detecting large blooms.

3.3.3 Total Suspended Solids Retrievals from Himawari-8

The top-performance ANN algorithm for TSS retrievals was P094 with 50 hidden-layer neurons. The TSS estimates presented reasonably good performance with RMSE of 2 mg L^{-1} and MAPE of ~75%, within the mission targets defined for Level 2 Sentinel-3 ocean colour products in Case 2 waters (Donlon, 2011). However, the validation excluded TSS lower than 0.1 mg L^{-1}, as large errors have been reported for TSS at or below this threshold (Dorji and Fearns, 2018; Ding et al., 2020; Hafeez et al., 2021). The uncertainties of estimating such low TSS concentrations can be associated with methodological differences between CSIRO and AIMS laboratories. Only CSIRO collected and measured TSS in triplicates. Triplicate *in situ* sampling is required to avoid potential outliers in the TSS gravimetric measurements and to reduce uncertainties passed to validations. Moreover, large uncertainties associated with radiometric and digitization noise (related to the sensor's sensitivity) were reported for TSS retrievals in different studies. Neukermans et al. (2009) applied a simple red band algorithm to estimate turbidity and associated TSS from atmospherically corrected SEVIRI geostationary observations in the coastal waters of the North Sea. The authors found uncertainties exceeding 100% for TSS lower than 1 mg L^{-1}, 32% for TSS between 5 and 10 mg L^{-1} and around 20% for TSS above 10 mg L^{-1}. The largest uncertainties were reported for pixels near clouds and coastlines subject to strong aerosol loads.

Conversely, Petus et al. (2010) reported difficulty in estimating TSS lower than 0.5 mg L^{-1} in European coastal waters, which was associated with the low sensitivity of the MODIS 250 m red and NIR bands utilised. Dorji and Fearns (2018) applied an empirical single-band algorithm to derive TSS from the atmospherically corrected red band (640 nm) of Himawari-8 AHI in coastal waters off Western Australia. The NIR and SWIR bands were utilised for atmospheric correction and TSS estimates yielded similar limitations when compared to the present physics-based algorithm. The authors reported RMSE up to 0.68 mg L^{-1} when cross validated against MODIS/Aqua TSS. Meanwhile the one-step inversion developed in the present study retrieves TSS with RMSE around 2 mg L^{-1}. Therefore, an explicit atmospheric correction with the NIR and SWIR bands may improve TSS retrievals with Himawari-8 (Vanhellemont and Ruddick, 2015). An intercomparison between the algorithm developed here and the one developed in Dorji and Fearns (2018) for Himawari-8 would better demonstrate the validity of one-step inversion against ones developed with explicit atmospheric correction. Additionally, Dorji and Fearns (2017) report that differences in spatial resolution of the satellite observations yield large uncertainties in TSS estimates for turbid waters. The spatial resolution of TSS can be improved because the Himawari-8 red band (640 nm) is originally scanned at 0.5 km, allowing the resampling of the associated visible bands for potentially improved estimates.

3.3.4 Yellow substances absorption Retrievals from Himawari-8

The top-performing ANN algorithm for YEL retrievals was the experiment P139 with 100 neurons in the hidden-layer. The YEL estimates presented moderate performance with MAPE within 50%, within the mission targets defined for Level 2 Sentinel-3 ocean colour products in Case 2 waters (Donlon, 2011). Improved accuracy was found for values larger than 0.3 m^{-1}, which mostly encompassed samples collected by LJCO and CSIRO campaigns. Hence, potential methodological differences and detection limits between *in situ* measurements from AIMS and CSIRO laboratories should be assessed to better understand the performance of validations.

Schroeder et al. (2012) successfully retrieved YEL (0.01-0.2 m^{-1}) in the coastal GBR from MODIS/Aqua observations through a physics-based algorithm (aLMI from Brando et al. (2012)). The method included an explicit ANN atmospheric correction with variable parameterization of regional inherent optical properties over the GBR, yielding MAPE of 67% and RMSE of 0.057 m^{-1}. The level of accuracy obtained can largely be explained by the efficacy of the atmospheric correction, which has a great impact on retrieval of optical properties that have strong absorption features in the blue bands. However, successful discrimination between CHL and YEL is likely due to the quantity and width of visible bands (5 between blue and green) of MODIS/Aqua sensor. As a result, YEL variations, particularly from endogenous sources, were less likely to be accurately estimated by utilising the limited spectral

set of Himawari-8. Additionally, the aLMI algorithm was tuned to seasonal and local parameterization of inherent optical properties, which was not fully addressed in the present study.

Despite the YEL ANN algorithm's moderate performance, values within 0.09 and 1.77m^{-1} collected at the surrounding waters of the Fitzroy River plume (by CSIRO) were generally retrieved with high accuracy. This was a remarkable result given the heterogeneity of the sampling area and the temporal and spatial mismatch between point-sampling and hourly aggregate of 3-by-3-pixel subsets. This result indicates the feasibility of estimating terrestrially sourced or exogenous YEL and its applicability to derive freshwater plume extent maps at diurnal frequency for the entire GBR. However, more *in situ* data need to be included in validation to better encompass the range of YEL values possibly found in flood plumes.

In summary, the performance of the ANN inversions parameterized for the GBR and for the Himawari-8 observations were reasonable when compared to the mission targets defined for Level 2 Sentinel-3 ocean colour products in Case-2 waters (Donlon, 2011), particularly for the retrievals of TSS. However, CHL and YEL retrievals presented large bias and RMSE errors and are not suitable for applications in the coastal GBR. Further parameterization of CHL absorption in the GBR waters as well as an explicit atmospheric correction are fundamental to reduce uncertainties in regional retrievals. Nevertheless, the performance of the present algorithms is comparable to or better than the performance of past algorithms specifically parameterized for the GBR (aLMI) or for Himawari-8. However, it is necessary to validate these different algorithms (such as of Brando et al. (2015) and (Dorji and Fearns, 2018)) utilising the same *in situ* datasets for a fair intercomparison.

Significant levels of uncertainties may arise from the *in-situ* data sampling, measurement techniques, experimental or environmental factors, and detection limits of the method of analysis. Only *in situ* observations located 1 km from the coastline were accepted for validation to avoid any potential bottom reflection and adjacency effects. However, *in situ* samples with geometrical water depths as low as 1.5 m were included in the validation, considering TSS values above 10 mg L^{-1}. The impact of including geometrically shallow *in situ* measurements on validation analysis should be investigated. Additionally, large uncertainties may arise from the spatial representativeness of *in situ* data (point sampling) compared to a spatial aggregate of information contained in large areas represented by a pixel or an average of pixels. At this stage, the next most relevant analysis is to calculate the signal to noise ratios of the Himawari-8 bands to evaluate the detection limits of the present method due to uncertainties arising from the quality of the observations (radiometric noise).

Chapter 4: Detection Limits of Total Suspended Solids Retrievals from Himawari-8

The accuracy of satellite derived ocean colour products primarily depends on the radiometric quality and stability of the observations (IOCCG, 2013, 2019). Meteorological satellite sensors are designed to detect bright targets (i.e., clouds), which are characterised by a strong spectral reflectance compared to the water signal (Hu et al., 2012b). As a result, the sensitivity of meteorological sensors are much lower than the sensitivity requirements of contemporary ocean colour satellite sensors (IOCCG, 2012b; Ruddick et al., 2014). Additionally, the limitations for deriving ocean colour products from satellite observations are determined by the accuracy of the algorithms employed and their ability to deal with noisy inputs.

Chapter 3 has demonstrated that moderate retrieval performances were achieved for the Himawari-8 CHL and YEL algorithm in the coastal GBR. Nevertheless, TSS may be retrieved from hourly Himawari-8 composites with reasonable performances for coastal waters (MAPE = 75% and RMSE = 2 mg L^{-1}), offering an opportunity for advanced applications. Although validation against *in situ* data is an acceptable average performance metric, the limitations of the algorithm and of the satellite observations themselves can be characterised in more detail. The key objective of this chapter was to investigate the algorithms' limitations to detect TSS fluctuations in the coastal GBR at multiple temporal resolutions (minutes - hours) from Himawari-8 observations. This chapter includes the calculation of Himawari-8 signal to noise levels; the algorithm's sensitivity to several input noise levels and associated detection limits; as well as a qualitative analysis of derived TSS products for 10-minute and hourly observations.

4.1 Signal to Noise Ratios of Himawari-8 bands

In optical sensors, the sources of noise are multiple, such as noise purely dependent on the spectral signal (i.e., photon noise), and the signal-independent noise associated with the electronics of the optical device itself (i.e., electronic noise). The degradation of the optical sensors over time results in systematic errors, which can be characterised and corrected by sensor calibration to ensure appropriate radiometric stability (see section 2.4.1). Meanwhile, the random flux of photons entering the detector at a certain time interval is the most significant source of photon noise in optical sensors (Landgrebe and Malaret, 1986; Hu et al., 2012b; Qi et al., 2017; Gillis et al., 2018; McKinna et al., 2019). The underlying atmospheric and environmental conditions largely contribute to the photon noise in remote sensing observations (Gillis et al., 2018). The photon noise is more evident at lower light levels, such as those coming from a cloud-free and spatially uniform ocean target (Hu et al., 2012b). Regardless

of the source, the photon noise at sensor level is unavoidable and impacts the derived ocean colour products leading to proportionate retrieval uncertainties (Gillis et al., 2018; McKinna et al., 2019). The Signal-to-Noise Ratio (SNR - Eq. 4.1) is a metric utilised to characterise the detector response to a signal over a certain target area, being a critical parameter to determine the precision of ocean colour products (Hu et al., 2001; 2012b). In this context, the target area is a typical cloud-free and homogeneous oceanic region, in which the pixel-to-pixel variations are due to the signal-dependent photon noise. The SNR is described as the ratio of the signal electrons (n_{signal}) to the number of noise electrons (n_{noise}) on the detector (Hu et al., 2012b; Gillis et al., 2018):

$$SNR = n_{signal}/n_{noise} \quad \text{Eq. 4.1}$$

$$n_{signal} = (\Phi/hv) * t * A * \eta \quad \text{Eq. 4.2,}$$

where n_{signal} (Eq. 4.2, (Gillis et al., 2018)) is a function of the power density $(\Phi\ [Wm^{-2}])$ falling on the detector, of the photon energy $(hv\ [Ws])$, the exposure time (t) in seconds, the pixel area $(A\ [m^{-2}])$, and of the quantum efficiency (η) of the detector for a certain wavelength. Therefore, the signal is proportional to exposure time and increasing integration time over a delimited area increases the number of signal electrons relative to the number of noise electrons. In this context, degrading Himawari-8's ultra-high temporal resolution from 10-minutes to hourly aggregated observations may increase the SNR to acceptable levels for ocean colour applications in coastal and turbid waters (Ruddick et al., 2014; Vanhellemont et al., 2014; Murakami, 2016b; Lavigne and Ruddick, 2018; Dorji and Fearns, 2018). Hourly composites may improve the quality of derived TSS and visually enhance surface features due to reduced pixelation noise, i.e., variations from pixel-to-pixel.

In this chapter, the SNR of Himawari-8 VNIR bands were calculated from both 10-minute[9] and hourly aggregated observations for comparison. The SNR were compared to pre-launch and typical SNR derived from multiple ocean colour sensors and to the Himawari-8 SNR calculated in previous studies. The SNR-derived percentage noise was utilised to evaluate the algorithm's sensitivity to noisy input data (Section 4.2).

[9] Each individual Himawari-8 observation, scanned every 10-minutes, is referred throughout this chapter as a single observation and hourly aggregated observations simply as aggregated observations.

4.1.1 Methods

The SNR were computed for the visible and near-infrared Himawari-8 observations scanned between 08:00 to 16:00 AEST (22:00 and 06:00 UTC) at selected dates and cloud-free areas of the Coral Sea. This investigation depended on concurrent cloud masking datasets, in which spatial availability was limited to the GBR and Coral Sea areas (10˚S, 29˚S; 140˚E, 155˚E). Only post-July 2017 observations were considered for this analysis, given that their calibration coefficients were corrected for coherent and horizontal striping noise (Japan Meteorological Agency, 2016, 2017). True colour Himawari-8 observations were browsed through the Himawari-8 Monitor P-Tree System (JAXA, 2020) for target area selection. The near-true colour snapshots were carefully inspected to ensure the areas selected were spatially uniform and unlikely to be influenced by clouds, sun-glint, bio-optical and atmospheric fluctuations (Hu et al., 2012b). The following criteria were utilised for dates and area selection:

1. True colour snapshots over the Coral Sea (offshore GBR Marine Park) were visually inspected to identify dates and areas where cloud coverage and sun glint were nearly absent during an entire day of observations.
2. The selected cloud-free areas/dates were visually inspected to ensure that no gradients in optical properties were visually conspicuous and that hourly CHL values were lower than ~0.1 mg L^{-1}.
3. Aerosol Optical Thickness and the Wildfire products available in the P-Tree System portal were checked to ensure the area selected was not subject to smoke plumes from terrestrial burning.

Two areas were selected based on the above criteria, and their dates, times, latitudes, and longitudes were recorded for image acquisition and processing. The corresponding Himawari-8 single L_{TOA} observations were calibrated, and subsets of 51-by-51-pixels were extracted, centred at the coordinates of selected areas. The choice of size and location of the subsets followed Dorji and Fearns (2018) study, where the Himawari-8 SNR was calculated for a delimited area of the open ocean off Western Australia. In addition, the single observation subsets, associated masks, and geometric parameters were hourly aggregated (i.e., average of 5 to 6 single observation subsets within an hour). The single and aggregated subsets were masked for clouds (with confidence level of 8), land, reefs and sun glint, and their near-true colour composites were inspected for undetected features such as coral cays, reefs, cloud shadows and sensor artefacts (Figure 4.1). The percentage of masked pixels within a subset was calculated and utilised for additional quality control. Single subsets were discarded if 25% or more of its pixels were masked, whereas in aggregated subsets the cut-off threshold was 50%. The threshold was less conservative for aggregated observations because averaging several observations

within an hour increases the probability of a pixel being masked and likely eliminating outliers. The unmasked pixels were selected for calculation of the SNR for all valid single and aggregated subsets.

A total of 61 single and 12 aggregated subsets were qualified for SNR analysis. The subsets were taken on 06/09/2017 (at 16.25˚S, 151˚E – with mean θ_v of 22.5˚) and on 25/09/2017 (at 20.60˚S, 153.53˚E – mean θ_v of 28.2˚), each at different locations in the Coral Sea. True colour snapshots of single subsets scanned on 25/09/2017 between 10:00 and 10:50 AEST and the corresponding aggregated observation (10:00 - 10:50) are shown in Figure 4.1 for illustration purposes. The average of six observations with variable colour and brightness yielded a darker aggregated observation (right-centred panel of Figure 4.1). Several pixels were masked within the area utilised for the calculation of SNR (red rectangle at the centre of each image). However, a visual inspection confirms the unmasked area was homogeneous and devoid of clouds, cloud shadows and associated environmental noise. The bright turquoise feature at the lower right corner of the images is a coral cay, which did not affect the SNR calculations within the subset (red rectangle area).

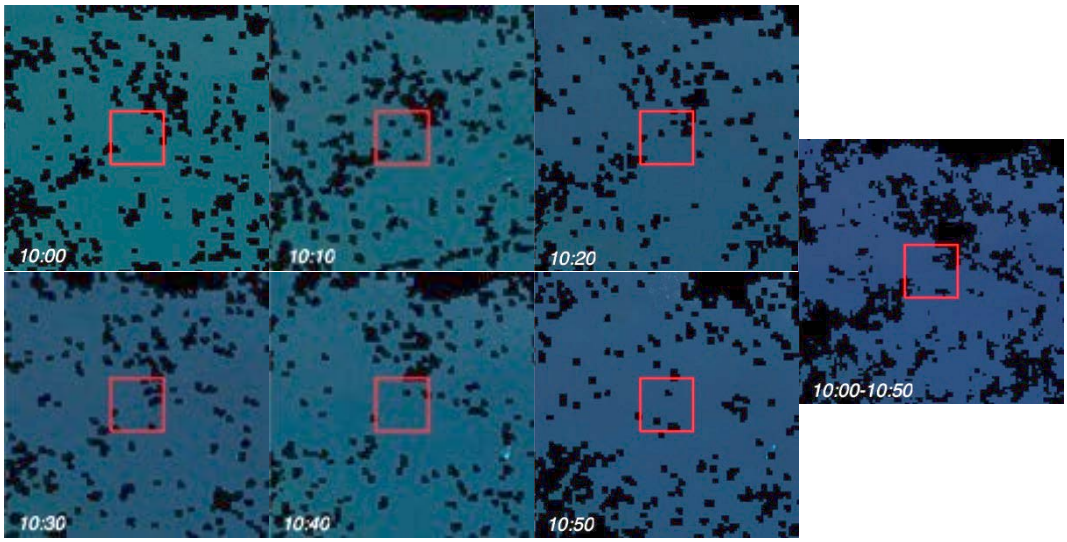

Figure 4.1: Masked near-true colour snapshots of single Himawari-8 observations taken on 25/09/2020, between 10:00 and 10:50 AEST. The corresponding aggregated observation is located at the right-centred panel. The area in the red square delimits the subset utilised for the calculation of SNR. Masked pixels are denoted in black.

The SNR calculated from single and aggregated observations were named SNR_{SING} and SNR_{AGG}, respectively. In addition, given that L_{TOA} can significantly vary as a function of θ_s (Hu et al., 2012b), only those subsets with θ_s variations lower than ±1 degrees were considered valid for analysis. Averaging L_{TOA} for all valid pixels within the target area gives $L_{typical}$, and taking the standard deviation of L_{TOA} within the area gives the noise equivalent radiance (L_{noise}). The SNR of valid subsets was calculated at the VNIR bands of Himawari-8, following Eq. 4.3, where μ is the mean value and σ is the standard deviation of L_{TOA} for all valid pixels within the subset.

$$SNR(\lambda) = \frac{L_{typical}(\lambda)}{L_{noise}(\lambda)} = \frac{\mu(L_{TOA}(\lambda))}{\sigma(L_{TOA}(\lambda))} \quad \text{Eq. 4.3}$$

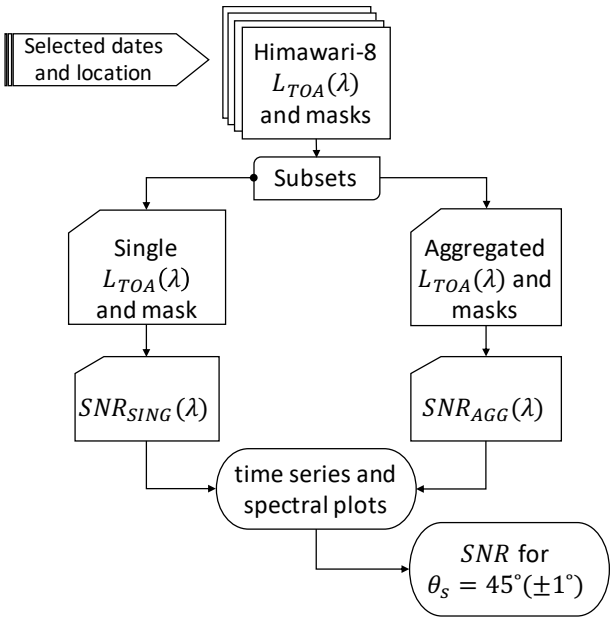

Figure 4.2: Summary of single (SNR_{SING}) and aggregated (SNR_{AGG}) SNR computation for the VNIR Himawari-8 bands. The temporal and spectral variability of SNR_{SING} and SNR_{AGG} were compared and the SNR values at θ_s of 45˚ (±1˚) were selected for further detection limits analysis.

The diurnal variability and magnitude differences between SNR_{SING} and SNR_{AGG} were inspected at each Himawari-8 VNIR band. The spectral characteristics of SNR_{SING} and SNR_{AGG} were evaluated for three ranges of θ_s (20˚-30˚, 30˚-40˚ and 40˚-50˚), because noise levels are known to vary with solar elevation (Hu et al., 2012b). Each range of θ_s contained at least three available observations for appropriate computation of standard deviations of SNR within each group. Additionally, $L_{typical}$, L_{noise}, SNR and associated percentage noise were computed for $\theta_s = 45^{\circ} \pm 1^{\circ}$, following the method of Hu et al. (2012b). The Himawari-8 percentage noise $(\%Noise)$ at $\theta_s = 45^{\circ} \pm 1^{\circ}$ was utilised in Section 4.2 to evaluate the algorithm's sensitivity to typical input noise levels over the ocean. The $\%Noise$ was calculated as in Eq. 4.4, where the compared value is L_{noise} and the reference value is $L_{typical}$. Calculating $\%Noise$ and $L_{typical}$ for $\theta_s = 45^{\circ} \pm 1^{\circ}$ allows consistent cross-comparison of estimated $\%Noise$, SNRs and uncertainties estimated from multiple sensors (Hu et al., 2012b), which is discussed in Section 4.4.1.

$$\%Noise = \left(\frac{L_{noise}}{L_{typical}}\right) 100\% \quad \text{Eq. 4.4}$$

4.1.2 Results

The diurnal variability of the SNR computed from two sets of observations sampled at different locations and different days is shown in Figure 4.3. A few single observations were missed due to intensive cloud coverage, particularly on the 06/09/2017. Nevertheless, diurnal variations of SNR_{SING} and SNR_{AGG} were evident, with highest SNR when θ_s was the lowest (<30˚).

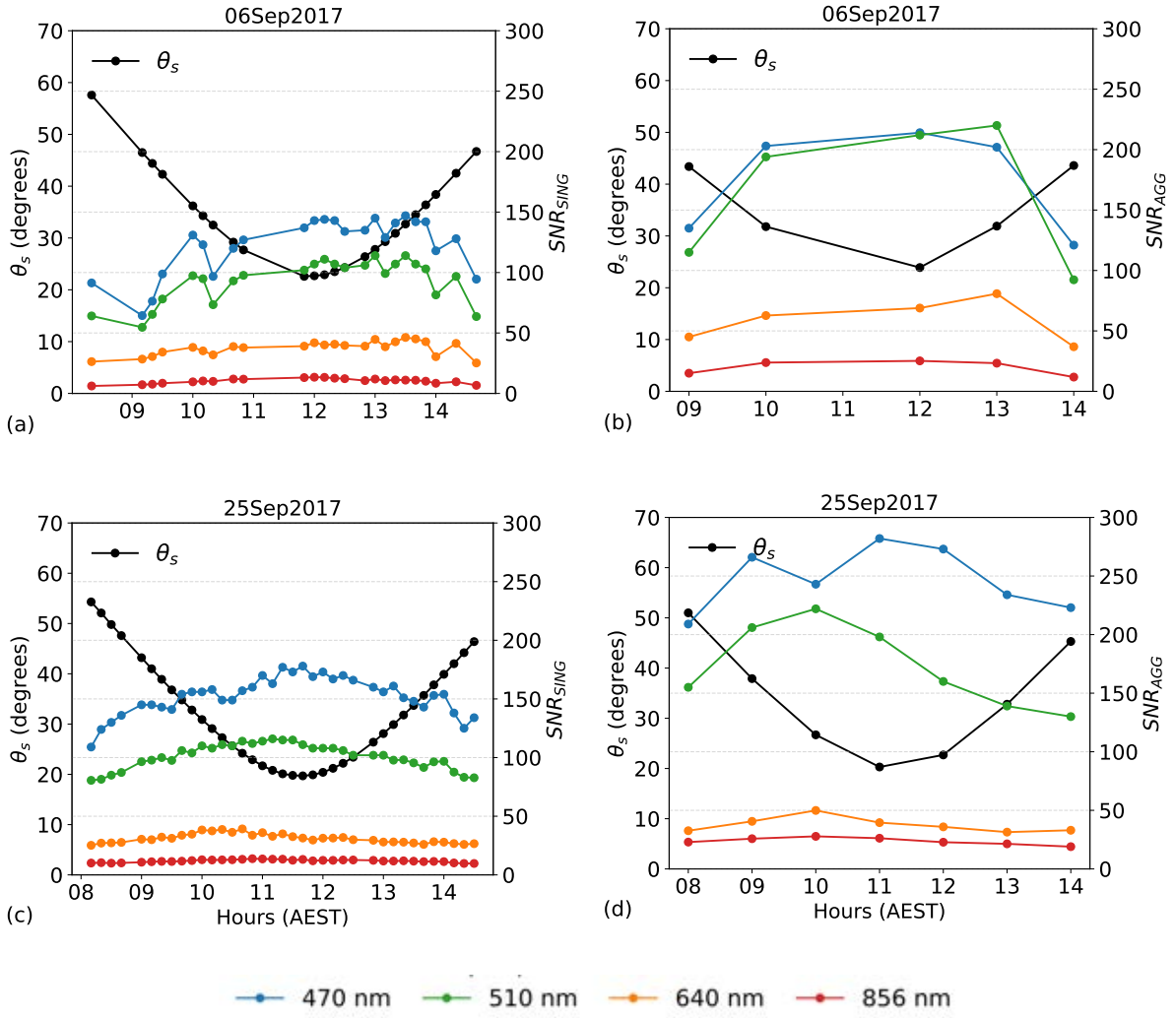

Figure 4.3: Time series of SNR (right axis) and the mean θ_s (left axis) computed for SNR_{SING} (a and c) and for SNR_{AGG} (b and d) at two different dates and locations. The SNR of each band is colour coded, where each dot marker represents SNR derived from single or aggregated observation. The time stamp of aggregated SNR and θ_s was rounded back to the nearest whole hour.

The SNR values and diurnal variability were higher for aggregated observations and at the blue and green bands (470 and 510 nm), compared to values computed for single observations. The SNR calculated for both temporal resolutions at the 640 nm and 856 nm bands were at least 3 times lower than the SNR computed for the blue and green bands, with subtle variations across a day. The diurnal fluctuations of SNR between days and locations were varied, especially for the blue band and from SNR_{AGG}. On the 06/09/2017 (mean θ_v of ~22˚), the SNR_{AGG} in the blue and green bands were similar in

magnitude (Figure 4.3b). On the 25/09/2017 (at a different location with mean θ_v ~28˚), the blue band presented SNR_{AGG} nearly twice as high as the green band (Figure 4.3d).

The spectral variability of SNR_{SING} and SNR_{AGG} is shown in Figure 4.4 for three groups of θ_s, where the standard deviations (σ) within each group were plotted as capped error bars. Only one aggregated observation was available for θ_s above 50˚, and thus its SNR was not included in the plots of Figure 4.4. A total of 61 single and 12 aggregated observations were plotted in Figure 4.4. The single observations typically yielded lower SNR than the aggregated observations in all bands, and SNR was the highest for $\theta_s < 30^{\circ}$, in agreement with the data presented in Figure 4.3. The standard deviations (σ) of SNR computed for single and aggregated observations were more pronounced for $\theta_s > 40^{\circ}$ and at the 470 nm and 510 nm bands. The SNR calculated for $\theta_s > 40^{\circ}$ at the 470 nm band presented σ of 27 and of 51 for SNR_{SING} and SNR_{AGG}, respectively, while the SNR computed for the 510 nm band presented σ of 13 and 26 for SNR_{SING} and SNR_{AGG}, respectively. These deviations are likely associated with the variable atmospheric conditions of each location, which are intensified at the blue and green bands and at high atmospheric pathlengths.

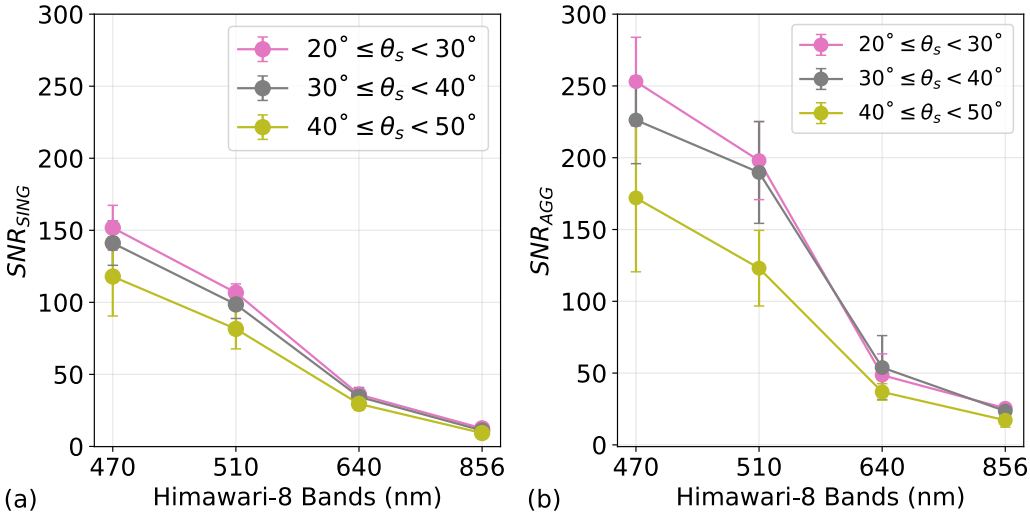

Figure 4.4: SNR_{SING} and SNR_{AGG} grouped for three ranges of θ_s. Error bars were computed as standard deviations (σ) of SNR within each group of θ_s.

The SNR_{AGG}, the $L_{typical}$ and L_{noise}, and associated percentage noise ($\%Noise$) for aggregated observations with $\theta_s = 45^{\circ} \pm 1^{\circ}$ were compiled in Table 4.1. Likewise, the SNR_{SING} computed for all single observations with $\theta_s = 45^{\circ} \pm 1^{\circ}$ and the percentage ratio ($\%Ratio$, as in Eq. 4.4) between SNR_{AGG} relative to SNR_{SING} were included. The SNR_{AGG} values compiled in Table 4.1 were twice as high as the corresponding SNR_{SING}, except at the 640 nm red band with only 18% difference. Nevertheless, the large noise levels in the red (640 nm with ~3%) and in the NIR band (~5%), indicate that the SNR_{AGG} may be mostly affected by the atmospheric signal despite the efforts in avoiding environmental

conditions in image selection. This is particularly evident at the NIR band, where the water leaving radiances are negligible in optically clear waters.

Table 4.1: Visible and near-infrared Himawari-8 bands $L_{typical}$ and L_{noise} with units $Wm^{-2}sr^{-1}\mu m^{-1}$, the associated percentage noise ($\%Noise$), SNR_{AGG} and SNR_{SING} calculated for $\theta_s = 45^{\circ} \pm 1^{\circ}$ and $\%Ratio$ of SNR_{AGG} relative to SNR_{SING}.

Band (nm)	$L_{typical}$	L_{noise}	*%Noise*	SNR_{AGG}	SNR_{SING}	$\%Ratio$
470	59.5	0.267	0.44	223	100	123%
510	38.3	0.292	0.76	130	74	74%
640	13.8	0.417	3.02	33	28	18%
865	3.42	0.180	5.26	19	8	137%

4.2 Algorithm's Sensitivity to Noisy Input Data

This section numerically assessed the TSS algorithm's sensitivity to the signal-dependent noise likely affecting the Himawari-8 bands. Additionally, the detection limits (i.e., minimum detectable amounts) of retrieving TSS with the current ANN algorithm (P094) were estimated. The latest GBR water quality guidelines suggest that annual average TSS should not exceed 2 mg L^{-1} in the inshore and mid-shelf and 0.7 mg L^{-1} in the offshore waters of the GBR (Great Barrier Reef Marine Park Authority, 2010). Based on this recommendation, the detection limits of the present TSS algorithm should be lower than 2.0 mg L^{-1} for relevant applications in the coastal GBR. Chapters 2 and 3 demonstrated that TSS below 0.1 mg L^{-1} may be consistently retrieved with significant relative errors (> 100%). However, the minimum TSS that can be accurately retrieved from Himawari-8 may be larger than 0.1 mg L^{-1}, as it has been previously suggested (Dorji and Fearns, 2018). Hence, the sensitivity and detection limits of retrieving TSS using the calculated noise levels were analysed for future applications.

4.2.1 Methods

The current TSS algorithm (P094) was trained with spectrally-flat[10] Gaussian noise (0.8%) added to the training dataset, assuming limited knowledge of sensor performance characteristics over oceanic targets. However, the noise levels calculated from Himawari-8 L_{TOA} observations (Table 4.1) are spectrally-dependent, reflecting the natural variability of the photon noise (Garcia et al., 2014; McKinna et al., 2019). To provide a baseline sensitivity analysis of the TSS algorithm, spectrally-flat photon noise of 0.1, 1.0 and 10 and 50% were added to the testing dataset. In addition, the noise associated with the Himawari-8 bands (from Table 4.1) were added to the testing dataset to elucidate the effects of spectrally-dependent noise levels on the accuracy of TSS retrievals.

[10] The spectrally-flat noise is equally added to the radiances irrespective of wavelength. Spectrally-dependent noise changes its percentage as a function of wavelength.

The simulated testing datasets (100 000 inputs) with spectrally-flat and spectrally-dependent noise perturbed L_{TOA} were recalled for TSS retrievals (P094 ANN experiment). The retrieval stability was interpreted in terms of constant increments of RMSE across a wide range of TSS (0.01 to 100 mg L^{-1}) equally spaced in logarithmic concentrations. The proportion between the retrieval RMSE to the respective RT_{TSS} (0.01, 0.1, 1.0, 10.0 and 100.0 mg L^{-1}) were calculated as a $\%Ratio$, according to Eq. 4.4, and included for each noise level. For instance, to retrieve RT_{TSS} of 0.01 mg L^{-1} with a spectrally-flat noise of 0.1%, the retrieval RMSE was of 0.03 mg L^{-1}, which is equivalent to a 300% increase to the RT_{TSS} (Table 4.2Table 4.2). Percentage ratios below 70% were regarded as good retrieval performances for TSS, following the mission targets (MAPE values) defined for Level 2 Sentinel-3 ocean colour products in Case-2 waters (Donlon, 2011).

4.2.2 Results

The outcomes of retrieving TSS (0.01 to 100 mg L^{-1}) with spectrally-flat and spectrally-dependent noise is illustrated in Figure 4.5, and results are compiled in Table 4.2. In summary, the P094 algorithm presents good performance ($\%Ratio$ < 50%) to retrieve TSS above 1 mg L^{-1}, even when 50% spectrally-flat noise is added to L_{TOA} at the Himawari-8 VNIR bands. Conversely, moderate retrieval performances ($\%Ratio$ of ~50%) were obtained for TSS > 0.1 mg L^{-1}, when adding spectrally-flat and spectrally-dependent noise, except when adding 50% of spectrally-flat noise ($\%Ratio$ of > 1000%). Meanwhile, large errors ($\%Ratio$ > 300%) were obtained for TSS retrievals below 0.1 mg L^{-1}, irrespective of noise type and level.

Table 4.2: Computed RMSE (in mg L^{-1}) and associated $\%Ratio$ for TSS retrievals between 0.01 and 100.0 mg L^{-1}. Results are shown for several levels of spectrally-flat noise (0.1 to 50%) and associated SNR (1000 to 2), and for spectrally-dependent noise computed for Himawari-8 in Table 4.1.

	RT_{TSS} *(mg L^{-1}) bins:*				
	0.01	0.1	1.0	10.0	100.0
Spectrally-flat noise:	Retrieval RMSE in mg/L $(\%Ratio)$:				
0.1% (SNR = 1000)	0.03 (300%)	0.05 (50%)	0.24 (24%)	1.73 (17%)	12.2 (12%)
1.0% (SNR = 100)	0.03 (300%)	0.05 (50%)	0.25 (25%)	1.74 (17%)	12.2 (12%)
10% (SNR = 10)	0.08 (800%)	0.05 (50%)	0.45 (45%)	2.03 (20%)	13.4 (13%)
50% (SNR = 2)	3.04 (>1000%)	1.31 (>1000%)	0.53 (53%)	5.00 (50%)	38.6 (38%)
Spectrally-dependent noise	0.03 (300%)	0.04 (40%)	0.36 (36%)	1.97 (19%)	13.0 (13%)

However, on a more realistic scenario with spectrally-dependent noise (Figure 4.5), constant increments of RMSE in logarithmic scale were only achieved for TSS above 0.25 mg L^{-1}. Thus, a detection limit of 0.25 mg L^{-1} was chosen for obtaining reliable retrievals from Himawari-8 with the current TSS

algorithm. For comparison, the detection limits of TSS retrievals computed from atmospherically corrected Himawari-8, as in Dorji and Fearns (2018), is represented in Figure 4.5 with a vertical dashed line at 0.15 mg L^{-1}.

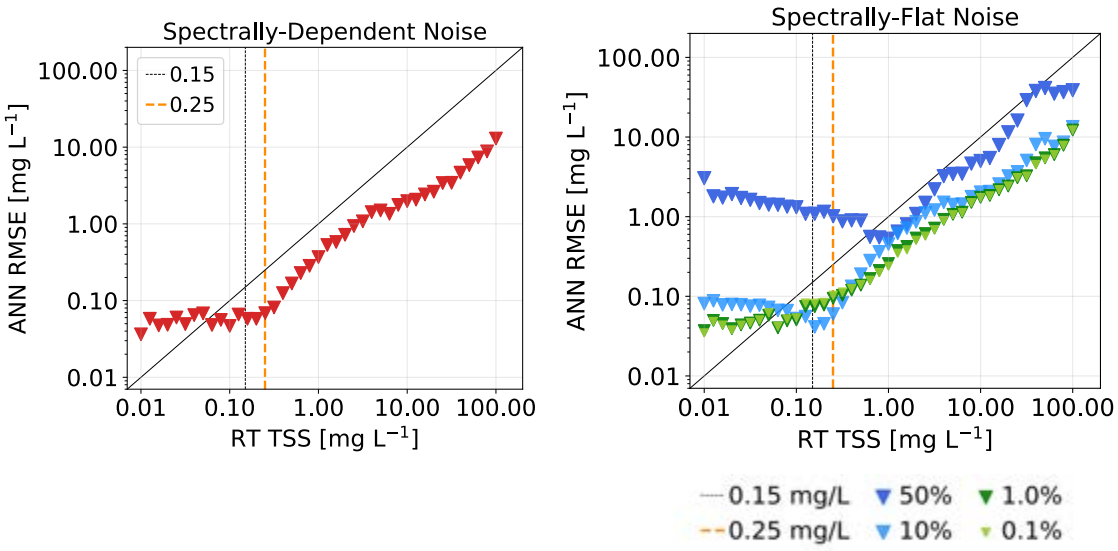

Figure 4.5: RMSE (in mg L^{-1}) retrieval errors for spectrally-dependent (left panel) and spectrally-flat (right panel) noise levels added to the simulated testing dataset at the Himawari-8 bands. Radiative Transfer (RT) TSS and RMSE values are presented in logarithmic base 10 scale. The vertical dashed line at TSS of 0.15 mg L^{-1} is the detection limit from Dorji and Fearns (2018), while the vertical dashed orange line at 0.25 mg L^{-1} is the detection limit of the present method.

4.3 Visual Analysis of Himawari-8 derived TSS products

The temporal aggregation of multiple observations within an hour increased SNR of Himawari-8 as it has been demonstrated in section 4.1 of this chapter, and suggested in the literature (Ruddick et al., 2014; Vanhellemont et al., 2014; Lavigne and Ruddick, 2018). However, sensor artefacts such as horizontal striping (along scan track) have been observed in hourly Himawari-8 CHL products (Murakami, 2016b; Japan Meteorological Agency, 2017; JAXA, 2020). In March 2016, a correction for coherent noise was implemented to improve image quality, reducing vertical or across scan track striping (Japan Meteorological Agency, 2016). In July 2017, the calibration coefficients of the VNIR bands were updated and reduced the horizontal or along scan track striping caused by incorrect calibration slopes derived from Solar Diffuser (SD) observations of Himawari-8 (Japan Meteorological Agency, 2017). Despite the calibration updates, the stripes were not completely removed and are visually detectable in derived CHL products available from July 2017 on (Okuyama et al., 2018; JAXA, 2020).

The aim of this section was to provide an integrated assessment on the spatial variability of the noise and sensor artefacts affecting Himawari-8 derived TSS for future applications in the GBR and

adjacent areas. Patterns resulting from sensor artefacts and radiometric quality, from data acquisition and processing, or from environmental noise were inspected. These patterns may be identified as vertical and horizontal stripes or unusually sharp gradients in TSS, or as a mix of randomly scattered bright and dark pixels (salt and pepper noise or granulation). In this context, the Himawari-8 derived TSS products acquired posterior to calibration updates (after July 2017) were compared to products acquired prior to updates (before March 2016). Spatial differences in noise and patterns were assessed for TSS derived from single and aggregated observations and filtering techniques were tested for noise reduction and quality improvement of Himawari-8 TSS products.

4.3.1 Methods

Himawari-8 observations scanned prior and posterior to calibration updates were selected (cloud and glint-free as possible), acquired and processed, according to section 2.4.1. The subset area included waters from the GBR and the adjacent Coral Sea (10˚S to 29˚S, 140˚E to 155˚E) for a comprehensive assessment of the spatial limitations of Himawari-8 in respect to noise and sensor artefacts over coastal and oceanic areas. The selected observations were both acquired in the same calendar month on dates prior and posterior to calibration updates (04/09/2015 and 09/09/2017). The observations were selected at identical timestamps, between 10:00 -10:50 AEST (00:00 - 00:50 UTC), to ensure compatible solar angles.

The TSS products were generated at two temporal resolutions for each date selected, namely single TSS (TSS_{SING}) and aggregated TSS (TSS_{AGG}). The TSS_{SING} maps were derived from a single Himawari-8 observation scanned at 10:00 AEST whereas TSS_{AGG} maps were generated from the average of six observations scanned between 10:00 and 10:50 AEST. TSS products ranged from 0.01 to 100 mg L^{-1}, irrespective of detection limits (0.25 mg L^{-1}) calculated in section 4.2, to allow a comprehensive assessment of the spatial limitations of the method. Each TSS product was masked for pixels over land and over the GBR reef matrix, over clouds, sun-glint (if necessary) and for pixels with ANN flags. A schematic diagram of the workflow is presented in Figure 4.7 and the visual assessment is explained in detail below.

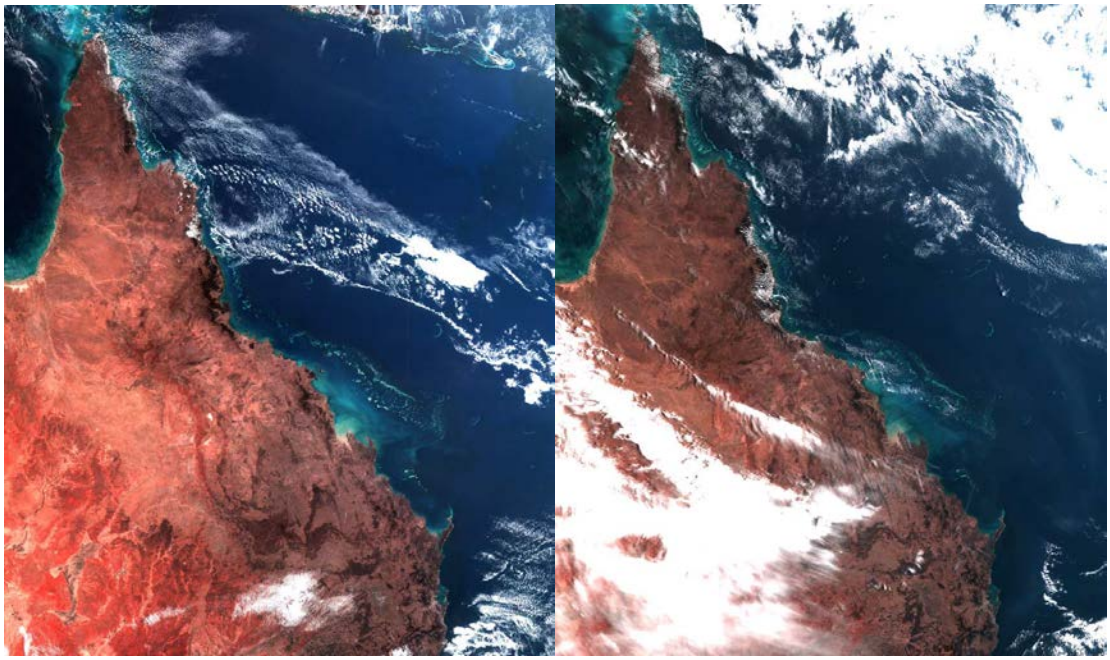

Figure 4.6: True colour imagery of Himawari-8 observations scanned at 00:00 UTC (10:00 AEST) on 04/09/2015 (left panel) and on 09/09/2017 (right panel) centred over the Great Barrier Reef and adjacent Coral Sea, including the continental area of Queensland, Australia.

First, the spatial distribution of environmental and sensor noise affecting TSS_{SING} and TSS_{AGG} products were visually identified. Then on a second step, latitudinal and longitudinal transects of mask-free TSS products taken in homogeneous waters of the coastal GBR and in the Coral Sea (Figure 4.8) were investigated for TSS products taken after updated calibration (2017). The spatial coherence of transects taken from TSS_{SING} and TSS_{AGG} products were compared at a pixel scale. Then, a histogram containing all valid (or mask-free) TSS_{SING} and TSS_{AGG} pixels were generated for a quantitative assessment of the differences between both temporal resolutions. The transects and histograms were extracted on 09/09/2017, posterior to calibration corrections. Finally, a boxcar median filter with a kernel size of 7-by-7-pixels was applied over TSS_{AGG} as a simple technique to reduce granulated noise, eliminate outliers and to improve image quality (Hu et al., 2001; Park and Park, 2021). The spatial filter was visually evaluated for a subset of TSS in open ocean and coastal waters.

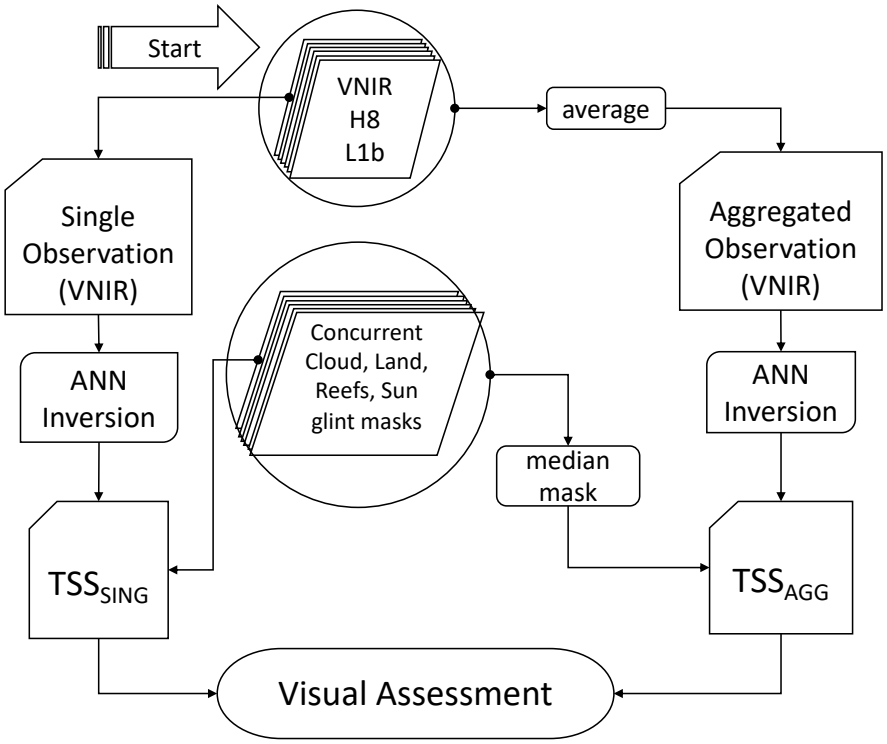

Figure 4.7: Flow diagram of Visual Assessment of noise analysis. The acronym H8 stands for Himawari-8 observations at the visible and near-infrared bands (VNIR), L1b for level 1b observations (per band), ANN for Artificial Neural Networks, TSS_{SING} for single observation-derived TSS, TSS_{AGG} for aggregated observation derived TSS.

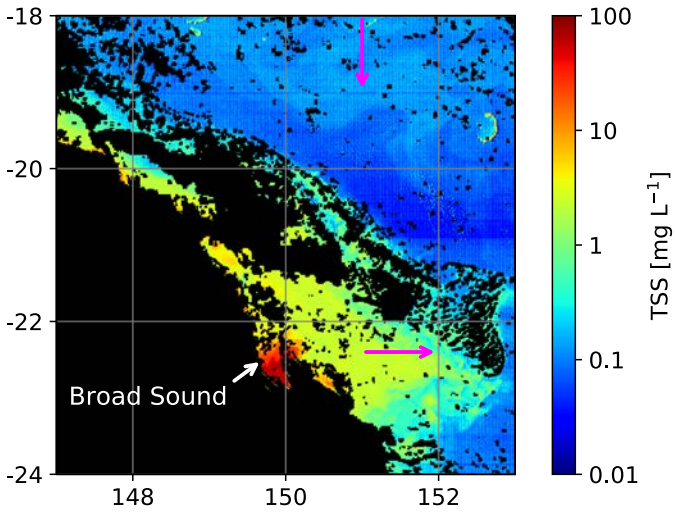

Figure 4.8: Location of latitudinal and longitudinal transects between 18˚S and 19˚S and between 150˚E and 151˚E (magenta), in the Coral Sea and coastal GBR respectively. The transects were taken from TSS_{SING} and TSS_{AGG} (this map) products on 09/09/2017 (between 10:00 and 10:50 AEST). Masked areas are marked in black, and the location of Broad Sound is indicated with white arrow for reference.

4.3.2 Results

The horizontal and vertical stripes were visually detectable at both TSS_{SING} and TSS_{AGG} (Figure 4.9), irrespective of TSS concentrations, prior to striping and coherent noise was addressed. The striping patterns were more evident in $TSS_{AGG,}$ particularly the horizontal stripe located in turbid waters (within the red circle at the top left of the image) and the vertical stripes in open ocean waters (indicated by white arrows). Nevertheless, the severe granulation observed in TSS_{SING} was noticeably reduced in TSS_{AGG}, improving visual quality of observations. Additionally, the masking of areas with persistent cloud coverage was intensified in TSS_{AGG} products, largely reducing noise at the cloud edges.

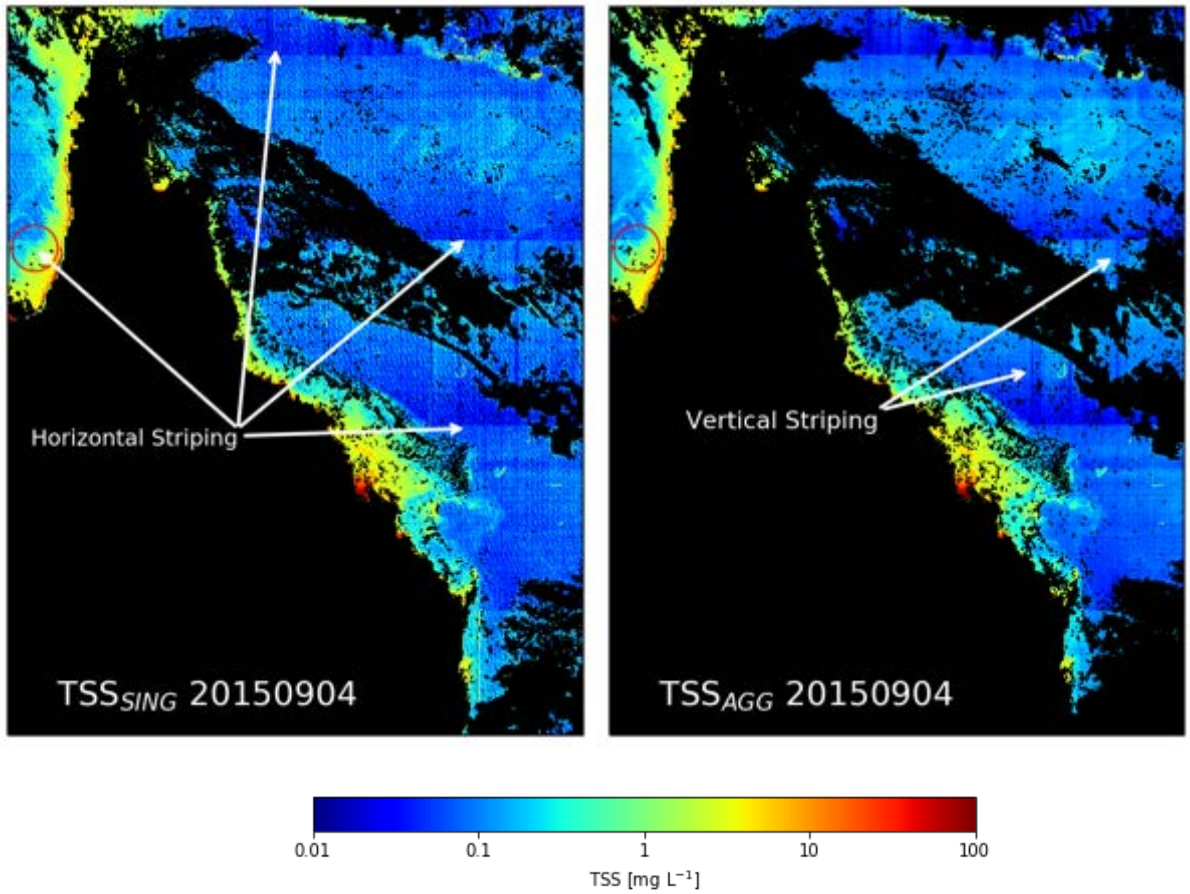

Figure 4.9: Total Suspended Solids (TSS) concentration (mg L^{-1}) derived prior to striping correction on 04/09/2015. The TSS map on the left panel was derived from a single observation acquired at 00:00 UTC (TSS_{SING}) whilst the right panel map was derived from aggregated observations between 00:00 UTC and 00:50 UTC. Clouds, sun glint, GBR reefs and land are masked in black. Horizontal and vertical stripes were identified with arrows and red circle for reference.

The maps of Figure 4.10 illustrate the TSS_{SING} and TSS_{AGG} products derived from observations acquired after calibration coefficients were corrected for striping and coherent noise (09/09/2017). The intensity of vertical and horizontal striping in more recent products was largely reduced, particularly in turbid coastal areas with TSS > ~1 mg L^{-1} (red circle). However, stripes are still evident in TSS_{SING} and TSS_{AGG} products over clear and open ocean areas (TSS < ~0.1 mg L^{-1}). Nevertheless, the open ocean

areas offshore the GBR include TSS values between 0.01 and ~0.1 mg L^{-1}, which are below detection limits of the present algorithm (0.25 mg L^{-1}) according to section 4.2.

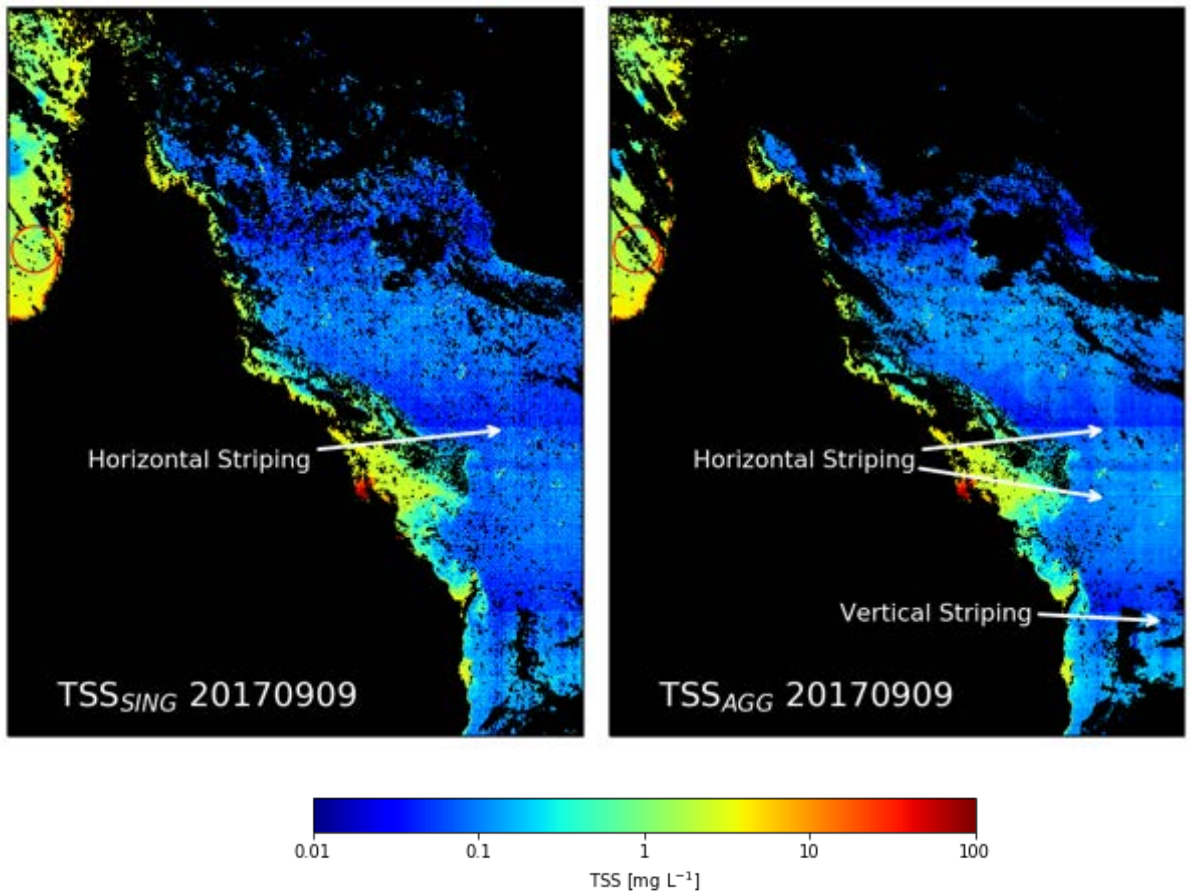

Figure 4.10: Total Suspended Solids (TSS) concentration (mg L^{-1}) derived posterior to striping correction on 09/09/2017. The TSS map on the left panel was derived from a single observation acquired at 00:00 UTC (TSS_{SING}) whilst the right panel map was derived from aggregated observations between 00:00 UTC and 00:50 UTC. Clouds, sun glint, GBR reefs and land are masked in black. The location of horizontal and vertical stripes is identified with arrows and with a red circle for reference.

The latitudinal transect sampled between 18˚S and 19˚S in the Coral Sea (Figure 4.11a) presented TSS_{SING} and TSS_{AGG} values mostly below the detection limits of the method (0.25 mg L^{-1}). However, the TSS_{SING} (blue dots) presented spikes or different orders of magnitude values occurring successively on a pixel scale (or within 1 km). As a result, TSS_{SING} differences of up to ~0.3 mg L^{-1} were observed between neighbouring pixels (indicated by plot annotations). Meanwhile the associated TSS_{AGG} (red dots) presented smoother pixel-to-pixel variations and reduced amplitude between minimum and maximum values (~0.06 mg L^{-1} difference).

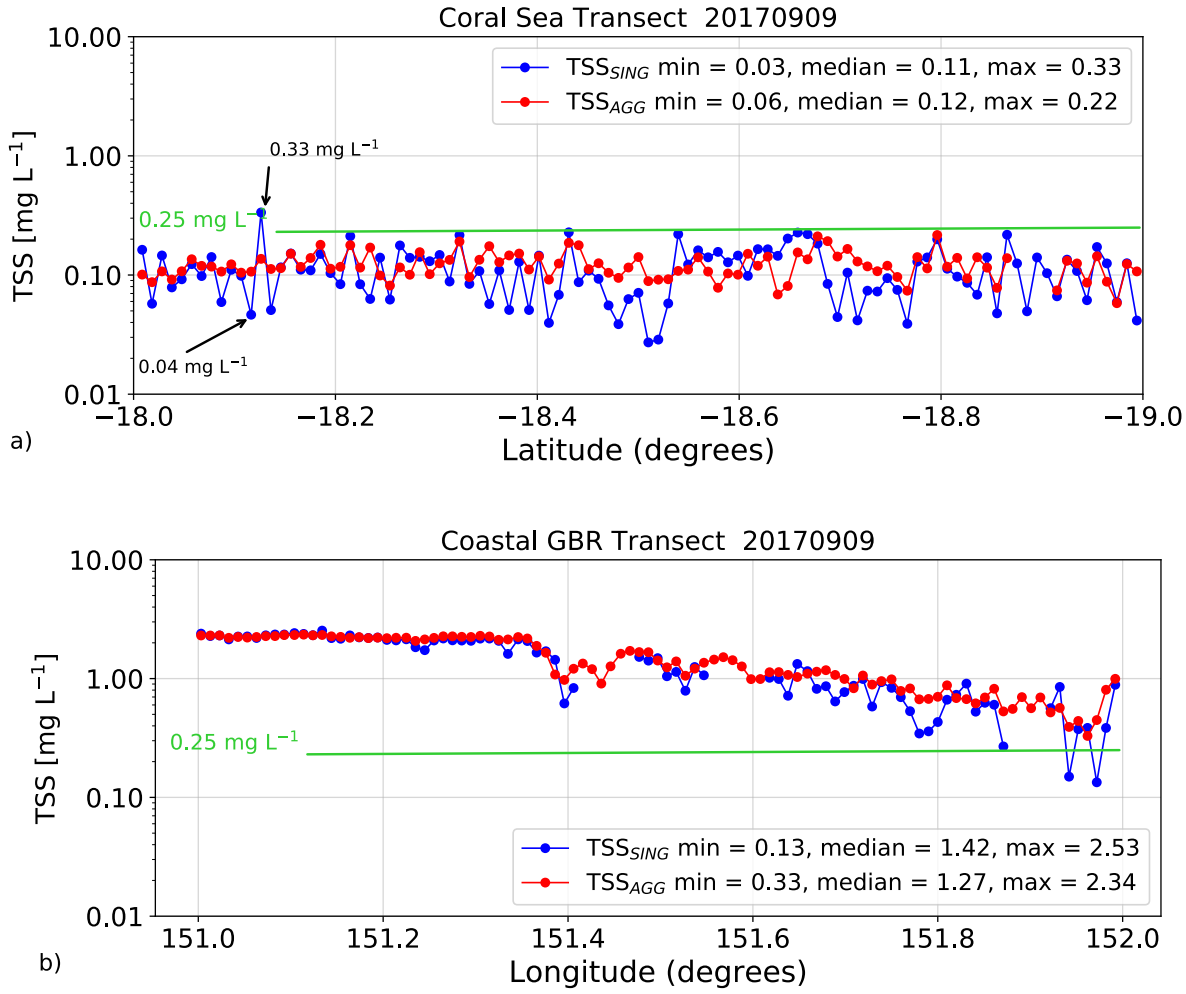

Figure 4.11: Transects of Himawari-8 derived TSS (mg L^{-1}) taken in the Coral Sea (a) and coastal GBR waters (b) respectively. The transects were derived from TSS_{SING} on 09/09/2017 at 10:00 AEST (blue dots) and TSS_{AGG} between 10:00 and 10:50 AEST (red dots). The data gaps represent pixels masked for clouds, land, sun glint or ANN flags, where appropriate. Minimum, maximum and median TSS values (mg L^{-1}) were presented for each transect. The annotated TSS (in black arrows) indicate pixel-to-pixel values and the green horizontal line represents the detection limit of the method.

The longitudinal transects of TSS_{SING} and TSS_{AGG} taken between 151˚E and 152˚E in the coastal GBR are shown in Figure 4.11b. Subtle differences were observed between TSS_{SING} and TSS_{AGG} for TSS larger than 1 mg L^{-1}. However, with increasing distance from the coast, TSS dropped below 1 mg L^{-1} and differences between TSS_{SING} and TSS_{AGG} were enhanced. Although most TSS_{SING} pixels below 1 mg L^{-1} were above detection limits (0.25 mg L^{-1}), they presented poor spatial coherency compared to their respective TSS_{AGG}. Thus, TSS_{AGG} and TSS_{SING} provide comparable results in the coastal GBR when TSS is above 1 mg L^{-1}. However, TSS_{AGG} presents better spatial coherency than TSS_{SING} for waters between the coastal GBR and the open ocean, particularly when TSS is above detection limits.

The frequency distribution of TSS values for TSS_{SING} and TSS_{AGG} products were presented in Figure 4.12, for all valid pixels sampled in the coastal GBR and Coral Sea (09/09/2017). The TSS_{SING} and

TSS_{AGG} shows a non-symmetrical log-normal distribution with central tendency around 0.1 mg L^{-1}, and secondary central tendency at around 2 mg L^{-1}. TSS_{SING} and TSS_{AGG} showed very similar distribution of values for TSS above 0.1 mg L^{-1}. However, the number of values below ~0.1 mg L^{-1}, and consequently below detection limits of the method (0.25 mg L^{-1}) were reduced about one order magnitude by utilising TSS_{AGG} products. This one order magnitude reduction in the number of pixels for TSS below 0.1 mg L^{-1} may be attributed to the improved product quality associated with aggregated observations and to the increased number of pixels masked in the TSS_{AGG} image.

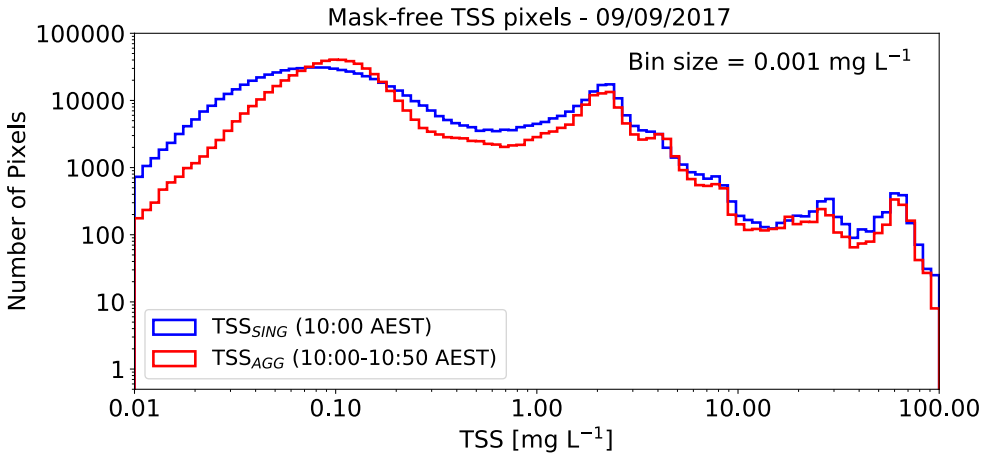

Figure 4.12: Histogram of TSS values derived from valid pixels taken from TSS_{SING} and TSS_{AGG} products on 09/09/2017. The bin size used in the plots was annotated (0.001 mg L^{-1}).

Finally, the median filter spatially smoothed TSS_{AGG} and enabled the visualisation of more detailed ocean colour features in oceanic areas while preserving coastal features such as turbid plumes (as in Broad Sound). The spatial filter removed likely outliers, such as pixels due to undetected clouds and granulated noise, which largely improved visual quality and spatial consistency of products in areas of TSS below 1 mg L^{-1}. However, the vertical and horizontal striping over the Coral Sea remained visually detectable even after spatially filtering the TSS_{AGG} product.

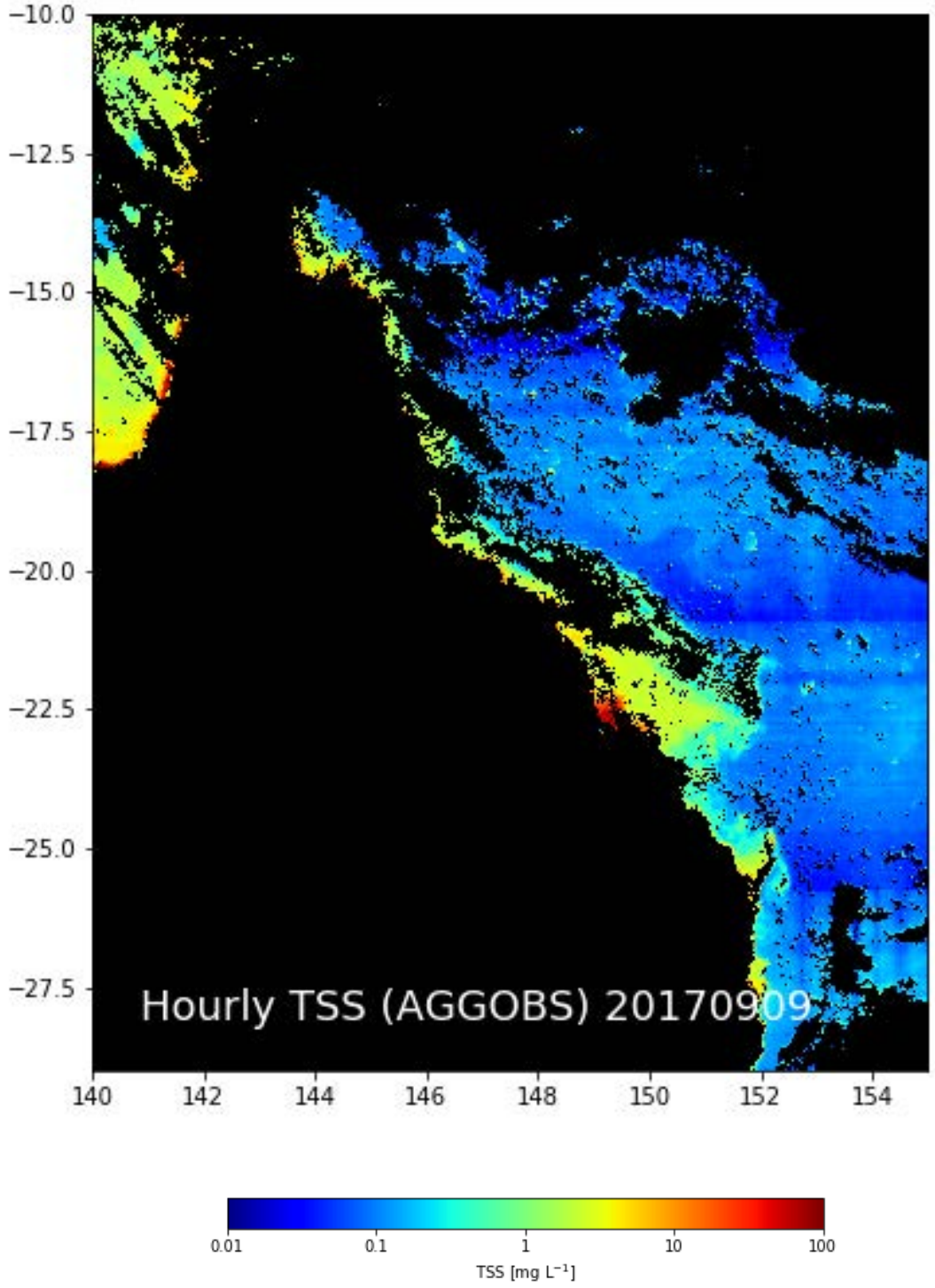

Figure 4.13: Himawari-8 derived TSS_{AGG} (mg L^{-1}) with median spatial filter applied. The observations utilised for the aggregated products were scanned between 10:00 and 10:50 AEST, on 09/09/2017.

4.4 Discussion of Detection Limits Chapter

The key objective of Chapter 4 was to characterise the limitations of retrieving TSS from Himawari-8 in the coastal GBR. First, Himawari-8 noise levels derived from both single and aggregated observations were quantitatively assessed. This was achieved by calculating the SNR for each band and investigating the detection limits of the physics-based method for the accurate retrieval of TSS in the coastal GBR. Next, a qualitative analysis of Himawari-8 derived TSS products was employed to investigate the spatial distribution of noise at both temporal resolutions.

4.4.1 Discussion of Signal-to-Noise Ratios of Himawari-8 bands

The SNR of Himawari-8 presented consistent diurnal variability with changing solar zenith angles (θ_s), especially in the blue and green bands (470 and 510 nm, respectively). This result has been previously observed from both LEO and GEO ocean colour observations (Hu et al., 2012b; Hu et al., 2012a; Dorji and Fearns, 2018; Concha et al., 2019). Although diurnal variability in SNR may also be attributed to underlying atmospheric, sea surface and biogeochemical conditions, the consistent patterns suggest that θ_s and increased atmospheric path length is a predominant influence in modulating the SNR (Concha et al., 2019).

The SNR calculated from aggregated observations were 10-100% higher than those from single observations, corroborating previous findings and recommendations (IOCCG, 2012b; Ruddick et al., 2014; Vanhellemont et al., 2014; Murakami, 2016b; Dorji and Fearns, 2018; Lavigne and Ruddick, 2018). In addition, the SNR's spectral dependence implies that a large source of input noise (3-5% in the red and NIR bands) may originate from the atmosphere in open ocean waters (Hu et al., 2012b). In the absence of biological or chemical processes, red and NIR light is predominantly and strongly absorbed by pure sea water. As a result, the open ocean water leaving signal in the red and NIR bands is usually small or overwhelmed by the atmospheric noise (Murakami, 2016b). Thus, an explicit atmospheric correction to the Himawari-8 visible bands may reduce the influence of environmental noise, improving the sensitivity to detect bio-optical changes in the ocean.

Because it is difficult to find a target area completely isolated from environmental noise, large standard deviations within groups of θ_s may be associated with the local atmospheric, sea surface state and biogeochemical conditions of each site investigated (Hu et al., 2012b; Gillis et al., 2018). In addition, differences in SNR computed between different days and locations may be associated to differing observation angles (θ_v varied by 6˚ between subsets), which may increase atmospheric path lengths. Supplementary diurnal sets of cloud-free Himawari-8 observations should be investigated for a more consistent analysis on the variability of SNR.

The sensors' sensitivity to noise largely depends on its radiometric resolution, which determines the quality of the observations and indicates the level of digitization noise, i.e., pixel-to-pixel differences (Bhatt et al., 2018). The SNR values computed for ocean colour sensors with superior radiometric resolution to Himawari-8, i.e., with more than 11 bits resolution, were at least 5 times greater than those computed here at similar $L_{typical}$ values (~61 $Wm^2sr^{-1}\mu m^{-1}$). For instance, Hu et al. (2012b) reported that the SNR of MODIS/Aqua and MERIS 443 nm band, with 12 bits resolution, were of 2225 and 1060, respectively. Himawari-8's SNR of 223 at the 470 nm band was only superior to the proof-of-concept CZCS 8-bit ocean colour sensor with SNR of 193 at 443 nm. Additionally, Himawari-8's SNR of 223 at 470 nm was largely superior to the SNR of sensors designed for land applications, such as Landsat TM and ETM (SNR=78 at 483 nm with 8 bits) (Hu et al., 2012b).

Therefore, Himawari-8 provides inferior SNR compared to past and currently operational ocean colour sensors (Hu et al., 2012b), and its sensitivity is far below minimum requirements for ocean colour applications, particularly over Case 1 waters (IOCCG, 2012b, a). However, due to Himawari-8's moderate radiometric resolution of 11 bits or 2048 levels, the VNIR bands are less likely to saturate over bright targets, such as clouds (Hu et al., 2012b). Thus, Himawari-8 VNIR bands may yield enough sensitivity to provide a reasonable level of discretization over extremely turbid coastal waters with TSS up to 100 mg L^{-1} with the present method. Additionally, Himawari-8's SNR could be further increased with the aggregation of all observations available during a day (Murakami, 2016b), providing nearly cloud-free daily observations across the entire GBR. However, a daily image would be insufficient to adequately resolve coastal water quality processes, such as those linked with tidal variability, and would only be useful to investigate trends and patterns in Case 1 waters, which is out of the scope of this thesis.

4.4.2 Discussion of the Algorithm's Sensitivity to Noisy Inputs

Estimating TSS lower than 0.25 mg L^{-1} is certainly below the detection limits of the present one-step inversion algorithm for Himawari-8. The absence of an explicit atmospheric correction procedure may be associated with the algorithm limitations. For instance, Dorji and Fearns (2018) retrieved TSS with atmospherically corrected Himawari-8 10-minute observations and found the lower detection limit to be around 0.15 mg L^{-1}. Neukermans et al. (2009) derived TSS from the Spinning Enhanced Visible and InfraRed Imager (SEVIRI) meteorological sensor onboard METEOSAT geostationary satellite. Retrieval uncertainties exceeded 200% for TSS below 1 mg L^{-1} and errors were associated with radiometric noise, digitization effects and imperfect atmosphere correction (Neukermans et al., 2009). Therefore, the limitations of deriving TSS from Himawari-8 with an implicit atmospheric correction were reasonable compared to those methods employing an explicit atmospheric correction. Nevertheless, it

is possible that an explicit atmospheric correction may largely benefit TSS retrievals in moderate to clear waters (< 1 mg L^{-1}, Figure 4.5), further improving the present method.

Finally, the algorithm detection limit of 0.25 mg L^{-1} is within the water quality guideline threshold value of 2 mg/L for open coastal and mid-shelf waters, as well as 0.7 mg L^{-1} for offshore waters (Great Barrier Reef Marine Park Authority, 2010). To put the present result in perspective, the detection limits of *in situ* TSS measured with the gravimetric method is ~0.4 mg L^{-1}, for AIMS and CSIRO. This would mean that for an *in situ* TSS of 2 mg L^{-1} in the coastal GBR, the associated measurement uncertainty is nearly twice as the detection limit of TSS obtained with the present algorithm (Table 4.2).

Relative uncertainties of the gravimetric method have been associated with the measurement protocol employed by different laboratories, which include differences in filter types, operator bias, salt rinsing, etc. (Neukermans et al., 2012a; Röttgers et al., 2014). For instance, salt crystals trapped in the glass fibre filters largely affect TSS measurements and salt should be removed by rinsing the filtration apparatus (Tilstone et al., 2002; Stavn et al., 2009). Yet, errors as large as 30% have been obtained employing different salt rinsing techniques, hindering the accurate determination of TSS lower than 1 mg (Tilstone et al., 2002). Therefore, the detection limits and relative uncertainties of *in situ* measurements and Himawari-8 derived TSS are comparable for the present study. This result suggests that Himawari-8 offers an opportunity to accurately monitor diurnal variability of water quality in the coastal GBR, for TSS between 0.25 and 100 mg L^{-1}.

4.4.3 Discussion of the Visual Analysis of Himawari-8 derived TSS products

Himawari-8 derived TSS products were inspected at 10-minutes (TSS_{SING}) and from hourly aggregates (TSS_{AGG}) for a comparative analysis of image quality. In general, a systematic horizontal striping, with size generally corresponding to individual horizontal scans (500 km), was visually detected in the present Himawari-8 observations and derived TSS products at both temporal resolutions. The striping was clearly identified by unusually sharp gradients of TSS, spanning one order of magnitude within a few kilometres in the open ocean. The latitudinal stripes were previously identified by Murakami (2016a) in 8-day composite Himawari-8 derived CHL maps. The striping resulted from differences in detector-to-detector calibration slopes derived from solar diffuser observations of the visible bands (Okuyama et al., 2018; Japan Meteorological Agency, 2020). Although the calibration coefficients were corrected for post-July 2017 observations, the horizontal striping patterns were still present in derived TSS below 1 mg L^{-1}. This result suggests that Himawari-8 observations acquired posterior to calibration corrections (July 2017) are more suitable for TSS retrievals in the coastal GBR than observations acquired prior to calibration updates. Nevertheless, striping correction needs to be addressed for appropriate ocean colour investigations with Himawari-8 observations in open ocean areas, which is not the focus of this study.

Additionally, severe granulation was observed in TSS products derived every 10-minutes, potentially associated with the low radiometric performance of the Himawari-8 sensor over water targets (Murakami, 2016b; Dorji and Fearns, 2018). However, the visual noise was largely reduced by temporal integration of several individual Himawari-8 observations or products into hourly derived TSS, as previously suggested (Vanhellemont et al., 2014; Murakami, 2016b; Lavigne and Ruddick, 2018). Fortunately, granulated noise was visually undetectable in coastal and moderately turbid waters (TSS above 1 mg L^{-1}) either from 10-minute or from hourly TSS products. This result may be associated with the increased backscattering of suspended particles, which leverages the water-leaving radiance and thus, the signal to noise of the image (Moses et al., 2012). Consequently, Himawari-8 derived TSS is more likely to be accurately observed over moderately turbid coastal waters than from the open ocean, corroborating the detection limits analysis (Section 4.2).

The visual analysis was supported by latitudinal and longitudinal transects of TSS extracted in homogeneous waters of the coastal GBR and in the Coral Sea. The pixel-to-pixel variations in open ocean areas (TSS < 0.25 mg L^{-1}) were likely related to the granulated patterns observed with visual inspection, due to the low sensitivity of the Himawari-8 sensor at 10-minute resolution. Noise-related uncertainties in TSS_{SING} below 0.25 mg L^{-1} were largely reduced in TSS_{AGG}, corroborating the previous analysis on Himawari-8 sensitivity (SNR) and visual inspection. Conversely, improved spatial coherency was observed in the coastal GBR transect for TSS above 1 mg L^{-1}. As a result, Himawari-8 10-minute derived TSS can be utilised with as much confidence as TSS derived from hourly aggregated observations in coastal areas. Obtaining TSS at every 10-minutes in the coastal GBR improves the discrimination of rapid-changing water quality fluctuations within an hour. However, utilising hourly aggregates improves coverage of pixels potentially affected by clouds and cloud shadows, which can help eliminate outliers and increase accuracy of TSS products. Further visual noise reduction was observed in the Coral Sea after the employment of a spatial median filter on hourly aggregated TSS products. Despite spatial filtering may be useful to eliminate outliers due to undetected clouds and environmental noise, deriving TSS with Himawari-8 in open ocean waters is not recommended due to the persistent noise levels associated with image artefacts and detection limits of the present method.

Chapter 5: Applications to Water Quality Monitoring in the Great Barrier Reef

The diel cycles of solar irradiance and coastal processes such as tides and winds regulate the fluctuations of key water quality parameters in the GBR, including of phytoplankton biomass and particle composition (Furnas et al., 2005; Oubelkheir et al., 2006; Blondeau-Patissier et al., 2009; Soja-Woźniak et al., 2019). However, the coastal water quality fluctuations are additionally affected by significant flood plume intrusions, particularly evident during wet-season (Devlin et al., 2015b; Petus et al., 2019), often covering the effects of diurnal processes (Ametistova, 2004; Oubelkheir et al., 2014). Therefore, there is a real need to monitor the state of water quality on a diurnal scale for a more complete understanding of baseline conditions and trends in the GBR (Steven et al., 2014; Great Barrier Reef Marine Park Authority, 2019a). In this context, a comprehensive and continuous monitoring system is imperative to effectively assess coastal water quality and its compliance to environmental regulations and management interventions in the GBR (State of Queensland and Commonwealth of Australia, 2018b).

The Himawari-8 TSS products provide the possibility to investigate synoptic fluctuations of coastal water quality from 10-minutes to hourly temporal resolution and beyond. Such high temporal frequency may surpass current observational capabilities and provide significant advances for quantifying and monitoring coastal water quality in the GBR (Petus et al., 2019; Gruber et al., 2020; Australian and Queensland Governments, 2020). Moreover, diurnal optical properties from ocean colour remote sensing may be assimilated for refined parameterization and validation of biogeochemical models and deepen our understanding of water quality impacts to ecosystems (Jones et al., 2016; Skerratt et al., 2020; Baird et al., 2020).

This chapter aims to demonstrate the usefulness of Himawari-8-derived TSS for investigating diurnal to seasonal scale water quality fluctuations in the GBR. As pointed out in Chapter 4, the developed and validated CHL and YEL products were not explored for applications in this thesis. First, Himawari-8 derived TSS products were compared to continuous optical properties and oceanographic variables measured *in situ* to assess their temporal coherency; Second, Himawari-8 derived TSS products were employed for the detection of spatiotemporal patterns of water quality to demonstrate its capability for prospective monitoring and management of the GBR system.

5.1 Diurnal Variability of Total Suspended Solids

In this section, the diurnal variability of TSS was investigated from Himawari-8 observations and from *in situ* measurements at the Lucinda Jetty Coastal Observatory (LJCO – 18.5˚S, 146.4˚E). The LJCO facility is located in the enclosed coastal waters of the central GBR, about 12 km from the Herbert River mouth (Figure 5.1). Water quality fluctuations at LJCO are strongly associated with the hydrodynamics of the Hinchinbrook tidal channel, which periodically drains a large mangrove area and the Herbert River (Wolanski et al., 1990; Soja-Woźniak et al., 2019). Semi-diurnal tides, wind driven circulation, interannual and seasonal fluctuations of freshwater discharge largely affect the seaward advection and evolution of the Herbert River plume (plume, hereafter) (Wolanski et al., 1990; Burrage et al., 2002).

Figure 5.1: True colour composite of Sentinel 2 (MultiSpectral Instrument) observations at 10 meters spatial resolution, taken on 25/03/2017, during wet season. The Lucinda Jetty Coastal Observatory (LJCO) is located at the end of the 5.7 km long jetty, about 12 km from the Herbert River mouth. Image courtesy of the European Space Agency (ESA).

The plume can fully develop during a complete tidal cycle, and waters with TSS up to ~200 mg L^{-1} may reach the LJCO facility and the mid-shelf reefs within an hour or less, particularly during wet season floods (Wolanski et al., 1981; Devlin et al., 2001; Ametistova, 2004; Ametistova and Jones, 2005; Soja-Woźniak et al., 2019). The rapid development of the plume is illustrated in the 5-minute snapshots of Figure 5.2, captured by a webcam installed at the LJCO facility on 24/02/2021. The plume of Figure

5.2 reached LJCO approximately 4 hours before the lowest tide (2 p.m.), after 250,000 ML/day were discharged in the Herbert River catchment (Queensland Government, 2021). The discharge followed a typical wet season week of intensive accumulated rainfall above 400 mm (Bureau of Meteorology of Australia, 2021b). In the absence of floods, TSS values can range from ~0.9 to 45 mg L^{-1} in the waters surrounding LJCO, depending on the tidal phase and local winds (Ametistova, 2004; Soja-Woźniak et al., 2019).

The contrasting optical features between the brown plume and the green-blue coastal waters at LJCO are also detectable from airborne surveys and from remote sensing observations (Burrage et al., 2002; Devlin and Schaffelke, 2009; Soja-Woźniak et al., 2019), as shown in image of Figure 5.1. Quantitative and qualitative information about the plume evolution is now available from the 10-minute Himawari-8 observations and TSS algorithm developed and validated in this study. Meanwhile, continuous *in situ* measurements of subsurface bio-optical properties, such as the backscattering and turbidity, have provided a quantitative overview of the diurnal water quality changes experienced at LJCO (Soja-Woźniak et al., 2019). In addition, fortnightly *in situ* TSS measurements have been acquired at LJCO for water quality monitoring and ocean colour validation activities. Although the fortnight *in situ* TSS measurements are temporally sparse for diurnal water quality assessments, they provide sufficient data for modelling its relationship to the bio-optical quantities and for deriving continuous TSS at LJCO (Soja-Woźniak et al., 2019). Continuous TSS measurements computed from bio-optical data allow the near-real time comparison with Himawari-8-derived TSS for an integrated assessment of their temporal coherency.

In this section, the temporal correlation between diurnal TSS obtained from Himawari-8 observations and TSS computed from bio-optical measurements at LJCO were investigated. To a lesser extent, the local mechanisms potentially driving the diurnal variations of TSS were examined. The objective was to demonstrate the applicability and advantages of utilising Himawari-8 for a comprehensive understanding of local fluctuations of TSS and its relationship with underlying coastal processes.

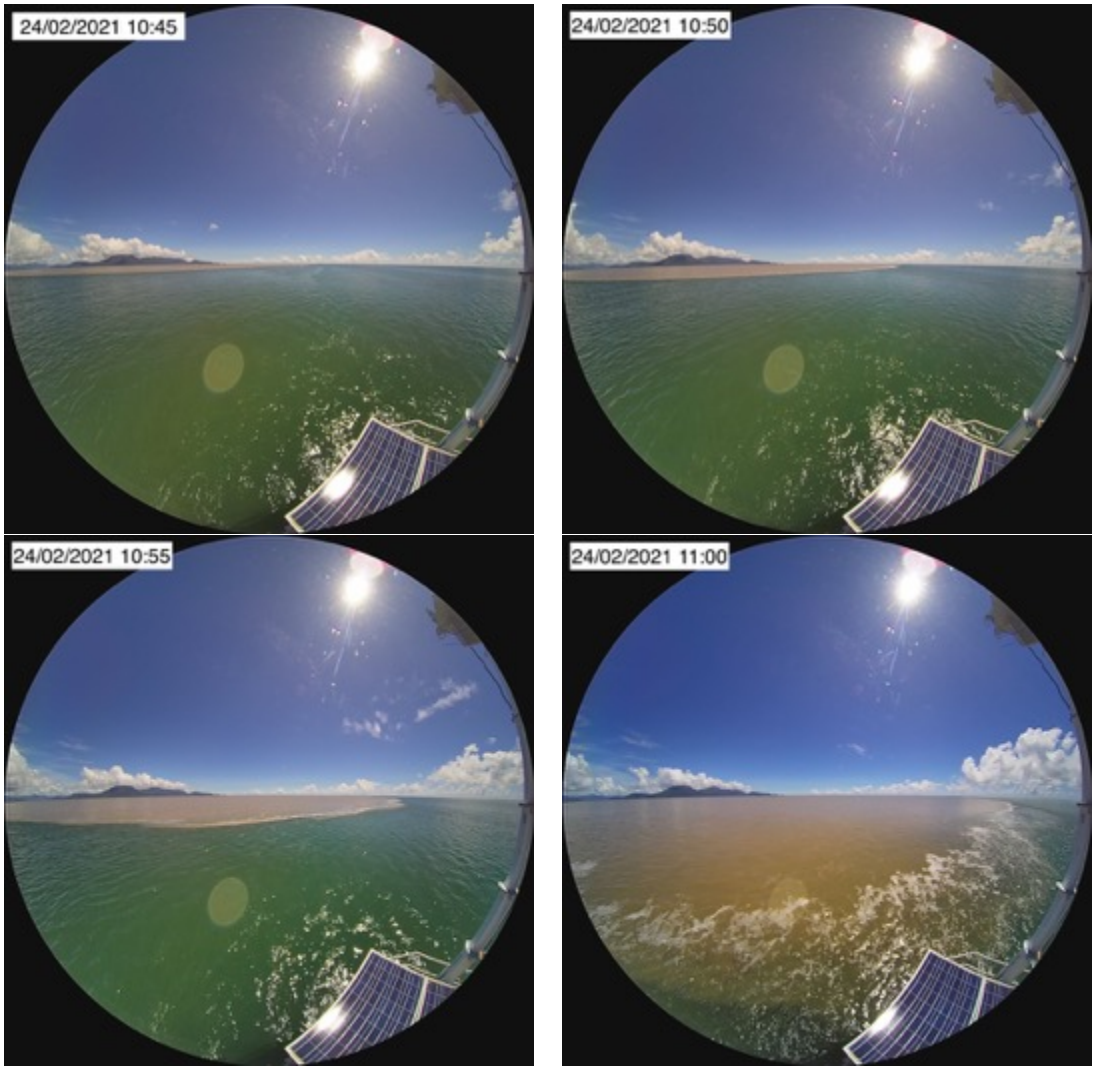

Figure 5.2: Every 5 minutes near-real time snapshots () of the Herbert River plume reaching the LJCO facility on the 24/02/2021, between 10:45 a.m. and 11:00 a.m. (AEST). The snapshots are continuously captured by a webcam installed at the top of the LJCO facility, facing north to the Hinchinbrook Island. Image courtesy of Thomas Schroeder.

5.1.1 Methods

The particulate backscattering coefficient (b_{bp}) has been recognised as a surrogate for particulate matter or TSS estimates, based on empirical formulations set up by Babin (2000); Babin et al. (2003b). The linear relationship between TSS and b_{bp} present reasonable correlations despite limitations of both measurement methods (Boss et al., 2009; Soja-Woźniak et al., 2019). Soja-Woźniak et al. (2019) derived a highly correlated relationship between the daily averages of b_{bp} (595 nm) and gravimetric TSS, from 34 pairs of measurements collected between 2014 and 2016 at LJCO. This relationship was reviewed here, utilising a larger dataset (2014 to 2019) of nearly concurrent *in situ* measurements of b_{bp}(595 nm) and of gravimetric TSS at LJCO. Then, continuous TSS computed from

b_{bp} measurements were compared against concurrent Himawari-8 TSS at 10-minutes temporal frequency in a time series analysis.

5.1.1.1 Modelling the Total Suspended Solids from Particulate Backscattering data

The continuous (every second) b_{bp} (595 nm) data was acquired at LJCO with the WET Labs ECO-BB9 instrument deployed at 3 meters depth. A rolling median (5 minutes window) filter was applied to eliminate potential noise-related outliers (illustrated in Figure 5.3), whilst preserving rapid optical changes within a 10 minute window.

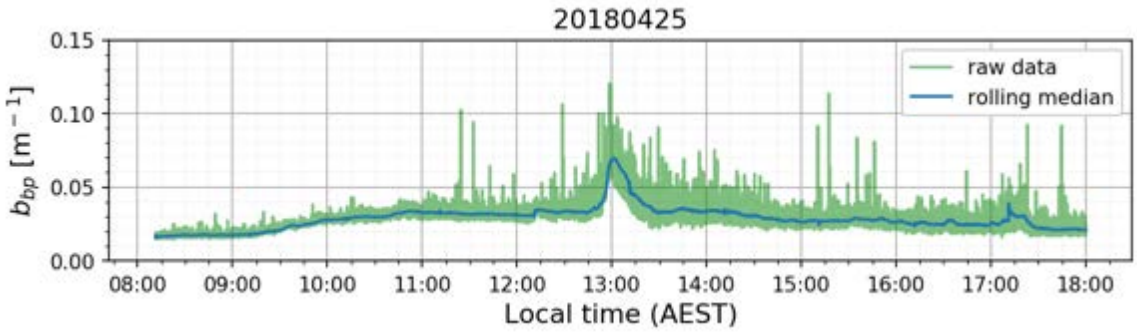

Figure 5.3: Time series of calibrated BB9 measurements of particulate backscattering coefficient (b_{bp}) at 595 nm (green) and the associated rolling median b_{bp} (with window of 5 minutes - blue line) extracted on 06/09/2017 local time (AEST).

Fortnightly maintenance activities are scheduled for bio-fouling cleaning of the optical instruments and *in situ* sampling of water quality parameters (i.e., TSS, CHL, YEL) at LJCO. To avoid potential contamination due to biofouling of the BB9 instrument, the b_{bp} measurements utilised here were acquired posterior to equipment cleaning and redeployment. As a result, the time difference between the closest available b_{bp} to the gravimetric TSS sample was variable, generally within 3 hours. Each selected pair of measurements were carefully inspected to reduce uncertainties associated with the temporal mismatch between b_{bp} and TSS. A linear relationship between near-concurrent pairs of gravimetric TSS and closest available b_{bp} (595 nm) was employed, based on Soja-Woźniak et al. (2019) (Figure 5.3 and Eq. 5.1). The *in situ* measurements of TSS ranging from 1.3 to 22.8 mg L^{-1} yielded a positive correlation (R^2 = 0.79) to b_{bp} between 0.005 and 0.17 m^{-1}.

$$\mathrm{TSS} = 117.94\, b_{bp} + 0.83 \qquad \text{Eq. 5.1}$$

The b_{bp} versus TSS relationship calculated in this study (black dashed line in Figure 5.3) was comparable to the relationships previously calculated for the GBR waters and elsewhere (Blondeau-Patissier et al., 2009; Zhang et al., 2010; Soja-Woźniak et al., 2019). For instance, the Soja-Woźniak et al. (2019) relationship (dashed green line) was calculated from 34 pairs of *in situ* TSS and daily

aggregated measurements of b_{bp} (595 nm) at LJCO, with the largest fraction of particles being of inorganic origin. Conversely, Blondeau-Patissier et al. (2009), presented a moderate relationship (dashed blue line - Figure 5.3) utilising 103 concurrent pairs of *in situ* b_{bp} (at 555 nm) and TSS sampled in several sites within the GBR lagoon during wet and dry seasons. However, despite all slopes of Figure 5.3 were being calculated for TSS roughly between 0.01 to 25 mg/L, the Blondeau-Patissier et al. (2009) relationship largely deviated from those in Figure 5.3. This result is likely related to the wide range of b_{bp} values Blondeau-Patissier et al. (2009) found in the coastal GBR (up to 1.18 m^{-1}), which is one order magnitude larger than the maximum b_{bp} value recorded here (~0.17 m^{-1}). Moreover, b_{bp} is slightly wavelength dependent and slopes calculated for b_{bp} at 555 nm may display small differences compared to those developed for b_{bp} at 595 nm.

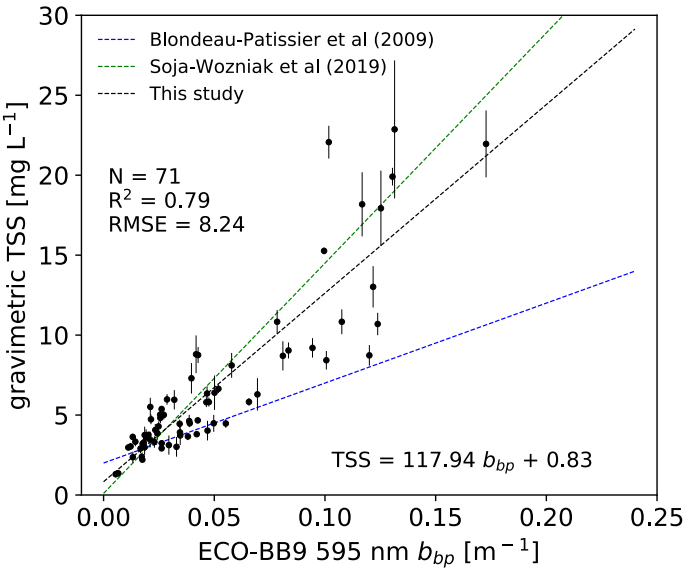

Figure 5.4: Scatterplot and computed linear relationship between gravimetric TSS and nearly concurrent ECO-BB9 b_{bp} (595 nm) measured at LJCO between 2014 and 2019. The dashed lines represent the relationship computed in the present study (in black) and in the works of Blondeau-Patissier et al. (2009) and Soja-Woźniak et al. (2019) (blue and green, respectively). The error bars were computed from the standard deviations of *in situ* triplicate gravimetric TSS.

5.1.1.2 Time Series of Total Suspended Solids at LJCO

The relationship computed in section 5.1.1.1 was applied to ECO-BB9 diurnal measurements of b_{bp} (at 595 nm) for deriving continuous *in situ* TSS (hereafter $TSS_{b_{bp}}$). The computed $TSS_{b_{bp}}$ time series were sampled every 10 minutes for comparison against concurrent Himawari-8-derived TSS (hereafter TSS_{H8}). A minimum of 4 hours of cloud-free TSS_{H8} products were required for a comprehensive analysis of diurnal variability within a semi-diurnal tidal cycle (Ruddick et al., 2014). The time series of concurrent $TSS_{b_{bp}}$ and of TSS_{H8} were extracted at the end of the 2017-2018 wet season, on the 25th and 26th of April (namely April #1 and April #2, respectively) and on the 11th and 12th of May

(namely May #1 and May #2, respectively) of 2018. The 10-minute H8-TSS products were masked for clouds, land, sun glint and ANN flags, and spatially smoothed with a boxcar median filter (7-by-7-pixel box) to eliminate any potential outliers due to undetected clouds or random noise features. Then, the median and standard deviation of all valid pixels within a 3-by-3-pixel subset centred at LJCO (18.5˚S, 146.4˚E) were extracted from each TSS_{H8} product. A temporal rolling median with window of 20 minutes was applied to the TSS_{H8}time series to fill in data gaps due to potentially masked subsets, without overly smoothing TSS fluctuations.

The H8-TSS and $TSS_{b_{bp}}$time series were visually compared, and their local maxima computed for assessment of temporal coherency. The TSS diurnal variability (ΔTSS in mg L^{-1} in Eq. 5.2) at LJCO was calculated from $TSS_{b_{bp}}$and from TSS_{H8} every 10 minutes for comparison. The ΔTSS of each pixel was calculated as the absolute difference between the minimum and maximum TSS of a given location (in this case, at LJCO) within a day of observations. The i in Eq. 5.2 denotes the index of the location where the time series of TSS values was extracted.

$$\Delta TSS^i = \left|\min\left(TSS^i\right) - \max(TSS^i)\right| \qquad \text{Eq. 5.2}$$

A linear correlation between the TSS_{H8} and $TSS_{b_{bp}}$ was computed for statistical assessment of their temporal coherency. The coefficient of determination (R^2), the root mean squared errors (RMSE) and the mean absolute percentage error (MAPE), described in section 3.1.5, were utilised.

5.1.1.3 Supplementary Observations

The concentration of non-algal particulate matter (NAP in mg L^{-1}) derived from daily MODIS-Aqua observations (MODISA-NAP) were utilised as a proxy of TSS and plotted in time series for inter-comparison. The MODISA-NAP products were accessed through the Marine Water Quality Dashboard (2020) data portal and details of the product are available in the eReefs Marine Water Quality Dashboard (2014) data processing specification. In addition, the overpass timing of Sentinel-3 (A and B) satellite sensors were extracted from European Space Agency Validation Data Centre (2020) online tool and overlayed in time series to illustrate the temporal superiority of Himawari-8 for diurnal assessments. The Sentinel satellites, launched between 2016 (3A) and 2018 (3B), are positioned in the same orbital plane but 140˚ apart (Clerc et al., 2020; Lamquin et al., 2020; European Space Agency, 2021). Each Sentinel-3 carries the OLCI (Ocean and Land Colour Instrument) sensor, acquiring ocean colour observations of the same location at every one or two days.

The April and May time series were recorded after a low-pressure atmospheric system passed through the Herbert River catchment area in March 2018, leaving over 800 mm of total accumulated rainfall within a month (Bureau of Meteorology of Australia, 2021a). Dataset on the volume of

freshwater discharged by the Herbert River was acquired from the Queensland Government Water Monitoring Information Portal (Queensland Government, 2021) to investigate the influence of catchment runoff on TSS fluctuations. Daily mean discharge levels in Megalitres per day (ML/day) were acquired from the Herbert River gauge station at Ingham (Site n° 116001F at -18.63°S, 146,14°E), 30.5 km from the stream mouth. During the November 2017 to April 2018 wet season, the Herbert River experienced the 5th major discharge event since 2010 (Figure 5.5a). The peak of freshwater discharge, with 500,000 ML/day, occurred in mid-March (Figure 5.5b) with a second peak of 300,000 ML/day in late-March. In early April, up to 50,000 ML were discharged per day (Figure 5.5b), indicating a residual flow of freshwater from the prevailing weeks of intense rainfall. However, discharge levels dropped below 6,000 ML/day for the April and May time series dates, as described in Table 5.1.

Table 5.1: Mean daily discharge levels (ML/day) for the Herbert River during the days investigated.

Date	*Mean Daily Discharge (ML/day)*
April #1: 25/4/18	5719.60
April #2: 26/4/18	5397.16
May #1: 11/5/18	3523.68
May #2: 12/5/18	3391.72

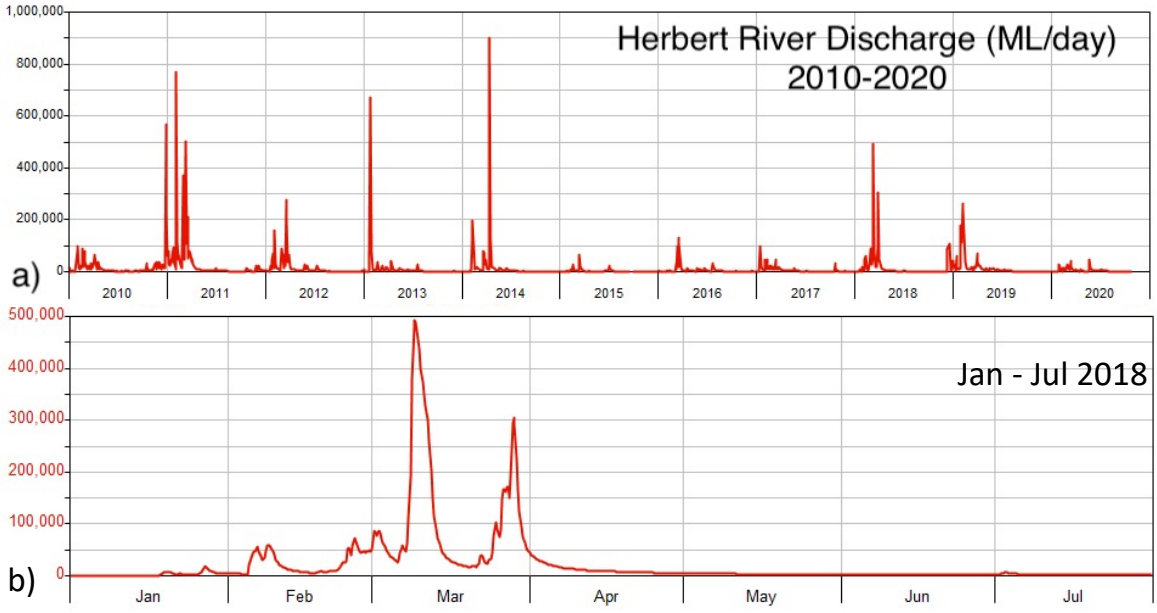

Figure 5.5 Herbert River daily mean discharge levels between 2010 and 2020 (a) and between January to July 2018 (b). Figure extracted from the Water Quality Information Portal (Queensland Government, 2021).

Above-water webcam snapshots at the LJCO facility (facing Hinchinbrook Island) were inspected to aid the interpretation of the time series. The 5-minute interval snapshots display the arrival of riverine plume waters at LJCO, for April and May time series (Figure 5.6). The estimated TSS_{H8}

median and standard deviation values were extracted from a 3-by-3-pixel box centred at LJCO and annotated in snapshots for the time of arrival of the plume. The timing of plume arrival, as identified by inspection of webcam images, was annotated in each time series plot (Figure 5.7) for comparison. In addition, the hourly tidal height measured at the Lucinda jetty by the Maritime Safety Queensland (2020), was overlaid to the time series to investigate the potential of tidal influences on TSS fluctuations.

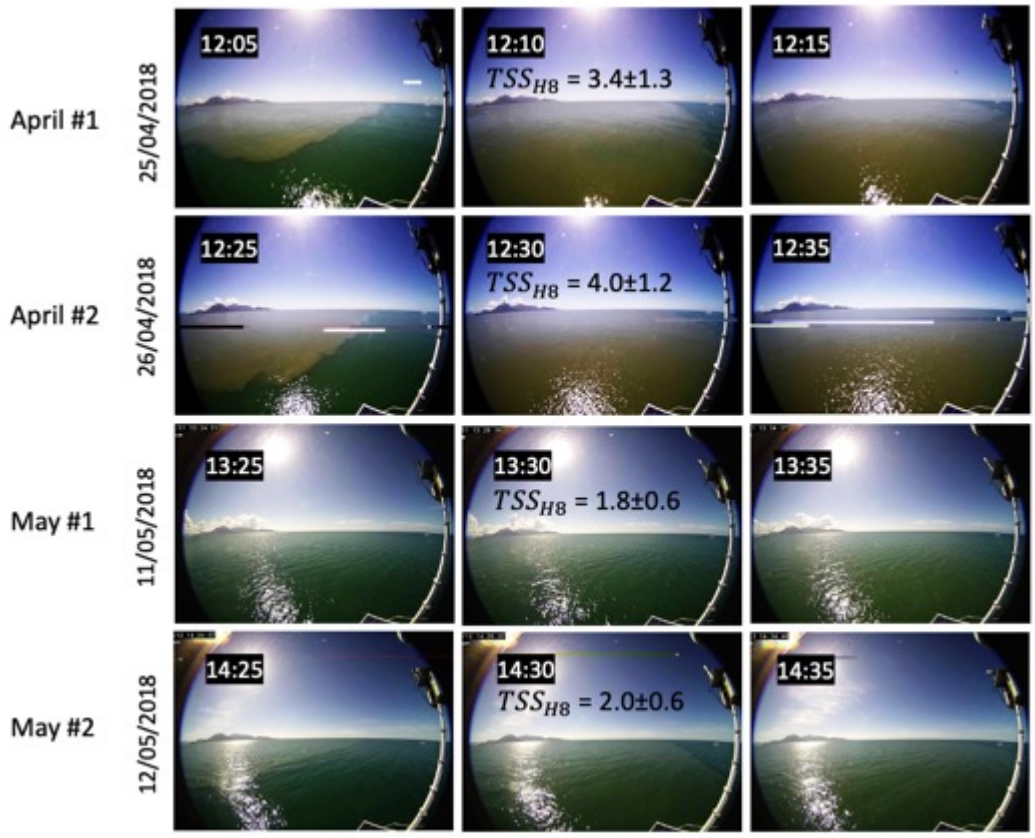

Figure 5.6: Webcam images of the Herbert River plume arriving at LJCO. Hinchinbrook Island is visible at the left edge of the picture. Dates of images were annotated on the left side of each row, and times were annotated in each image. The median and standard deviation of TSS_{H8} (mg L^{-1}) is annotated for the time of plume arrival at LJCO.

Finally, maps of TSS_{H8} were derived at hourly temporal resolution to help the interpretation of the spatial variability of the plume (for TSS ranging between 0.01 and 100.0 mg L^{-1}). The hourly aggregated spatial maps of TSS were centred at the coordinates of LJCO (18.52˚S and 146.39˚E), where the time-series of TSS_{H8} 10-minute data were extracted.

5.1.2 Results

The snapshots of Figure 5.6 revealed that the plume moved rapidly, covering LJCO and surrounding waters within 10 minutes. The colour change between the plume (brown) and coastal (green) waters were clearly distinct in the April images and otherwise subtle for the May ones. Despite

both time series were being recorded during neap tides, only two weeks apart, the April time series presented relatively larger tidal ranges (~ 2.7 m), compared to the May ones (~ 2.3 m) (Table 5.2).

The diurnal variability of TSS ($\Delta TSS_{b_{bp}}$ and ΔTSS_{H8}), the global maximum $G_{max}(TSS_{b_{bp}})$ and $G_{max}(TSS_{H8})$, and the time difference between TSS_{H8} and $TSS_{b_{bp}}$ global maximum ($G_{max}(\Delta t)$) were compiled in Table 5.2 for each of the dates investigated. The intra-pixel standard deviation at the $G_{max}(TSS_{H8})$ value was included between brackets for each date. In addition, the tidal range of each time series and the MODISA-NAP versus the concurrent TSS_{H8} values were added.

Table 5.2: Summary data for TSS time series: values of $\Delta TSS_{b_{bp}}$ and ΔTSS_{H8}, respective global maxima $G_{max}(TSS_{b_{bp}})$ and $G_{max}(TSS_{H8})$ with units in mg L^{-1}; $G_{max}(\Delta t)$ in hours and minutes; tidal range for each date; and MODISA-NAP *vs.* concurrent TSS_{H8} values in mg L^{-1}.

	April #1	*April #2*	*May #1*	*May #2*
$\Delta TSS_{b_{bp}}$	6.1	4.2	1.4	2.0
ΔTSS_{H8}	7.3	6.7	1.2	1.5
$G_{max}(TSS_{b_{bp}})$	8.8	8.1	3.4	4.2
$G_{max}(TSS_{H8})$	9.8 (±3)	9.0(±4)	3.0(±1)	2.5(±0.5)
$G_{max}(\Delta t)$	00:10	01:10	00:40	01:00
Tidal range (m)	2.5	2.7	2.3	2.0
MODISA-NAP vs. TSS_{H8}	5.0 vs. 4.8	4.5 vs. 5.2	1.3 vs. 1.7	1.0 vs. 1.8

Overall, TSS_{H8} closely matched the $TSS_{b_{bp}}$ temporal variability (Figure 5.7), with significant fluctuations (ΔTSS_{H8} up to 7.3 mg L^{-1}) observed within 8 hours (Table 5.2). In addition, the $G_{max}(\Delta t)$ were mostly within 1 hour, with April #1 exhibiting the closest temporal match between TSS_{H8} and $TSS_{b_{bp}}$ ($G_{max}(\Delta t)$ = 10 minutes). The intra-pixel standard deviations computed for TSS_{H8} varied within a day of observations, with largest values (~4 mg L^{-1}) occurring concurrently with $G_{max}(TSS_{H8})$, around the time of plume arrival.

Strong diurnal variability of TSS ($\Delta TSS_{b_{bp}}$> 4.2 mg L^{-1}) were observed in the April time series (Figure 5.7 a and b). The ΔTSS_{H8} was consistently higher (7.3 and 6.9 mg L^{-1}) compared to the $\Delta TSS_{b_{bp}}$(6.1 and 4.2 mg L^{-1}). In both April scenarios, the TSS reached its magnitude peak ($G_{max}(TSS_{H8})$ ~9 mg L^{-1}) during the slack tide, between 12 and 2 p.m. Meanwhile, moderate diurnal variability ($\Delta TSS_{b_{bp}}$ < 2 mg L^{-1}) were observed in the May time series (Figure 5.7 c and d). The values of ΔTSS_{H8} (1.2 and 1.5 mg L^{-1}) were comparable to those of $\Delta TSS_{b_{bp}}$ (1.4 and 2.0 mg L^{-1}, respectively). In May #1, the TSS global maxima, $G_{max}(TSS_{b_{bp}})$ and $G_{max}(TSS_{H8})$, occurred during the slack tide, consistent with the April time series. In May #2, both global maxima occurred 2-3 hours before the slack of the tide, followed by subtle fluctuations of TSS for the remainder of the day.

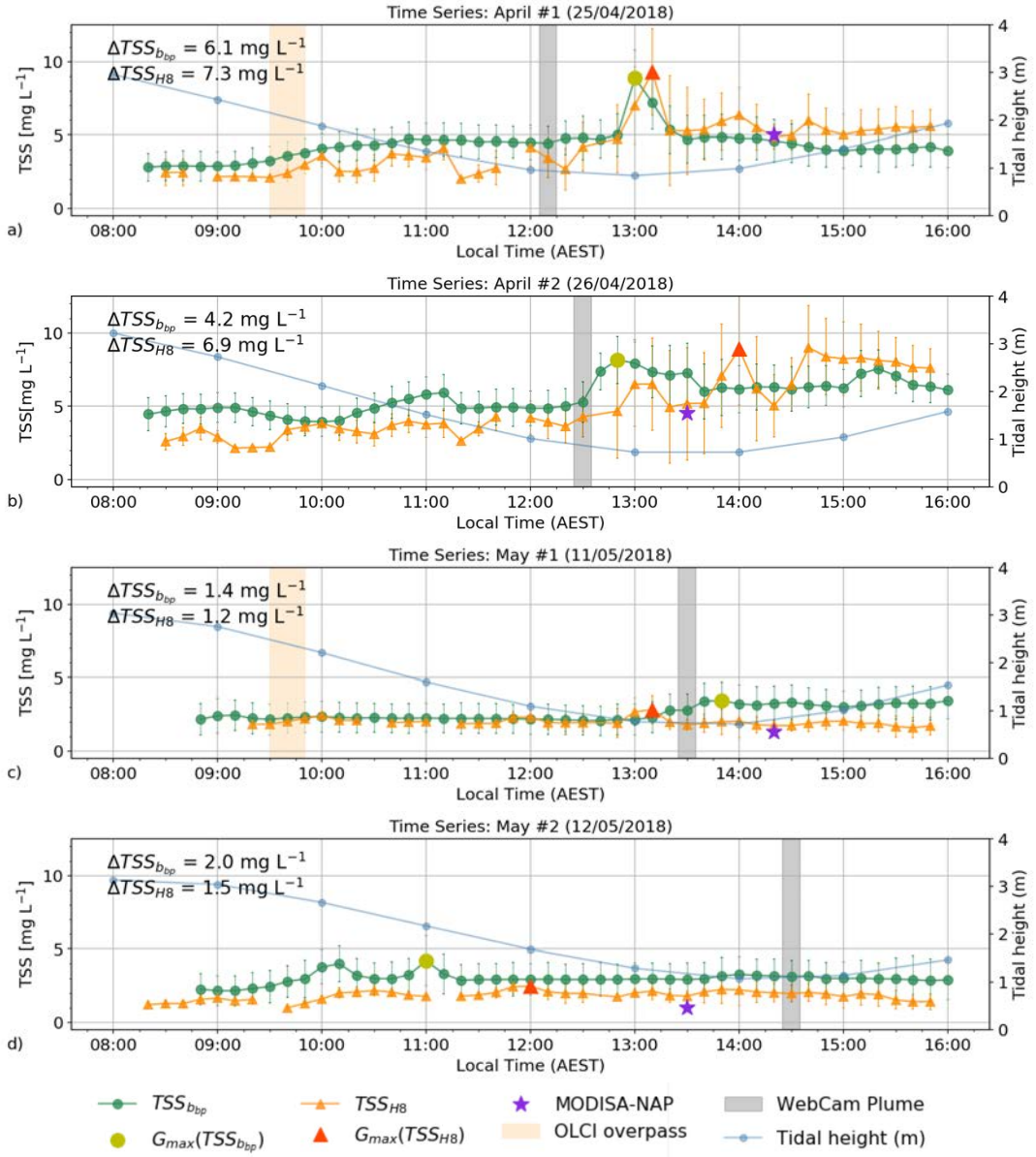

Figure 5.7: Time series of 10-minute TSS_{H8} (orange) and $TSS_{b_{bp}}$(green) extracted in April (a and b) and May (c and d) 2018 at LJCO. G_{max} values were marked in neon-green and red. Values of $\Delta TSS_{b_{bp}}$and $\Delta TSS_{b_{bp}}$ were annotated. The MODISA-NAP value (purple star), Sentinel-3 OLCI overpass timing (orange shade), webcam-derived time of plume arrival (grey shade) and the hourly tidal height (blue) were included. Error bars represent the standard deviation of each TSS measurement.

The MODISA-NAP values closely matched the concurrent TSS_{H8} in all scenarios investigated, with mean absolute differences within 0.8 mg L^{-1} (Table 5.2). The overpass of Sentinel-3 OLCI satellite at LJCO on April #1 and May #1 time series (orange shade in Figure 5.7), occurred at the start of the ebbing tide, missing the plume arrival and TSS peaks at LJCO.

The webcam images at LJCO (Figure 5.6) revealed the timing when the Herbert River plume reached the facility, indicated by a grey vertical shade in the time series of Figure 5.7. The webcam-derived timing of plume arrival reasonably matched the $G_{max}(TSS_{b_{bp}})$ and $G_{max}(TSS_{H8})$ (except for

May #2). However, the visual identification of the plume arriving at LJCO was off by at least 20 minutes, compared to the peak of TSS computed from *in situ* bio-optical data. Figure 5.8 shows the scatter between concurrent TSS_{H8} and $TSS_{b_{bp}}$ from April and May time series of Figure 5.7. Overall, the TSS_{H8} was generally underestimated and moderately correlated with $TSS_{b_{bp}}$ (R^2 < 0.49). However, the small relative differences (RMSE < 1.7 mg L^{-1}) and absolute percentage differences (MAPE < 38%) indicate that TSS_{H8} values were reasonably comparable to $TSS_{b_{bp}}$ in most instances.

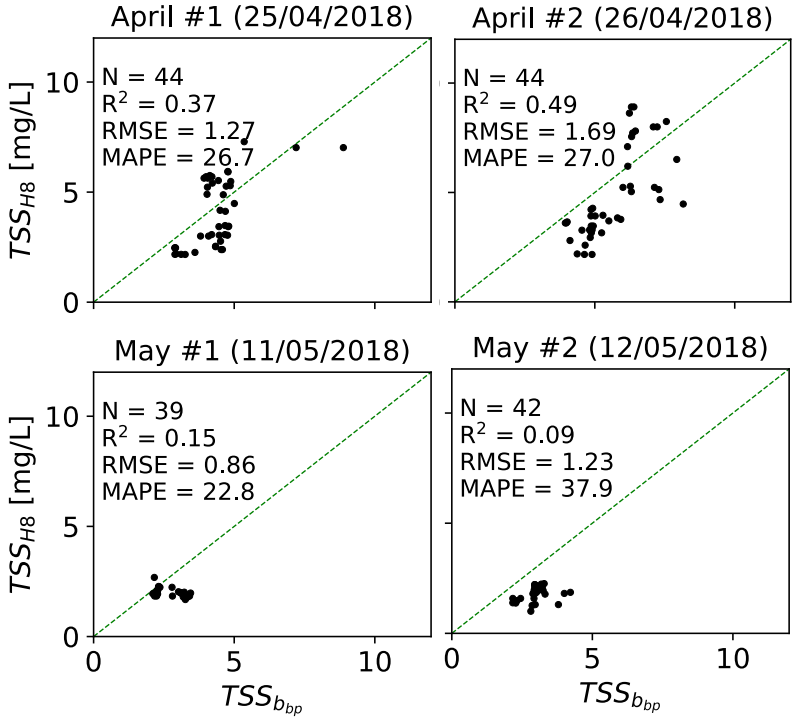

Figure 5.8: Scatterplots between concurrent $TSS_{b_{bp}}$ and TSS_{H8} (both in mg L^{-1}), sampled every 10 minutes. Statistical metrics were annotated. N is the number of available pairs for a given day.

Hourly maps of Himawari-8 TSS were utilised for a spatio-temporal assessment of the April #2 and May #2 time series (Figure 5.9 and Figure 5.10, respectively). The hourly TSS maps showed evidence of the riverine plume dynamics on both sides of the Hinchinbrook channel, and the heterogeneous spatiotemporal distribution of TSS in the GBR lagoon. The Herbert River plume characterised by orange-red areas with TSS > ~5 mg L^{-1} was visually identified in April #2 and May #2 hourly maps. In April #1 (Figure 5.9), most of the area centred at LJCO (indicated by a cross marker) were covered by plume waters as the tide retreated (ebbing from 8 a.m. to 2 p.m.). However, the plumes identified in May #2 hourly maps were notably smaller and its waters seldom reached LJCO. In fact, subtle TSS fluctuations ($\Delta TSS_{b_{bp}}$ < 2 mg L^{-1}) occurred throughout the day for May #2 time series, despite marked changes in water colour were observed from the webcam (Figure 5.6). Nevertheless, is it possible that the perceived water colour changes, as seen from the webcam snapshots at 2:30 p.m., were caused by

riverine waters with TSS < 2 mg L^{-1}, which is not visually detectable from the hourly TSS maps at 1 km spatial resolution.

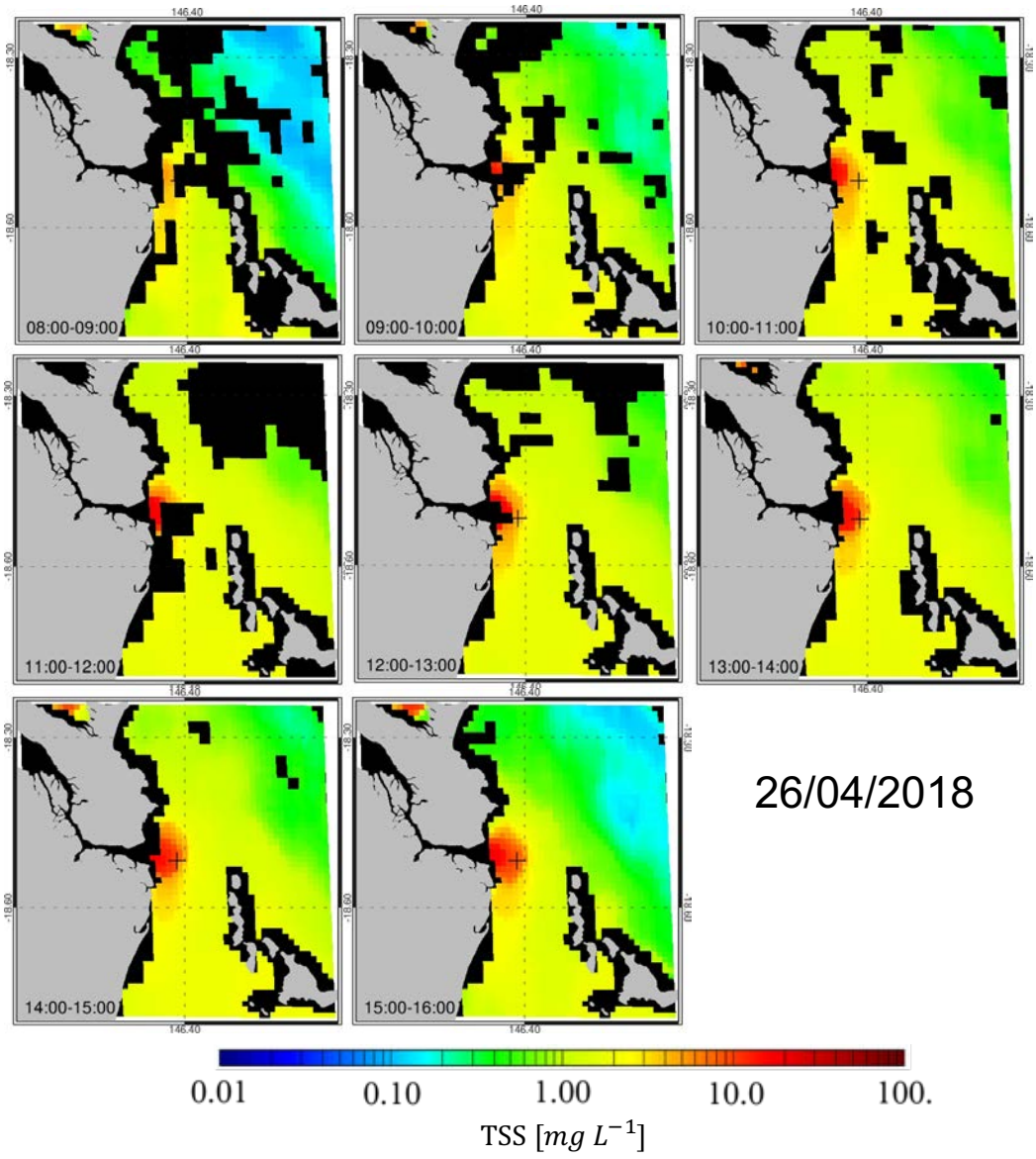

Figure 5.9: Himawari-8 hourly derived TSS over LJCO from 8 a.m. to 4 p.m. local time (AEST) on the 26/04/2018 (April #2). Masked areas for land in grey and for the reef matrix and clouds in black. A black cross marker indicates the location of LJCO. The time range annotated in each plot refers to the interval of observations utilised for hourly aggregation.

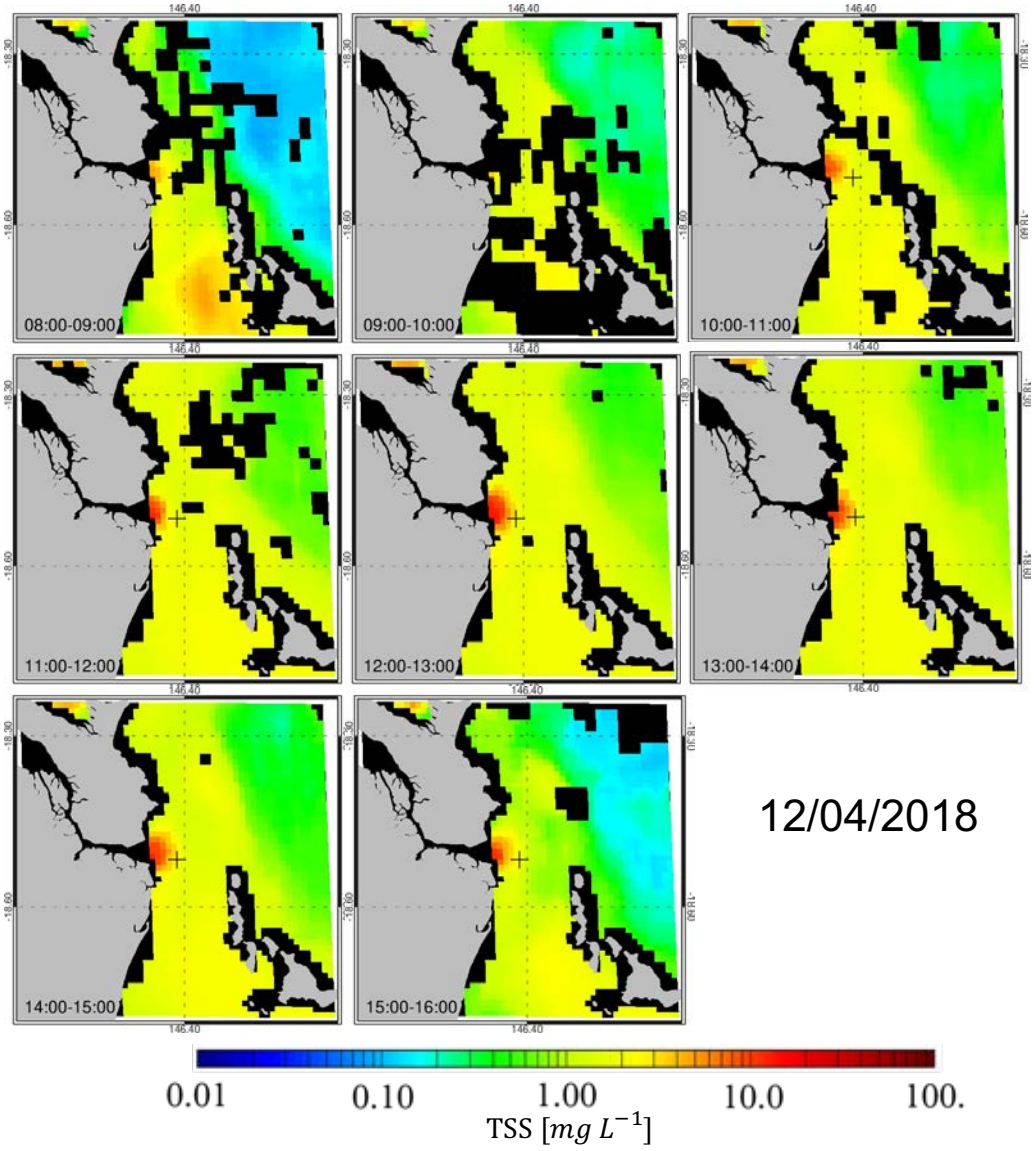

Figure 5.10: Same as Figure 5.9, but for May #2 (12/05/2018) time series.

5.2 Great Barrier Reef Maximum Diurnal Changes in Total Suspended Solids

The diurnal variability of bio-optical properties has been previously assessed at discrete *in situ* locations in the GBR (Oubelkheir et al., 2006; Blondeau-Patissier et al., 2009), including at LJCO (Soja-Woźniak et al., 2019). Optical properties are known to fluctuate with the high-frequency coastal oceanographic processes and conventional ocean colour remote sensing is insufficient for providing a systematic overview of diurnal changes in the GBR. The first section of this chapter investigated the diurnal changes in Himawari-8 derived TSS products and compared these to the *in situ* bio-optical measurements at LJCO. In this section, a spatial assessment of the diurnal fluctuations of TSS was conducted for a year of available images GBR-wide. The key objective of this section is to critically evaluate the applicability of Himawari-8-derived TSS for the detection of monthly and seasonal patterns of diurnal variability in water quality. Maps of maximum diurnal variability of TSS were utilised to determine the spatial extent of TSS features, where diurnal fluctuations were above a certain threshold within a given month. The maximum diurnal variability maps were utilised to identify locations with extreme diurnal fluctuations of TSS that would otherwise be overlooked by utilising weekly to monthly average composites and ultimately, by LEO satellite observations.

5.2.1 Methods

In section 5.1 of this chapter, it was revealed that TSS derived every 10-minutes from Himawari-8 were suitable to detect diurnal water quality fluctuations at LJCO, within a 9-pixel subset area. However, deriving 10-minute TSS products for the entire GBR is unrealistic for routine water quality monitoring efforts. To speed up the processing of information and to provide useful products at a reporting level, hourly aggregated observations were chosen for the monthly analysis in the coastal GBR. All individual 10-minute Himawari-8 observations acquired between 8 a.m. and 4 p.m. and between August 2017 and July 2018 were extracted for the GBR area, according to processing steps of Figure 2.21. As a result, up to 8 hourly aggregated observations were computed for each day, and up to 248 hourly aggregates were computed for each month.

An hourly aggregated observation corresponded to the temporal median of all 10-minute observations available within 1 hour. At least five out of six of the single observations available within 1 hour were required for the computation of aggregates, to ensure the composites were representative of a certain timestamp. The single Himawari-8 observations were aggregated by taking their temporal median, as to eliminate potential outliers associated to undetected clouds and environmental noise likely present in the Himawari-8 bands. TSS products were retrieved from hourly aggregated observations through the application of the validated ANN inversion experiment (P094). An aggregated mask was computed and applied to each hourly TSS product, masking pixels due to land, clouds, and

sun glint. The out-of-range TSS values were masked in each hourly product, using the associated ANN flags computed after the inversion procedure. Values of ΔTSS were computed for each pixel-index (across the pixels of a given index of the image), representing the absolute difference between the maximum and minimum TSS observed within a day (as in Eq. 5.2). The ΔTSS computation took at least 4 (out of 8) mask-free hourly aggregated products per pixel, per day, as the minimum number of observations required to resolve diurnal variations (Ruddick et al., 2014). The maximum value of ΔTSS, $Max_{\Delta TSS}$, was calculated for each pixel-index utilising all values of ΔTSS available within a given month.

Maps of $Max_{\Delta TSS}$ were monthly computed (between August 2017 and July 2018) and spatially smoothed with a 7-by-7 boxcar median filter. Any value of $Max_{\Delta TSS}$ or median TSS below 0.25 mg L^{-1} were masked out to comply with the detection limits of the algorithm. The monthly maps of $Max_{\Delta TSS}$ were grouped into the wet and dry season for illustrative purposes, regardless of the year of observation and chronological time. In addition, for illustrative purposes, the monthly median TSS was calculated for comparison against $Max_{\Delta TSS}$ at LJCO. The monthly median was calculated including at least 4 mask-free observations per pixel, per day, as in $Max_{\Delta TSS}$ calculations.

5.2.2 Results

The maps Figure 5.11 show the diurnal variability of TSS (i.e., ΔTSS) around the LJCO site within a given day. The non-smoothed original product (Figure 5.11a) is highly heterogeneous with a mixture of high and low ΔTSS in the coastal and open ocean areas, likely related to noise and adjacency effects. In this case, the most distinctive feature is the ΔTSS above 5.25 mg L^{-1}, associated with the Herbert River plume on both sides of the Hinchinbrook tidal channel. Meanwhile, the spatially filter image cleared the potential outliers and generated a smoothed image (Figure 5.11b), emphasising the main TSS features. In this case, the main plume feature at LJCO has a distinctive dark red colour and is characterised by ΔTSS above 5.25 mg L^{-1}, while a southern branch of the plume developed with ΔTSS below 3.25 mg L^{-1}, illustrated in yellow and green.

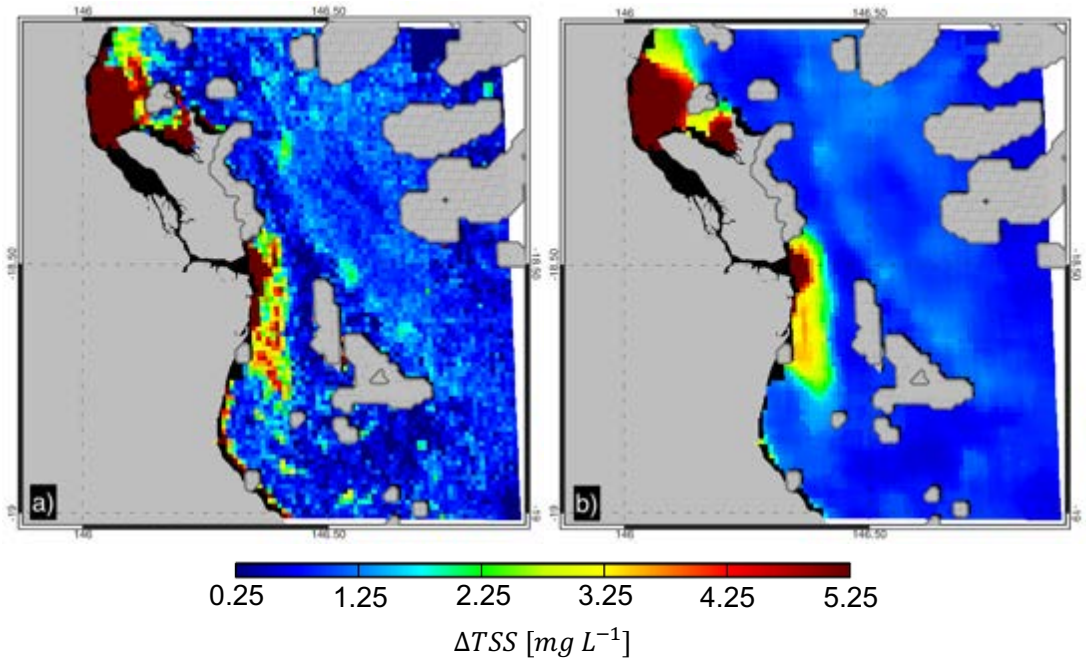

Figure 5.11: Spatial distribution of ΔTSS [mg L^{-1}] centred at LJCO for hourly TSS products computed on 06/09/2017. ΔTSS is presented without (a) and with a spatial median filter applied (b).

The spatial distribution of $Max_{\Delta TSS}$ for September 2017 (Figure 5.12a) reveals features of large diurnal variability (>4.25 mg L^{-1}) at both outlets of the Hinchinbrook Channel. Meanwhile, the computed monthly median smooths out the feature at LJCO observed in Figure 5.12a, only emphasising the northern branch of the plume with TSS above 3.25 mg L^{-1}. While the median map indicates areas where TSS values are consistently high (> 3.25 mg L^{-1}) within a month, the $Max_{\Delta TSS}$ indicate areas where episodic events, such as floods, may have occurred and rapidly increased TSS values within a day.

The $Max_{\Delta TSS}$ was then utilised to investigate the occurrence of episodic events contributing to the water quality dynamics in the GBR between August 2017 and July 2018. In this section, the term 'TSS feature' was roughly defined as waters with $Max_{\Delta TSS}$ larger than 5.25 mg L^{-1}, visually discerned as the dark red areas in the $Max_{\Delta TSS}$ maps. Thus, the spatial distribution of $Max_{\Delta TSS}$ values larger than 5.25 mg L^{-1} was interpreted in the present work as the maximum TSS feature extent observed within a month, based on the records of diurnal variability of TSS for that month.

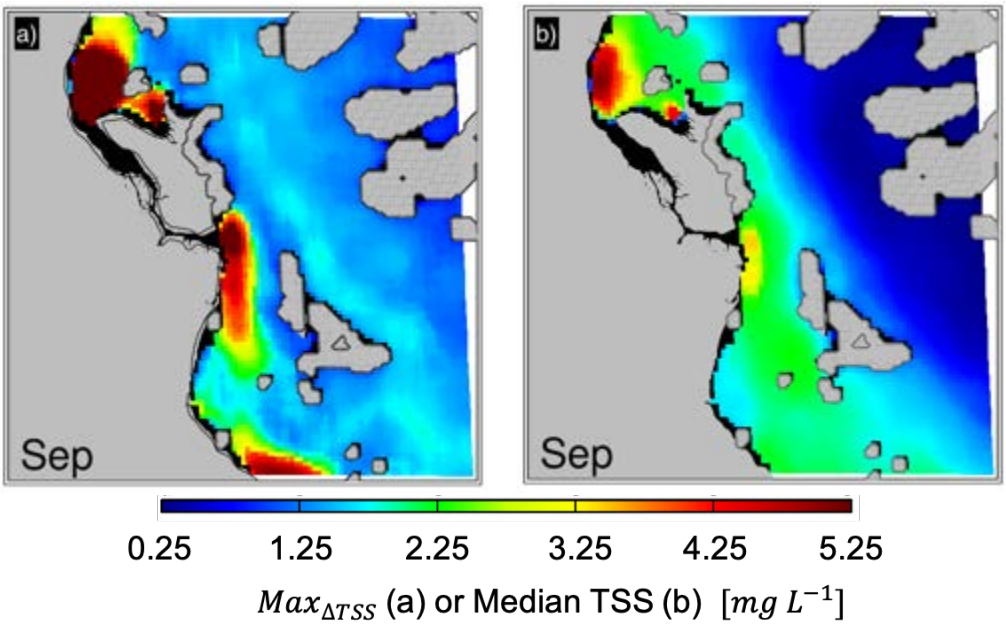

Figure 5.12: Comparison between monthly $Max_{\Delta TSS}$ (a) and monthly median TSS (b) at LJCO and surrounding areas in the GBR lagoon.

The number of valid ΔTSS observations available for each pixel within a month were spatially represented in Figure 5.13. In general, there were marked seasonal differences, with wet season months presenting less available data than dry season across the entire GBR. Between 1 and 20 observations per month were available within the GBR lagoon during the wet season. The dry season, otherwise, accounts for 20 to 30 days of valid observations within a month, mostly distributed in the central and southern GBR lagoon, and in the Coral Sea. ΔTSS observations were consistently unavailable (areas in black) in the northern GBR, mostly during the dry season. Consequently, the northern GBR may present no $Max_{\Delta TSS}$ values at all, depending on the month evaluated. Therefore, the following analysis concentrated on investigating patterns of variability of $Max_{\Delta TSS}$ in the central and southern coastal GBR, as depicted in Figure 5.14. This region includes the major catchments draining to the GBR, delineated by the Burdekin and Fitzroy Rivers, between 18˚S and 24˚S.

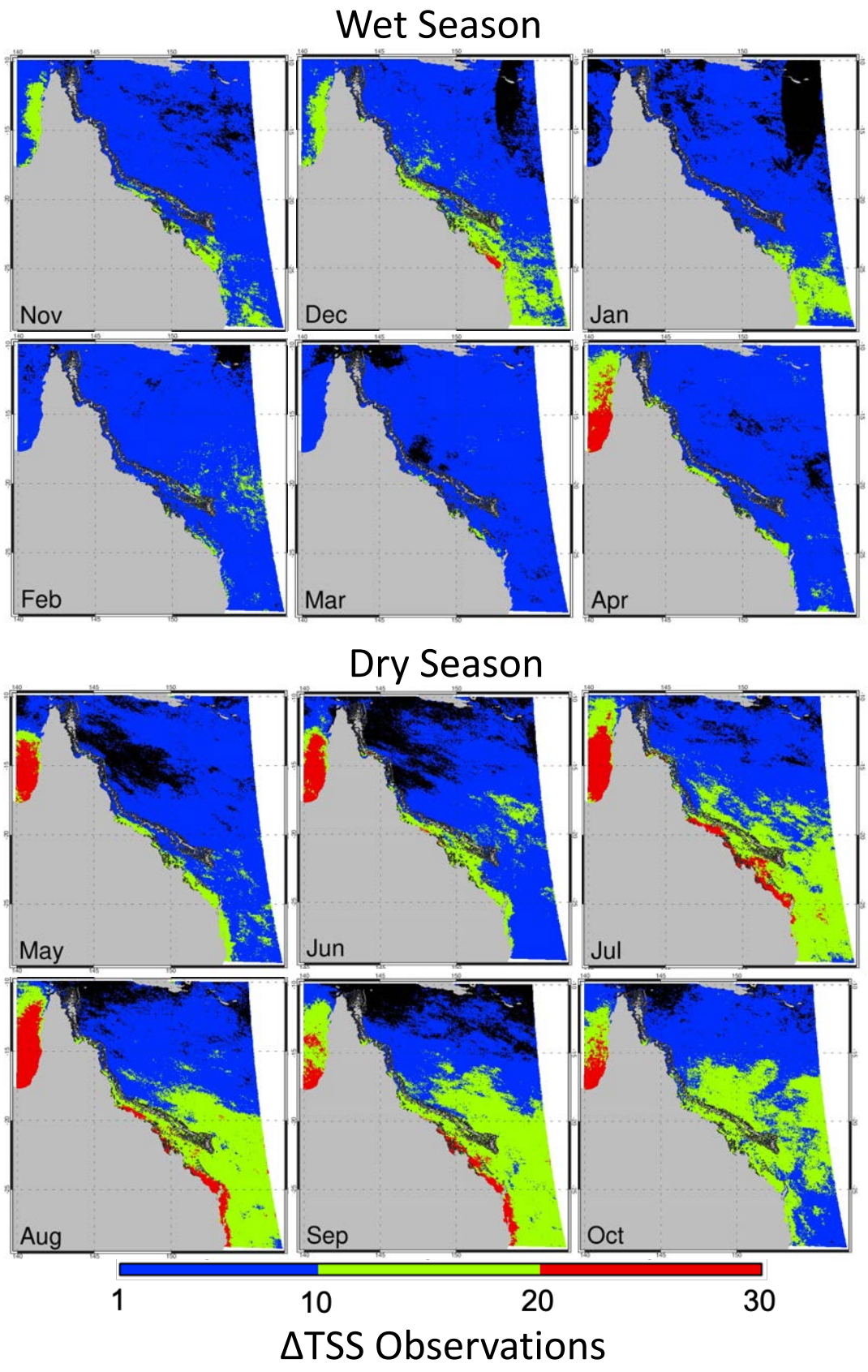

Figure 5.13: Spatial distribution of the total number of ΔTSS available within a month for the GBR and adjacent areas. The land areas masked in grey and masked water pixels in black.

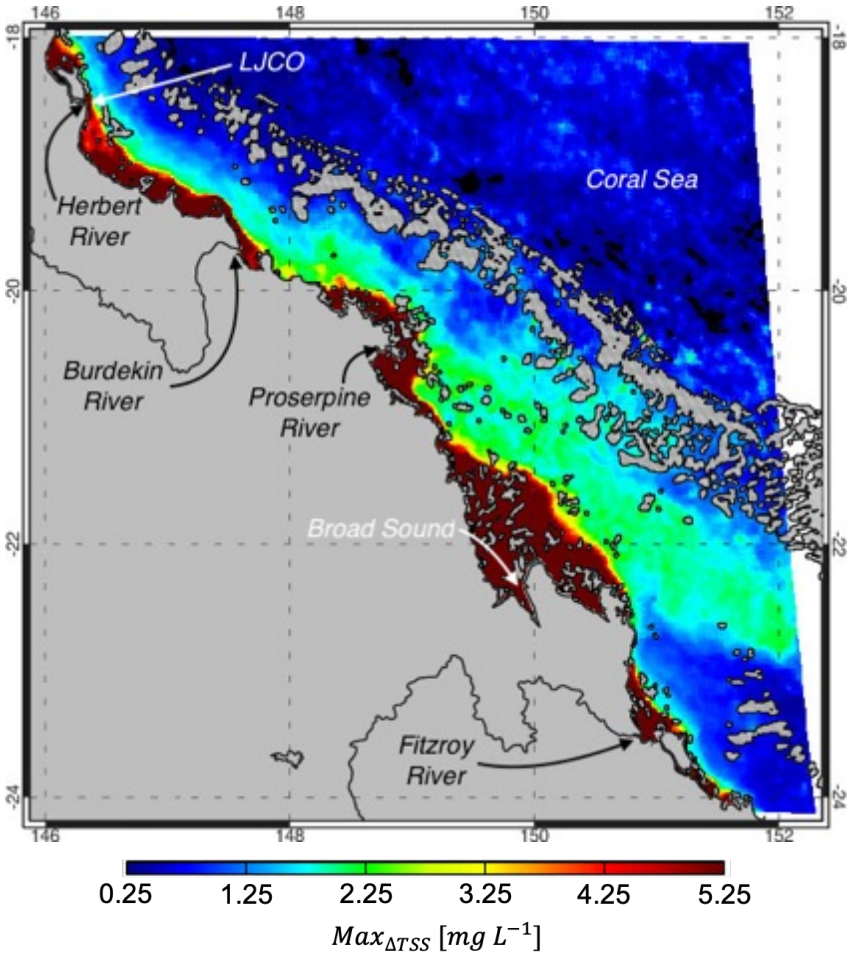

Figure 5.14: Example of $Max_{\Delta TSS}$ between 18˚S and 24˚S including the major catchments to the GBR, indicated by the Burdekin and Fitzroy Rivers, as well as the mouth of the Herbert and the Proserpine Rivers indicated. LJCO and Broad Sound and the Coral Sea are indicated in white text and arrows. The land and GBR reef matrix areas were masked in grey.

In the central-south GBR the water body adjacent to the coast, presented moderate to high (from 3.25 to 5.25 mg L^{-1} and above) $Max_{\Delta TSS}$ for all months evaluated. The locations where $Max_{\Delta TSS}$ was moderate to high (3.25 to 5.25 mg L^{-1} and above) in both wet (Figure 5.15) and dry seasons (Figure 5.16) were compatible with the regions of significant spring tidal ranges (> 3 m) along the GBR shelf waters (Pickard et al., 1977). Meanwhile, the GBR lagoon experienced moderate to low (< 3.25 mg L^{-1}) $Max_{\Delta TSS}$ during the typical wet season months (Figure 5.15 - November to April). During typical dry season months (May to October), a moderate (1.25 to 3.25 mg L^{-1}) $Max_{\Delta TSS}$ took place in the lagoon with patches of $Max_{\Delta TSS}$ higher than 3.5 mg L^{-1}. Furthermore, the dry season months presented a larger spatial extent of moderate to high (>2.25 mg L^{-1}) $Max_{\Delta TSS}$, compared to the wet season. Low to moderate (1.25 -2.25 mg L^{-1}) $Max_{\Delta TSS}$ was observed within the reef matrix, which was more pronounced in dry season months.

The TSS features, where $Max_{\Delta TSS}$ was higher than 5.25 mg L^{-1} (dark red areas), were persistent through wet and dry seasons in some locations such as in Broad Sound (22˚S – detail in Figure 5.14).

The visual extent of the TSS feature was larger in May 2018 (at the end of wet season), where waters with $Max_{\Delta TSS}$ above 5.25 mg L^{-1} were almost entirely connected across the south and central GBR. In Broad Sound, the TSS feature was evidently pronounced during the wet and dry seasons, presenting a sharp gradient between enclosed waters (of $Max_{\Delta TSS}$ > 5.35 mg L^{-1}) and the adjacent coastal waters (of $Max_{\Delta TSS}$ lower than 2.25 mg L^{-1}). The Broad Sound TSS feature is slightly retracted between the end of the dry season and the start of the wet season (September to November). At the mouth of the Burdekin River, the TSS feature was persistent for most of the year with moderate variation of its extent through the months. Meanwhile, at the mouth of the Fitzroy, the TSS feature was nearly permanent with little variation in its extent. Month-to-month variations of TSS feature extent were observed in several areas of the central-southern GBR, such as in the waters surrounding Whitsundays Islands (mainly around the Proserpine River at its southern side), and where the LJCO facility is located, at the mouth of the Herbert River. Diurnal variations were generally lower than 3.25 mg L^{-1} between the mouth of the Burdekin and the Whitsundays area.

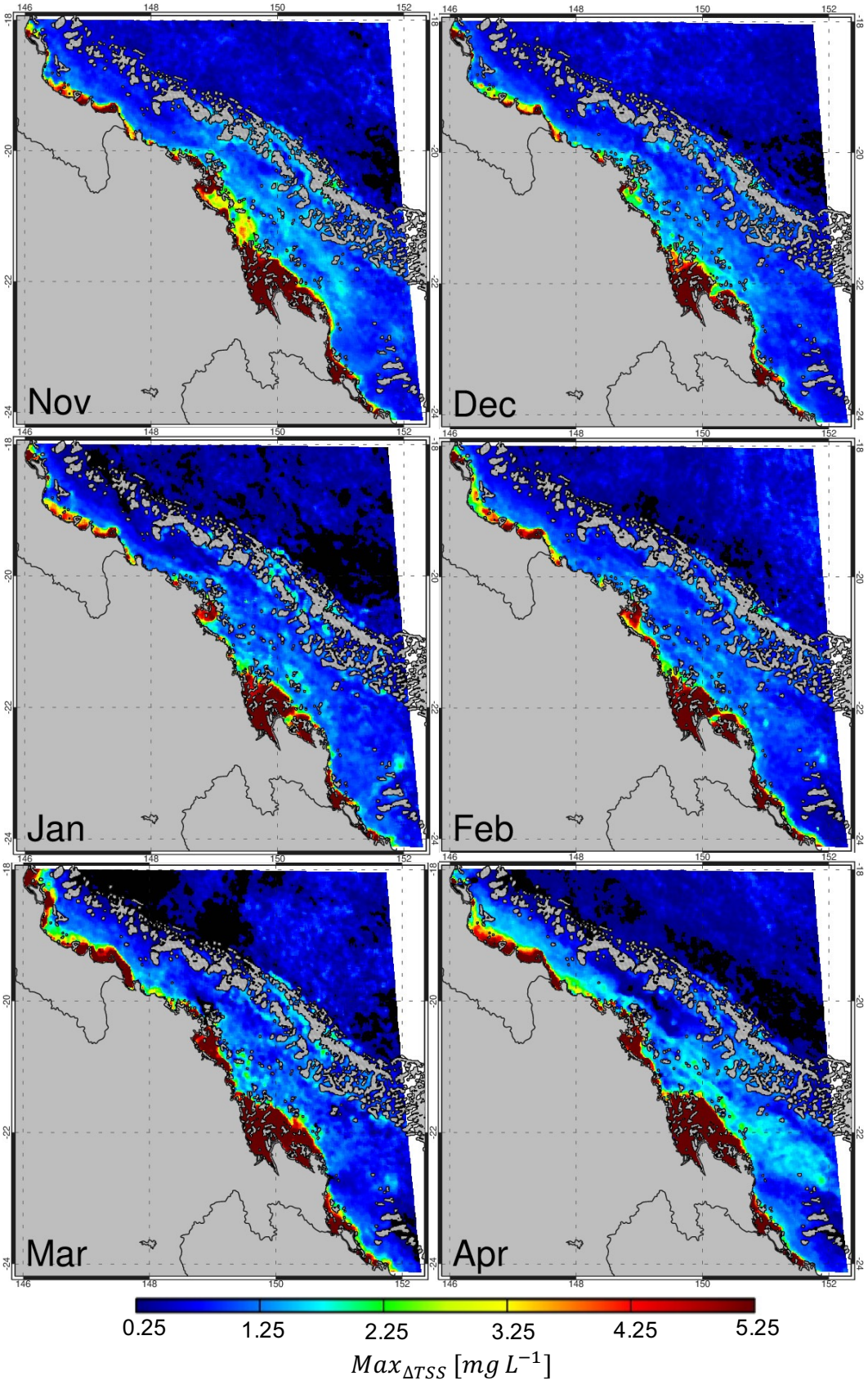

Figure 5.15: $Max_{\Delta TSS}$ (mg L^{-1}) in the central GBR between 18˚S and 24˚S, for the wet season. The black areas represent masked pixels due to unavailable observations and $Max_{\Delta TSS}$ lower than 0.25 mg L^{-1}. Land and the GBR reef areas are masked in grey.

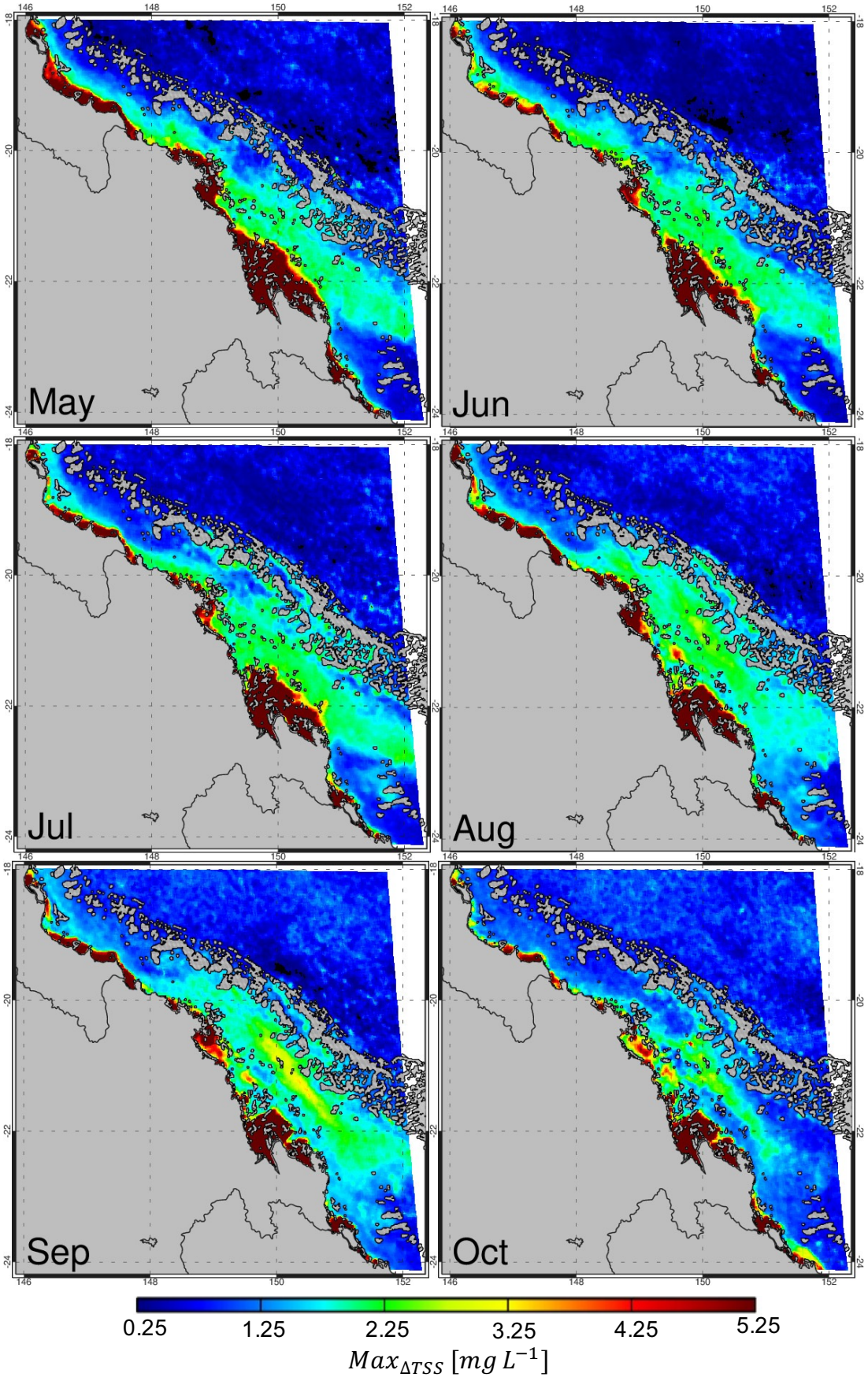

Figure 5.16: Same as Figure 5.15 but for the dry season months.

The $Max_{\Delta TSS}$ was investigated at LJCO and its adjacent areas for the typical wet and dry season months between 2017 and 2018 (Figure 5.18). Variable values of $Max_{\Delta TSS}$ were present across the months at LJCO, regardless of the seasons. Thus, it was difficult to define wet and dry season patterns of diurnal variability. The TSS feature of the Herbert River, at south and north of the Hinchinbrook Channel, was clearly delineated by $Max_{\Delta TSS}$ larger than 5.25 mg L^{-1}. Both branches generally presented high (> 5.25 mg L^{-1}) $Max_{\Delta TSS}$ across all months, except for the southern branch in October, with $Max_{\Delta TSS}$ reaching about 2.25 mg L^{-1}. During the start of wet season (November to January) the southern TSS feature was usually constricted around the channel outlet, forming a distinctive estuarine plume. However, as the wet season developed (February-May), the southern branch of the TSS feature connected itself to waters from the southern coastal areas. In March, the TSS feature extended further towards the offshore areas, following intensive discharges (~ 500 000 ML/day) from the wet season (Figure 5.5). In May, a contiguous coastal feature of moderate-high (> 4.25 mg L^{-1}) $Max_{\Delta TSS}$ was delineated with a sharp gradient of $Max_{\Delta TSS}$ between the enclosed coastal waters and the mid-shelf lagoon. From June to September, waters with $Max_{\Delta TSS}$ of around 1.5 mg L^{-1} were present further offshore and eventually reached the reef matrix. Additionally, the southern branch of the Herbert River developed into a tongue-shaped plume directed southward, which was evident between June and September.

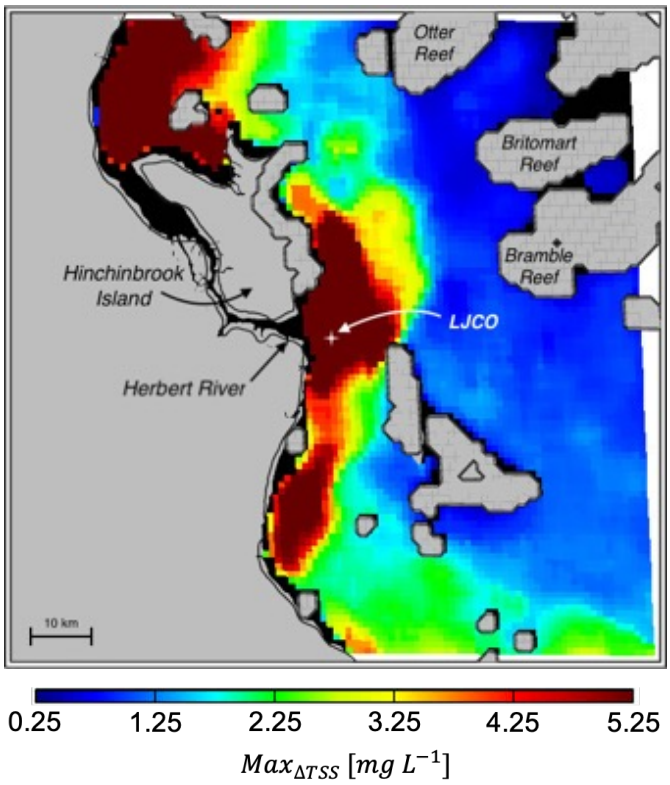

Figure 5.17: $Max_{\Delta TSS}$ (mg L^{-1}) for a given month with the map centred at LJCO. Adjacent areas include Bramble, Britomart and Otter Reefs, Hinchinbrook Island, and the mouth of the Herbert River.

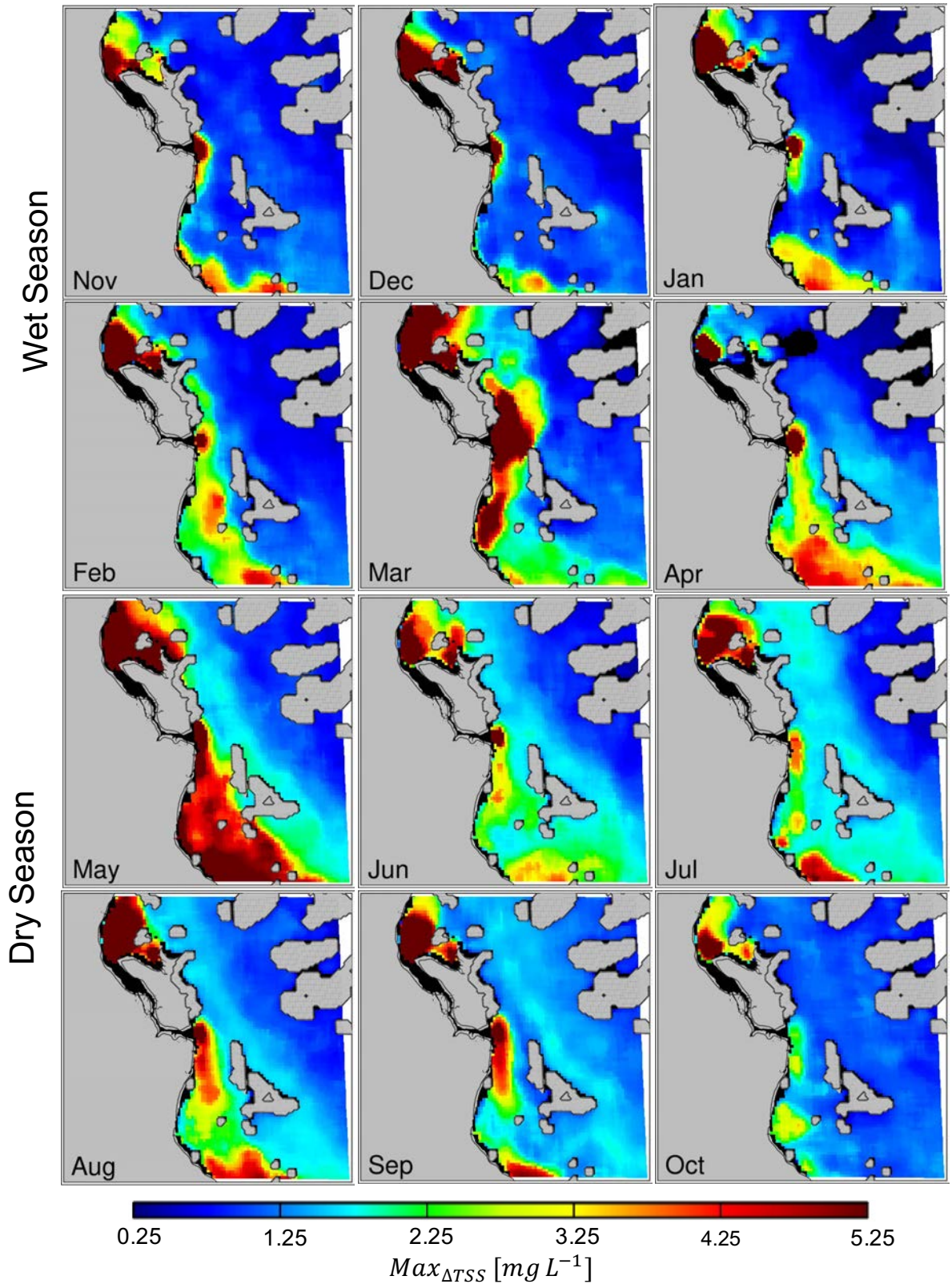

Figure 5.18: $Max_{\Delta TSS}$ at LJCO (18.52˚S, 139.46˚E) and adjacent areas, for wet and dry seasons between 2017 and 2018. The black areas represent masked pixels due to unavailable observations and $Max_{\Delta TSS}$ lower than 0.5 mg L^{-1} as well as the GBR reef matrix. Land areas were masked in grey.

5.3 Discussion of Applications Chapter

5.3.1 Discussion of Diurnal Variability of Total Suspended Solids at LJCO

Diurnal fluctuations of TSS were investigated utilising concurrent *in situ* and Himawari-8 data at the Lucinda Jetty Coastal Observatory (LJCO). The continuous measurements of particulate backscattering and its computed TSS ($TSS_{b_{bp}}$), supported a near-real time comparison with the 10-minute Himawari-8-derived TSS (TSS_{H8}) for an integrated assessment of water quality. Overall, TSS_{H8} agreed remarkably well (MAPE within 38%) with the concurrent $TSS_{b_{bp}}$ at LJCO (Figure 5.7), despite methodological differences. TSS_{H8} fluctuations of up to 7 mg L^{-1} were observed within a day at LJCO, corroborating previous studies employing geostationary observations for diurnal water quality assessments (Neukermans et al., 2012b; Vanhellemont et al., 2014; Ding et al., 2020; Hafeez et al., 2021). The temporal difference between TSS_{H8} and $TSS_{b_{bp}}$ global maxima ranged between 10 minutes to 1 hour. Likewise, Neukermans et al. (2012b) observed good correspondence between the SEVERI-derived TSS and *in situ* turbidity diurnal variations, with average temporal lag of 11 minutes between global maxima values.

The observed TSS fluctuations during two days of April and of May 2018 were associated with the Herbert River fluxes and with the local tidal dynamics. In most cases, the plume arrived at LJCO at the slack tide, followed by rapid (< 1 hour) and significant increases of TSS up to 7.3 mg L^{-1}. These results are supported by previous findings, suggesting a persistent semi-diurnal tidal influence on the bio-optical variability at LJCO (Soja-Woźniak et al., 2019). However, the sharp contrast between river plume and coastal waters (Figure 5.6), as well as the peak TSS concentrations (~9 mg L^{-1}), indicate that the April plume waters were largely influenced by the residual volume of freshwater discharged from the prevailing wet season. The high volume discharged from the Herbert River prior to April 2018 (~500,000 ML/day) may have overwhelmed the tidal influence at LJCO, by increasing the horizontal advection and vertical mixing and thus, modulating significant diurnal fluctuations of TSS. Moreover, the diurnal fluctuations of TSS presented in this study were recorded during neap tides on the first and third quarter moon, with ranges of up to 2.7 m. Therefore, greater diurnal fluctuations of TSS (> 7 mg L^{-1}) may be experienced during spring tides at LJCO, with tidal ranges larger than 3 m likely increasing the exchange of water volumes and TSS advection (Eleveld et al., 2014).

The 10-minute TSS and hourly maps from Himawari-8 were useful and complementary tools to investigate diurnal variability in the coastal GBR. The 10-minute observations from Himawari-8 were appropriate to track rapid (< 1 hour) and moderate (> 1 mg L^{-1}) fluctuations in turbid coastal waters with the time series analysis. Meanwhile, the hourly Himawari-8 derived TSS was helpful and sufficient to diurnal mapping and tracking of riverine plumes in the coastal GBR. The MODIS-NAP products yielded

comparable results to concurrent TSS_{H8}, with minor discrepancies possibly associated with algorithm parameterization and atmospheric correction of MODIS-Aqua observations, as reported in Dorji and Fearns (2018). A comprehensive inter-comparison between concurrent MODIS-Aqua, Sentinel-3 and Himawari-8 derived TSS products should provide more understanding on their methodological differences and limitations. While Sentinel-3A and 3B and MODIS-Aqua and VIIRS may provide a morning and afternoon overview (Bracaglia et al., 2019; Bracaglia et al., 2020), these sensors together would still be insufficient to fully depict the local bio-optical diurnal variability, as represented by Himawari-8-derived TSS at LJCO every 10 minutes.

Although TSS_{H8} provided unprecedented amount of data for water quality observations in the coastal GBR, it presented a temporal mismatch as well as a systematic underestimation of $TSS_{b_{bp}}$. The differences in magnitude could be attributed to the current limitations of the present method (discussed in detection limits), and from the limitations in utilising b_{bp} data as a proxy for TSS. At LJCO, the particles are a mix of white organic marine carbonate sands and brown inorganic terrigenous muds, each of which exhibits a distinctive relationship against b_{bp} (Soja-Woźniak et al., 2019). As a result, the functional relationship between b_{bp} and gravimetric TSS may assume several distinctive slopes depending on proportion of organic to inorganic material in the dataset utilised. In fact, Neukermans et al. (2009) derived TSS from SEVIRI based on a reflectance algorithm with a constant coefficient to describe the relationship between b_{bp} and TSS (Nechad et al., 2010). It was recognised that the relationship between b_{bp} and TSS may be largely limited due to frequent variations in particle composition (Neukermans et al., 2009). Moreover, given the complex variability between b_{bp} and TSS in the coastal GBR, a non-linear fit as presented by Thursby et al. (2015) may be an alternative solution to the relationship between those parameters. In addition, the accuracy to which TSS can be derived from b_{bp} in highly dynamic coastal waters is possibly limited by the time difference between each pair of measurements. As a result, derived TSS can be over or underestimated, depending on the stability of local particle composition to different tidal stages. Further improvements could include limiting the time difference between measurements of b_{bp} and TSS within 1 hour to avoid a mismatch due to sample collection at different tidal stages.

Additionally, it was recognised that $TSS_{b_{bp}}$ presented a delayed response compared to the visual timing of the plume reaching LJCO from the webcam images. This temporal lag may be associated with a strong vertical stratification due to salinity differences induced by the plume waters while moving cross-shelf (King et al., 2002). The buoyant plume of freshwater may be restricted to the surface as a wedge, when reaching LJCO. Consequently, the b_{bp} sensor deployed at 3 m depth miss the arrival of the plume waters at the surface, until more vigorous vertical mixing takes place, causing a sharp gradient (generally larger than 2 mg L^{-1}) in the b_{bp} and derived TSS. Although sub-surface b_{bp}

measurements compare well to satellite derived products in open ocean waters (Bisson et al., 2019), this assumption may not be valid in optically complex waters. Alternative bio-optical measurements, such as absorption and turbidity (Neukermans et al., 2012b) can be explored and provide more clarity on understanding the timing of plume arrival at LJCO and the relationship to Himawari-8 derived TSS.

Nevertheless, the present method's main limitations were due to the low sensitivity of Himawari-8 VNIR bands to small changes in ocean colour. The algorithm developed in the present work retrieves TSS from Himawari-8 with a MAPE of 75.5% and RMSE of 2 mg L^{-1} compared to *in situ* data (section 3.2.2). Additionally, a sensitivity analysis suggested that Himawari-8 TSS within 0.25 mg L^{-1} were likely below the detection limits of the developed algorithm, presenting errors with up to three orders of magnitude difference. Thus, $TSS_{b_{bp}}$ fluctuations lower than 0.25 mg L^{-1} were not well discriminated by TSS_{H8} on some occasions, which was illustrated in the time series extracted on May #1 (11/05/2018) and May #2 (12/05/2018).

The temporal difference between TSS_{H8} and $TSS_{b_{bp}}$ global maxima may be explained by the spatial mismatch between the *in situ* point sample, represented by the $TSS_{b_{bp}}$, and the 3-by-3 pixel-box (9 km^2) representing TSS_{H8}. In fact, TSS_{H8} derived from the spatial median of 9 pixels generally presented increased intra-pixel standard deviations with rapid increases of TSS, indicating intra-pixel heterogeneity likely caused by the plume arrival. It is acknowledged that the TSS retrievals are largely impacted by the nominal spatial resolution utilised (Dorji and Fearns, 2017), particularly in coastal waters with high spatial variability. The Himawari-8 640 nm band original spatial resolution is of 0.5 km and may be sought for improved TSS retrievals in the coastal GBR.

5.3.2 Discussion of GBR Maximum Diurnal Changes of TSS in the GBR

In section 5.2, the spatial patterns of diurnal variability events in the GBR between August 2017 and July 2018 were investigated. The maximum diurnal variability of TSS ($Max_{\Delta TSS}$) was computed to explore the maximum extent of TSS features in the GBR during dry and wet season months. A TSS feature was defined in this work as the area adjacent to the coast where the $Max_{\Delta TSS}$ was higher than 5.25 mg L^{-1}, which was visually detected by a sharp edge in contrast to lower ΔTSS. The TSS range of 5 - 15 mg L^{-1} was designated as the annual water quality guideline threshold for enclosed coastal waters of the Wet Tropics and Central Coast, respectively (Great Barrier Reef Marine Park Authority, 2010). However, the TSS feature represented waters where the daily variations potentially exceeded the annually averaged threshold values for TSS in these enclosed coastal waters. Consequently, the intensive presence of the TSS features (as designated in this chapter section) may indicate a water quality exceedance above the limits suggested for enclosed coastal waters.

The fluctuations of $Max_{\Delta TSS}$ may be largely associated to short lived, seasonal and intra-annual events known for mobilising TSS such as: tidal currents and jets (Delandmeter et al., 2017), wind driven resuspension (Orpin et al., 2004; Orpin and Ridd, 2012), and seasonal freshwater discharge (Schroeder et al., 2012; Lough et al., 2015). The short-lived events, however, might happen sporadically or during a few days within a month, such as the spring tides, and might be missed by observations from LEO satellites. Geostationary observations from the Himawari-8 meteorological satellite provided for the first time, at hourly temporal resolution, empirical evidence of the influence of such short-lived events in the GBR water quality.

The monthly analysis of the maximum diurnal extent of TSS features exposed intricate spatiotemporal variations in the central-southern GBR. Seasonal variations were more pronounced in the southern GBR lagoon, with the dry season presenting large areas with moderate (~ 2.25 mg L^{-1}) $Max_{\Delta TSS}$. The marked seasonal patterns in $Max_{\Delta TSS}$ may be associated with prevailing winds and resultant swells, which are known to be the main mechanism for sediment resuspension in the central-south GBR (Larcombe et al., 1995; Larcombe and Woolfe, 1999; Browne et al., 2013). The trade winds blow persistently from east or south-east during the dry season (April to November), potentially generating swells that mobilise bottom sediments and increase the concentration of suspended sediments in the water column. In fact, it has been shown that turbidity measurements have increased three orders of magnitude within an hour in an inshore site in the central GBR (Orpin et al., 2004). The rapid increase in turbidity was linked to a constant wind speed (> 20 km/h) and significant wave height (up to 80 cm) that occurred as result of an extreme weather event, which was not associated with any tropical cyclone (Orpin et al., 2004). In this context, dry season wind stress might be associated with the long-term decline in water clarity (Larcombe et al., 2001; Browne et al., 2013).

Meanwhile, tidal variability is thought to be a minor factor influencing the resuspension of bottom sediments, and more associated with the periodical flushing of estuaries and bays into the GBR (Larcombe et al., 1995). However, tides not only affect water level and circulation, but also induce variations in the rates of sediment resuspension, mixing and settling, contributing to changes in water clarity and quality. According to Fabricius et al. (2016), tides largely modulate the spatial complexity of long-term values of water quality parameters (i.e., photic depth) in the coastal GBR. In this study, the latitudinal variations of $Max_{\Delta TSS}$ were associated with differences in tidal ranges along the Queensland coast. The spring tidal ranges have a marked latitudinal gradient from the northern to the southern GBR. Average tidal ranges between 2-4 m are common for coastal and outer reef regions between 10˚S and 20˚S, while the largest tidal ranges (> 4 m) occur in the central-southern coastal GBR between 20˚S and 25˚S (Pickard et al., 1977).

In fact, the most persistent TSS features with $Max_{\Delta TSS}$ (>5.25 mg L^{-1}) were confined to the central and southern coastal GBR, including the feature at Broad Sound. Broad Sound is a highly turbid, funnel shaped estuary in the southern GBR (Figure 5.14) dominated by exceptional (8-10 m) tidal ranges (Pickard et al., 1977; Kleypas, 1996), however no major rivers flow into it. Kleypas (1996) investigated the diurnal variability of TSS in Broad Sound and concluded that the strong tidal ranges induced resuspension and advection of TSS for several consecutive tidal cycles, until neap tides allowed sediment resettlement. Therefore, consistent $Max_{\Delta TSS}$ features, such as at Broad Sound and in the central-southern GBR (Figure 5.15), may be linked to the long-lasting resuspension effects of the semi-diurnal tides. In addition, moderate diurnal variability of TSS was observed within the GBR reef matrix, with higher variations during the dry season. These TSS features are potentially related to resuspension resulting from short lived tidal jets (Drew, 2011). The tidal jets have been previously investigated in the GBR utilising field data, aerial surveys, numerical models (Wolanski et al., 1988; Wolanski and Spagnol, 2000) and satellite data (Young et al., 1994; Delandmeter et al., 2017). The tidal jets have been associated with localized upwelling and nutrient exchange between the Coral Sea and the GBR lagoon (Thompson and Golding, 1981; Thomson and Wolanski, 1984; Wolanski et al., 1988). The location and occurrence of tidal jets are scarcely described due to lack of appropriate spatial and temporal resolution observations. However, Himawari-8 observations have the potential to identify and track such features at the required temporal resolution for resolving short-lived coastal processes.

The central-north GBR received above average rainfalls during the 2017-2018 wet season, resulting from a low-pressure system and the subsequent passage of tropical cyclone *Nora* in late March 2018 (Bureau of Meteorology, 2018). *Nora* approached the west coast of Cape York peninsula, after crossing the Gulf of Carpentaria and made landfall on the 24th of March as a category 3 system. As a result, extreme rainfalls and flash floods were experienced and the Herbert River discharge peaked at 500,000 ML/day in March, as the 4th major discharge event since 2010. Conversely, Fabricius et al. (2016) point out that short-lived discharge events may have long lasting impacts and reduce photic depth (water clarity) for many months after rivers started flowing. The authors identified that the lowest levels of photic depth were recorded in May, when river flows subsided, and recovery started. This corroborates the present findings that May was the month with the largest extent of TSS feature in the central and southern GBR, after experiencing high volumes of freshwater discharge from the wet season. Therefore, wet season freshwater discharge may be linked to the increased spatial extent of TSS features during dry season months, while seasonal wind patterns may be linked to the moderate-high diurnal variations of TSS found in the central and southern GBR lagoon. Finally, the tidal ranges may be associated with semi-permanent features of high diurnal variability adjacent to the coastal areas. Further investigation and correlation with continuous weather and oceanographic data are

needed for an improved understanding of the diurnal patterns of TSS in the GBR. Additional work is suggested to help to delineate more realistic boundaries of water quality guidelines, honestly reflecting the variability of coastal water quality.

The main limitation of this analysis concerns the reduced number of available observations in areas such as the central and northern GBR, as well as the Coral Sea, during the wet season. The reduced number of observations in the northern GBR is resultant from the effects of sun glint passage and intensive cloud cover in the area. The principal point of sun glint and its projected sun disk is generally closer to the GBR and to the southern hemisphere during the summer months. In addition, cloud cover intensifies during the monsoonal wet season, due to more frequent storms and the passage of low-pressure systems, such as tropical cyclones. As a result, a significant reduction in the number of days where ΔTSS was available may be expected during the wet season, whereas the observational gap during dry season can be largely associated with persistent cloud cover. Fortunately, the sun glint effects can be generally neglected in the GBR when utilising Himawari-8 observations during dry season months. In this case, the principal point of sun glint lies north of the equator and the projected sun disk seldom reaches the southern hemisphere, yielding more observations for the entire GBR. Nonetheless, sun glint correction of Himawari-8 observations is suggested for expanding image and products availability in the tropics all year round.

Chapter 6: Summary and Outlook

Synoptic monitoring of water quality in the extensive and optically complex GBR still is a priority and great challenge for environmental managers and researchers (Devlin et al., 2015b; Brodie et al., 2019). Ocean colour sensors, such as MODIS/Aqua, VIIRS and Sentinel-3, provide a cost-effective and synoptic monitoring tool for daily to inter-annual water quality assessments of the GBR (Schroeder et al., 2012; Petus et al., 2019; Gruber et al., 2020). However, the revisit frequency of current ocean colour sensors onboard LEO satellites has hindered the broader understanding of water quality dynamics driven by diurnal coastal processes. Meteorological sensors onboard geostationary satellites acquire observations at a higher temporal resolution (e.g., 10 minutes) compared to LEO satellites, and have encouraged studies on ocean colour at diurnal scales (Neukermans et al., 2012b; Lavigne and Ruddick, 2018; Dorji and Fearns, 2018). Himawari-8 is a next-generation meteorological sensor onboard a geostationary platform launched in July 2014. It provides observations over Australia every 10 minutes, with improved spectral, spatial, and radiometric capabilities compared to its predecessors. Although ocean colour remote sensing has stringent radiometric and spectral requirements, Himawari-8 offers an unprecedented number of observations for the advanced water quality monitoring of the GBR. An extensive review (Chapter 1) revealed that there are currently no advanced remote sensing methods that have been locally validated for the synoptic monitoring of water quality at diurnal scales in the GBR.

The objective of this thesis was to develop and validate a physics-based algorithm to determine the diurnal dynamics of coastal water quality parameters in the GBR from Himawari-8 observations. The algorithm was developed with radiative transfer simulations of the Himawari-8 visible and near-infrared bands, which served as training and testing datasets for a one-step inversion with multi-layer perceptron (Chapter 2). The developed inversions were applied to Himawari-8 observations for validation against concurrent *in situ* datasets of CHL, TSS and YEL in the GBR (Chapter 3). The limitations of the best-performing algorithm were evaluated (Chapter 4), and the algorithm was then applied to investigate the diurnal variability of water quality in the coastal GBR (Chapter 5). The results revealed spatio-temporal fluctuations of TSS not previously reported by conventional monitoring methods and have advanced our knowledge on water quality dynamics in the GBR.

6.1 Summary of Algorithm Development

The present work made a significant contribution to the development of inversion methods for ocean colour remote sensing from geostationary satellites. Radiative transfer simulations of the ocean-atmosphere system were suitable for the development of an advanced physics-based algorithm for

coastal water quality retrievals with Himawari-8. A large, representative, and high-quality training dataset is the premise of good machine learning algorithms, especially for optically complex problems in remote sensing, which is the case for the coastal GBR. The coupled ocean-atmosphere radiative transfer simulations provided a large and robust database of the top of atmosphere radiances (L_{TOA}) distribution in the Himawari-8 visible and near-infrared bands. The L_{TOA} were simulated for a wide range of solar and observation angles, incorporating diurnal changes in illumination conditions, to match those experienced by Himawari-8. In addition, the synthetic IOPs input to the simulations were generated by employing bio-optical assumptions regionally tuned for the optical variability of the GBR. Moreover, the algorithm's robustness to input noise was especially advantageous considering Himawari-8 does not meet the minimum radiometric requirements of an ocean colour sensor and environmental noise, particularly from the atmosphere, can largely impact the retrievals.

The ANN algorithm developed in this work allowed the direct inversion of L_{TOA} to ocean colour products (CHL, TSS and YEL), without an explicit atmospheric correction procedure. This is of great advantage compared to traditional methods based on the inversion of normalized water-leaving reflectances, in which the accuracy of the final inversion is subject to the accuracy of the atmospheric correction procedure (Schroeder et al., 2007a; Brockmann et al., 2016; Hieronymi et al., 2017). Despite Himawari-8 spectral limitations, the ANN retrievals compared well to target outputs from simulated testing datasets and provided confidence in the quality of the trained algorithms. These results encouraged further employment of developed ANN algorithms to Himawari-8 observations and validation against *in situ* water quality data in the GBR.

6.2 Summary of Algorithm Validation

The trained and tested ANN experiments were applied to cloud and glint-free hourly aggregated Himawari-8 observations. The derived CHL, TSS and YEL products were validated with an extensive database of *in situ* water quality parameters collected in the coastal GBR. In general, the retrieval performances improved by using hourly aggregated Himawari-8 observations (instead of the closest 10-minute observation per matchup), corroborating previous studies (Ruddick et al., 2014; Murakami, 2016b; Lavigne and Ruddick, 2018). The validation protocol employed careful assessment and quality control of *in situ* measurements and satellite observations, following the extensive experience of previous validation exercises in the GBR and in other coastal waters (Doerffer, 2002; Schroeder et al., 2018). Employing a rigorous validation protocol is critical considering that the *in situ* datasets were collected in optically complex waters by multiple research agencies, with potentially varying sampling methodologies.

The moderate performance to estimate CHL and YEL in the coastal GBR were largely associated with Himawari-8's insufficient spectral resolution and the width of the visible bands to resolve their overlapping absorption features. Moreover, Himawari-8 may provide insufficient radiometric accuracy for CHL and YEL retrievals. Although hourly aggregated observations improved retrieval performances, an explicit atmospheric correction may further reduce errors in estimating CHL and YEL from Himawari-8 in the coastal GBR (Schroeder et al., 2007b). TSS was estimated within the accuracy targets defined for ocean colour retrievals with Sentinel-3 in Case 2 waters (Donlon, 2011), particularly for TSS above 0.1 mg L^{-1}. The present algorithm compares well with those using atmospherically corrected Himawari-8 observations (Dorji and Fearns, 2018; Ding et al., 2020; Hafeez et al., 2021), indicating the suitability of deriving coastal TSS with one-step inversions. Nevertheless, an explicit atmospheric correction procedure may improve retrievals for the lowest range of TSS (< 1.0 mg L^{-1}), which are likely affected by the low radiometric performance of Himawari-8.

The algorithm performance was largely dependent on how well the bio-optical model represented the local variability of the optical constituents. In this study, a conventional bio-optical model based on a global database of phytoplankton absorption properties (Bricaud et al., 1998) was employed for CHL parameterization. Thus, the bio-optical models utilised for CHL would benefit from a regionalised parameterization, rather than a more generalized assumption, to encompass the optical complexity found in the GBR. Improvements in algorithm parameterization would require a large and comprehensive database of *in situ* bio-optical measurements covering the relevant spatial and temporal scales of variability associated with coastal processes.

Despite the efforts of multiple research agencies in collecting valuable water quality data, *in situ* datasets remain scarce over the GBR and tend to be focused on wet season flood events. One exception is the LJCO, which provides a consistent and continuous database of bio-optical and water quality parameters in the coastal GBR. LJCO is the only facility in the southern hemisphere that simultaneously collects in-water and above-water observations specifically for ocean colour validation activities. The fortnightly laboratory measurements of TSS, CHL and YEL at LJCO constituted about one-third of the entire quality-controlled validation dataset available between 2014 and 2018 in the coastal GBR.

However, rigorous protocols need to be followed to reduce uncertainties in *in situ* measurements used for algorithm parameterization and validation in coastal waters. For instance, triplicate samples are recommended for the determination of TSS with the gravimetric method, and High Performance Liquid Chromatography is preferred over fluorometry for deriving total CHL and associated pigments (Mueller, 2003; Hooker et al., 2012). In addition, validation samples should be taken in spatially homogeneous waters (Doerffer, 2002), which is especially difficult in coastal and

highly transitional waters, such as during flood plumes. Nevertheless, water quality *in situ* measurements have been made available by multiple research agencies with diverse scientific priorities employing distinctive sampling and analysis methods. Considerable deviations have been reported from individual laboratories when analysing water samples for the measurement of TSS, and a ring-test analysis is recommended. In addition, meticulous quality control of multiple datasets is required for an accurate parameterization and evaluation of ocean colour algorithms, which is usually carried out with the expertise of remote sensing specialists.

6.3 Summary of Detection Limits

The qualitative and quantitative limitations of the algorithm developed for TSS were investigated at two distinct temporal resolutions: 10-minutes and hourly aggregates. A visual analysis revealed that TSS products presented a horizontal striping pattern associated with the instrument calibration and severe granulation associated with Himawari-8 radiometric quality and environmental noise. The granulated patterns were largely reduced in hourly composites and with the application of a boxcar spatial filter, particularly in areas where TSS was below 1 mg L^{-1}. Spatial filtering improved visual quality while retaining consistency of products, showing mesoscale features offshore the GBR lagoon that were previously veiled by granulation. Additionally, the spatial filtering was efficient for the elimination of outliers potentially associated with undetected clouds or cloud edges. However, striping correction needs to be further addressed for appropriate ocean colour investigations with Himawari-8 observations in open ocean areas (Murakami, 2016b; Okuyama et al., 2018).

Nonetheless, coastal waters with moderate-turbid levels of TSS (> 1 mg L^{-1}) were less affected by striping and granulation patterns, at both temporal resolutions investigated. The marine signal over coastal and turbid waters may be larger than noise levels and reasonable SNR can be achieved for ocean colour applications (Neukermans et al., 2009; Vanhellemont et al., 2014; Kudela et al., 2019), sparing the need for aggregating observations. Still, aggregating observations may be useful for decreasing data gaps due to transient clouds and cloud shadows (Qi et al., 2017) and may speed up the inversion of large Himawari-8 images for operational activities. Thus, noise reduction can be achieved with hourly composites of 10-minute Himawari-8 observations, while offering enough observations to capture tidal processes.

The SNR of the Himawari-8 visible and near-infrared bands were quantified over a typical cloud-free oceanic target. As expected, the SNR of hourly aggregated observations was superior compared to the ones calculated for 10-minute observations, confirming prior recommendations (IOCCG, 2012b; Vanhellemont et al., 2014; Ruddick et al., 2014). However, the Himawari-8 SNRs were at least 3 times lower than the baseline SNR recommended for contemporary ocean colour sensors (IOCCG, 2012a;

Muller-Karger et al., 2018). Still, the ANN algorithm for TSS was stable against several levels of noise added to the input data, which is suitable for the inversion of the low SNR Himawari-8 observations. The application of an explicit atmospheric correction scheme may further improve retrievals and reduce noise levels, especially in open ocean waters. Finally, the detection limit of estimating TSS with Himawari-8 (0.25 mg L^{-1}) was comparable to the detection limits of TSS determined with the gravimetric method (0.4 mg L^{-1}) by multiple laboratories. Despite current limitations, the present algorithm developed for Himawari-8 can be confidently applied to retrieve TSS and to investigate diurnal processes in the coastal GBR.

6.4 Summary of Algorithm Application

Himawari-8 ultra-high temporal resolution of 10 minutes is a striking advantage, compared to once/twice-a-day MODIS, Sentinel-3 and VIIRS scanning capabilities. At least 48 images per day can be obtained from Himawari-8, which is a fifty-fold increase in observations compared to contemporary ocean colour sensors. This chapter assessed Himawari-8 products' ability to quantify and monitor the diurnal variability of water quality in the GBR. In general, Himawari-8 TSS products compared remarkably well to concurrent measurements of *in situ* TSS derived from particulate backscattering measurements at LJCO. Significant hourly fluctuations of TSS (5 mg L^{-1}) were shown at LJCO, otherwise underrepresented by daily *in situ* measurements or ocean colour observations. The diurnal fluctuations of TSS were primarily associated with the local tidal oscillations and with freshwater discharge from the Herbert River. Moreover, Himawari-8 hourly observations allowed the tracking and mapping of the Herbert River plume, revealing intricate coastal dynamics driving plume extent and direction. Additionally, the plume arrival was visually captured by a webcam installed at LJCO, providing an integrated assessment of plume dynamics substantially backed by Himawari-8 spatial observations.

Although the analysis was carried in one specific site for a few instances, the results confirm the ability of using Himawari-8 for improved monitoring of the coastal GBR. Himawari-8 provides an unprecedented increase in quantitative observations at spatial scales far exceeding the monitoring capabilities currently employed in the GBR. In addition, the Himawari-8 inversion with the ANN procedure is fast, taking ~1 minute to retrieve water quality parameters for the entire GBR area, and allowing the near-real time dissemination of large volumes of satellite data products at operational levels. The second section of this chapter revealed that diurnal changes of TSS > 5 mg L^{-1} are a persistent feature in the inshore and mid-shelf GBR throughout the year. The TSS diurnal changes generally exceeded the guideline threshold value of 2.0 mg L^{-1} for the inshore and mid-shelf GBR, indicating poor coastal water quality all year round. However, diurnal changes of TSS were more pronounced during

the dry season, particularly in the southern mid-shelf GBR, most likely due to the short temporal scale processes, such as tides, winds, and episodic floods.

6.5 Future Research

This study demonstrated the potential of a physics-based algorithm to provide accurate water quality retrievals from a geostationary sensor in the GBR. Nevertheless, inaccuracies related to sensor noise, parameterization of bio-optical models, physical and environmental effects, and the inaccuracy of the *in-situ* measurements themselves are required to be addressed for improved retrievals. Moreover, the accuracy of the method will be influenced by the physical effects not included in the simulations, such as wind-dependent whitecaps, polarization, bottom reflectance, and fluorescence. The inclusion of these effects in the radiative transfer simulations are likely to improve the accuracy of the estimated coastal water quality parameters and should be tested in future work. More specifically, the accuracy for deriving CHL and YEL from Himawari-8 may be improved if considering fluorescence (Dall'Olmo and Gitelson, 2005) and employing an explicit atmospheric correction (Schroeder et al., 2007a).

Although the present method does not employ an explicit atmospheric correction, the NIR band (865 nm) of Himawari-8 was chosen for the algorithm. However, the sensitivity analysis demonstrated that turbid waters such as over flood plumes (TSS ~ 100 mg L^{-1}), or during blooms of *Trichodesmium* (McKinna et al., 2011) may contribute to the L_{TOA} in the NIR band. Alternatively, the Himawari-8 short-wave infrared (SWIR) bands (1610 and 2257 nm) could be added for improved retrievals because no signal from the ocean is detected at this band (Ruddick et al., 2014; Vanhellemont and Ruddick, 2015). The Himawari-8 SWIR bands scans at a 2 km spatial resolution (whereas VNIR bands at 1 km) and may be too coarse to resolve the atmospheric signal in coastal waters. However, it has been demonstrated that the Himawari-8 SWIR bands improve the atmospheric correction and subsequent TSS retrievals over turbid waters at 2 km spatial resolution (Dorji and Fearns, 2018; Ding et al., 2020; Hafeez et al., 2021). In addition, the use of SWIR bands could be especially critical for atmospheric correction if water quality retrievals in clear and open ocean waters are to be explored from Himawari-8.

Future methods should consider including the effects of whitecaps, sun glint, bottom reflectance, CHL and YEL fluorescence, BRDF, polarization and the detection of large algal blooms. Swell waves and resultant whitecaps and bubbles may largely affect ocean colour retrievals at fine scale spatial resolutions (< 30 m) (Stramska and Petelski, 2003; Dierssen, 2019). A simple parameterization based on wind-speed (Cox and Munk, 1954) is suggested to account for whitecaps at the Himawari-8 bands at 0.5 to 1 km spatial resolution. Sun glint daily covers large areas of the tropical oceans from the

geostationary point of view, masking the spectral variability from the ocean. The effects of sun glint at the Himawari-8 L_{TOA} are already considered in the radiative transfer simulations employed in this study. Therefore, a sun glint correction is suggested (IOCCG, 2012b) for accurate retrievals near the edges of the sun disk and for reduced data gaps, allowing more observations to be available during summer in the entire GBR.

Although Himawari-8 broad VNIR bands are centred near the YEL and CHL fluorescence peaks, increased spectral and radiometric resolutions are required to accurately estimate fluorescence from L_{TOA} (Ahn et al., 2012). A different version of the MOMO code includes inelastic scattering calculations (Hollstein et al., 2010; Bismarck and Fischer, 2013). This could be employed for assessment of inelastic scattering effects on the performance of water quality retrievals from Himawari-8. Likewise, a version of the MOMO code which accounts for the polarization is available, and including its effects could improve water quality retrievals (Hollstein and Fischer, 2012). Moreover, floating mats of macroalgae, such as *Sargassum* and *Ulva* have been successfully tracked and mapped with Himawari-8 (Chen et al., 2019). A parameterization of the model-based algorithm for detecting different species of algal blooms in the coastal GBR is suggested.

It has been previously demonstrated that Himawari-8 derived TSS compared reasonably well against TSS concurrently derived from MODIS/Aqua and Landsat-8/OLI sensors (Dorji and Fearns, 2018). An inter-comparison exercise against concurrent products from Sentinel-3 OLCI sensor would further enlighten the strengths and limitations of the present algorithm developed for Himawari-8. In addition, the relationship between TSS and turbidity (as an alternative to particulate backscattering) can be established from continuous measurements at LJCO and serve for deriving continuous TSS to validate Himawari-8 products.

This study briefly demonstrated that the inshore and mid-shelf GBR may experience very rapid fluctuations in water quality associated with underlying coastal processes and weather events. However, a multivariate statistical analysis between Himawari-8 TSS and concurrent oceanographic observations would help to determine the drivers of short temporal scale water quality fluctuations in the GBR (Bierman et al., 2011; Kitsiou and Karydis, 2011; Ha et al., 2020). For instance, diurnal measurements of tidal ranges, wind speed and direction, salinity, turbidity, and absorption, etc., are available at LJCO for this task. In addition, the Herbert River discharge is measured 13 km upstream the river mouth and would be a useful dataset to elucidate the influence of freshwater plumes at LJCO.

Himawari-8 provides a sufficiently large (2015-2021) dataset and with enough temporal resolution to investigate diurnal to inter-annual trends and patterns of water quality in the GBR. High-frequency dynamics of water quality could be explored with Hovmöller diagrams of Himawari-8 TSS

(every 10 minutes) across a specific latitude or longitude. Himawari-8 derived TSS is comparable to and provides superior temporal coverage to GOCI (every 1h) derived TSS (Ding et al., 2020).

This study provides evidence that the Marine Water Quality Metric based on annual averages of TSS need to be reviewed for more accurate assessments of water quality in the GBR. Concerns have been previously expressed by the Reef Plan Independent Science Panel (Reef Plan ISP) about the spatial and temporal insensitivities of the metric associated with annually averaging data over large areas. This is not surprising, considering daily ocean colour observations may introduce significant bias on calculating long term trends (Eleveld et al., 2014) and may not reflect the actual coastal dynamics of the GBR. The water quality metric currently used for the Reef Report Card is derived from a biogeochemical model that assimilates daily atmospherically corrected surface reflectance from Sentinel-3A (Australian and Queensland Governments, 2020). In this context, the water quality products derived at diurnal scale from Himawari-8 offer an opportunity to: reassess the current methodology employed for tracking and mapping flood plumes (Petus et al., 2019); to calculate the frequency that the GBR's ecosystems are exposed to freshwater discharge and pollutants (Alvarez-Romero et al., 2013; Gruber et al., 2020); and to increase the data available for validation and assimilation into biogeochemical and ocean colour models currently being employed for the GBR (Baird et al., 2016; Baird et al., 2020).

Himawari-8 has been useful for monitoring and tracking large patches of harmful algal blooms in Lake Taihu in China, at diurnal scales, with comparable performance to GOCI and MODIS/Aqua (Chen et al., 2019). The floating algae index derived every 10 minutes from Himawari-8 revealed more frequent events than those observed by GOCI at hourly temporal resolution. Thus, Himawari-8 ultra-high frequency measurements have the potential to improve coastal monitoring at scales relevant for environmental management and emergency response. Nevertheless, a tailored parameterization of the bio-optical models are required to contemplate the macroscopic optical properties of distinctive algal blooms (Ebert, 2009). In addition, Himawari-8 bands may be sufficient to estimate terrestrially sourced YEL, offering the opportunity to map the freshwater extent into the GBR (Schroeder et al., 2012) at diurnal scales.

In summary, this thesis has demonstrated the potential of Himawari-8 observations for mapping and quantifying the water quality over the entire GBR at diurnal to seasonal scales. It is remarkable that accurate and relevant information could be extracted from Himawari-8, considering it is not a dedicated ocean colour sensor and presents challenging limitations for marine retrievals. However, the results presented in this thesis are a clear and significant improvement on the scarce information provided by contemporary ocean colour sensors such as MODIS/Aqua, VIIRS and Sentinel-3. Additionally, the algorithm presented in this study can be directly employed to Himawari-9

observations, which is identical to and planned to succeed Himawari-8 by 2029. Similarly, the Advanced Meteorological Imager (AMI) on board the GEOKOMPSAT-2A as well as the GOCI-II (GEOKOMPSAT-2B) are currently observing Australia and East Asia with a payload comparable or superior to Himawari-8/9. The next-generation Himawari mission (Himawari-10) is in the planning phase and additional channels in the visible range, as well as improved sensitivity and spatial resolution are a possibility. Based on the lessons learned here and on recent efforts in the field (Neukermans et al., 2009; IOCCG, 2012b; Ruddick et al., 2014; Kwiatkowska et al., 2015; Murakami, 2016b; Lavigne and Ruddick, 2018), the recommendations for the next-generation GEO meteorological sensors to improve their ocean colour applications would include:

- Additional bands in the visible spectrum, such as 412 and 443 nm for resolving the overlapping absorption features of CHL and YEL and between 660-710 nm for retrieval of CHL and fluorescence and absorption in turbid waters
- Sufficient SWIR bands for turbid water atmospheric correction with compatible spatial resolution to the visible bands
- Narrower bandwidths (~10 nm) for the visible channels
- Increased nominal spatial resolutions (~300 m) for coastal waters
- Higher radiometric sensitivity (i.e., SNR 1000: 1) and resolution (> 12 bits)
- Solar diffuser to perform on-board calibration and to track the radiometric stability of the visible and near-infrared sensors
- Extended lifetime (~10 years) and mission continuation to provide measurements for long-term assessments of trends and patterns

These characteristics would largely advance the capabilities of ocean colour algorithms developed for geostationary sensors, allowing more accurate retrievals in coastal waters at diurnal scales. Hopefully, a constellation of geostationary satellites with sufficient capabilities for ocean colour remote sensing will be progressively available and a synergistic approach could exponentially increase the data coverage for water quality monitoring in the GBR. In this context, the present study provides an advanced algorithm and a prospect of potential applications to be developed when ocean colour sensors onboard geostationary platforms become a reality for Australia.

Chapter 7: References

AERONET. (2020). Aerosol Robotic Network. Retrieved from https://aeronet.gsfc.nasa.gov/ (accessed on 10/03/2017).

Ahmed, S., El-Habashi, A., Lovko, V. (2017). Neural network retrievals of phytoplankton absorption and Karenia brevis harmful algal blooms in the West Florida Shelf. Paper presented at the Proceedings of SPIE.

Ahn, J.-H., Park, Y.-J., Ryu, J.-H., Lee, B. (2012). Development of atmospheric correction algorithm for Geostationary Ocean Color Imager (GOCI). Ocean Science Journal, 47(3), 247-259.

Alvarez-Romero, J.G., Devlin, M., Teixeira da Silva, E., Petus, C., Ban, N.C., Pressey, R.L., Kool, J., Roberts, J.J., Cerdeira-Estrada, S., Wenger, A.S., Brodie, J. (2013). A Novel Approach to Model Exposure of Coastal Marine Ecosystems to Riverine Flood Plumes Based on Remote Sensing Techniques. Journal of environmental management, 119, 194-207.

Ametistova, L. (2004). Ocean Colour Remote Sensing of Flood Plumes in the Great Barrier Reef, Australia. (PhD Thesis). University of Sydney.

Ametistova, L., Jones, I.S.F. (2005). Sediments flows in the Great Barrier Reef lagoon as revealed by MERIS satellite data. Paper presented at the Proceedings, 31st International Symposium on Remote Sensing of Environment, ISRSE 2005: Global Monitoring for Sustainability and Security.

Australian and Queensland Governments. (2020). Marine Modelling Methods, Reef Water Quality Report Card 2019. Report Card. State of Queensland. https://www.reefplan.qld.gov.au/__data/assets/pdf_file/0017/211670/report-card-2019-methods-marine-modelling.pdf

Australian Ocean Data Network, A. (2020). Australia's Integrated Marine Observing System (IMOS). Retrieved from https://portal.aodn.org.au/ (accessed on 20/02/2017).

Babin, M. (2000). Coastal surveillance through observation of ocean colour (COASTLOOC). Laboratoire de Physique et Chimie Marines, Villefranche-Sur-Mer, France

Babin, M., Morel, A., Fournier-Sicre, V., Fell, F., Stramski, D. (2003a). Light scattering properties of marine particles in coastal and open ocean waters as related to the particle mass concentration. Limnology and Oceanography, 48(2), 843-859.

Babin, M., Morel, A., Gentili, B. (1996). Remote sensing of sea surface Sun-induced chlorophyll fluorescence: consequences of natural variations in the optical characteristics of phytoplankton and the quantum yield of chlorophyll a fluorescence. International Journal of Remote Sensing, 17(12), 2417-2448.

Babin, M., Stramski, D., Ferrari, G.M., Claustre, H., Bricaud, A., Obolensky, G., Hoepffner, N. (2003b). Variations in the light absorption coefficients of phytoplankton, nonalgal particles, and dissolved organic matter in coastal waters around Europe. Journal of Geophysical Research: Oceans, 108(C7).

Bailey, S.W., Werdell, P.J. (2006). A multi-sensor approach for the on-orbit validation of ocean color satellite data products. Remote Sensing of Environment, 102(1-2), 12-23.

Bainbridge, Z., Lewis, S., Bartley, R., Fabricius, K., Collier, C., Waterhouse, J., Garzon-Garcia, A., Robson, B., Burton, J., Wenger, A., Brodie, J. (2018). Fine sediment and particulate organic matter: A review and case study on ridge-to-reef transport, transformations, fates, and impacts on marine ecosystems. Marine pollution bulletin, 135, 1205-1220.

Bainbridge, Z.T., Wolanski, E., Álvarez-Romero, J.G., Lewis, S.E., Brodie, J.E. (2012). Fine sediment and nutrient dynamics related to particle size and floc formation in a Burdekin River flood plume, Australia. Marine pollution bulletin, 65(4–9), 236-248.

Baird, M.E., Cherukuru, N., Jones, E., Margvelashvili, N., Mongin, M., Oubelkheir, K., Ralph, P.J., Rizwi, F., Robson, B.J., Schroeder, T., Skerratt, J., Steven, A.D.L., Wild-Allen, K.A. (2016). Remote-sensing reflectance and true colour produced by a coupled hydrodynamic, optical, sediment, biogeochemical model of the Great Barrier Reef, Australia: Comparison with satellite data. Environmental Modelling & Software, 78, 79-96.

Baird, M.E., Wild-Allen, K.A., Parslow, J., Mongin, M., Robson, B., Skerratt, J., Rizwi, F., Soja-Woźniak, M., Jones, E., Herzfeld, M. (2020). CSIRO Environmental Modelling Suite (EMS): scientific description of the optical and biogeochemical models (vB3p0). Geoscientific Model Development, 13(9), 4503-4553.

Barnes, B.B., Hu, C., Schaeffer, B.A., Lee, Z., Palandro, D.A., Lehrter, J.C. (2013). MODIS-derived spatiotemporal water clarity patterns in optically shallow Florida Keys waters: A new approach to remove bottom contamination. Remote Sensing of Environment, 134, 377-391.

Bartlett, J.S., Voss, K.J., Sathyendranath, S., Vodacek, A. (1998). Raman scattering by pure water and seawater. Applied optics, 37(15), 3324-3332.

Bartley, R., Waters, D., Turner, R., Kroon, F., Garzon-Garcia, A., Kuhnert, P., Lewis, S., Smith, R., Bainbridge, Z., Olley, J. (2017). 2017 Scientific Consensus Statement: land use impacts on the Great Barrier Reef water quality and ecosystem condition, Chapter 2: sources of sediment, nutrients, pesticides and other pollutants to the Great Barrier Reef.

Beer, A. (1852). Bestimmung der absorption des rothen lichts in farbigen flussigkeiten. Ann. Physik, 162, 78-88.

Behrenfeld, M.J., Falkowski, P.G. (1997). A consumer's guide to phytoplankton primary productivity models. Limnology and Oceanography, 42(7), 1479-1491.

Behrenfeld, M.J., Westberry, T.K., Boss, E., O'Malley, R.T., Siegel, D.A., Wiggert, J.D., Franz, B., McClain, C., Feldman, G., Doney, S.C. (2009). Satellite-detected fluorescence reveals global physiology of ocean phytoplankton. Biogeosciences, 6(5), 779-794.

Bennartz, R., Fischer, J. (2000). A modified k-distribution approach applied to narrow band water vapour and oxygen absorption estimates in the near infrared. Journal of Quantitative Spectroscopy and Radiative Transfer, 66(6), 539-553.

Bernardo, N., Alcântara, E., Watanabe, F., Rodrigues, T., Carmo, A., Gomes, A., Andrade, C. (2018). Glint Removal Assessment to Estimate the Remote Sensing Reflectance in Inland Waters with Widely Differing Optical Properties. Remote Sensing, 10(10), 1655.

Bessho, K., Date, K., Hayashi, M., Ikeda, A., Imai, T., Inoue, H., Kumagai, Y., Miyakawa, T., Murata, H., Ohno, T. (2016). An introduction to Himawari-8/9—Japan’s new-generation geostationary

meteorological satellites. Journal of the Meteorological Society of Japan. Ser. II, 94(2), 151-183.

Bhatt, R., Doelling, D., Haney, C., Scarino, B., Gopalan, A. (2018). Consideration of Radiometric Quantization Error in Satellite Sensor Cross-Calibration. Remote Sensing, 10(7), 1131.

Bierman, P., Lewis, M., Ostendorf, B., Tanner, J. (2011). A review of methods for analysing spatial and temporal patterns in coastal water quality. Ecological Indicators, 11(1), 103-114.

Bismarck, J.v., Fischer, J. (2013). An examination of errors in computed water-leaving radiances due to a simplified treatment of water Raman scattering effects. Paper presented at the AIP Conference Proceedings.

Bisson, K., Boss, E., Westberry, T., Behrenfeld, M. (2019). Evaluating satellite estimates of particulate backscatter in the global open ocean using autonomous profiling floats. Optics express, 27(21), 30191-30203.

Blondeau-Patissier, D., Brando, V.E., Lønborg, C., Leahy, S.M., Dekker, A.G. (2018). Phenology of Trichodesmium spp. blooms in the Great Barrier Reef lagoon, Australia, from the ESA-MERIS 10-year mission. PloS one, 13(12), e0208010.

Blondeau-Patissier, D., Dekker, A.G., Schroeder, T., Brando, V.E., Committee, S.o.t.E. (2011). Phytoplankton dynamics in shelf waters around Australia. CSIRO Land & Water. Report prepared for the Australian Government Department of Sustainability, Environment, Water, Population and Communities on behalf of the State of the Environment 2011 Committee. Canberra: DSEWPaC, 2011.

Blondeau-Patissier, D., Gower, J.F.R., Dekker, A.G., Phinn, S.R., Brando, V.E. (2014a). A review of ocean color remote sensing methods and statistical techniques for the detection, mapping and analysis of phytoplankton blooms in coastal and open oceans. Progress in Oceanography, 123, 123-144.

Blondeau-Patissier, D., Schroeder, T., Brando, V., Maier, S., Dekker, A., Phinn, S. (2014b). ESA-MERIS 10-Year Mission Reveals Contrasting Phytoplankton Bloom Dynamics in Two Tropical Regions of Northern Australia. Remote Sensing, 6(4), 2963-2988.

Blondeau-Patissier, D., Schroeder, T., Irving, P., Witte, C., Steven, A. (2020). Satellite detection of oil spills in the Great Barrier Reef using the Sentinel-1,-2 and-3 satellite constellations. A technical assessment of a synergistic approach using SAR, optical and thermal information. CSIRO Oceans and Atmosphere (CSIRO O&A). Brisbane, Australia https://doi.org/10.25919/5e46e030e3029

Blondeau-Patissier, D., Brando, V.E., Oubelkheir, K., Dekker, A.G., Clementson, L.A., Daniel, P. (2009). Bio-optical variability of the absorption and scattering properties of the Queensland inshore and reef waters, Australia. Journal of Geophysical Research, 114(C5).

Blum, M., Rozanov, V., Burrows, J., Bracher, A. (2012). Coupled ocean-atmosphere radiative transfer model in the framework of software package SCIATRAN: Selected comparisons to model and satellite data. Advances in Space Research, 49(12), 1728-1742.

Boss, E., Taylor, L., Gilbert, S., Gundersen, K., Hawley, N., Janzen, C., Johengen, T., Purcell, H., Robertson, C., Schar, D.W. (2009). Comparison of inherent optical properties as a surrogate

for particulate matter concentration in coastal waters. Limnology and Oceanography: Methods, 7(11), 803-810.

Bowers, D.G., Md-Suffian, I., Mitchelson-Jacob, E.G. (2012). Bio-optical properties of east coast Malaysia waters in relation to remote sensing of chlorophyll. International Journal of Remote Sensing, 33(1), 150-169.

Bracaglia, M., Santoleri, R., Volpe, G., Colella, S., Braga, F., Bellafiore, D., Brando, V.E. (2020). A Virtual Geostationary Ocean Colour Sensor to characterise the river-sea interaction over the North Adriatic Sea. Paper presented at the EGU General Assembly Conference Abstracts.

Bracaglia, M., Volpe, G., Colella, S., Santoleri, R., Braga, F., Brando, V.E. (2019). Using overlapping VIIRS scenes to observe short term variations in particulate matter in the coastal environment. Remote Sensing of Environment, 233, 111367.

Brajard, J., Jamet, C., Moulin, C., Thiria, S. (2006a). Use of a neuro-variational inversion for retrieving oceanic and atmospheric constituents from satellite ocean colour sensor: application to absorbing aerosols. Neural networks : the official journal of the International Neural Network Society, 19(2), 178-185.

Brajard, J., Jamet, C., Moulin, C., Thiria, S. (2006b). Validation of a neuro-variational inversion of ocean colour images. Advances in Space Research, 38(10), 2169-2175.

Brando, V., Dekker, A., Schroeder, T., Park, Y.J., Clementson, L.A., Steven, A., Blondeau-Patissier, D. (2008). Satellite retrieval of chlorophyll CDOM and NAP in optically complex waters using a semi-analytical inversion based on specific inherent optical properties. A case study for Great Barrier Reef coastal waters. Paper presented at the In: Proceedings of Ocean Optics XIX; 6-10 October 2008; 0445. Barga, Italy. http://hdl.handle.net/102.100.100/122146?index=1

Brando, V., Dekker, A.G., Park, Y.J., Schroeder, T. (2012). Adaptive semianalytical inversion of ocean color radiometry in optically complex waters. Applied optics, 51(15).

Brando, V., Keen, R., Daniel, P., Baumeister, A., Nethery, M., Baumeister, H., Hawdon, A., Swan, G., Mitchell, R., Campbell, S., Schroeder, T., Park, Y.J., Edwards, R., Steven, A.D., Allen, S., Clementson, L., Dekker, A.G. (2010). The Lucinda Jetty Coastal Observatory's role in satellite ocean colour calibration and validation for Great Barrier Reef coastal waters. Paper presented at the In OCEANS 2010 IEEE-Sydney (pp. 1-8). IEEE.

Brando, V., Schroeder, T., King, E., Dyce, P. (2015). Reef Rescue Marine Monitoring Program: Using remote sensing for GBR-wide water quality Final Report for 2012/13 Activities.

Brekke, C., Solberg, A.H. (2005). Oil spill detection by satellite remote sensing. Remote sensing of environment, 95(1), 1-13.

Brewin, R.J.W., Sathyendranath, S., Müller, D., Brockmann, C., Deschamps, P.-Y., Devred, E., Doerffer, R., Fomferra, N., Franz, B., Grant, M., Groom, S., Horseman, A., Hu, C., Krasemann, H., Lee, Z., Maritorena, S., Mélin, F., Peters, M., Platt, T., Regner, P., Smyth, T., Steinmetz, F., Swinton, J., Werdell, J., White, G.N. (2015). The Ocean Colour Climate Change Initiative: III. A round-robin comparison on in-water bio-optical algorithms. Remote Sensing of Environment, 162, 271-294.

Bricaud, A., Babin, M., Morel, A., Claustre, H. (1995). Variability in the chlorophyll-specific absorption coefficients of natural phytoplankton: Analysis and Parameterization. Journal of Geophysical Research, 100(C7), 13, 321-332.

Bricaud, A., Morel, A., Babin, M., Allali, K., Claustre, H. (1998). Variations of light absorption by suspended particles with chlorophyllaconcentration in oceanic (case 1) waters: Analysis and implications for bio-optical models. Journal of Geophysical Research: Oceans, 103(C13), 31033-31044.

Bricaud, A., Morel, A., Prieur, L. (1981). Absorption by dissolved organic matter of the sea (yellow substance) in the UV and visible domains. Limnology and Oceanography, 26(1), 43-53.

Brockmann, C., Doerffer, R., Peters, M., Stelzer, K., Embacher, S., Ruescas, A. (2016). Evolution of the C2RCC neural network for Sentinel 2 and 3 for the retrieval of ocean colour products in normal and extreme optically complex waters. Paper presented at the European Space Agency, (Special Publication) ESA SP.

Brodie, J., Devlin, M., Lewis, S. (2017). Potential enhanced survivorship of crown of thorns starfish larvae due to near-annual nutrient enrichment during secondary outbreaks on the central mid-shelf of the Great Barrier Reef, Australia. Diversity, 9(1), 17.

Brodie, J., Grech, A., Pressey, B., Day, J., Dale, A., Morrison, T., Wenger, A. (2019). The future of the Great Barrier Reef: the water quality imperative Trans.). In (Ed.), Coasts and Estuaries (ed., Vol. pp. 477-499). Elsevier.

Brodie, J., Schroeder, T., Rohde, K., Faithful, J., Masters, B., Dekker, A., Brando, V., Maughan, M. (2010). Dispersal of suspended sediments and nutrients in the Great Barrier Reef lagoon during river-discharge events: Conclusions from satellite remote sensing and concurrent flood-plume sampling. Marine and Freshwater Research, 61(6), 651-664.

Brodie, J., Waterhouse, J., Lewis, S., Bainbridge, Z., Johnson, J. (2009). Current loads of priority pollutants discharged from Great Barrier Reef Catchments to the Great Barrier Reef. ACTFR Report, 9(02).

Browne, N.K., Smithers, S.G., Perry, C.T. (2013). Spatial and temporal variations in turbidity on two inshore turbid reefs on the Great Barrier Reef, Australia. Coral Reefs, 32(1), 195-210.

Browning, T.J., Bouman, H.A., Moore, C.M. (2014). Satellite-detected fluorescence: Decoupling nonphotochemical quenching from iron stress signals in the South Atlantic and Southern Ocean. Global Biogeochemical Cycles, 28(5), 510-524.

Buckton, D., O'Mongain, E., Danaher, S. (1999). The use of Neural Networks for the estimation of oceanic constituents based on the MERIS instrument. International Journal of Remote Sensing, 20(9), 1841-1851.

Bukata, R.P., Jerome, J.H., Borstad, G.A., Brown, L.N., Gower, J.F. (2004). Mitigating the impact of trans-spectral processes on multivariate retrieval of water quality parameters from case 2 waters. Canadian journal of remote sensing, 30(1), 6-18.

Bukata, R.P., Jerome, J.H., Kondratyev, A.S., Pozdnyakov, D.V. (1995). Optical properties and remote sensing of inland and coastal waters. CRC press.

Bulgarelli, B., Zibordi, G. (2018). On the detectability of adjacency effects in ocean color remote sensing of mid-latitude coastal environments by SeaWiFS, MODIS-A, MERIS, OLCI, OLI and MSI. Remote sensing of environment, 209, 423-438.

Bureau of Meteorology, B. (2018). Queensland in March 2018: Tropical cyclone Nora; flooding in the northern tropics. Monthly Climate Summary. Retrieved from http://www.bom.gov.au/climate/current/month/qld/archive/201803.summary.shtml (accessed on 10/03/2018).

Bureau of Meteorology of Australia, B. (2016). Queensland Tide Tables. Retrieved from http://www.bom.gov.au/australia/tides/#!/qld-lucinda-offshore (accessed on 04/09/2016).

Bureau of Meteorology of Australia, B. (2021a). Recent and historical rainfall maps. Retrieved from http://www.bom.gov.au/climate/maps/rainfall/ (accessed on 01/05/2021).

Bureau of Meteorology of Australia, B. (2021b). Weekly Rainfall Update. Retrieved from http://www.bom.gov.au/climate/rainfall/archive/20210223.archive.shtml (accessed on 02/06/2021).

Burrage, D.M., Heron, M.L., Hacker, J.M., Stieglitz, T.C., Steinberg, C.R., Prytz, A. (2002). Evolution and dynamics of tropical river plumes in the Great Barrier Reef: An integrated remote sensing and in situ study. Journal of Geophysical Research: Oceans, 107(C12), SRF 17-11-SRF 17-22.

Cannizzaro, J.P., Carder, K.L. (2006). Estimating chlorophyll a concentrations from remote-sensing reflectance in optically shallow waters. Remote Sensing of Environment, 101(1), 13-24.

Chami, M., Larnicol, M., Minghelli, A., Migeon, S. (2020). Influence of the Suspended Particulate Matter on the Satellite Radiance in the Sunglint Observation Geometry in Coastal Waters. Remote Sensing, 12(9), 1445.

Chapron, B., Garello, R., Weissman, D.E. (2008). Ocean remote sensing: Challenges for the future. Paper presented at the OCEANS 2008.

Chen, J., Cui, T., Quan, W. (2015). A neural network-based four-band model for estimating the total absorption coefficients from the global oceanic and coastal waters. Journal of Geophysical Research: Oceans, 120(1), 36-49.

Chen, X., Shang, S., Lee, Z., Qi, L., Yan, J., Li, Y. (2019). High-frequency observation of floating algae from AHI on Himawari-8. Remote sensing of environment, 227, 151-161.

Cherukuru, N., Brando, V.E., Blondeau-Patissier, D., Ford, P.W., Clementson, L.A., Robson, B.J. (2017). Impact of wet season river flood discharge on phytoplankton absorption properties in the southern Great Barrier Reef region coastal waters. Estuarine, Coastal and Shelf Science, 196, 379-386.

Ciotti, A.M., Lewis, M.R., Cullen, J.J. (2002). Assessment of the relationships between dominant cell size in natural phytoplankton communities and the spectral shape of the absorption coefficient. Limnology and Oceanography, 47(2), 404-417.

Claasen, D.V.R., Jupp, D., Bolton, J., Zell, L. (1984). An initial investigation into the mapping of seagrass and water color with CZCS and Landsat in North Queensland, Australia. Paper presented at the Proc. 10th Int. Symp. for Machine Processing of Remotely Sensed Data, Purdue University, West Lafayette.

Clarke, G.L., Ewing, G.C., Lorenzen, C.J. (1970). Spectra of Backscattered Light from the Sea Obtained from Aircraft as a Measure of Chlorophyll Concentration. Science, 167.

Clementson, L.A., Parslow, J.S., Turnbull, A.R., Bonham, P.I. (2004). Properties of light absorption in a highly coloured estuarine system in south-east Australia which is prone to blooms of the toxic dinoflagellate Gymnodinium catenatum. Estuarine, Coastal and Shelf Science, 60(1), 101-112.

Clementson, L.A., Parslow, J.S., Turnbull, A.R., McKenzie, D.C., Rathbone, C.E. (2001). Optical properties of waters in the Australasian sector of the Southern Ocean. Journal of Geophysical Research: Oceans, 106(C12), 31611-31625.

Clerc, S., Donlon, C., Borde, F., Lamquin, N., Hunt, S.E., Smith, D., McMillan, M., Mittaz, J., Woolliams, E., Hammond, M. (2020). Benefits and lessons learned from the Sentinel-3 tandem phase. Remote Sensing, 12(17), 2668.

Committee on Extension to the Standard Atmosphere. (1976). U.S. Standard Atmosphere. NASA. Washington, D.C.

Concha, J., Mannino, A., Franz, B., Kim, W. (2019). Uncertainties in the Geostationary Ocean Color Imager (GOCI) Remote Sensing Reflectance for Assessing Diurnal Variability of Biogeochemical Processes. Remote Sensing, 11(3), 295.

Cox, C., Munk, W. (1954). Measurement of the Roughness of the Sea Surface from Photographs of the Sun's Glitter. J. Opt. Soc. Am., 44(11), 838-850.

D'Alimonte, D., Zibordi, G., Berthon, J.-F., Canuti, E., Kajiyama, T. (2012). Performance and applicability of bio-optical algorithms in different European seas. Remote Sensing of Environment, 124, 402-412.

D'Alimonte, D., Zibordi, G., Berthon, J.F. (2004). Determination of CDOM and NPPM Absorption Coefficient Spectra From Coastal Water Remote Sensing Reflectance. IEEE transactions on Geoscience and Remote Sensing, 42(8).

Da, C. (2015). Preliminary assessment of the Advanced Himawari Imager (AHI) measurement onboard Himawari-8 geostationary satellite. Remote Sensing Letters, 6(8), 637-646.

Dall'Olmo, G., Gitelson, A.A. (2005). Effect of bio-optical parameter variability on the remote estimation of chlorophyll-a concentration in turbid productive waters: experimental results. Applied optics, 44(3), 412-422.

De'ath, G., Fabricius, K.E., Sweatman, H., Puotinen, M. (2012). The 27-year decline of coral cover on the Great Barrier Reef and its causes. Proceedings of the National Academy of Sciences of the United States of America, 109(44), 17995-17999.

De'ath, G.A., Fabricius, K.K. (2008). Water quality of the Great Barrier Reef: distributions, effects on reef biota and trigger values for the protection of ecosystem health. Final Report to the Great Barrier Reef Marine Park Authority. Commonwealth of Australia and Australian Institute of Marine Science. Townsville

Deirmendjian, D. (1962). Scattering and polarization properties of polydispersed suspensions with partial absorption. RAND CORP SANTA MONICA CA.

Delandmeter, P., Lambrechts, J., Marmorino, G.O., Legat, V., Wolanski, E., Remacle, J.-F., Chen, W., Deleersnijder, E. (2017). Submesoscale tidal eddies in the wake of coral islands and reefs: satellite data and numerical modelling. Ocean Dynamics, 67(7), 897-913.

Devlin, M. (2005). Spatial and temporal patterns of flood plumes in the Great Barrier Reef, Australia. (PhD Thesis). James Cook University.

Devlin, M., Brodie, J. (2005). Terrestrial discharge into the Great Barrier Reef Lagoon: nutrient behavior in coastal waters. Marine pollution bulletin, 51(1-4), 9-22.

Devlin, M., Brodie, J., Bainbridge, Z., Lewis, S. (2008). Flood plumes in the GBR The Burdekin and Fitzroy flood plumes, 2007/08 Case studies for Marine Monitoring Program. Australian Centre for tropical Freshwater research, James Cook University, townsville.

Devlin, M., da Silva, E.T., Petus, C., Tracey, D. (2015a). Marine Monitoring Program: Final report of JCU Activities 2012/13 - Flood Plumes and Extreme weather monitoring for the Great Barrier Reef Marine Park Authority. James Cook University. Townsville, Australia

Devlin, M., Da Silva, E.T., Petus, C., Wenger, A.S., Zeh, D., Tracey, D., Álvarez-Romero, J.G., Brodie, J. (2013). Combining in-situ water quality and remotely sensed data across spatial and temporal scales to measure variability in wet season chlorophyll-a: Great Barrier Reef lagoon (Queensland, Australia). Ecological Processes, 2(1), 1-22.

Devlin, M., McKinna, L.W., Alvarez-Romero, J.G., Petus, C., Abott, B., Harkness, P., Brodie, J. (2012a). Mapping the pollutants in surface riverine flood plume waters in the Great Barrier Reef, Australia. Marine pollution bulletin, 65(4-9), 224-235.

Devlin, M., Petus, C., da Silva, E.T., Tracey, D., Wolff, N., Waterhouse, J., Brodie, J. (2015b). Water Quality and River Plume Monitoring in the Great Barrier Reef: An Overview of Methods Based on Ocean Colour Satellite Data. Remote Sensing, 7(10), 12909-12941.

Devlin, M., Schaffelke, B. (2009). Spatial extent of riverine flood plumes and exposure of marine ecosystems in the Tully coastal region, Great Barrier Reef. Marine and Freshwater Research, 60(11), 1109-1122.

Devlin, M., Schroeder, T., McKinna, L., Brodie, J., Brando, V., Dekker, A. (2012b). Monitoring and Mapping of Flood Plumes in the Great Barrier Reef Based on In Situ and Remote Sensing Observations Trans.). In Chang, N.-B. (Ed.), Advances in Environmental Remote Sensing to Monitor Global Changes (ed., Vol. pp. 147-191). Environmental Remote Sensing and Systems Analysis (pp.147-190): CRC Press. https://doi.org/10.1201/b11702.

Devlin, M., Waterhouse, J., McKinna, L., Lewis, M. (2010). Terrestrial Runoff in the Great Barrier Reef. Marine Monitoring Program: Tully and Burdekin case studies. James Cook University, Reef and Rainforest Research Centre. Townsville, Australia

Devlin, M., Waterhouse, J., Taylor, J., Brodie, J. (2001). Flood Plumes in the Great Barrier Reef: Spatial and Temporal Patterns in Composition and Distribution. Townsville, Australia

Dierssen, H.M. (2010). Perspectives on empirical approaches for ocean color remote sensing of chlorophyll in a changing climate. Proceedings of the National Academy of Sciences of the United States of America, 107(40), 17073-17078.

Dierssen, H.M. (2019). Hyperspectral Measurements, Parameterizations, and Atmospheric Correction of Whitecaps and Foam From Visible to Shortwave Infrared for Ocean Color Remote Sensing. Frontiers in Earth Science, 7(14).

Ding, J., Yang, P., King, M.D., Platnick, S., Liu, X., Meyer, K.G., Wang, C. (2019). A fast vector radiative transfer model for the atmosphere-ocean coupled system. Journal of Quantitative Spectroscopy and Radiative Transfer, 239, 106667.

Ding, K., Gordon, H.R. (1994). Atmospheric correction of ocean-color sensors: effects of the Earth's curvature. Applied optics, 33(30), 7096-7106.

Ding, X., He, X., Bai, Y., Zhu, Q., Gong, F., Li, H., Li, J. (2020). High-frequency and tidal period observations of suspended particulate matter in coastal waters by AHI/Himawari-8. Optics express, 28(19), 27387-27404.

Doerffer, R. (2002). Protocols for the validation of MERIS water products. ESA Publication PO-TN-MEL-GS-0043. GKSS, Forschungszentrum. Geesthacht Germany

Doerffer, R., Schiller, H. (2007). The MERIS Case 2 water algorithm. Int. J. Remote Sens., 28(3-4), 517-535.

Donlon, C. (2011). Sentinel-3 Mission Requirements Traceability Document (MRTD). European Space Agency (ESA) - ESTEC. The Netherlands

Dorji, P., Fearns, P. (2017). Impact of the spatial resolution of satellite remote sensing sensors in the quantification of total suspended sediment concentration: A case study in turbid waters of Northern Western Australia. PloS one, 12(4), e0175042.

Dorji, P., Fearns, P. (2018). Atmospheric correction of geostationary Himawari-8 satellite data for Total Suspended Sediment mapping: A case study in the Coastal Waters of Western Australia. ISPRS journal of photogrammetry and remote sensing, 144, 81-93.

Doxaran, D., Cherukuru, R.C.N., Lavender, S.J. (2005). Use of reflectance band ratios to estimate suspended and dissolved matter concentrations in estuarine waters. International Journal of Remote Sensing, 26(8), 1763-1769.

Doxaran, D., Lamquin, N., Park, Y.-J., Mazeran, C., Ryu, J.-H., Wang, M., Poteau, A. (2014). Retrieval of the seawater reflectance for suspended solids monitoring in the East China Sea using MODIS, MERIS and GOCI satellite data. Remote Sensing of Environment, 146, 36-48.

Dransfeld, S., Tatnall, A., Robinson, I., Mobley, C. (2004). A comparison of Multi-layer Perceptron and multilinear regression algorithms for the inversion of synthetic ocean colour spectra. International Journal of Remote Sensing, 25(21), 4829-4834.

Drew, E. (2011). Tidal Jets Trans.). In Hopley, D. (Ed.), Encyclopedia of Modern Coral Reefs: Structure, Form and Process (ed., Vol. pp. 1091-1092). Dordrecht: Springer Netherlands.

Dzwonkowski, B., Yan, X.H. (2005). Development and application of a neural network based ocean colour algorithm in coastal waters. International Journal of Remote Sensing, 26(6), 1175-1200.

Ebert, K. (2009). Exceptional Phytoplankton Bloom Recognition from Visible Spectral Satellite Radiometry Data. (PhD Thesis). Free University Berlin.

El-Habashi, A., Ahmed, S., Ondrusek, M., Lovko, V. (2019). Analyses of satellite ocean color retrievals show advantage of neural network approaches and algorithms that avoid deep blue bands. Journal of Applied Remote Sensing, 13(2).

El-Habashi, A., Duran, C.M., Lovko, V., Tomlinson, M.C., Stumpf, R.P., Ahmed, S. (2017). Satellite retrievals of Karenia brevis harmful algal blooms in the West Florida shelf using neural networks and impacts of temporal variabilities. Journal of Applied Remote Sensing, 11(3).

Eleveld, M.A. (2012). Wind-induced resuspension in a shallow lake from Medium Resolution Imaging Spectrometer (MERIS) full-resolution reflectances. Water Resources Research, 48(4).

Eleveld, M.A., van der Wal, D., van Kessel, T. (2014). Estuarine suspended particulate matter concentrations from sun-synchronous satellite remote sensing: Tidal and meteorological effects and biases. Remote Sensing of Environment, 143, 204-215.

Emecen, E., Kara, G., Erdogmus, F., Gardashov, R. (2006). The determination of sunglint locations on the ocean surface by observation from geostationary satellites. TAO: Terrestrial, Atmospheric and Oceanic Sciences, 17(1), 253.

European Space Agency, E. (2021). Sentinel Online: Orbit. Retrieved from https://sentinel.esa.int/web/sentinel/missions/sentinel-3/satellite-description/orbit (accessed on 20/04/2021).

European Space Agency Validation Data Centre. (2020). Orbit Prediction Tool. Retrieved from https://evdc.esa.int/orbit/ (accessed on 20/11/2020).

Fabricius, K., De'ath, G., McCook, L., Turak, E., Williams, D.M. (2005). Changes in algal, coral and fish assemblages along water quality gradients on the inshore Great Barrier Reef. Marine pollution bulletin, 51(1-4), 384-398.

Fabricius, K.E. (2005). Effects of terrestrial runoff on the ecology of corals and coral reefs: review and synthesis. Marine pollution bulletin, 50(2), 125-146.

Fabricius, K.E., Logan, M., Weeks, S., Brodie, J. (2014). The effects of river run-off on water clarity across the central Great Barrier Reef. Marine pollution bulletin, 84(1-2), 191-200.

Fabricius, K.E., Logan, M., Weeks, S.J., Lewis, S.E., Brodie, J. (2016). Changes in water clarity in response to river discharges on the Great Barrier Reef continental shelf: 2002–2013. Estuarine, Coastal and Shelf Science.

Fell, F., Fischer, J. (2001). Numerical simulation of the light field in the atmosphere-ocean system using the matrix-operator method. Journal of Quantitative Spectroscopy and Radiative Transfer, 69, 351-388.

Feng, J., Chen, H., Zhang, H., Li, Z., Yu, Y., Zhang, Y., Bilal, M., Qiu, Z. (2020). Turbidity estimation from GOCI satellite data in the turbid estuaries of China's coast. Remote Sensing, 12(22), 1-20.

Feng, L., Hu, C. (2016). Comparison of Valid Ocean Observations Between MODIS Terra and Aqua Over the Global Oceans. IEEE Transactions on Geoscience and Remote Sensing, 54(3), 1575-1585.

Fischer, J., Grassl, H. (1984). Radiative transfer in an atmosphere–ocean system: an azimuthally dependent matrix-operator approach. Applied optics, 23(7), 1032-1039.

Fournier, G.R., Forand, J.L. (1994). Analytic phase function for ocean water. Proceedings of SPIE, 2258, 194-201.

Furnas, M. (2003). Catchment and Corals: Terrestrial Runoff to the Great Barrier Reef. Australian Institute of Marine Science. Townsville, Australia

Furnas, M., Mitchell, A., Skuza, M., Brodie, J. (2005). In the other 90%: phytoplankton responses to enhanced nutrient availability in the Great Barrier Reef Lagoon. Marine pollution bulletin, 51(1–4), 253-265.

Gabric, A., Hoffenberg, P., Boughton, W. (1990). Spatio-temporal variability in surface Chlorophyll distribution in the Central Great Barrier Reef as derived from CZCS imagery. Marine and Freshwater Research, 41(3), 313-324.

Garcia, R.A., McKinna, L.I.W., Hedley, J.D., Fearns, P.R.C.S. (2014). Improving the optimization solution for a semi-analytical shallow water inversion model in the presence of spectrally correlated noise. Limnology and Oceanography: Methods, 12(10), 651-669.

Gardashov, R.H., Eminov, M.S. (2015). Determination of sunglint location and its characteristics on observation from a METEOSAT 9 satellite. International Journal of Remote Sensing, 36(10), 2584-2598.

Gillis, D.B., Bowles, J.H., Montes, M.J., Moses, W.J. (2018). Propagation of sensor noise in oceanic hyperspectral remote sensing. Optics express, 26(18), A818-A831.

González Vilas, L., Spyrakos, E., Torres Palenzuela, J.M. (2011). Neural network estimation of chlorophyll a from MERIS full resolution data for the coastal waters of Galician rias (NW Spain). Remote Sensing of Environment, 115(2), 524-535.

Gordon, H.R. (1978). Removal of Atmospheric Effects from Satellite Imagery of the Oceans. Appl. Optics, 17.

Gordon, H.R. (1979). Diffuse reflectance of the ocean: the theory of its augmentation by chlorophyll a fluorescence at 685 nm. Applied optics, 18(8), 1161-1166.

Gordon, H.R. (1989). Theoretical aspects of hydrologic optics. Limnology and Oceanography, 34(8), 1389-1409.

Gordon, H.R. (1999). Contribution of Raman scattering to water-leaving radiance: a reexamination. Applied optics, 38(15), 3166-3174.

Gordon, H.R. (2014). Influence of Raman scattering on the light field in natural waters: a simple assessment. Optics express, 22(3), 3675-3683.

Gordon, H.R., Clark, D.K., Mueller, J.L., Hovis, W.A. (1980). Phytoplankton Pigments from the Nimbus-7 Coastal Zone Color Scanner: Comparisons with Surface Measurements. Science, 210(4465).

Gordon, H.R., Franz, B.A. (2008). Remote sensing of ocean color: Assessment of the water-leaving radiance bidirectional effects on the atmospheric diffuse transmittance for SeaWiFS and MODIS intercomparisons. Remote Sensing of Environment, 112(5), 2677-2685.

Gordon, H.R., Morel, A. (1983). Remote Assessment of Ocean Colour for Interpretation of Satellite Visible Imagery. Lecture Notes on Coastal and Estuarine Studies. New York

Gordon, I.E., Rothman, L.S., Hill, C., Kochanov, R.V., Tan, Y., Bernath, P.F., Birk, M., Boudon, V., Campargue, A., Chance, K. (2017). The HITRAN2016 molecular spectroscopic database. Journal of Quantitative Spectroscopy and Radiative Transfer, 203, 3-69.

Gower, J.F.R., Borstad, G.A. (1990). Mapping of phytoplankton by solar-stimulated fluorescence using an imaging spectrometer. International Journal of Remote Sensing, 11(2), 313-320.

Graßl, H. (2011). The Global Distribution of Aerosols Trans.). In (Ed.), Persistent Pollution–Past, Present and Future (ed., Vol. pp. 287-298). Springer.

Great Barrier Reef Marine Park Authority. (1975). The Great Barrier Reef Marine Park Act. Commonwealth of Australia.

Great Barrier Reef Marine Park Authority. (1981). Nomination of the Great Barrier Reef by the Commonwealth of Australia for Inclusion in the World Heritage List: United Nations Educational Scientific and Cultural Organization. Great Barrier Reef Marine Park Authority.

Great Barrier Reef Marine Park Authority. (2010). Water Quality Guidelines for the Great Barrier Reef Marine Park. Great Barrier Reef Marine Park Authority.

Great Barrier Reef Marine Park Authority (2014). Great Barrier Reef Features in Shapefiles. Retrieved from: http://www.gbrmpa.gov.au/geoportal/). .

Great Barrier Reef Marine Park Authority. (2019a). Great Barrier Reef Outlook Report 2019 (0648357058). Great Barrier Reef Marine Park Authority.

Great Barrier Reef Marine Park Authority. (2019b). Marine Monitoring Program quality assurance and quality control manual 2017–18. Great Barrier Reef Marine Park Authority. Townsville http://elibrary.gbrmpa.gov.au/jspui/handle/11017/3487

Gross, L., Thiria, S., Frouin, R. (1999). Applying artificial neural network methodology to ocean color remote sensing. Ecological Modelling, 120, 237-246.

Gross, L., Thiria, S., Frouin, R., Mitchell, B.G. (2000). Artificial neural networks for modeling the transfer function between marine reflectance and phytoplankton pigment concentration. Journal of Geophysical Research: Oceans, 105(C2), 3483-3495.

Gruber, R., Waterhouse, J., Logan, M., Petus, C., Howley, C., Lewis, S., Tracey, D., Langlois, L., Tonin, H., Skuza, M., Costello, P., Davidson, J., Gunn, K., Lefevre, C., Moran, D., Robson, B., Shanahan, M., Zagorskis, I., Shellberg, J., Neilen, A. (2020). Marine Monitoring Program: Annual report for inshore water quality monitoring 2018-19 (2208-4096). Report for the Great Barrier Reef Marine Park Authority. Great Barrier Reef Marine Park Authority. Townsville

Gruber, R., Waterhouse, J., Logan, M., Petus, C., Howley, C., Lewis, S., Tracey, D., Langlois, L., Tonin, H., Skuza, M., Costello, P., Davidson, J., Gunn, K., Wright, M., Zagorskis, I., Kroon, F.J., Neilen, A., Lefevre, C., Shanahan, M. (2019). Marine Monitoring Program: Annual report for inshore water quality monitoring 2017-18 (2208-4096). Report for the Great Barrier Reef Marine Park Authority - Marine Monitoring Program - Inshore Water Quality. Townsville

Ha, H.J., Kim, H., Kwon, B.-O., Khim, J.S., Ha, H.K. (2020). Influence of tidal forcings on microphytobenthic resuspension dynamics and sediment fluxes in a disturbed coastal environment. Environment International, 139, 105743.

Hafeez, S., Wong, M.S., Abbas, S., Jiang, G. (2021). Assessing the Potential of Geostationary Himawari-8 for Mapping Surface Total Suspended Solids and Its Diurnal Changes. Remote Sensing, 13(3), 336.

Hale, G.M., Querry, M.R. (1973). Optical constants of water in the 200-nm to 200-µm wavelength region. Applied optics, 12(3), 555-563.

Hansen, J.E., Travis, L.D. (1974). Light scattering in planetary atmospheres. Space science reviews, 16(4), 527-610.

Haynes, D., Waterhouse, J., Innes, J., Vella, K., Furnas, M., Schaffelke, B., Great Barrier Reef Marine Park, A. (2005). First Annual Marine Monitoring Programme Report September 2005. Great Barrier Reef Marine Park Authority. Townsvilile http://hdl.handle.net/11017/677

He, S., Fischer, J., Schaale, M., He, M.-x. (2014). Optical closure of parameterized bio-optical relationships. Chinese journal of oceanology and limnology, 32(2), 480.

Hedley, J., Harborne, A., Mumby, P. (2005). Simple and robust removal of sun glint for mapping shallow-water benthos. International Journal of Remote Sensing, 26(10), 2107-2112.

Hidy, G.M. (2003). Aerosols Trans.). In Meyers, R.A. (Ed.), Encyclopedia of Physical Science and Technology (Third Edition) (ed., Vol. pp. 273-299). New York: Academic Press.

Hieronymi, M. (2019). Spectral band adaptation of ocean color sensors for applicability of the multi-water biogeo-optical algorithm ONNS. Optics express, 27(12), A707-A724.

Hieronymi, M., Müller, D., Doerffer, R. (2017). The OLCI Neural Network Swarm (ONNS): A Bio-Geo-Optical Algorithm for Open Ocean and Coastal Waters. Frontiers in Marine Science, 4(140).

Hinton, G., Deng, L., Yu, D., Dahl, G.E., Mohamed, A.-r., Jaitly, N., Senior, A., Vanhoucke, V., Nguyen, P., Sainath, T.N. (2012). Deep neural networks for acoustic modeling in speech recognition: The shared views of four research groups. IEEE Signal Processing Magazine, 29(6), 82-97.

Holben, B.N., Eck, T.F., Slutsker, I., Tanré, D., Buis, J.P., Setzer, A., Vermote, E., Reagan, J.A., Kaufman, Y.J., Nakajima, T., Lavenu, F., Jankowiak, I., Smirnov, A. (1998). AERONET—A Federated Instrument Network and Data Archive for Aerosol Characterization. Remote Sensing of Environment, 66(1), 1-16.

Hollstein, A., Bismarck, v.J., Fishcer, J., Preusker, R. (2010). Description of the vector radiative transfer model momo. ESA support to science project waterradiance document (contract AO 1-5859/08/NL/CT).

Hollstein, A., Fischer, J. (2012). Radiative transfer solutions for coupled atmosphere ocean systems using the matrix operator technique. Journal of Quantitative Spectroscopy and Radiative Transfer, 113(7), 536-548.

Hooker, S., Clementson, L., Thomas, C., Schlüter, L., Allerup, M., Ras, J., Claustre, H., Normandeau, C., Cullen, J., Kienast, M. (2012). The Fifth SeaWiFS HPLC Analysis Round-Robin Experiment (SeaHARRE-5) NASA Tech Memo 2012-217503. NASA Goddard Space Flight Center, Greenbelt, Maryland.

Hornik, K. (1991). Approximation capabilities of multilayer feedforward networks. Neural Networks, 4(2), 251-257.

Hsu, P.-C., Ho, C.-Y., Lee, H.-J., Lu, C.-Y., Ho, C.-R. (2020). Temporal Variation and Spatial Structure of the Kuroshio-Induced Submesoscale Island Vortices Observed from GCOM-C and Himawari-8 Data. Remote Sensing, 12(5), 883.

Hu, C. (2011). An empirical approach to derive MODIS ocean color patterns under severe sun glint. Geophysical Research Letters, 38(1), n/a-n/a.

Hu, C., Barnes, B.B., Feng, L., Wang, M., Jiang, L. (2019). On the Interplay Between Ocean Color Data Quality and Data Quantity: Impacts of Quality Control Flags. IEEE Geoscience and Remote Sensing Letters.

Hu, C., Carder, K.L., Muller-Karger, F.E. (2001). How precise are SeaWiFS ocean color estimates? Implications of digitization-noise errors. Remote Sensing of Environment, 76(2), 239-249.

Hu, C., Feng, L., Lee, Z. (2012a). Evaluation of GOCI sensitivity for At-Sensor radiance and GDPS-Retrieved chlorophyll-a products. Ocean Science Journal, 47(3), 279-285.

Hu, C., Feng, L., Lee, Z., Davis, C.O., Mannino, A., McClain, C.R., Franz, B.A. (2012b). Dynamic range and sensitivity requirements of satellite ocean color sensors: learning from the past. Applied optics, 51(25), 6045-6062.

Hughes, T., Kerry, J., Simpson, T. (2018a). Large-scale bleaching of corals on the Great Barrier Reef. Ecology, 99(2), 501-501.

Hughes, T.P., Kerry, J.T., Baird, A.H., Connolly, S.R., Dietzel, A., Eakin, C.M., Heron, S.F., Hoey, A.S., Hoogenboom, M.O., Liu, G. (2018b). Global warming transforms coral reef assemblages. Nature, 556(7702), 492-496.

Ibrahim, A., Franz, B.A., Ahmad, Z., Bailey, S.W. (2019). Multiband Atmospheric Correction Algorithm for Ocean Color Retrievals. Frontiers in Earth Science, 7(116).

Ioannou, I., Gilerson, A., Gross, B., Moshary, F., Ahmed, S. (2011). Neural network approach to retrieve the inherent optical properties of the ocean from observations of MODIS. Applied optics, 50(19), 3168-3186.

Ioannou, I., Gilerson, A., Gross, B., Moshary, F., Ahmed, S. (2013). Deriving ocean color products using neural networks. Remote Sensing of Environment, 134, 78-91.

IOCCG. (1998). Minumum Requirements for an Operational, Ocean-Coulour Sensor for the Open Ocean (IOCCG Report Number 1). Reports of the International Ocean-Colour Coordinating Group. IOCCG. Dartmouth, Nova Scotia, Canada

IOCCG. (2000). Remote Sensing of Ocean Colour in Coastal and Other Optically-Complex Waters (IOCCG Report Number 3). Reports of the International Ocean-Colour Coordinating Group. Darthmouth, Nova Scotia, Canada

IOCCG. (2012a). Mission Requirements for Future Ocean-Colour Sensors (IOCCG Report Number 13). Reports of the International Ocean-Colour Coordinating Group IOCCG. Darthmouth, Nova Scotia, Canada

IOCCG. (2012b). Ocean-Colour Observations from a Geostationary Orbit (IOCCG Report Number 12). Reports of the International Ocean-Colour Coordinating Group. IOCCG. Darthmouth, Canada

IOCCG. (2013). In-flight Calibration of Satellite Ocean-Colour Sensors (IOCCG Report Number 14). Reports of the International Ocean-Colour Coordinating Group. IOCCG. Dartmouth, Nova Scotia, Canada

IOCCG. (2018). Earth Observations in Support of Global Water Quality Monitoring. (IOCCG Report Number 17). Reports of the International Ocean Colour Coordinating Group IOCCG. Dartmouth, Canada.

IOCCG. (2019). Uncertainties in Ocean Colour Remote Sensing (IOCCG Report Number 18). Reports of the International Ocean Colour Coordinating Group. Dartmouth, Nova Scotia, Canada. http://dx.doi.org/10.25607/OBP696

IOCCG. (2020). Synergy between Ocean Colour and Biogeochemical/Ecosystem Models (IOCCG Report Number 19). Reports of the International Ocean-Colour Coordinating Group. IOCCG. Dartmouth, Nova Scotia, Canada https://ioccg.org/what-we-do/ioccg-publications/ioccg-reports/

Jain, A.K., Mao, J., Mohiuddin, K.M. (1996). Artificial Neural Networks: A Tutorial. Computer, 29(3), 31-44.

Jamet, C., Loisel, H., Dessailly, D. (2012). Retrieval of the spectral diffuse attenuation coefficient Kd(λ) in open and coastal ocean waters using a neural network inversion. Journal of Geophysical Research: Oceans, 117(C10), n/a-n/a.

Jamet, C., Thira, S., Moulin, C., Crepon, M. (2005). Use of a Neurovariational Inversion for Retrieving Oceanic and Atmospheric Constituents from Ocean Color Imagery: A Feasibility Study. Journal of Atmospheric and Oceanic Technology, 22, 460-475.

Japan Meteorological Agency. (2015). Himawari-8 Performance Test Results. https://www.data.jma.go.jp/mscweb/en/himawari89/space_segment/fig/AHI8_performance_test_en.pdf

Japan Meteorological Agency. (2016). Quality improvement of Himawari-8 observation data. https://www.data.jma.go.jp/mscweb/en/oper/eventlog/20161117_Quality_improvement_of_Himawari-8_observation_data.pdf

Japan Meteorological Agency. (2017). Improvement of Himawari-8 observation data quality. https://www.data.jma.go.jp/mscweb/en/oper/eventlog/Improvement_of_Himawari-8_data_quality.pdf

Japan Meteorological Agency. (2020). Impacts of Spacecraft Events and Calibration on Himawari-8 Images: Striping. Retrieved from http://www.data.jma.go.jp/mscweb/en/oper/image_info.html#005 (accessed on 16/11/2020).

JAXA. (2020). Himawari Monitor P-Tree System. Retrieved from https://www.eorc.jaxa.jp/ptree/index.html (accessed on

Jeffrey, S.t., Humphrey, G. (1975). New spectrophotometric equations for determining chlorophylls a, b, c1 and c2 in higher plants, algae and natural phytoplankton. Biochemie und physiologie der pflanzen, 167(2), 191-194.

Jiang, B., Fan, D., Ji, Q., Obodoefuna, D.C. (2020). Dynamic Diurnal Changes in Green Algae Biomass in the Southern Yellow Sea Based on GOCI Images. Journal of Ocean University of China, 19(4), 811-817.

Joint, I., Groom, S.B. (2000). Estimation of phytoplankton production from space: current status and future potential of satellite remote sensing. Journal of experimental marine Biology and Ecology, 250(1), 233-255.

Jones, E.M., Baird, M.E., Mongin, M., Parslow, J., Skerratt, J., Lovell, J., Margvelashvili, N., Matear, R.J., Wild-Allen, K., Robson, B., Rizwi, F., Oke, P., King, E., Schroeder, T., Steven, A., Taylor, J. (2016). Use of remote-sensing reflectance to constrain a data assimilating marine biogeochemical model of the Great Barrier Reef. Biogeosciences, 13(23), 6441-6469.

Juhls, B., Paul Overduin, P., Hölemann, J., Hieronymi, M., Matsuoka, A., Heim, B., Fischer, J. (2019). Dissolved organic matter at the fluvial-marine transition in the Laptev Sea using in situ data and ocean colour remote sensing. Biogeosciences, 16(13), 2693-2713.

Jupp, D.L.B., Mayo, K.K., Kuchler, D.A., Claasen, D.V.R., Kenchington, R.A., Guerin, P.R. (1985). Remote sensing for planning and managing the great barrier reef of Australia. Photogrammetria, 40(1), 21-42.

Kalnay, E., Kanamitsu, M., Kistler, R., Collins, W., Deaven, D., Gandin, L., Iredell, M., Saha, S., White, G., Woollen, J. (1996). The NCEP/NCAR 40-year reanalysis project. Bulletin of the American meteorological Society, 77(3), 437-472.

Kanamitsu, M., Ebisuzaki, W., Woollen, J., Yang, S.-K., Hnilo, J.J., Fiorino, M., Potter, G.L. (2002). NCEP–DOE AMIP-II Reanalysis (R-2). Bulletin of the American Meteorological Society, 83(11), 1631-1644.

Keiner, L.E. (1999). Estimating oceanic chlorophyll concentrations with neural networks. International Journal of Remote Sensing, 20(1), 189-194.

Keiner, L.E., Yan, X.-H. (1998). A Neural Network Model for Estimating Sea Surface Chlorophyll and Sediments from Thematic Mapper Imagery. Remote Sensing of Environment, 66(2), 153-165.

King, B., McAllister, F., Done, T.J. (2002). Modelling the impact of the Burdekin, Herbert, Tully and Johnstone River plumes on the central Great Barrier Reef. Citeseer.

King, E., Schroeder, T., Brando, V., Suber, K., (2014). A Pre-operational System for Satellite Monitoring of Great Barrier Reef Marine Water Quality. Wealth from Oceans Flagship Report. CSIRO Land & Water: Canberra, Australia.

Kinsey, J.D., Corradino, G., Ziervogel, K., Schnetzer, A., Osburn, C.L. (2018). Formation of Chromophoric Dissolved Organic Matter by Bacterial Degradation of Phytoplankton-Derived Aggregates. Frontiers in Marine Science, 4(430).

Kirk, J.T.O. (1994). Light and photosynthesis in aquatic ecosystems. UK, Cambridge University Press.

Kirk, J.T.O. (2010). Light and Photosynthesis in Aquatic Ecosystems. UK, Cambridge University Press.

Kistler, R., Kalnay, E., Collins, W., Saha, S., White, G., Woollen, J., Chelliah, M., Ebisuzaki, W., Kanamitsu, M., Kousky, V. (2001). The NCEP–NCAR 50-year reanalysis: monthly means CD-ROM and documentation. Bulletin of the American Meteorological society, 82(2), 247-268.

Kitsiou, D., Karydis, M. (2011). Coastal marine eutrophication assessment: a review on data analysis. Environment international, 37(4), 778-801.

Kleypas, J. (1996). Coral reef development under naturally turbid conditions: fringing reefs near Broad Sound, Australia. Coral Reefs, 15(3), 153-167.

Kotchenova, S.Y., Vermote, E.F., Matarrese, R., Klemm Jr, F.J. (2006). Validation of a vector version of the 6S radiative transfer code for atmospheric correction of satellite data. Part I: Path radiance. Applied optics, 45(26), 6762-6774.

Krasnopolsky, V., Nadiga, S., Mehra, A., Bayler, E. (2018). Adjusting neural network to a particular problem: Neural network-based empirical biological model for chlorophyll concentration in the upper ocean. Applied Computational Intelligence and Soft Computing, 2018.

Kroon, F.J., Kuhnert, P.M., Henderson, B.L., Wilkinson, S.N., Kinsey-Henderson, A., Abbott, B., Brodie, J.E., Turner, R.D. (2012). River loads of suspended solids, nitrogen, phosphorus and herbicides delivered to the Great Barrier Reef lagoon. Marine pollution bulletin, 65(4-9), 167-181.

Kroon, F.J., Thorburn, P., Schaffelke, B., Whitten, S. (2016). Towards protecting the Great Barrier Reef from land-based pollution. Global Change Biology, n/a-n/a.

Kuchler, D.A., Jupp, D.L.B., van R. Claasen, D.B., Bour, W. (1986). Coral reef remote sensing applications. Geocarto International, 1(4), 3-15.

Kudela, R.M., Hooker, S.B., Houskeeper, H.F., McPherson, M. (2019). The Influence of Signal to Noise Ratio of Legacy Airborne and Satellite Sensors for Simulating Next-Generation Coastal and Inland Water Products. Remote Sensing, 11(18), 2071.

Kurucz, R. (1995). The solar spectrum: atlases and line identifications. Paper presented at the Laboratory and Astronomical High Resolution Spectra.

Kwiatkowska, E.J., Ruddick, K., Ramon, D., Vanhellemont, Q., Brockmann, C., Lebreton, C., Bonekamp, H.G. (2015). Ocean colour products from geostationary platforms, opportunities with Meteosat Second and Third Generation. Ocean Science Discussions, 12(6), 3143-3167.

Lam, V.Y.Y., Chaloupka, M., Thompson, A., Doropoulos, C., Mumby, P.J. (2018). Acute drivers influence recent inshore Great Barrier Reef dynamics. Proceedings of the Royal Society B: Biological Sciences, 285(1890), 20182063.

Lamquin, N., Déru, A., Clerc, S., Bourg, L., Donlon, C. (2020). OLCI A/B Tandem Phase Analysis, Part 2: Benefits of Sensors Harmonisation for Level 2 Products. Remote Sensing, 12, 2702.

Landgrebe, D.A., Malaret, E. (1986). Noise in remote-sensing systems: The effect on classification error. IEEE Transactions on Geoscience and Remote Sensing, (2), 294-300.

Larcombe, P., Costen, A., Woolfe, K.J. (2001). The hydrodynamic and sedimentary setting of nearshore coral reefs, central Great Barrier Reef shelf, Australia: Paluma Shoals, a case study. Sedimentology, 48(4), 811-835.

Larcombe, P., Ridd, P., Prytz, A., Wilson, B. (1995). Factors controlling suspended sediment on inner-shelf coral reefs, Townsville, Australia. Coral reefs, 14(3), 163-171.

Larcombe, P., Woolfe, K. (1999). Increased sediment supply to the Great Barrier Reef will not increase sediment accumulation at most coral reefs. Coral reefs, 18(2), 163-169.

Laurentiis, L.D., Jones, C.E., Holt, B., Schiavon, G., Frate, F.D. (2020). Deep Learning for Mineral and Biogenic Oil Slick Classification With Airborne Synthetic Aperture Radar Data. IEEE Transactions on Geoscience and Remote Sensing, 1-15.

Lavigne, H., Ruddick, K. (2018). The potential use of geostationary MTG/FCI to retrieve chlorophyll-a concentration at high temporal resolution for the open oceans. International Journal of Remote Sensing, 39(8), 2399-2420.

Lee, Z., Carder, K., Arnone, R., He, M. (2007). Determination of primary spectral bands for remote sensing of aquatic environments. Sensors, 7(12), 3428-3441.

Lee, Z., Carder, K.L., Mobley, C.D., Steward, R.G., Patch, J.S. (1999). Hyperspectral remote sensing for shallow waters: 2. Deriving bottom depths and water properties by optimization. Applied optics, 38(18), 3831-3843.

Lee, Z., Jiang, M., Davis, C., Pahlevan, N., Ahn, Y.-H., Ma, R. (2012). Impact of multiple satellite ocean color samplings in a day on assessing phytoplankton dynamics. Ocean Science Journal, 47(3), 323-329.

Lee, Z., Marra, J., Perry, M.J., Kahru, M. (2015). Estimating oceanic primary productivity from ocean color remote sensing: A strategic assessment. Journal of Marine Systems, 149, 50-59.

Lee, Z.P., Carder, K.L., Arnone, R. (2002). Deriving inherent optical properties from water color: a multiband quasi-analytical algorithm for optically deep waters. Applied optics, 41(27), 5755-5772.

Leifer, I., Lehr, W.J., Simecek-Beatty, D., Bradley, E., Clark, R., Dennison, P., Hu, Y., Matheson, S., Jones, C.E., Holt, B., Reif, M., Roberts, D.A., Svejkovsky, J., Swayze, G., Wozencraft, J. (2012). State of the art satellite and airborne marine oil spill remote sensing: Application to the BP Deepwater Horizon oil spill. Remote Sensing of Environment, 124, 185-209.

Lewis, S., Brodie, J., Ledee, E., Alewijnse, M. (2006). The Spatial Extent of Delivery of Terrestrial Materials from the Burdekin Region in the Great Barrier Reef Lagoon. ACTFR Report. James Cook University, Townsville, QLD.

Lin, H., Kuzminov, F.I., Park, J., Lee, S., Falkowski, P.G., Gorbunov, M.Y. (2016). The fate of photons absorbed by phytoplankton in the global ocean. Science, 351(6270), 264-267.

Lin, S., Borstad, G.A., Gower, J.F.R. (1984). Remote Sensing of Chlorophyll in the Red Spectral Region Trans.). In Nihoul, J.C.J. (Ed.), Elsevier Oceanography Series (ed., Vol. 38, pp. 317-336). Elsevier.

Linke, F. (1953). Linkes Meteorologisches Taschenbuch. Geest & Portig.

Liu, D.C., Nocedal, J. (1989). On the limited memory BFGS method for large scale optimization. Mathematical programming, 45(1-3), 503-528.

Lou, X., Hu, C. (2014). Diurnal changes of a harmful algal bloom in the East China Sea: Observations from GOCI. Remote Sensing of Environment, 140, 562-572.

Lough, J., Lewis, S., Cantin, N. (2015). Freshwater impacts in the central Great Barrier Reef: 1648–2011. Coral Reefs, 34(3), 739-751.

Lough, J.M. (2007). Tropical river flow and rainfall reconstructions from coral luminescence: Great Barrier Reef, Australia. Paleoceanography, 22(2).

MacNeil, M.A., Mellin, C., Matthews, S., Wolff, N.H., McClanahan, T.R., Devlin, M., Drovandi, C., Mengersen, K., Graham, N.A. (2019). Water quality mediates resilience on the Great Barrier Reef. Nature ecology & evolution, 3(4), 620-627.

Marine Water Quality Dashboard, e. (2014). eReefs Marine Water Quality Dashboard Data Processing Specification. Bureau of Meteorology, Commonwealth of Australia. http://www.bom.gov.au/environment/activities/mwqd/documents/data-product-specification.pdf

Marine Water Quality Dashboard, e. (2020). Online Database of Near-real time Marine Water Quality Observations. Australian Bureau of Meteorology http://www.bom.gov.au/marinewaterquality/

Maritime Safety Queensland. (2020). Storm tide monitoring sites. The Tidal Unit. Retrieved from https://www.msq.qld.gov.au/, https://www.qld.gov.au/environment/coasts-waterways/beach/storm/storm-sites/lucinda (accessed on 26/09/2020).

Maritorena, S., Siegel, D.A., Peterson, A.R. (2002). Optimization of a semianalytical ocean color model for global-scale applications. Applied optics, 41(15).

Marrari, M., Hu, C., Daly, K. (2006). Validation of SeaWiFS chlorophyll a concentrations in the Southern Ocean: A revisit. Remote Sensing of Environment, 105(4), 367-375.

Marzano, F.S., Iacobelli, M., Orlandi, M., Cimini, D. (2020). Coastal Water Remote Sensing From Sentinel-2 Satellite Data Using Physical, Statistical, and Neural Network Retrieval Approach. IEEE Transactions on Geoscience and Remote Sensing.

Matthews, S., Mellin, C., Pratchett, M. (2020). Larval connectivity and water quality explain spatial distribution of crown-of-thorns starfish outbreaks across the Great Barrier Reef Trans.). In (Ed.), (ed., Vol. 87, pp.).

McCulloch, M., Fallon, S., Wyndham, T., Hendy, E., Lough, J., Barnes, D. (2003). Coral record of increased sediment flux to the inner Great Barrier Reef since European settlement. Nature, 421(6924), 727-730.

McKenzie, L., Collier, C., Langlois, L., Yoshida, R.L., Uusitalo, J., and, Waycott, M. (2021). Marine Monitoring Program: Annual Report for Inshore Seagrass Monitoring 2018-19. . Report for the Great Barrier Reef Marine Park Authorithy. Centre for Tropical Water & Aquatic Ecosystem Research (TropWATER), James Cook University. Townsville

McKergow, L.A., Prosser, I.P., Hughes, A.O., Brodie, J. (2005). Regional scale nutrient modelling: exports to the Great Barrier Reef World Heritage Area. Marine pollution bulletin, 51(1-4), 186-199.

McKinna, L.I., Werdell, P.J. (2018). Approach for identifying optically shallow pixels when processing ocean-color imagery. Optics express, 26(22), A915-A928.

McKinna, L.I.W., Cetinić, I., Chase, A.P., Werdell, P.J. (2019). Approach for Propagating Radiometric Data Uncertainties Through NASA Ocean Color Algorithms. Frontiers in Earth Science, 7(176).

McKinna, L.I.W., Fearns, P.R.C., Weeks, S.J., Werdell, P.J., Reichstetter, M., Franz, B.A., Shea, D.M., Feldman, G.C. (2015). A semianalytical ocean color inversion algorithm with explicit water column depth and substrate reflectance parameterization. Journal of Geophysical Research: Oceans, 120(3), 1741-1770.

McKinna, L.I.W., Furnas, M.J., Ridd, P.V. (2011). A simple, binary classification algorithm for the detection of Trichodesmium spp. within the Great Barrier Reef using MODIS imagery. Limnology and Oceanography: Methods, 9(2), 50-66.

Mellin, C., Matthews, S., Anthony, K.R.N., Brown, S.C., Caley, M.J., Johns, K.A., Osborne, K., Puotinen, M., Thompson, A., Wolff, N.H., Fordham, D.A., MacNeil, M.A. (2019). Spatial resilience of the Great Barrier Reef under cumulative disturbance impacts. Global Change Biology, 25(7), 2431-2445.

Mie, G. (1908). Beiträge zur Optik trüber Medien, speziell kolloidaler Metallösungen. Annalen der Physik, 330(3), 377-445.

Miller, S.D., Schmit, T.L., Seaman, C.J., Lindsey, D.T., Gunshor, M.M., Kohrs, R.A., Sumida, Y., Hillger, D. (2016). A Sight for Sore Eyes: The Return of True Color to Geostationary Satellites. Bulletin of the American Meteorological Society, 97(10), 1803-1816.

Minghelli, A., Lei, M., Charmasson, S., Rey, V., Chami, M. (2019). Monitoring suspended particle matter using GOCI satellite data after the tohoku (Japan) tsunami in 2011. IEEE Journal of Selected Topics in Applied Earth Observations and Remote Sensing, 12(2), 567-576.

Minsky, M., Papert, S.A. (1969). Perceptrons: An introduction to computational geometry. MIT press.

Mobley, C.D. (1989). A numerical model for the computation of radiance distributions in natural waters with wind-roughened surfaces. Limnology and oceanography, 34(8), 1473-1483.

Mobley, C.D. (1994). Light and water: radiative transfer in natural waters. .

Moore, K.D., Voss, K.J., Gordon, H.R. (2000). Spectral reflectance of whitecaps: Their contribution to water-leaving radiance. Journal of Geophysical Research: Oceans, 105(C3), 6493-6499.

Morel, A. (1974). Optical properties of pure water and pure seawater Trans.). In Nielsen, J.S. (Ed.), Optical Aspects of oceanography (ed., Vol. pp. 1-24).

Morel, A. (1980). In-water and Remote Measurements of Ocean Color. Boundary Layer Meteorology, 18, 177-201.

Morel, A. (1988). Optical Modeling of the Upper Ocean in Relation to its Biogenous Matter Content (Case 1 Waters). Journal of Geophysical Research, 93(C9), 10,749-710,768.

Morel, A. (2001). Bio-optical models. Elements of Physical Oceanography: A derivative of the Encyclopedia of Ocean Sciences, 247.

Morel, A., Gentili, B. (1996). Diffuse reflectance of oceanic waters. III. Implication of bidirectionality for the remote-sensing problem. Applied optics, 35(24), 4850-4862.

Morel, A., Maritorena, S. (2001). Bio-optical properties of oceanic waters: A reappraisal. Journal of Geophysical Research, 106(C4), 7163-7180.

Morel, A., Prieur, L. (1977). Analysis of Variations in Ocean Color. Limnology and Oceanog., 22.

Morel, A., Smith, R.C. (1982). Terminology and units in optical oceanography. Marine Geodesy, 5(4), 335-349.

Moses, W.J., Bowles, J.H., Lucke, R.L., Corson, M.R. (2012). Impact of signal-to-noise ratio in a hyperspectral sensor on the accuracy of biophysical parameter estimation in case II waters. Optics express, 20(4), 4309-4330.

Mueller, J.L. (2003). Ocean Optics Protocols for Satellite Ocean Color Sensor Validation, Revision 4: Introduction, background, and conventions. Goddard Space Flight Center.

Muller-Karger, F.E., Hestir, E., Ade, C., Turpie, K., Roberts, D.A., Siegel, D., Miller, R.J., Humm, D., Izenberg, N., Keller, M., Morgan, F., Frouin, R., Dekker, A.G., Gardner, R., Goodman, J., Schaeffer, B., Franz, B.A., Pahlevan, N., Mannino, A.G., Concha, J.A., Ackleson, S.G., Cavanaugh, K.C., Romanou, A., Tzortziou, M., Boss, E.S., Pavlick, R., Freeman, A., Rousseaux, C.S., Dunne, J., Long, M.C., Klein, E., McKinley, G.A., Goes, J., Letelier, R., Kavanaugh, M., Roffer, M., Bracher, A., Arrigo, K.R., Dierssen, H., Zhang, X., Davis, F.W., Best, B., Guralnick, R., Moisan, J., Sosik, H.M., Kudela, R., Mouw, C.B., Barnard, A.H., Palacios, S., Roesler, C., Drakou, E.G., Appeltans, W., Jetz, W. (2018). Satellite sensor requirements for monitoring essential biodiversity variables of coastal ecosystems. Ecological Applications, 28(3), 749-760.

Murakami, H. (2016a). Minutes of the 2016 Annual GSICS Joint Working Groups Meeting: JAXA Himawari-8 ocean color and aerosol. Annual Meeting of GRWG+GDWG. Tsukuba, Japan

Murakami, H. (2016b). Ocean color estimation by Himawari-8/AHI. Paper presented at the Remote Sensing of the Oceans and Inland Waters: Techniques, Applications, and Challenges,.

Nakajima, T.Y., Murakami, H., Hori, M., Nakajima, T., Aoki, T., Oishi, T., Tanaka, A. (2003). Efficient use of an improved radiative transfer code to simulate near-global distributions of satellite-measured radiances. Applied optics, 42(18), 3460-3471.

National Institute of Information and Communications Technology, N. (2021). Himawari-8 Science Cloud. Retrieved from https://sc-nc-web.nict.go.jp/wsdb_osndisk/shareDirDownload/bDw2maKV?sI=D531106,D531107,TI,D531106m,D531107m,TIm,evm&sIt=data_im&lang=en (accessed on 20/02/2021).

National Oceanic and Atmospheric Administration, N. (2020a). NCEP Reanalysis 2 Meterological data. Retrieved from https://psl.noaa.gov/data/gridded/data.ncep.reanalysis2.html (accessed on 01/12/2020).

National Oceanic and Atmospheric Administration, N. (2020b). Total Ozone Analysis using SBUV/2 and TOVS (TOAST). Retrieved from https://www.ospo.noaa.gov/Products/atmosphere/toast/index.html (accessed on 01/12/2020).

National Oceanic and Atmospheric Administration, N. (2021). Satellite Swath - Real-time. Science on a Sphere. Retrieved from https://sos.noaa.gov/datasets/satellite-swath-real-time/ (accessed on 22/02/2021).

Nechad, B., Ruddick, K.G., Park, Y. (2010). Calibration and validation of a generic multisensor algorithm for mapping of total suspended matter in turbid waters. Remote Sensing of Environment, 114(4), 854-866.

Nelson, N.B., Coble, P.G. (2009). Optical analysis of chromophoric dissolved organic matter Trans.). In (Ed.), Practical Guidelines for the Analysis of Seawater (ed., Vol. pp. 91-108). CRC Press.

Neukermans, G., Ruddick, K., Bernard, E., Ramon, D., Nechad, B., Deschamps, P.-Y. (2009). Mapping total suspended matter from geostationary satellites: a feasibility study with SEVIRI in the Southern North Sea. Optics express, 17(16), 14029-14052.

Neukermans, G., Ruddick, K., Loisel, H., Roose, P. (2012a). Optimization and quality control of suspended particulate matter concentration measurement using turbidity measurements. Limnology and Oceanography: Methods, 10(12), 1011-1023.

Neukermans, G., Ruddick, K.G., Greenwood, N. (2012b). Diurnal variability of turbidity and light attenuation in the southern North Sea from the SEVIRI geostationary sensor. Remote Sensing of Environment, 124, 564-580.

O'Reilly, J.E., Maritorena, S., Mitchell, B.G., Siegel, D.A., Carder, K.L., Garver, S.A., Kahru, M., McClain, C. (1998). Ocean color chlorophyll algorithms for SeaWiFS. Journal of Geophysical Research: Oceans, 103(C11), 24937-24953.

Observing Systems Capability Analysis and Review Tool, O. (2021). Retrieved from https://www.wmo-sat.info/oscar/ (accessed on 12/01/2021).

Okuyama, A., Takahashi, M., Date, K., Hosaka, K., Murata, H., Tabata, T., Yoshino, R. (2018). Validation of Himawari-8/AHI radiometric calibration based on two years of in-orbit data. Journal of the Meteorological Society of Japan. Ser. II, 96, 91-109.

Orpin, A.R., Ridd, P.V. (2012). Exposure of inshore corals to suspended sediments due to wave-resuspension and river plumes in the central Great Barrier Reef: A reappraisal. Continental Shelf Research, 47, 55-67.

Orpin, A.R., Ridd, P.V., Thomas, S., Anthony, K.R., Marshall, P., Oliver, J. (2004). Natural turbidity variability and weather forecasts in risk management of anthropogenic sediment discharge near sensitive environments. Marine pollution bulletin, 49(7-8), 602-612.

Ortiz, J.-C., Wolff, N.H., Anthony, K.R., Devlin, M., Lewis, S., Mumby, P.J. (2018). Impaired recovery of the Great Barrier Reef under cumulative stress. Science advances, 4(7), eaar6127.

Oubelkheir, K., Clementson, L.A., Webster, I.T., Ford, P.W., Dekker, A.G., Radke, L.C., Daniel, P. (2006). Using inherent optical properties to investigate biogeochemical dynamics in a tropical macrotidal coastal system. Journal of Geophysical Research, 111(C7).

Oubelkheir, K., Ford, P.W., Clementson, L.A., Cherukuru, N., Fry, G., Steven, A.D.L. (2014). Impact of an extreme flood event on optical and biogeochemical properties in a subtropical coastal periurban embayment (Eastern Australia). Journal of Geophysical Research: Oceans, 119(9), 6024-6045.

Pahlevan, N., Smith, B., Binding, C., Gurlin, D., Li, L., Bresciani, M., Giardino, C. (2020). Hyperspectral retrievals of phytoplankton absorption and chlorophyll-a in inland and nearshore coastal waters. Remote Sensing of Environment.

Park, J.-E., Park, K.-A. (2021). Application of Deep Learning for Speckle Removal in GOCI Chlorophyll-a Concentration Images (2012–2017). Remote Sensing, 13(4), 585.

Petus, C., Chust, G., Gohin, F., Doxaran, D., Froidefond, J.-M., Sagarminaga, Y. (2010). Estimating turbidity and total suspended matter in the Adour River plume (South Bay of Biscay) using MODIS 250-m imagery. Continental Shelf Research, 30(5), 379-392.

Petus, C., Collier, C., Devlin, M., Rasheed, M., McKenna, S. (2014a). Using MODIS data for understanding changes in seagrass meadow health: a case study in the Great Barrier Reef (Australia). Marine environmental research, 98, 68-85.

Petus, C., da Silva, E.T., Devlin, M., Wenger, A.S., Alvarez-Romero, J.G. (2014b). Using MODIS data for mapping of water types within river plumes in the Great Barrier Reef, Australia: towards the production of river plume risk maps for reef and seagrass ecosystems. Journal of environmental management, 137, 163-177.

Petus, C., Devlin, M., Thompson, A., McKenzie, L., Teixeira da Silva, E., Collier, C., Tracey, D., Martin, K. (2016). Estimating the Exposure of Coral Reefs and Seagrass Meadows to Land-Sourced Contaminants in River Flood Plumes of the Great Barrier Reef: Validating a Simple Satellite Risk Framework with Environmental Data. Remote Sensing, 8(3), 210.

Petus, C., Waterhouse, J., Lewis, S., Vacher, M., Tracey, D., Devlin, M. (2019). A flood of information: Using Sentinel-3 water colour products to assure continuity in the monitoring of water quality trends in the Great Barrier Reef (Australia). Journal of environmental management, 248, 109255.

Pickard, G.L., Donguy, J.-R., Hénin, C., Rougerie, F. (1977). A review of the physical oceanography of the Great Barrier Reef and western Coral Sea.

Plass, G.N., Kattawar, G.W., Catchings, F.E. (1973). Matrix operator theory of radiative transfer. 1: Rayleigh scattering. Applied optics, 12(2), 314-329.

Pope, R.M., Fry, E.S. (1997). Absorption spectrum (380–700 nm) of pure water. II. Integrating cavity measurements. Applied optics, 36(33), 8710-8723.

Pratchett, M.S., Caballes, C.F., Wilmes, J.C., Matthews, S., Mellin, C., Sweatman, H.P.A., Nadler, L.E., Brodie, J., Thompson, C.A., Hoey, J., Bos, A.R., Byrne, M., Messmer, V., Fortunato, S.A.V., Chen, C.C.M., Buck, A.C.E., Babcock, R.C., Uthicke, S. (2017). Thirty Years of Research on Crown-of-Thorns Starfish (1986–2016): Scientific Advances and Emerging Opportunities. Diversity, 9(4), 41.

Qi, L., Lee, Z., Hu, C., Wang, M. (2017). Requirement of minimal signal-to-noise ratios of ocean color sensors and uncertainties of ocean color products. Journal of Geophysical Research: Oceans, 122(3), 2595-2611.

Qin, Y., Brando, V.E., Dekker, A.G., Blondeau-Patissier, D. (2007). Validity of SeaDAS water constituents retrieval algorithms in Australian tropical coastal waters. Geophysical Research Letters, 34(21).

Qin, Y., Steven, A.D.L., Schroeder, T., McVicar, T.R., Huang, J., Cope, M., Zhou, S. (2019). Cloud Cover in the Australian Region: Development and Validation of a Cloud Masking, Classification and Optical Depth Retrieval Algorithm for the Advanced Himawari Imager. Frontiers in Environmental Science, 7(20).

Qiu, Z., Li, Z., Bilal, M., Wang, S., Sun, D., Chen, Y. (2018). Automatic method to monitor floating macroalgae blooms based on multilayer perceptron: Case study of Yellow Sea using GOCI images. Optics express, 26(21), 26810-26829.

Queensland Government. (2021). Water Monitoring Information Portal (WMIP). Streamflow data Retrieved from https://water-monitoring.information.qld.gov.au/ (accessed on 30/03/2021).

Ramon, D., Steinmetz, F., Jolivet, D., Compiègne, M., Frouin, R. (2019). Modeling polarized radiative transfer in the ocean-atmosphere system with the GPU-accelerated SMART-G Monte Carlo code. Journal of Quantitative Spectroscopy and Radiative Transfer, 222-223, 89-107.

Reichstein, M., Camps-Valls, G., Stevens, B., Jung, M., Denzler, J., Carvalhais, N., Prabhat. (2019). Deep learning and process understanding for data-driven Earth system science. Nature, 566(7743), 195-204.

Reichstetter, M., Fearns, P.R., Weeks, S.J., McKinna, L.I., Roelfsema, C., Furnas, M. (2015). Bottom reflectance in ocean color satellite remote sensing for coral reef environments. Remote Sensing, 7(12), 16756-16777.

Ricardo, G.F., Jones, R.J., Clode, P.L., Humanes, A., Negri, A.P. (2015). Suspended sediments limit coral sperm availability. Scientific Reports, 5(1), 18084.

Roesler, C.S., Perry, M.J. (1995). In sity phytoplankton absorption, fluorescence emission, and particulate backscattering spectra determined from reflectance. Journal of Geophysical Research, 100(C7).

Röttgers, R., Heymann, K., Krasemann, H. (2014). Suspended matter concentrations in coastal waters: Methodological improvements to quantify individual measurement uncertainty. Estuarine, Coastal and Shelf Science, 151, 148-155.

Rozanov, V.V., Buchwitz, M., Eichmann, K.U., de Beek, R., Burrows, J.P. (2002). Sciatran - a new radiative transfer model for geophysical applications in the 240–2400 NM spectral region: the pseudo-spherical version. Advances in Space Research, 29(11), 1831-1835.

Rozanov, V.V., Rozanov, A.V., Kokhanovsky, A.A., Burrows, J.P. (2014). Radiative transfer through terrestrial atmosphere and ocean: Software package SCIATRAN. Journal of Quantitative Spectroscopy and Radiative Transfer, 133, 13-71.

Ruddick, K., Neukermans, G., Vanhellemont, Q., Jolivet, D. (2014). Challenges and opportunities for geostationary ocean colour remote sensing of regional seas: A review of recent results. Remote Sensing of Environment, 146, 63-76.

Ruddick, K., Vanhellemont, Q., Yan, J., Neukermans, G., Wei, G., Shang, S. (2012). Variability of suspended particulate matter in the Bohai Sea from the geostationary Ocean Color Imager (GOCI). Ocean Science Journal, 47(3), 331-345.

Sathyendranath, S., Hoge, F.E., Platt, T., Swift, R.N. (1994). Detection of phytoplankton pigments from ocean color: improved algorithms. Applied optics, 33(6), 1081-1089.

Sathyendranath, S., Lazzara, L., Prieur, L. (1987). Variations in the spectral values of specific absorption of phytoplankton. Limnology and Oceanography, 32(2), 403-415.

Sathyendranath, S., Prieur, L., Morel, A. (1989). A three-component model of ocean colour and its application to remote sensing of phytoplankton pigments in coastal waters. International Journal of Remote Sensing, 10(8), 1373-1394.

Saulquin, B., Fablet, R., Bourg, L., Mercier, G., d'Andon, O.F. (2016). MEETC2: Ocean color atmospheric corrections in coastal complex waters using a Bayesian latent class model and potential for the incoming sentinel 3 — OLCI mission. Remote Sensing of Environment, 172, 39-49.

Schaale, M., Schroeder, T. (2013). An extended validation test for data input into parameterized retrieval algorithms.

Schaffelke, B., Carleton, J., Skuza, M., Zagorskis, I., Furnas, M.J. (2012). Water quality in the inshore Great Barrier Reef lagoon: Implications for long-term monitoring and management. Marine pollution bulletin, 65(4-9), 249-260.

Schaffelke, B., Mellors, J., Duke, N.C. (2005). Water quality in the Great Barrier Reef region: responses of mangrove, seagrass and macroalgal communities. Marine pollution bulletin, 51(1-4), 279-296.

Schiller, H., Doerffer, R. (1999). Neural network for emulation of an inverse model operational derivation of Case II water properties from MERIS data. International Journal of Remote Sensing, 20(9), 1735-1746.

Schiller, H., Doerffer, R. (2005). Improved Determination of Coastal Water Constituent Concentrations from MERIS Data. IEEE transactions on Geoscience and Remote Sensing, 43(7).

Schroeder, T. (2005). Fernerkundung von Wasserinhaltsstoffen in Küstengewässern mit MERIS unter Anwendung expliziter und impliziter Atmosphärenkorrekturverfahren. (Doctoral Thesis). Freie Universität Berlin.

Schroeder, T., Behnert, I., Schaale, M., Fischer, J., Doerffer, R. (2007a). Atmospheric correction algorithm for MERIS above case-2 waters. International Journal of Remote Sensing, 28(7), 1469-1486.

Schroeder, T., Devlin, M.J., Brando, V.E., Dekker, A.G., Brodie, J.E., Clementson, L.A., McKinna, L. (2012). Inter-annual variability of wet season freshwater plume extent into the Great Barrier Reef lagoon based on satellite coastal ocean colour observations. Marine pollution bulletin, 65(4-9), 210-223.

Schroeder, T., Lovell, J., King, E., Clementson, L., Scott, R. (2016). IMOS Ocean Colour Validation Report 2015-16, Report to the Integrated Marine Observing System (IMOS). CSIRO Oceans and Atmosphere.

Schroeder, T., Lovell, J., King, E., Clementson, L., Scott, R., (2017). IMOS Ocean Colour Validation Report 2016-17, Report to the Integrated Marine Observing System (IMOS). CSIRO Oceans and Atmosphere.

Schroeder, T., Lovell, J., King, E., Clementson, L., Scott, R. (2018). IMOS Ocean Colour Validation Report 2017-18, Report to the Integrated Marine Observing System (IMOS). CSIRO Oceans and Atmosphere.

Schroeder, T., Schaale, M., Fischer, J. (2007b). Retrieval of atmospheric and oceanic properties from MERIS measurements: A new Case-2 water processor for BEAM. International Journal of Remote Sensing, 28(24), 5627-5632.

Segal-Rozenhaimer, M., Li, A., Das, K., Chirayath, V. (2020). Cloud detection algorithm for multi-modal satellite imagery using convolutional neural-networks (CNN). Remote Sensing of Environment, 237, 111446.

Shettle, E.P., Fenn, R.W. (1979). Models for the aerosols of the lower atmosphere and the effects of humidity variations on their optical properties (AFGL-TR-79-0214, USAF). Environmental Research Papers. Airforce Geophysics Laboratory. Hanscom Airforce Base, Massachussets

Sirjacobs, D., Alvera-Azcárate, A., Barth, A., Lacroix, G., Park, Y., Nechad, B., Ruddick, K., Beckers, J.-M. (2011). Cloud filling of ocean colour and sea surface temperature remote sensing products over the Southern North Sea by the Data Interpolating Empirical Orthogonal Functions methodology. Journal of Sea Research, 65(1), 114-130.

Skerratt, J., Mongin, M., Baird, M., Wild-Allen, K., Robson, B., Schaffelke, B., Davies, C., Richardson, A., Margvelashvili, N., Soja-Wozniak, M. (2019). Simulated nutrient and plankton dynamics in the Great Barrier Reef (2011–2016). Journal of Marine Systems, 192, 51-74.

Skerratt, J., Soja-Wozniak, M., Baird, M.E., Mongin, M., Wild-Allen, K., Robson, B., Margvelashvili, N. (2020). A novel bio-optical model that allows incorporation of traditional plankton and remote sensing methods and observations and improves the assessment of biogeochemical processes. Paper presented at the Ocean Sciences Meeting 2020.

Soja-Woźniak, M., Baird, M., Schroeder, T., Qin, Y., Clementson, L., Baker, B., Boadle, D., Brando, V., Steven, A.D.L. (2019). Particulate Backscattering Ratio as an Indicator of Changing Particle Composition in Coastal Waters: Observations From Great Barrier Reef Waters. Journal of Geophysical Research: Oceans, 0(0).

Soja-Woźniak, M., Laiolo, L., Baird, M.E., Matear, R., Clementson, L., Schroeder, T., Doblin, M.A., Suthers, I.M. (2020). Effect of phytoplankton community size structure on remote-sensing reflectance and chlorophyll a products. Journal of Marine Systems, 211, 103400.

Spurr, R., Stamnes, K., Eide, H., Li, W., Zhang, K., Stamnes, J. (2007). Simultaneous retrieval of aerosols and ocean properties: A classic inverse modeling approach. I. Analytic Jacobians from the linearized CAO-DISORT model. Journal of Quantitative Spectroscopy and Radiative Transfer, 104(3), 428-449.

State of Queensland and Commonwealth of Australia, (2018a). Paddock to Reef Integrated Monitoring, Modelling and Reporting Program: Program Design 2018-2022., in: Government, Q. (Ed.), Brisbane, Australia.

State of Queensland and Commonwealth of Australia, (2018b). Reef 2050 Water Quality Improvement Plan 2017-2022., in: Government, Q. (Ed.), Brisbane, Australia.

State of Queensland and Commonwealth of Australia. (2021). Reef Report Cards. Retrieved from https://www.reefplan.qld.gov.au/tracking-progress/reef-report-card (accessed on 02/04/2021).

Stavn, R.H., Rick, H.J., Falster, A.V. (2009). Correcting the errors from variable sea salt retention and water of hydration in loss on ignition analysis: Implications for studies of estuarine and coastal waters. Estuarine, Coastal and Shelf Science, 81(4), 575-582.

Steinmetz, F., Deschamps, P.-Y., Ramon, D. (2011). Atmospheric correction in presence of sun glint: application to MERIS. Optics express, 19(10), 9783-9800.

Stephens, G.L., Li, J., Wild, M., Clayson, C.A., Loeb, N., Kato, S., L'ecuyer, T., Stackhouse Jr, P.W., Lebsock, M., Andrews, T. (2012). An update on Earth's energy balance in light of the latest global observations. Nature Geoscience, 5(10), 691-696.

Steven, A., Hodge, J., Cannard, T., Carlin, G., Franklin, H., McJannet, D., Moesender, C., Searle, R. (2014). Continuous Water Quality Monitoring on the Great Barrier Reef. CSIRO Final Report to Great Barrier Reef Foundation. CSIRO.

Steven, A.D., Baird, M.E., Brinkman, R., Car, N.J., Cox, S.J., Herzfeld, M., Hodge, J., Jones, E., King, E., Margvelashvili, N., Robillot, C., Robson, B., Schroeder, T., Skerratt, J., Tickell, S., Tuteja, N., Wild-Allen, K., Yu, J. (2019). eReefs: an operational information system for managing the Great Barrier Reef. Journal of Operational Oceanography, 12(sup2), S12-S28.

Stramska, M., Petelski, T. (2003). Observations of oceanic whitecaps in the north polar waters of the Atlantic. Journal of Geophysical Research: Oceans, 108(C3).

Stramski, D., Boss, E., Bogucki, D., Voss, K.J. (2004). The role of seawater constituents in light backscattering in the ocean. Progress in Oceanography, 61(1), 27-56.

Strickland, J., Parsons, T. (1972). A practical handbook of seawater analysis. Ottawa, Ontario, Fisheries Research Board of Canada.

Tabata, T., Andou, A., Bessho, K., Date, K., Dojo, R., Hosaka, K., Mori, N., Murata, H., Nakayama, R., Okuyama, A. (2016). Himawari-8/AHI latest performance of navigation and calibration. Paper presented at the Earth Observing Missions and Sensors: Development, Implementation, and Characterization IV.

Tanaka, N., Kishino, M., Doerffer, R., Schiller, H., Oishi, T., Kubota, T. (2004). Development of a Neural Network Algorithm for Retriev- ing Concentrations of Chlorophyll, Suspended Matter and Yellow Substance from Radiance Data of the Ocean Color and Temperature Scanner. Journal of Oceanography, 60, 519-530.

Thompson, A., Costello, P., Davidson, J., Logan, M., Coleman, G. (2021). Marine Monitoring Program: Annual report for inshore coral reef monitoring 2018–19.

Thompson, A., Schroeder, T., Brando, V.E., Schaffelke, B. (2014). Coral community responses to declining water quality: Whitsunday Islands, Great Barrier Reef, Australia. Coral Reefs, 33(4), 923-938.

Thompson, R.O.R.Y., Golding, T.J. (1981). Tidally induced 'upwelling' by the Great Barrier Reef. Journal of Geophysical Research: Oceans, 86(C7), 6517-6521.

Thomson, R.E., Wolanski, E.J. (1984). Tidal period upwelling within Raine island entrance great barrier reef. Journal of Marine Research, 42(4), 787-808.

Thursby, G.B., Rego, S., Keith, D. (2015). Data report for calibration of a bio-optical model for Narragansett Bay. US Environmental Protection Agency, Office of Research and Development. https://cfpub.epa.gov/si/si_public_file_download.cfm?p_download_id=525010&Lab=NHEERL

Tian, L., Zeng, Q., Tian, X., Li, J., Wang, Z., Li, W. (2016). Water environment remote sensing atmospheric correction of Geostationary Ocean Color Imager data over turbid coastal waters in the Bohai Sea using artificial neural networks. Current Science, 110(6), 1079-1085.

Tilstone, G., Moore, G., Sørensen, K., Doerfeer, R., Røttgers, R., Ruddick, K., Pasterkamp, R., Jørgensen, P. (2002). Regional validation of MERIS chlorophyll products in North Sea coastal waters. REVAMP Methodologies EVGI-CT-2001-00049.

Toming, K., Kutser, T., Uiboupin, R., Arikas, A., Vahter, K., Paavel, B. (2017). Mapping water quality parameters with Sentinel-3 Ocean and Land Colour Instrument imagery in the Baltic Sea. Remote Sensing, 9(10).

Torres-Huitzil, C., Girau, B. (2017). Fault and error tolerance in neural networks: A review. IEEE Access, 5, 17322-17341.

Tracey, D., Waterhouse, J., Da Silva, E. (2016). Preliminary investigation of alternative approaches for the Reef Plan Report Card Water Quality Metric report. Great Barrier Reef Marine Park Authority.

Trees, C.C., Kennicutt II, M.C., Brooks, J.M. (1985). Errors associated with the standard fluorimetric determination of chlorophylls and phaeopigments. Marine Chemistry, 17(1), 1-12.

Trenberth, K.E., Fasullo, J.T., Kiehl, J. (2009). Earth's global energy budget. Bulletin of the American Meteorological Society, 90(3), 311-323.

van de Hulst, H.C. (1963). A new look at multiple scattering. NASA Institute for Space Studies, Goddard Space Flight Center.

Van Heukelem, L., Thomas, C.S. (2001). Computer-assisted high-performance liquid chromatography method development with applications to the isolation and analysis of phytoplankton pigments. Journal of Chromatography A, 910(1), 31-49.

Vanhellemont, Q. (2019). Adaptation of the dark spectrum fitting atmospheric correction for aquatic applications of the Landsat and Sentinel-2 archives. Remote Sensing of Environment, 225, 175-192.

Vanhellemont, Q., Neukermans, G., Ruddick, K. (2014). Synergy between polar-orbiting and geostationary sensors: Remote sensing of the ocean at high spatial and high temporal resolution. Remote Sensing of Environment, 146, 49-62.

Vanhellemont, Q., Ruddick, K. (2015). Advantages of high quality SWIR bands for ocean colour processing: Examples from Landsat-8. Remote Sensing of Environment, 161, 89-106.

Wang, M., Bailey, S.W. (2001). Correction of sun glint contamination on the SeaWiFS ocean and atmosphere products. Applied optics, 40(27), 4790-4798.

Wang, M., Shi, W. (2007). The NIR-SWIR combined atmospheric correction approach for MODIS ocean color data processing. Optics express, 15(24), 15722-15733.

Wang, S., Mao, Y., Zheng, L., Qiu, Z., Bilal, M., Sun, D. (2020). Remote sensing of water turbidity in the Eastern China Seas from Geostationary Ocean Colour Imager. International Journal of Remote Sensing, 41(11), 4080-4101.

Waterhouse, J., Brodie, J., Tracey, D., Smith, R., VanderGragt, M., Collier, C., Petus, C., Baird, M., Kroon, F., Mann, R. (2017a). 2017 Scientific Consensus Statement: land use impacts on the Great Barrier Reef water quality and ecosystem condition, Chapter 3: the risk from anthropogenic pollutants to Great Barrier Reef coastal and marine ecosystems.

Waterhouse, J., Lønborg, C., Logan, M., Petus, C., Tracey, D., Lewis, S., Howley, C., Harper, E.-L., Tonin, H., Skuza, M., Doyle, J., Costello, P., Davidson, J., Gunn, K., Wright, M., Zagorskis, I., Kroon, F., Gruber, R. (2018). Marine Monitoring Program: Annual report for inshore water quality monitoring 2016-2017. Report for the Great Barrier Reef Marine Park Authority. Townsville

Waterhouse, J., Schaffelke, B., Bartley, R., Eberhard, R., Brodie, J., Thorburn, P., Rolfe, J., Ronan, M., Taylor, B., Star, M., Kroon, F.J., (2017b). Scientific Consensus Statement Summary: Land Use Impacts on Great Barrier Reef Water Quality and Ecosystem Condition. State of Queensland, Townsville, Australia.

Waters, D.K., Carroll, C., Ellis, R., Hateley, L., McCloskey, G.L., Packett, R., Dougall, C. (2014). Modelling reductions of pollutant loads due to improved management practices in the Great Barrier Reef catchments – Whole of GBR. Toowoomba, Queensland

Weeks, S., Werdell, P., Schaffelke, B., Canto, M., Lee, Z., Wilding, J., Feldman, G. (2012). Satellite-Derived Photic Depth on the Great Barrier Reef: Spatio-Temporal Patterns of Water Clarity. Remote Sensing, 4(12), 3781-3795.

Werdell, P.J., Bailey, S.W. (2005). An improved in-situ bio-optical data set for ocean color algorithm development and satellite data product validation. Remote Sensing of Environment, 98(1), 122-140.

Whitney, J.L., Gove, J.M., McManus, M.A., Smith, K.A., Lecky, J., Neubauer, P., Phipps, J.E., Contreras, E.A., Kobayashi, D.R., Asner, G.P. (2021). Surface slicks are pelagic nurseries for diverse ocean fauna. Scientific Reports, 11(1), 3197.

Wolanski, E. (1994). Physical oceanographic processes of the Great Barrier Reef. Boca Raton, CRC Press.

Wolanski, E., Drew, E., Abel, K.M., O'Brien, J. (1988). Tidal jets, nutrient upwelling and their influence on the productivity of the alga Halimeda in the Ribbon Reefs, Great Barrier Reef. Estuarine, Coastal and Shelf Science, 26(2), 169-201.

Wolanski, E., Jones, M., Williams, W.T. (1981). Physical Properties of Great Barrier Reef Lagoon Waters near Townsville. II Seasonal Variations
. Australian Journal of Freshwater Research, 32, 321-334.

Wolanski, E., Mazda, Y., King, B., Gay, S. (1990). Dynamics, flushing and trapping in Hinchinbrook channel, a giant mangrove swamp, Australia. Estuarine, Coastal and Shelf Science, 31(5), 555-579.

Wolanski, E., Spagnol, S. (2000). Sticky Waters in the Great Barrier Reef. Estuarine, Coastal and Shelf Science, 50(1), 27-32.

Wolff, N.H., Mumby, P.J., Devlin, M., Anthony, K.R. (2018). Vulnerability of the Great Barrier Reef to climate change and local pressures. Global change biology, 24(5), 1978-1991.

Wooldridge, S.A. (2017). Preventable fine sediment export from the Burdekin River catchment reduces coastal seagrass abundance and increases dugong mortality within the Townsville region of the Great Barrier Reef, Australia. Marine pollution bulletin, 114(2), 671-678.

World Climate Research Programme, W. (1986). A preliminary cloudless standard atmosphere for radiation computation. Radiation Comission WCP-112. Int. Ass. For Meteorological and Atmospheric Physics https://www.wcrp-climate.org/

Xiao, Y., Wang, X.H., Ritchie, E.A., Rizwi, F., Qiao, L. (2019). The development and evolution of the Burdekin River estuary freshwater plume during Cyclone Debbie (2017). Estuarine, Coastal and Shelf Science, 224, 187-196.

Yang, H., Han, H.-J., Heo, J., Jeong, J., Lee, T., Hu, W., Kwak, S. (2018). Ocean Color Algorithm Development Environment for High-Speed Data Processing of GOCI-II. IGARSS 2018 - 2018 IEEE International Geoscience and Remote Sensing Symposium, 7968-7971.

Yanyan, K., Xianrong, D., Xiaoping, G. (2018). Using Geostationary Ocean Color Imager to Map the Diurnal Dynamics of Suspended Sediment Concentration in Estuary Area. Journal of Coastal Research, 85, 101-105.

Young, A. (1980). Revised depolarization corrections for atmospheric extinction. Applied optics, 19(20), 3427-3428.

Young, I.R., Black, K.P., Heron, M.L. (1994). Circulation in the Ribbon Reef Region of the Great Barrier Reef. Continental Shelf Research, 14(2), 117-142.

Yu, B., Xu, L., Peng, J., Hu, Z., Wong, A. (2020). Global chlorophyll- a concentration estimation from moderate resolution imaging spectroradiometer using convolutional neural networks. Journal of Applied Remote Sensing, 14(3).

Yu, F., Wu, X. (2016). Radiometric Inter-Calibration between Himawari-8 AHI and S-NPP VIIRS for the Solar Reflective Bands. Remote Sensing, 8(3).

Zaneveld, J.R.V., Twardowski, M.J., Barnard, A., Lewis, M.R. (2005). Introduction to radiative transfer. Remote sensing of coastal aquatic environments, 1-20.

Zhang, M., Tang, J., Song, Q., Dong, Q. (2010). Backscattering ratio variation and its implications for studying particle composition: A case study in Yellow and East China seas. Journal of Geophysical Research: Oceans, 115(C12).

Zhang, T. (2003). Retrieval of Oceanic Constituents with Artificial Neural Network Based on Radiative Transfer Simulation Techniques. (Doctoral Thesis). Freie Universität Berlin.

Zhang, T., Fell, F., Fischer, J., (2002). Modelling the backscattering ratio of marine particles in Case-2 waters, in Proceedings of the Ocean Optics XVI, Santa Fe, USA.

Zhang, T., Fell, F., Liu, Z.S., Preusker, R., Fischer, J., He, M.X. (2003). Evaluating the performance of artificial neural network techniques for pigment retrieval from ocean color in Case I waters. Journal of Geophysical Research: Oceans, 108(C9).

Zhang, X., Hu, L., He, M.-X. (2009). Scattering by pure seawater: effect of salinity. Optics express, 17(7), 5698-5710.

Zhao, D., Feng, L. (2020). Assessment of the Number of Valid Observations and Diurnal Changes in Chl-a for GOCI: Highlights for Geostationary Ocean Color Missions. Sensors (Basel, Switzerland), 20(12), 3377.

Zorrilla, N.A., Vantrepotte, V., Ngoc, D.D., Huybrechts, N., Gardel, A. (2019). Automated SWIR based empirical sun glint correction of Landsat 8-OLI data over coastal turbid water. Optics express, 27(8), A294-A318.